Metabolite Profiles in the Investigation of Childhood Brain Tumours

By Christopher Daniel Bennett

A thesis submitted to
the University of Birmingham for the Degree of
DOCTOR OF PHILOSOPHY

Institute of Cancer and Genomic Sciences
College of Medical and Dental Sciences
University of Birmingham
November 2018

Abstract

Paediatric brain tumours are the leading cause of cancer mortality in 0-14 year olds. New diagnostic and prognostic tools are required, as are new therapeutic targets to improve survival. Metabolism is a powerful characterising feature of tumours, with potential to aid the management of these diseases.

This thesis acquires metabolite profiles from paediatric brain tumour tissue, primarily by High Resolution Magic Angle Spinning NMR (HR-MAS), which are statistically analysed.

Firstly, metabolite profiles obtained by HR-MAS were shown to accurately and robustly classify tissue from the three main cerebellar tumours. When compared to current histological intraoperative testing, metabolites profiles correctly diagnosed histologically ambiguous tumours.

Secondly, survival analysis identified markers of prognosis. High glutamine concentration was associated with better clinical outcome both in terms of overall survival in a mixed tumour cohort and progression-free survival in a cohort of pilocytic astrocytomas.

Finally, metabolic pathway analysis identified pathways altered by cerebellar tumours relative to each other, supported with mass spectrometry and independent gene expression data. Pathways identified include alanine, aspartate and glutamate metabolism, taurine and hypotaurine metabolism and glycine, serine and threonine metabolism.

Considered together, this work provides strong reasoning for incorporating tissue metabolite profiles into clinical workflows for paediatric brain tumours.

Dedication

This thesis is dedicated to my wife Lillie, whose ceaseless love and support has been integral to the completion of this work.

Declaration

I declare that the work presented in this thesis is my own and that I participated in the design of the study, analysis of the data and writing of this thesis. The following were undertaken in collaboration:

1. The HR-MAS protocol was developed by Dr Martin Wilson.
2. Details concerning tumour specific clinical management of patients were written in consultation with Professor Andrew Peet.
3. Dr Simrandip Gill and Dr Sarah Kohe assisted in the assignment and quantification of the HR-MAS spectra.
4. Clinical pilocytic astrocytoma BRAF fusion and mutation testing was performed and reported by the Division of Neuropathology, University College London Institute of Neurology for chapter 5.
5. Dr Neelakshi Ghosh compiled pilocytic astrocytoma progression free survival data and Dr Adam Oates measured residual pilocytic astrocytoma tumour volume from clinical post-operative MRI scans
6. The Phenome Centre Birmingham performed the metabolite extraction and acquired the mass spectrometry data on post HR-MAS brain tumour samples for chapter 6.

Acknowledgements

First and foremost, I would like to give my sincere gratitude to my supervisors Professor Andrew Peet, Dr Sarah Kohe and Dr Daniel Tennant for their limitless wisdom, patience and guidance. Furthermore, I would like to thank all members of the Children's Brain Tumour Research Team based at Birmingham Children's Hospital, who provide endless support, discussion and coffee. It has been a true pleasure to work with you all.

I would also like to thank Action Medical Research, the Brain Tumour Charity and the NIHR for funding this project and allowing me to present the work at international conferences.

Further thanks go to the staff at the Henry Wellcome Building for NMR at the University of Birmingham, for their help in maintaining the spectrometer and troubleshooting technical problems. In addition, the staff of the Histopathology Department at Birmingham Children's Hospital were instrumental to this work through storing and retrieving archived tissue in a timely manner.

Finally, I would like to thank my family for their support during this PhD, especially my wife Lillie who has remained loving and understanding at all times. I hope I continue to make you proud.

Publications

First author journal publications

Bennett CD, Kohe SE, Gill SK, Davies NP, Wilson M, Storer LCD, et al. Tissue metabolite profiles for the characterisation of paediatric cerebellar tumours. Scientific reports. 2018;8(1):11992.

Named author journal publications

Kohe SE, **Bennett CD**, Gill SK, Wilson M, McConville C, Peet AC. Metabolic profiling of the three neural derived embryonal pediatric tumors retinoblastoma, neuroblastoma and medulloblastoma, identifies distinct metabolic profiles. Oncotarget. 2018;9(13):11336-51.

First author oral presentations

24th British Chapter ISMRM Postgraduate Symposium, GSK, Stevenage, April 2015; **Bennett CD**, Gill SK, Kohe S, Wilson MP, Davies NP, Arvanitis TN, Peet AC; Discrimination of Medulloblastoma and Ependymoma using HR MAS of ex vivo brain tumour tissue.

First author conference abstracts

1. 17th International Symposium on Pediatric Neuro-Oncology, Liverpool, 2016; **Bennett CD**, Gill SK, Kohe S, Zarinabad N, Davies NP, Wilson M, Storer L, Ritzmann T, Paine S, Scott , Nicklaus I, Grundy RG, Peet AC; Tissue metabolite profiles in the characterisation and diagnosis of childhood posterior fossa tumours.

2. 18th International Symposium on Pediatric Neuro-Oncology, Denver, 2018; **Bennett CD**, Kohe SE, Gill SK, Davies NP, Storer LCD, Ritzmann T, Dunn WB, Tennant DA, Grundy RG, Peet AC; Mass spectrometry of common cerebellar tumours identifies differences in metabolism
3. 18th International Symposium on Pediatric Neuro-Oncology, Denver, 2018; **Bennett CD**, Kohe SE, Gill SK, Ghosh N, Manias K, Oates A, English M, Adamski J, Tennant DA, Peet AC; Ex vivo tissue metabolite profiles predict progression free survival in paediatric cerebellar pilocytic astrocytomas.

Named author conference abstracts

1. 17th International Symposium on Pediatric Neuro-Oncology, Liverpool, 2016; Gill SK, **Bennett CD**, Kohe S, Wilson M, Davies NP, Arvanitis TN, Peet AC; Metabolism as a predictor of survival in children's brain tumours
2. 17th International Symposium on Pediatric Neuro-Oncology, Liverpool, 2016; Kohe S, Gill SK, Hicks D, Schwalbe EC, Crosier S, Storer L, Lourdusamy A, **Bennett CD**, Wilson M, Bailey S, Williamson D, Grundy RG, Clifford SC, Peet AC; Identification of medulloblastoma molecular subgroups using metabolite profiles.
3. 18th International Symposium on Pediatric Neuro-Oncology, Denver, 2018; Kohe SE, Babourina-Brooks B, Scerif F, Hicks D, Schwalbe EC, Crosier S, Lindsey J, Adiamah M, Storer LCD, Lourdusamy A, Gill SK, **Bennett CD**, Wilson M, Avula S, Mitra D, Dineen R, Bailey S, Williamson D, Grundy RG, Clifford SC, Peet AC; In-vivo metabolite profiles for the non-invasive and rapid identification of molecular subgroup in medulloblastoma.

4. 18th International Symposium on Pediatric Neuro-Oncology, Denver, 2018; Ghosh N, Manias K, **Bennett CD**, Oates A, English M, Peet AC, Adamski J; Residual tumour size as a predictor of progression for paediatric low-grade glioma.

Contents

List of figures

List of tables

Abbreviations

AA – Anaplastic astrocytoma

Ace - Acetate

ACPP – Atypical choroid plexus papilloma

Ala - Alanine

Asc - Ascorbate

Asp - Aspartate

ATRT – Atypical Teratoid/Rhabdoid Tumour

Cho - Choline

CPC – Choroid plexus carcinoma

CPP – Choroid plexus papilloma

Cr - Creatine

DNET – Dysembryoplastic neuro-ectodermal tumour

EP - Ependymoma

GABA – Gamma aminobutyric acid

GBM – Glioblastoma multiforme

GG – ganglioglioma

Glc - Glucose

Gln - Glutamine

Glu - Glutamate

Gly - Glycine

GPC - Glycerophosphocholine

GSH – Glutathione

H&E – Haematoxylin and eosin

HR-MAS – High Resolution Magic Angle Spinning NMR

hTau – hypotaurine

IHC - Immunohistochemistry

Iso - Isoleucine

Lac - Lactate

Leu - Leucine

MB - Medulloblastoma

mIns – Myo-inositol

MRI - Magnetic Resonance Imaging

MRS – Magnetic Resonance Spectroscopy

NAA – N-acetyl aspartate

NMR – Nuclear Magnetic Resonance

PA – Pilocytic astrocytoma

PCh - Phosphocholine

PNET – Primitive neuroepithelial tumour

Ser - Serine

sIns – Scyllo-inositol

Suc - Succinate

Tau - taurine

UPLC-MS – Ultra performance liquid chromatography mass spectrometry

Val - Valine

CHAPTER 1: Introduction

1.1 Introduction

Childhood brain tumours are the leading cause of cancer related death in childhood and a significant source of morbidity (1). In order to improve survival and reduce the neurological deficits suffered by these patients, new methods are needed to improve diagnosis of tumours, identify those that are likely to follow an aggressive clinical course, and identify novel therapeutic targets.

Metabolism is a hallmark of cancer, altered in tumour tissue to allow an uncontrolled increase in biomass (2). As a tumours' metabolism in part depends upon the underlying drivers of the cancer, metabolism is a strong characterising feature of tumours (3). Additionally, as tumours adapt their metabolism to augment their growth, metabolite profiles can identify more aggressive disease (4). Metabolite profiles of tumours therefore have utility in the clinical management of patients, through improved diagnosis of tumours and identifying patients with higher risk disease.

The altered metabolism of tumours can be visualised and quantified by Magnetic Resonance Spectroscopy (MRS), which can measure the concentration of biochemical intermediaries, or metabolites, from a region of interest in the brain non-invasively during a patient's clinical MR imaging (5). These studies are low resolution, and limit the metabolite information that can be gained from the tumour. Studies performed on resected tissue using High Resolution Magic Angle Spinning Nuclear Magnetic Resonance (HR-MAS), are capable of accurately quantifying known metabolites as well as others not readily observed *in vivo*, and have the potential to aid in the clinical management of paediatric brain tumour patients (6, 7). Furthermore, the use of historic tissue allows the construction of larger cohorts than *in vivo* spectroscopic studies in real time, where large trials are required to accrue large enough cohorts. Studies such as these allow robust identification of markers of diagnosis, prognosis, and have the potential to identify novel therapeutic targets (8) which, when combined, promise to help improve the survival rate of paediatric brain tumour patients.

1.2 Brain tumour background

Paediatric cancers are the leading cause of death from illness from the ages of 1 to 14 (1) with an incidence rate of approximately 160 cases per one million 0-14 year olds in the UK. Males are more likely to be diagnosed than females, and the under-five age group has the highest incidence of cancer for both sexes (9). Brain tumours are the most common solid tumours presenting in children, accounting for approximately 25% of new cancer cases in the UK (around 400 new cases a year) (**Figure 1.1**). They are the leading cause of cancer related deaths in this population, with 5-year overall survival for brain tumours as a group reported to be around 70% (2). Individual tumour types have distinct prognoses associate with them, as will be discussed later; whilst some tumours have a very good survival others have dismal outcomes. Tumours can occur in all anatomical compartments of the brain (**Figure 1.2**). Although the leading cause of cancer death in children, they are relatively rare and therefore difficult to study.

Little is understood about the pathogenesis of paediatric brain tumours. Inherited cancer predisposition syndromes have been associated with some diagnoses; for example, Neurofibromatosis type I (NF1) is associated with pilocytic astrocytomas, whilst Gorlin syndrome is associated with sonic hedgehog subtype medulloblastoma (more examples of predisposition syndromes can be found in a review by Bleeker et al (10)). It has been suggested that predisposing germline mutations are present in 7-8% of paediatric brain tumours (11), implying >90% of cases are caused by de novo genetic events. Therapeutic ionising radiation is the only established risk factor associated with brain tumour development; however, the modulation of risk by factors such as parental age, nervous system anomalies at birth, diagnostic ionising radiation, prenatal vitamin supplements and residential pesticide use are suggested (12).

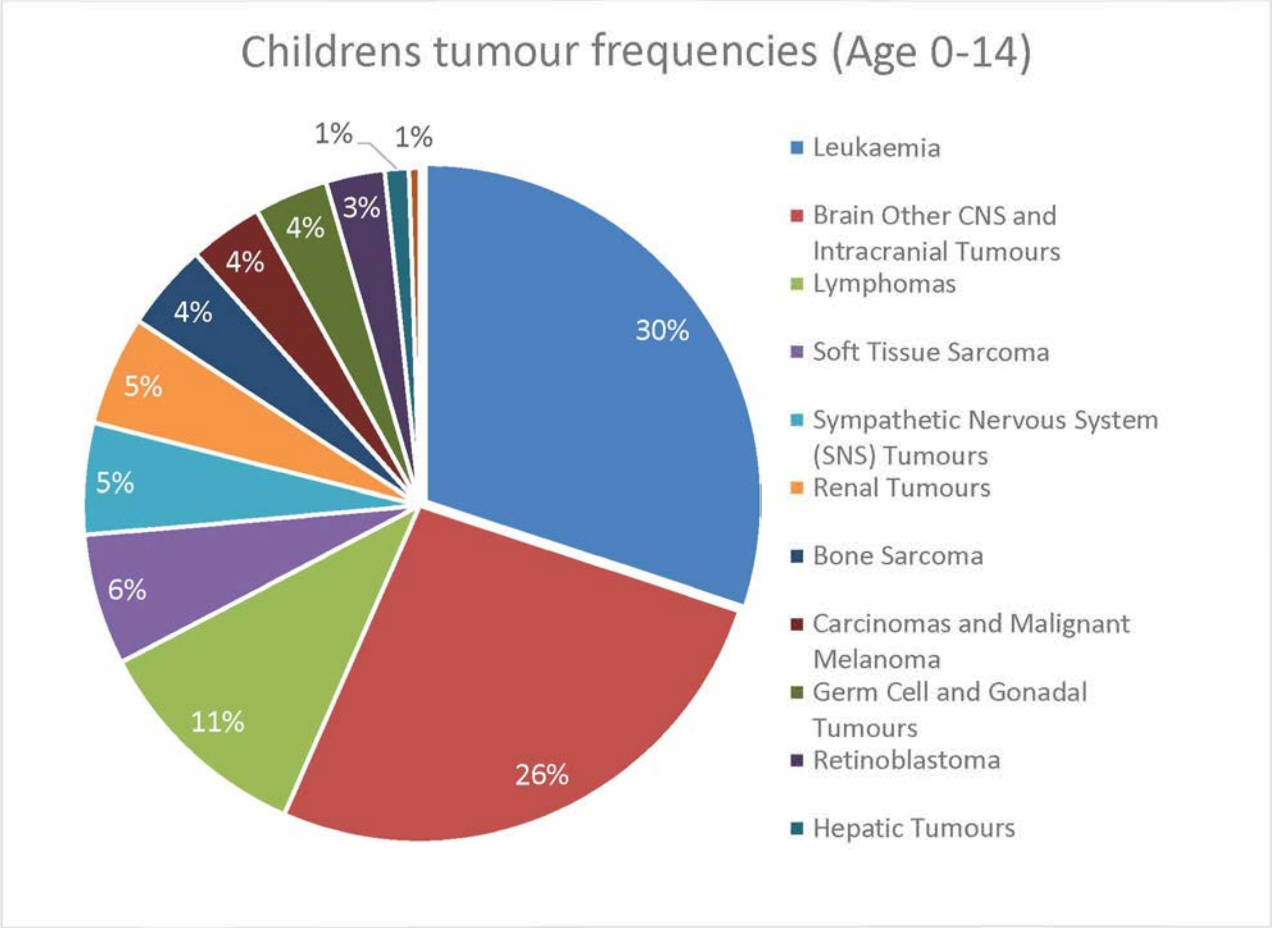

Figure 1.1 – The frequency of paediatric cancers arising in 0–14 year olds in the UK. Brain tumours are the most common solid tumours in children, second only to leukaemia in cancer frequencies. Figure produced with data from Cancer Research UK (13).

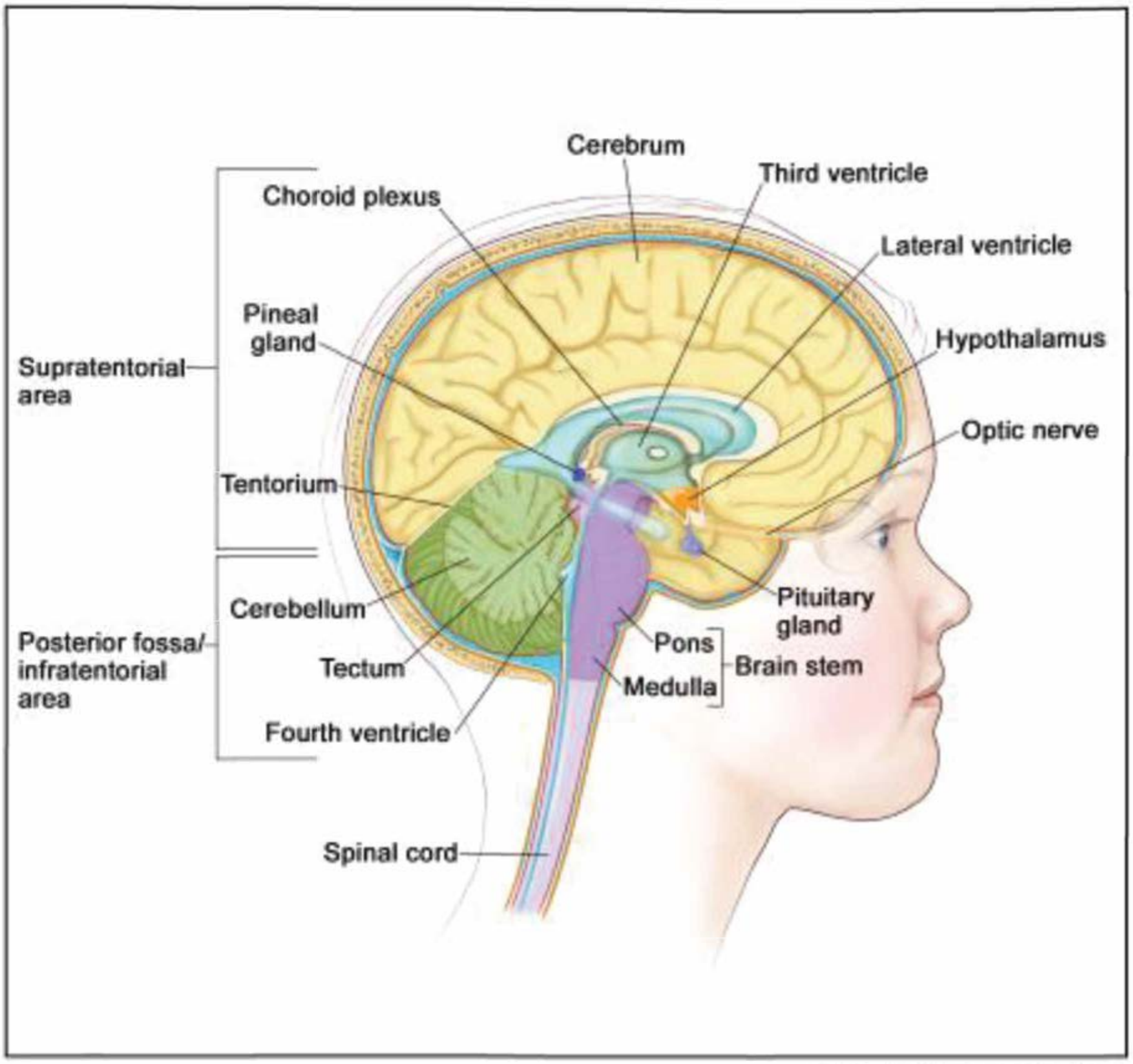

Figure 1.2 – basic diagram of brain anatomy. The posterior fossa of the brain contains the cerebellum and the brain stem. The supratentorial compartment is the part of the brain above the tentorium, and includes cerebral hemispheres and other forebrain structures (14).

Paediatric tumours are currently classified based upon observable morphological features of tumour tissue under a light microscope (15) and graded on a scale of I to IV according to the aggressiveness of the lesion, with Grade I tumours being the least aggressive and Grade IV the most aggressive (7). Features assessed for grading include nuclear pleomorphism, cellularity, mitotic rate, necrosis and microvascular proliferation. Paediatric brain tumours are a diverse group of tumours (**Figure 1.3**) broadly classed as gliomas, tumours derived from the non-neuronal cells in the CNS, and embryonal tumours, which comprise of undifferentiated embryonal cells.

1.2.1 Gliomas

Gliomas are the most common group of brain tumours, accounting for over 50% of cases. A range of tumour diagnoses and grades are included in this group. Astrocytomas are the most common group of tumours presenting in children, generally being further separated into low grade and high-grade groups. Low grade gliomas include WHO Grade I and II tumours whilst high-grade gliomas include WHO Grade III and IV tumours. Treatment for these tumours varies according to diagnosis. The most common entities are introduced further below.

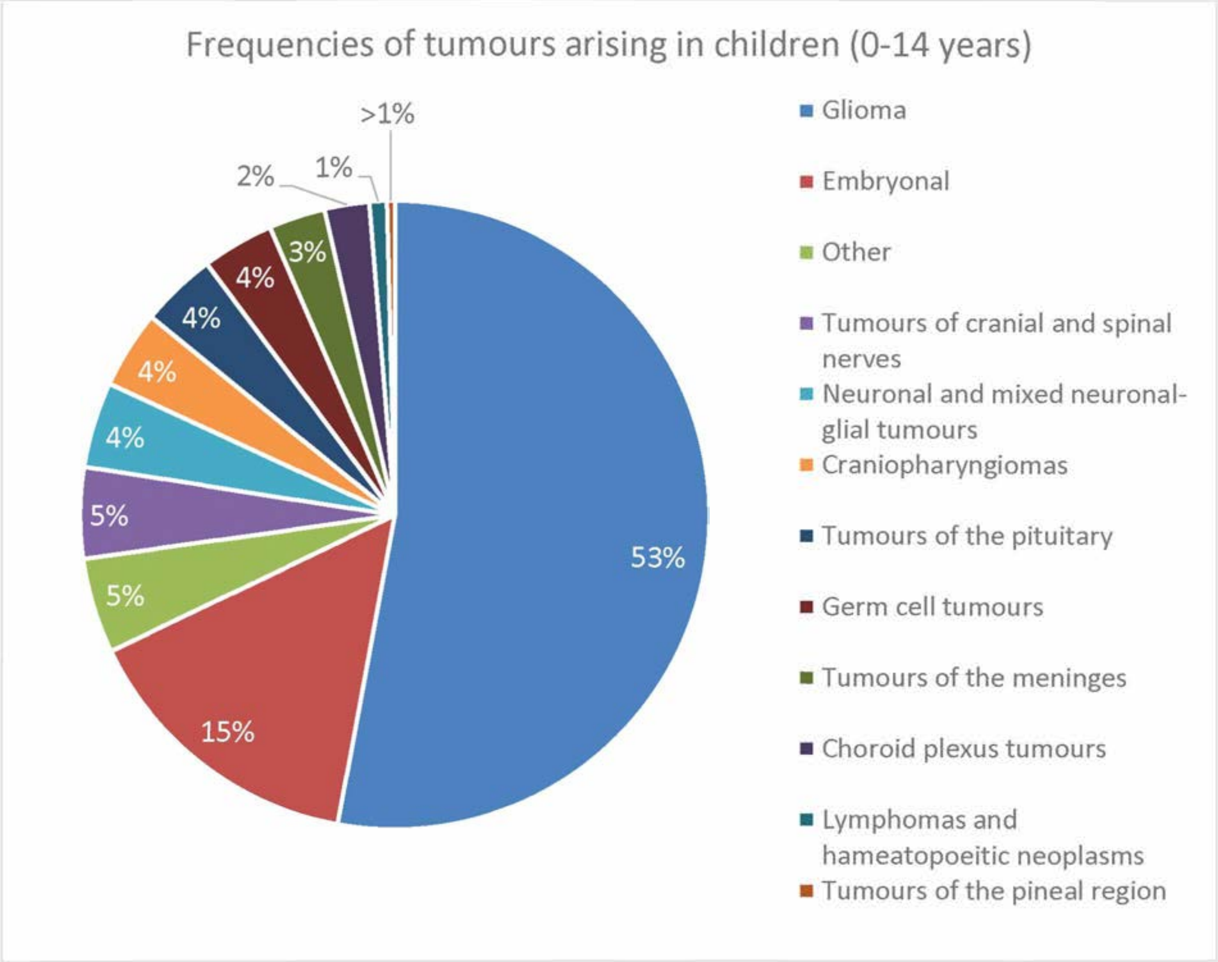

Figure 1.3 – The frequencies of brain tumours occurring in children between the ages of 0 and 14. Each section represents a histological group of tumours and does not represent individual diagnoses. Figure produced using data from CBTRUS (9).

1.2.1.1 Pilocytic astrocytoma (PA)

PAs are the most common brain tumour type diagnosed in children accounting for approximately 18% of brain tumour diagnoses (9). Prognosis for patients is considered favourable; 5-year overall survival has been reported to be over 90% and consequently it is graded as WHO Grade I. These tumours grow slowly and rarely invade local tissue or metastasise; however, aggressive behaviour is a possibility and has been reported (16). PAs can occur throughout the CNS, but most commonly arises in the cerebellum and optic pathway. Children diagnosed with NF1 are predisposed to developing PAs; 15% of NF1 patients develop PAs, usually arising along the optic pathway (17, 18).

Where a patient is NF1 negative, PAs are characterised by genetic abnormalities involving the BRAF gene. Most commonly, a duplication of a region on chromosome 7 creates a BRAF-KIAA:1549 fusion gene where the regulatory region of BRAF is replaced (19, 20). BRAF-KIAA:1549 fusion genes are reported in 55-80% of spontaneous PAs (21). The well described BRAF V600E mutation is occasionally observed in PA, as are other novel BRAF fusions and mutations in upstream signalling genes (22-24). As all known recurring mutations occur in the MAPK pathway, it is often considered a single pathway disease. The frequency of alterations varies according to anatomical location; BRAF:KIAA1549 fusions are observed in around 90% of cerebellar cases but are less frequent in supratentorial locations .

Treatment for PA commonly involves maximum safe resection when the tumour is in a surgically favourable position. Further treatment may be recommended for incomplete resections or upon progression of disease and depends on age, symptoms and NF1 status. Chemotherapy is commonly the first line of treatment where surgical resection is not possible with focal radiotherapy being reserved for patients with resistant disease but avoided in the young and those with NF1. There is increasing interest in replacing conventional radiotherapy with proton therapy. Cerebellar tumours experience a high rate of total resection because of relatively easy access and often require no further treatment. Supratentorial tumours are more difficult to manage as the tumour often occurs along or within delicate structures such as the optic pathway and hypothalamus and many have multiple courses of chemotherapy.

1.2.1.2 Other low Grade Gliomas

Low grade gliomas are a heterogeneous group generally defined as WHO grade I or II glial tumours. PAs are included in this group and are by far the most common. Other entities include diffuse astrocytomas, pleomorphic xanthoastrocytomas and oligodendrogliomas. This group can be extended to include other rare neuronal, mixed glial-neuronal tumours such as gangliogliomas and dysembryoplastic neuroepithelial tumours.

The majority of low-grade gliomas are driven by mutations in the MAPK pathway, with the BRAF V600E being a commonly observed recurrent mutation. Upstream of BRAF, FGFR mutations and fusions are also observed, which cause constitutive activation of the MAPK signalling cascade. Other alterations have been documented outside of the MAPK signalling cascade, including changes in MYB amplifications and IDH1/2 mutations (25), although these are more common in adults.

Although a very heterogeneous group, low grade gliomas are treated in a similar manner to PAs; surgery is the first line treatment and, where complete resection is achieved, prognosis tends to be good. Tumours for which complete resection is not possible are managed with chemotherapy regimens combining vincristine and carboplatin for younger patients and radiotherapy for older patients. Some low grade gliomas progress to higher grade tumours but this is mainly restricted to a small group of grade II diffuse astrocytomas. It should be noted that the more common aggressive midline gliomas may appear to be low grade on a small biopsy.

1.2.1.3 High grade gliomas

High grade gliomas are a group of WHO Grade III and IV glial tumours consisting mainly of astrocytomas and a small number of oligodendrogliomas. The grading is determined by the degree of nuclear atypia, cellularity, proliferation, necrosis and pseudo-palisading. Historically poorly understood, the recent identification of recurring mutations in histone 3 variant 3 (H3K27M, H3G34R/V) and other genes involved in epigenetic regulation is increasing the understanding of these tumours (26). The prognosis for high grade glioma remains poor. Treatment for these tumours consists of resection of the tumour with concurrent chemotherapy and radiotherapy (27). The infiltrative nature of these tumours makes complete resection difficult to achieve, with recurrence almost inevitable in all but the very young. Anaplastic astrocytomas (AA) and glioblastoma multiforme (GBM) are the most common high grade gliomas.

Mutations in the metabolic enzyme isocitrate dehydrogenase (IDH) 1/2 have been observed in high grade gliomas. These gain of function driver mutations catalyse the conversion of the TCA cycle intermediate isocitrate to 2-hyroxyglutarate instead of α-ketoglutarate. The structure of 2-hydroxyglutarate allows it to inhibit α-ketoglutarate dependent processes, including prolyl hydroxylases, ten-eleven translocation (TET) dioxygenases and histone demethylases (28). Inhibition of these processes drives tumorigenesis through stabilisation of the hypoxia-inducible factor (HIF) transcription factors and altered gene expression through deregulation of DNA and histone methylation.

A subset of GBM tumours have been shown to harbour methylated arginosuccinate synthase 1 (ASS1) promoter regions, leading to silencing of ASS1 gene transcription (29). The enzyme coded by this gene catalyses the rate limiting step of arginine biosynthesis, the loss of which renders tumours reliant on exogenous arginine. These tumours are therefore sensitive to PEGylated arginine deaminase, an enzyme that hydrolyses exogenous arginine to citrulline (30). ASS1 promoter methylated cells starved of arginine use autophagy to access arginine from cellular structures, eventually leading to autophagy induced cell death.

A large proportion of tumours with homozygous CDKN2A deletion also display co-deletion of methylthioadenosine phosphorylase (MTAP), an enzyme solely responsible for the degradation of methylthioadenosine (MTA) following polyamine synthesis (31). Loss of MTAP leads to an accumulation of MTA, a metabolite that shows a range of effects in the cell (32). There is evidence that MTAP deletion sensitises cells to inhibition of protein arginine methyltransferase 5 (PRMT5), an enzyme responsible for transferring methyl units to arginine residues on proteins, including those in signal transduction pathways and histone subunits. *In vitro* analyses show reduced cell viability when PRMT5 is inhibited in MTAP deficient cells (31, 33).

1.2.1.4 Ependymomas (EP)

EP are the third most common CNS tumour presenting in children, accounting for around 10% of paediatric brain tumours (34). Ependymoma have WHO grades ranging from I-III; WHO grade I ependymomas include subependymoma and myxopapillary ependymoma whilst anaplastic ependymoma are WHO Grade III. Most children with ependymoma have a grade II or III tumour. They can occur throughout the CNS, but most commonly present in the posterior fossa in children (35). The five-year overall survival is 73% for 0-14 year old patients (9). The prognosis for infants is poorer, with a five-year overall survival of 60%.

Drivers of ependymoma historically remained unknown, with no recurring genetic mutations being identified. Progress into understanding the biology of these tumours has been made through DNA methylation profiling which identified 9 molecular subgroups. 3 groups of ependymoma exist in each of the spinal, posterior fossa and supratentorial compartment. Each anatomical location contains a WHO grade I subependymal tumour subgroup; however, these tumours arise far more commonly in adults. The two subgroups from the posterior fossa that occur in children are termed group A (PF-EPN-A) and group B (PF-EPN-B), with PF-EPN-A occurring more frequently in this age group. PF-EPN-A tumours are the most aggressive and have a poor prognosis, with 10-year overall survival and 10-year progression free survival of 50% and 20% respectively. There is no known molecular driver, and few have genetic copy number alterations, the most common change is a gain of chromosome 1q. PF-EPN-B tumours have a better prognosis, the 10-year overall survival and progression free survival is 90% and 60% respectively. The tumours of this subgroup are chromosomally unstable with gains and losses of large amounts of genetic material. Ependymal tumours that arise in the supratentorial compartment of children are called ST-EPN-RELA and ST-EPN-YAP1. Tumours in the ST-EPN-RELA subgroup are characterised by gene fusions involving RELA, an NF-κB component. Tumours in this group display chromothripsis and have a poor prognosis with approximate 5-year overall survival and progression free survival of 75% and 30% respectively. ST-EPN-YAP1 tumours are less aggressive, with approximate 5 year overall survival and progression free survival of 100% and 65% respectively (36). The RELA fusion positive ependymoma designation was added to the WHO brain tumour classification in 2016.

Grade II and III ependymomas are treated with maximal possible resection followed by adjuvant treatment (37). Radiotherapy is considered the most effective adjuvant treatment but chemotherapy may be used in those with residual tumour post-surgery prior to radiotherapy and as the sole adjuvant treatment in the very young. Whilst molecular subgroups may have prognostic value, the strongest currently accepted prognostic marker remains extent of resection, with subtotal resection predicting poorer survival.

1.2.2 Embryonal tumours

Embryonal tumours represent about 15% of all paediatric brain tumours. They are all Grade IV tumours that are predominantly seen in children.

1.2.2.1 Medulloblastoma (MB)

MB are the second most common paediatric brain tumour type after PA, with a peak occurrence between the ages of 6 and 8 years (38) and arise solely in the cerebellum. The current 5-year overall survival is over 70% for MB patients.

Several transcriptomic studies identified differences in gene expression and suggested that MB consisted of distinct molecular subgroups. The consensus paper published by Taylor et al (39) describes four molecular subgroups, namely Sonic Hedgehog (SHH), Wingless (WNT), Group 3 and Group 4. Mutations in the PTCH1, SMO and/or SUFU genes leads to over activation of the SHH pathway, therefore the pathway effectors GLI1, SFRP1 and GAB1 have been proposed as immunohistochemical markers for SHH tumours (40). WNT tumours have mutations in the CTNNB1 gene encoding the β-catenin transcription factor or the β-catenin inhibitor APC (41) leading to an accumulation of β-catenin in the nucleus, which is detectable in clinical diagnostic laboratories (42). Group 3 and Group 4 are less well characterised; However, MYC is commonly amplified in Group 3. WNT tumours have a very good prognosis; 5 year progression free survival is approximately 90% (40). SHH and Group 4 have intermediate prognoses (5-year overall survival approximately 75%) and Group 3 has a poor prognosis (5-year overall survival approximately 55%) (43). TP53 mutations are enriched in SHH and WNT MBs; however, this only has prognostic significance for SHH tumours. The 5-year overall survival for TP53 mutants and TP53 wildtype SHH patients is reported to be 41% and 81% respectively (44). The prognostic information that molecular subgrouping provides has allowed their incorporation into the most recent WHO classification of brain tumours (15).

MB is treated with surgical resection of the primary tumour followed by adjuvant treatment. Older children have craniospinal radiotherapy with a boost to the posterior fossa and chemotherapy. Young children are usually treated with very intensive chemotherapy regimens after surgery. Small residual tumour post-surgery is in general more effectively treated by adjuvant chemotherapy and radiotherapy than for ependymomas. Overall survival is about 60% at 5 years (45) but depends greatly on age, stage and subtype. Whilst current treatment regimens are effective, patients usually suffer severe neurological sequelae including reduced IQ, processing speed, executive functioning, working memory, psychomotor abilities and hearing loss (46, 47). De-escalation of therapy for favourable prognosis WNT tumours is currently the basis of on-going clinical trials in an effort to reduce the long-term neurological impacts of treatment.

1.2.2.2 Atypical Teratoid Rhabdoid tumour (ATRT)

ATRTs are very aggressive embryonal tumours arising predominantly in infants and have a poor prognosis. They occur throughout the CNS, being more common in the posterior fossa than other anatomical compartments. Intense chemotherapy following maximal safe resection and radiotherapy has been shown to increase survival in these patients. The recent Rhabdoid 2007 registry study reported 6-year overall survival of 46% (48).

These tumours can appear similar to MBs, with some tumours displaying rhabdoid features(49). ATRT are characterised by loss of function of INI1 (50), a gene involved in the chromatin remodelling SWI/SNF complex. Whilst ATRT have a poor prognosis, there is a subset of long-term survivors, which suggests that there are subgroups of this tumour (51). Molecular analysis suggests there are three subgroups named after their gene expression profiles and are termed ATRT-MYC, ATRT-TYR and ATRT-SHH (52). Whether these groups have any prognostic potential remains unknown.

1.2.3 Other rare tumours

Whilst the entities described above represent the majority of brain tumours occurring in children, there are many other rare tumours that are known. These rare tumours include mixed neuronal glial tumours such as gangliogliomas (GG), dysembryoplastic neuroepithelial tumours (DNET). The majority of these tumours are low grade and treated with similar protocols to low grade gliomas. Tumours of the choroid plexus also occur and are classified as choroid plexus papillomas (CPP), atypical choroid plexus papillomas (ACPP) and choroid plexus carcinomas (CPC). The papillomas are low grade but CPCs are aggressive grade III tumours. Additionally, other rare embryonal tumours can occur in throughout the brain. These tumours are aggressive grade IV tumours which are only just becoming characterised and often have a poor prognosis.

1.2.4 Differences between paediatric and adult brain tumours

Brain tumours arising in children differ significantly from those encountered in adults in terms of the types of tumours seen, the location of the tumours within the brain and the molecular drivers of tumours. Paediatric brain tumours are more variable; embryonal tumours are common in children, as are low grade glial tumours whilst adults predominantly present with high grade glial tumours (53). Tumours in children commonly arise in the posterior fossa, whilst in adults malignant tumours most frequently occur above the tentorium (53). Furthermore, the genetic drivers are known to be different between children and adults; IDH and TP53 mutations are rare in children but common in adults. Conversely, histone modifications are common drivers of paediatric grade III and IV tumours. Temozolomide, a standard treatment for adult tumours, was not shown to improve the survival for children diagnosed with infiltrating low grade gliomas (54). Consequently, paediatric and adult brain tumours should not be considered the same diseases and should be studied independently to improve survival rates.

1.3 Diagnosis of paediatric brain tumours

Obtaining a diagnosis is key to deciding a patient's treatment. Children with brain tumours often present with symptoms linked to the location of the tumour, the age of the child and the presence of hydrocephalus (55). A diagnosis is reached by a multidisciplinary team which integrates information from the patients' presentation and history, imaging and tissue studies.

1.3.1 MR imaging of paediatric brain tumours

When a brain tumour is suspected, the first opportunity to investigate the tumour's properties is usually by imaging. MRI is the preferred imaging modality because of the high-quality soft tissue detail the images show. Standard T_1 and T_2 imaging protocols give information regarding the anatomical location of the tumour, its size, structures involved with the tumour, growth pattern (solid or diffuse) and tumour composition (cysts, solid masses, necrosis, edema). Brain tumours that have leaky blood vessels are highlighted by using a contrast agent, which causes enhancement of the image where the contrast agent affects the magnetic properties of water molecules.

Advanced MR imaging protocols have been developed which provide more information about the tumour. Diffusion weighted imaging estimates the extent with which the tumour restricts the movement of water molecules. Those tumours in which water is more restricted have a lower apparent diffusion coefficient (ADC) and indicate higher cellularity. The opposite is also true; tumours that restrict water movement to a lesser degree have a higher ADC and a lower cellularity. The directionality of water diffusion can be visualised, which highlights nerve tracts.

1.3.2 Histological examination of brain tumours

Imaging alone can be used to diagnose tumours, particularly if the patient has a cancer predisposition syndrome. Patients with NF1 and low grade-appearing tumours are often diagnosed without the need for a biopsy. However, most cases will require tissue samples to provide an accurate diagnosis. Tissue removed during surgery will be sent for histopathological assessment, where it is prepared for examination by squash preparation or frozen section and stained with haematoxylin and eosin (H&E). By examining the stained tissue under a microscope a pathologist can provide an opinion on the likely diagnosis to the neurosurgeon (56, 57). The opinion of the pathologist is invaluable for identifying neoplastic tissue versus normal, whilst a diagnosis has the potential to alter the management by the neurosurgeon. Further examination of the tissue allows the pathologist to comment on cellular morphology, cellularity, mitoses, other visible features and tissue structure, although this is not typically done during the timescale of an operation.

Production of the slides for intraoperative assessment is time and labour intensive, the quality of frozen sections is variable, both frozen sections and squash preparations consume tissue and the architectural detail is harder to discern than in formalin-fixed and paraffin- embedded (FFPE) tissue before staining.

Whilst the qualitative features may be enough to provide a diagnosis, there is considerable overlap between tumours (58). Retrospective studies have examined the accuracy of intraoperative cytological diagnosis, and report diagnostic accuracies with considerable variation (59-61). Further refinement of differential diagnoses requires combinations of immunohistochemical (IHC) staining, karyotyping or gene sequencing. Such investigations cause a significant delay which can complicate the management of a patient, particularly those with highly aggressive tumours.

1.4 Metabolism

The understanding of the molecular drivers of paediatric CNS cancers has been accelerated by studying each functional molecular level.

Genome sequencing was instrumental in linking TP53 mutations in medulloblastoma patients with Li Fraumeni syndrome to chromothripsis seen predominantly in SHH MB (62). More recently, genome sequencing has identified histone mutations enriched in high grade gliomas (63).

Gene expression studies using competitive hybridization microarrays have identified groups of tumour that do not have recurring genetic mutations, like non-WNT and non-SHH medulloblastomas (39), whilst RNAseq experiments have been important in identifying RELA fusions in supratentorial EP (64) and rare alterations in PA (23).

More recently, the epigenome has been used to study tumours. Methylation of DNA changes its conformation and restricts access to genes, thereby regulating transcription. Methylation patterns are thought to be representative of cell development, and act as a means of permanently reducing transcription of genes. Methylation arrays have been used to identify subgroups of tumours, such as ATRTs (52) and PNETs (65), and construct classifiers for paediatric brain tumours (66).

Whilst the genome, epigenome and transcriptome have been important in subgrouping tumours, it is difficult to draw conclusions regarding the functional biology due to the levels of regulation beyond gene transcription. Proteomics, by measuring the relative amount of protein species from samples, can provide functional information, as the proteome is the ultimate outcome of gene expression. A key study published by Archer et al that performed LC-MS/MS on a cohort of medulloblastoma samples, observed subgroup specific proteome profiles. Amongst these proteins were subgroup specific differences of kinase expression, many of which are druggable. But perhaps the most intriguing finding was the observation that the clustering of the subgroups for the proteome was rather different to those of the methylations array and gene expression (67).

Metabolism represents the biochemical processes a cell requires to maintain life, the biochemical intermediates of which are called metabolites. The metabolome is the entire complement of metabolites contained within a system of interest. The two components of metabolism are catabolic processes, which break down organic molecules such as glucose to pyruvate, and anabolic processes, which synthesise molecules such as lipids.

Metabolism is controlled through the expression and activity of metabolic enzymes, which are themselves subject to control at the levels of RNA transcription, protein translation and post-translational modification. Therefore, the metabolome represents the observable phenotype of the biological system after all levels of regulation. Alterations in regulation result in changes to the metabolome; metabolite profiles have been shown to alter with changes in expression of oncogenes such as MYC (68-70). It should be noted that the metabolome also represents the interaction of the system of interest with the environment; studies have shown that metabolite concentrations in the paediatric brain vary by anatomical location and age (71-73).

1.4.1 Normal brain metabolism

The brain contains distinct cell populations including neurons, endothelial cells, astrocytes, oligodendrocytes, oligodendrocyte precursor cells and microglia (74). Whilst it was assumed that cells in the central nervous system all fully oxidised glucose to CO_2 and water, differences in expression of key genes regulating energy metabolism have been identified that suggest cells have complementary metabolic coupling (75). Astrocytes import a disproportionately large amount of glucose relative to their estimated energy needs(76), and display a more glycolytic phenotype. A large amount of the glucose they take up is metabolised to lactate, which is exported from the cell into the extracellular space (77). Neurons show a preference for taking up lactate over glucose (78), which is imported and oxidised to pyruvate. The lactate derived pyruvate then enters the TCA cycle to be fully oxidised to CO_2 and water.

Another well-known example of metabolic coupling in the brain is the glutamine-glutamate cycle existing between neurons and astrocytes. Glutamate is the major excitatory metabolite in the human brain and is synthesised by presynaptic neurons from glutamine that has been taken up from the extracellular space. Deamidation of glutamine by glutaminase enzymes generate glutamate and ammonia (79). The glutamate is packaged into vesicles and released into the synaptic cleft when an action potential arrives at the presynaptic neuron. Glutamate must be rapidly cleared from the synaptic cleft to prevent excitotoxicity, which is accomplished by the astrocytes surrounding the synaptic cleft (80). The glutamate is imported by the astrocytes and undergoes a condensation reaction with ammonia to form glutamine. The glutamine is exported into the extracellular space and made available again for neuronal uptake.

GABA is a major inhibitory neurotransmitter synthesised by neurons through the GABA shunt. This pathway begins with the transamination of alpha ketoglutarate, a TCA cycle intermediate, to glutamate. Further decarboxylation of glutamate generates GABA, which is stored in pre-synaptic vesicles. After release into the synaptic cleft, GABA is taken up by neurons on both sides of the cleft, as well as surrounding astrocytes. A transamination reaction using GABA and alpha ketoglutarate generate succinate semialdehyde and glutamate. In neurons, glutamate can be deaminated to reform GABA, whilst succinate semialdehyde can be oxidised to succinate and re-enter the TCA cycle (81).

1.4.2 Metabolism as a hallmark of cancer

In order to undergo unrestricted cell division, cancer cells must adapt their metabolism to meet the biosynthetic demand. Cells must generate sufficient energy in the form of ATP, synthesise necessary macromolecular components and maintain the cellular chemical environment by balancing redox reactions. To generate energy, many cancers show a preference for up-regulated glycolysis and down-regulated oxidative phosphorylation, even in the presence of sufficient oxygen. This is the most well-known metabolic adaption, initially observed by Otto Warburg (82). Although glycolysis alone is inefficient compared to glycolysis linked to oxidative phosphorylation, producing substantially less ATP per mole of glucose, ATP is generated rapidly without the need for oxygen and allows the use of the carbon from glucose to synthesise other molecules such as nucleosides and amino acids.

Altered metabolism of choline compounds for membrane synthesis is accepted as another hallmark of cancer. Up-regulation of choline transporters, as well as choline kinase, have been reported in a variety of cancers. This leads to an accumulation of phosphocholine in the tumour cells. Regulation of the rate limiting step of phosphatidylcholine synthesis is complex and not fully understood, as there is evidence that the enzyme CTP:phosphocholine cytidylyltransferase is inhibited regulated by ERK and JNK, members of the MAPK pathway frequently up-regulated in cancers (83).

Increased uptake and metabolism of essential and non-essential amino acids is important for cancer proliferation. Tumours show an increase in uptake and metabolism of branched chain amino acids, glutamine and serine. Alongside their incorporation into proteins, these amino acids have other biochemical functions. Branched chain amino acids are important transaminase substrates for BCAT1/2, the ketoacid products of which can be used by mitochondria to generate energy (84).

Glutamine is the nitrogen source for de novo nucleotide synthesis, as well as providing an abundant carbon source for TCA cycle metabolism. Increased glutamine metabolism has been linked to higher grade tumours, with some tumours becoming dependent on glutamine to meet their energetic and synthetic needs (85).

Increased serine biosynthesis and metabolism is another of the many changes observed in tumours. The committing step for serine synthesis involves dehydrogenation of the glycolysis intermediate 3-phosphoglycerate through phosphoglycerate dehydrogenase (PHGDH) (86). Serine is a key input to the one carbon cycle that generates methyl units for methylation reactions for histone modifications and nucleotide synthesis (87). It is also a precursor for cysteine and glycine, both components of glutathione. Furthermore, serine is required for sphingosine synthesis (88), a lipid signalling molecule, as well as phosphoserine membrane lipids (89).

Changes in lipid metabolism are an important feature of cancer cell metabolism. Gliomas have been shown to have altered concentrations of polyunsaturated fatty acids alongside reduced abundance of phosphatidylserine and phosphatidylethanolamine (90). Gliomas have been shown to have highly up-regulated sterol regulatory element-binding protein 1 (SREBP-1), a transcription factor regulating genes associated with glucose metabolism and fatty acid synthesis. Other genes that catalyse the formation of fatty acids have been shown to be up-regulated in gliomas including acetyl-CoA carboxylase (ACC) and fatty acid synthase (FASN) (91). Inhibiting the synthesis of lipids in GBM cells has been shown to reduce their rate of proliferation *in vitro* (92).

All the described metabolic changes allow cancer tissues to generate the biomass required for continued proliferation.

1.4.3 Examining metabolism

Tumour metabolism is a powerful characterising feature of tumours providing a snapshot of the phenotype of the tumour; however, metabolites are diverse in terms of their chemical properties and measuring the concentration of metabolites in the metabolome with the greatest coverage is a technical challenge. Two main platforms have been developed to measure the concentration of metabolites in tissue and liquids; Nuclear Magnetic Resonance (NMR) and mass spectrometry (MS).

NMR is a powerful technique for characterising the metabolome of a sample. It is a quantitative technique that does not necessarily require complex sample preparation. NMR relies upon the concept of spin, a property that atomic nuclei possess if they have an odd mass number. Examples of such nuclei used in biological studies are ^{1}H, ^{13}C, ^{15}N and ^{31}P; ^{1}H is the most common nucleus used in studies due to its high abundance in organic molecules and high gyromagnetic ratio which produces the highest signal. Such nuclei have magnetic moments, all of which are randomly orientated under normal conditions. When a sample containing these nuclei is placed into an external magnetic field (B_0), the magnetic moments of the nuclei align with B_0, creating a net magnetic moment, M. Using radiofrequency pulses, M can be pushed into an orientation that is perpendicular to B_0, where it precesses at a frequency defined by the nuclei's gyromagnetic ratio and the strength of B_0. Nuclei in different chemical environments experience differing degrees of shielding by electrons, which affects the rate at which these nuclei precess. The precessing magnetic moments of the nuclei in the sample create a detectable electrical current in receiver coils. The signal appears as a complex wave formed of overlapping sine waves which decay exponentially. Fourier transform of this wave from the time domain into the frequency domain produces a spectrum. Each metabolite is represented by a unique set of peaks along the frequency axis of the spectrum, the area under which is proportional to the number of nuclei contributing to the resonance and the concentration of the metabolite (**Figure 1.4**). The exponential decay of the signal in the time domain, termed T_2 relaxation, leads to a broadening of the peaks and is influenced by factors such as the size of the molecule and its mobility.

Protons in close proximity to each other in the same molecule and existing in different chemical environments interact with each other through j-coupling, giving rise to peak splitting. The number of peaks observed is dependent on the number of protons bound to the adjacent carbon atom, generally following the n+1 rule. When there is a single adjacent proton, the splitting pattern will be a doublet. When there are 2 adjacent protons, the splitting pattern will form a triplet. The ratio of peak heights is predicted by Pascal's triangle; a doublet will always have a ratio of 1:1, whilst a triplet will have a ratio of 1:2:1. Higher order splitting patterns are possible, and where there are differences in coupling constants complex patterns such as doublets of doublets and doublets of triplets are observable. The predictable splitting pattern provides information on the structure of a molecule.

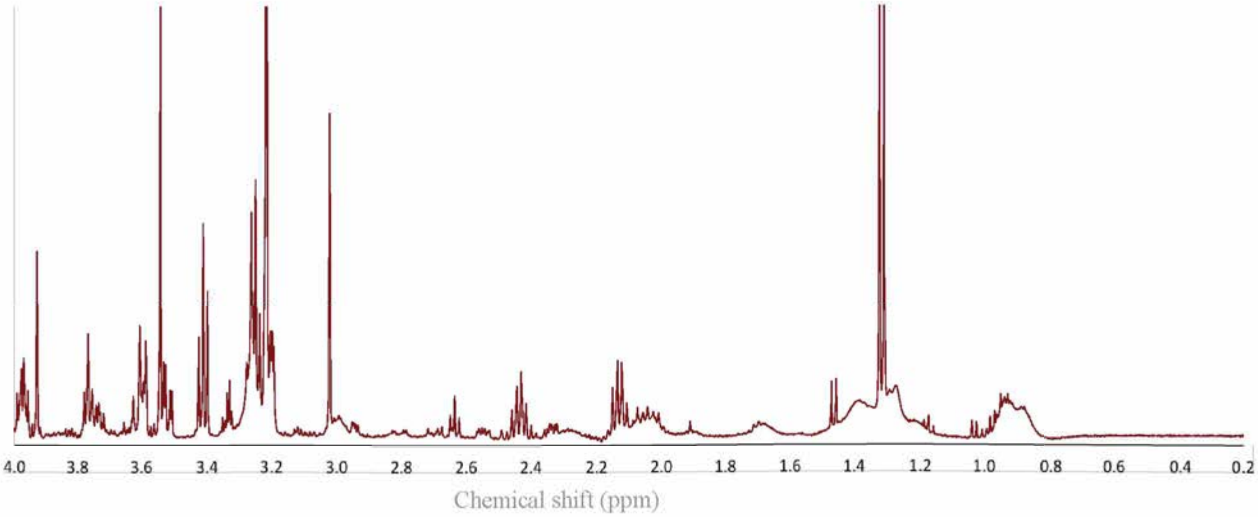

Figure 1.4 – An example ^{1}H HR-MAS spectrum acquired using a 500 MHz spectrometer. Note the narrow width of the peaks allowing relatively easy identification and quantification of metabolites.

1.4.3.1 High Resolution Magic Angle Spinning NMR (HR-MAS)

Spectroscopic studies can be performed on resected tissue using HR-MAS. The high strength of B_0 and the close proximity of the receiver coils to the sample provide a high signal to noise ratio. However, constraints placed upon metabolite mobility by tissue membranes leads to dipolar interactions that are insufficiently averaged and cause spectral line broadening. Dipolar interactions are orientation dependent, and average to 0 at the "magic angle" θ_m relative to B_0, defined as:

$$\theta_m = cos^{-1}\, {}^{1}\!/_{\sqrt{3}} \approx 54.74°$$

Spinning the sample at the magic angle with regards to the direction of B_0 averages the dipolar interactions to 0, reduces linewidth and produces spectra with resolution similar to that of liquid state NMR, (**Figure 1.5**).

The pulse sequences used in an NMR experiment determine the data obtained. Nuclear Overhauser effect spectroscopy (NOESY) and Carr Purcell Meiboom Gill (CPMG) sequences are the most commonly encountered pulse sequences for metabolomic studies. The NOESY pulse sequence is used in this thesis over the simpler pulse-acquire sequences due to the improved water suppression and volume selection from B_1 inhomogeneity.

The NOESY sequence involves two 90° excitation pulses followed by a mixing period. A third 90° excitation pulse is followed immediately by FID acquisition. 90° excitation pulses are used in this thesis to provide the greatest signal to noise ratio, as the net magnetic moment will be perpendicular to B_0.

CPMG sequences use a single 90° excitation pulse which is then followed by a specified number of 180° pulses before FID acquisition. The 180° pulses act as a T_2 filter, allowing the decay of signals from lipids and macromolecules which have short T_2 relaxation times, whilst retaining the signals from metabolites with longer T_2 relaxation times.

Metabolites are quantified by comparing the area of the peaks representing a metabolite to the area of a peak representing an internal standard of known concentration, taking into account the number of protons contributing to each resonance. The most common internal standard encounter in HR-MAS of tissue is 3-(trimethylsilyl)proprionic-2,2,3,3-d4 acid (TMSP). TMSP has several important features that make it ideal as a concentration standard; it has a large singlet resonance from 9 equivalent protons, the resonance does not overlap any metabolite resonances and it is biologically inert.

As the protons in water are several orders of magnitude greater in concentration than the protons in the metabolites of interest, both NOESY and CPMG sequences rely on water suppression to remove the water signal and allow the metabolites to be quantified. In both sequences, water suppression is achieved through presaturation, which involves irradiating the sample with a long, low power radiofrequency pulse. This pulse reduces the difference in equilibrium populations between the high and low energy states for protons with resonance frequencies equal to that of the pulse. The design of the NOESY pulse also provides benefits with regards to water suppression. T_1 discrimination, volume selection, phase cycling and gradient pulses contribute to water suppression beyond the water presaturation pulse (93, 94).

Water experiences a fast T_1 relaxation rate relative to the metabolites due to radiation damping. Such an effect allows water to relax into the positive z axis during the mixing time of the NOESY pulse, which improves water suppression by accelerating the return of water to its equilibrium state before the next presaturation pulse. Volume selection attenuates signals originating from areas of the sample experiencing an inhomogeneous B_1 magnetic field by being situated close to the end of the coils. NOESY achieves this by realigning the net magnetic moment with the positive z axis in alternating acquisitions. Therefore, metabolites experience an effective 270° pulse followed by an effective 90° pulse. Resonances in the inhomogeneous B_1 field do not experience full excitation, and are deemphasised when the signals from both scans are added together. Phase cycling subtracts signals from the spectrum by cycling the phase of the receiver coils to subtract unwanted resonances whist allowing addition of metabolite resonances. Gradient pulses can be included into NOESY sequences to destroy any xy magnetisation prior to the application of a non-selective high power RF pulse. The NOESY pulse sequence used in this work uses two gradient pulses. The first follows the water presaturation pulse, and the second gradient pulse follows the second 90° pulse (93, 94).

1.4.3.1.1 Key metabolites observed by HR-MAS

The metabolites below are the major metabolites that will be encountered in this thesis. The properties of the metabolite will be briefly discussed along with its distinguishing spectral features. A full list of annotations can be found in chapter 2.

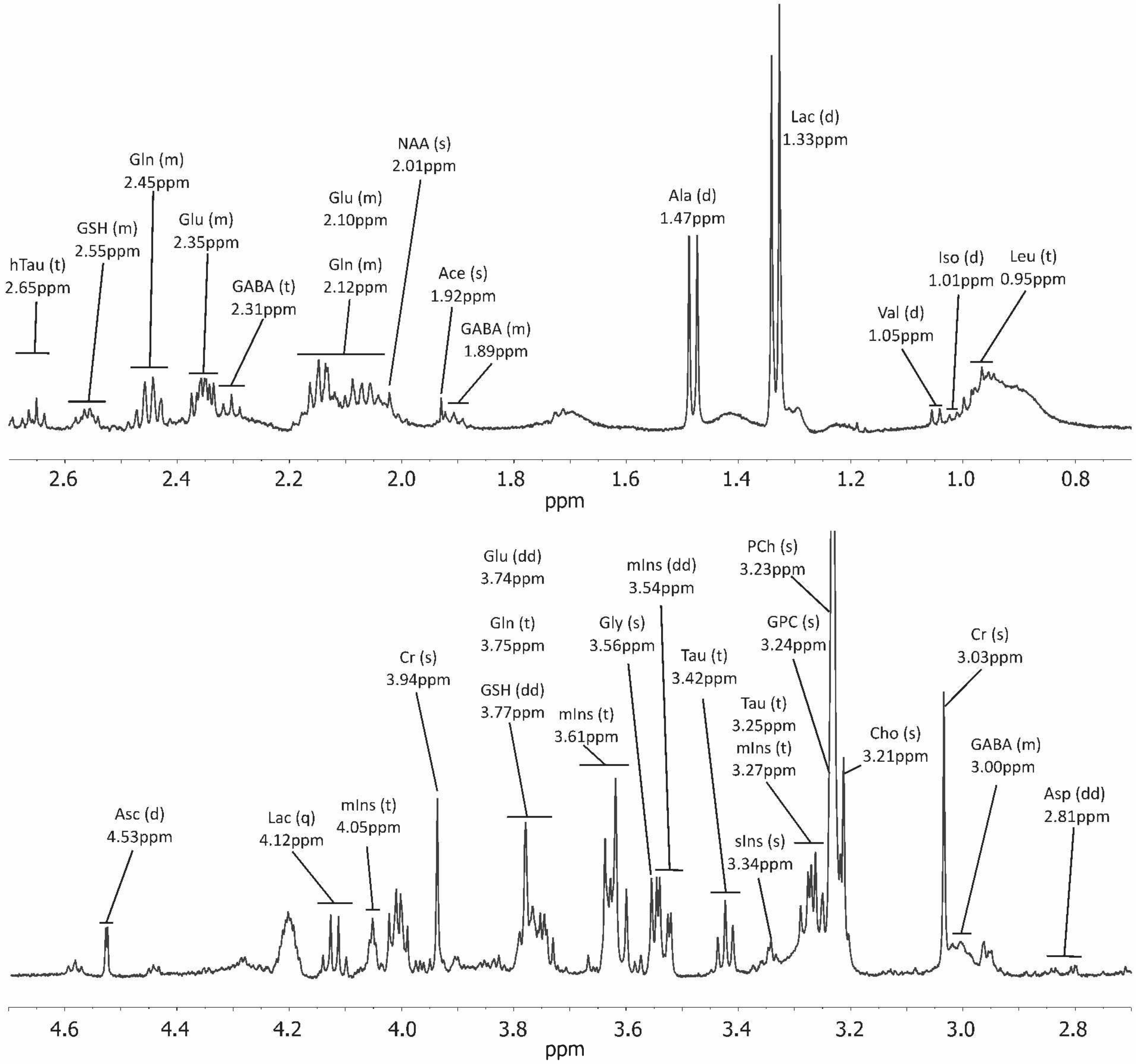

Figure 1.5 – An example HR-MAS spectrum with metabolites annotated. Abbreviations – Ace, acetate; Ala, alanine; Asc, ascorbate; Asp, aspartate; Cho, choline; Cr, creatine; GABA, γ amino butyric acid; Gln, glutamine; Glu, glutamate; GSH, glutathione; Gly, glycine; GPC, glycerophosphocholine; hTau, hypotaurine; Iso, isoleucine; Lac, lactate; Leu, leucine; mIns, *myo* inositol; NAA, N-acetylaspartate; PCh, phosphocholine; sIns, *scyllo* inositol; Tau, taurine; Val, valine; s, singlet; d, doublet, dd, doublet of doublets; m, multiplet; q, quartet; t, triplet.

Lipids and macromolecules

Broad lipid and macromolecular resonances are created by large molecules with fast T_2 relaxation times. Lipid resonances are believed to be caused by cytoplasmic lipid droplets with enough free movement to be visible to NMR techniques as opposed to membrane lipids (95). Mobile lipids have been associated with a poorer prognosis in paediatric brain tumours (4, 96).

Branched chain amino acids

This group of amino acids consists of isoleucine (Iso), leucine (Leu) and valine (Val). All three are essential amino acids as they cannot be synthesised by humans and must be acquired from the diet. They are called branched chain amino acids as all three have branched, aliphatic side chains. The splitting pattern for these amino acids is complicated. Val has two doublets, one at 0.98ppm and another at 1.05ppm. Iso is observable as a doublet at 1.01ppm, whilst Leu can be seen as a triplet at 0.95ppm.

Alanine (Ala)

Ala is an amino acid with a prominent doublet observed at 1.47ppm. A quartet resonance is at 3.77ppm, but overlaps with other resonances. Ala is a key metabolite in the alanine-glucose cycle. Tissues that metabolise amino acids accumulate amino groups that are stored as glutamate. After undergoing transamination with pyruvate, Ala is formed along with α-ketoglutarate. Ala is transported via the blood to the liver, where is it converted back to pyruvate with the formation of urea (97).

Gamma aminobutyric acid (GABA)

GABA is well known as an inhibitory neurotransmitter synthesised from glutamate by glutamate decarboxylase in the GABA shunt. GABA can be further metabolised to the TCA cycle intermediate succinate. The clearest feature for GABA is a triplet at 2.31ppm. GABA also has multiplet features at 1.89ppm and 3.00ppm.

Glutamate (Glu)

Glu is an amino acid that acts as a neurotransmitter in the brain. Formed as a product of Gln metabolism, Glu has many metabolic functions in the cell. Glu can be converted to GABA via the GABA shunt and then to succinate. Glutamate dehydrogenase can convert Glu to α-ketoglutarate for anaplerotic fuelling of the TCA cycle. Furthermore, it is also a key component of glutathione, along with glycine and cysteine. Glu is a potential negative prognostic marker in MB when measured using *in vivo* Magnetic Resonance Spectroscopy (MRS) (98). Glu can most easily be seen as a multiplet at 2.35ppm. Other features of Glu include a multiplet centred at 2.10ppm and a doublet of doublets at 3.74ppm, both of which overlap with resonances of glutamine and glutathione.

Succinate (Suc)

Suc is a TCA intermediary, and metabolic product of GABA metabolism. Four equivalent protons give rise to a singlet at 2.41ppm. Suc accumulates in tumours harbouring SDH mutations, such as paragangliomas and pheochromocytomas (99).

Glutamine (Gln)

Gln is the most abundant amino acid in the plasma and an important resource for tumours. The nitrogen from the amide group in its side chain is required for synthesis of nucleotide bases, and can also be used to form glucosamine-6-phosphate, the precursor of amino sugars. These processes all create Glu as a by-product. Gln can also be converted to Glu by glutaminase enzymes, which releases ammonium as a by-product. Gln has previously been identified as a marker of positive prognosis in paediatric brain tumours, in that higher Gln concentration in the tumour predicts better survival (4). Although difficult to separate from other resonances *in vivo*, Gln is observable as a multiplet at 2.45ppm in HR-MAS. Other features include a multiplet at 2.12ppm and a triplet at 3.75ppm, both of which overlap with resonances of Glu and glutathione.

Glutathione (GSH) GSH is the key cellular antioxidant in cells. A tripeptide formed of Glu, glycine and cysteine, the clearest resonance is a multiplet visible at 2.55ppm. However, it also has resonances at 2.15ppm (multiplet), 2.93ppm (doublet of triplets), 2.98ppm (doublet of triplets) and 3.77ppm (doublet of doublets).

Hypotaurine (hTau)

hTau is a sulfinic acid thought to be the biosynthetic precursor to taurine. Very little is known about its function; however, it has been linked to hypoxic signalling (100). Its protons create a triplet splitting pattern at 2.65ppm, and a second triplet at 3.34ppm.

Aspartate (Asp)

Asp is an amino acid with a structure similar to Glu, however, there is one less methanediyl group in its side chain. Asp is observable as a doublet of doublets centred at 2.81ppm; however, it can be obscured by a lipid group at the same resonance. Other resonances include doublets of doublets at 2.65ppm and 3.89ppm. Asp can be used to synthesise asparagine and arginine. A by-product of synthesising the latter is the TCA cycle intermediate fumarate. Aspartate is the precursor to N-acetylaspartate, a brain specific metabolite, which is synthesised in neurons and used by oligodendrocytes to myelinate neuronal axons during development. It may also play roles in signalling between cells, generating energy and regulating osmotic potential (101).

Creatine (Cr)

Creatine is a metabolite that, along with its phosphorylated form phosphocreatine, maintains an energy buffer. Creatine is synthesised using arginine and glycine, with the resulting guanidinoacetate being methylated to form creatine. Both creatine and phosphocreatine give rise to a prominent singlet observed at 3.03ppm, and a second singlet at 3.94ppm. The two metabolites cannot be distinguished using HR-MAS, and so Cr in this thesis will represent the sum of these metabolites.

Choline compounds

Choline compounds consist of free choline (Cho), phosphocholine (PCh) and glycerophosphocholine (GPC). They are difficult to discriminate using *in vivo* MRS and are usually summed as total choline (tCho). Cho, PCh and GPC each have 9 equivalent protons in the $N^+(CH_3)_3$ groups, which give rise to relatively tall peaks at 3.21ppm (Cho), 3.23ppm (PCh) and

3.24ppm (GPC). All three choline compounds give rise to other resonances between 3.50ppm and 4.00ppm which overlap with resonances from other metabolites. Choline is a key constituent of cell membranes in the form of phosphatidylcholine. Increased concentrations of choline compounds are associated with a higher membrane turnover and cancerous lesions (83).

Taurine (Tau)

Tau is a sulfonic acid with many functions associated with it, including osmoregulation, anti-oxidation (102), neurotransmission (103) and developmental processes (104-107). Tau has been shown to be higher in embryonal tumours with *in vivo* MRS (108). Tau is clearly observed as a triplet at 3.42ppm; it also has a second triplet centred at 3.25ppm which overlaps with a *myo*-inositol resonance.

Myo-inositol (mIns)

A hexose sugar, mIns has several functions within the cell. Free mIns is a precursor to the phosphatidylinositol, a membrane constituent. It also acts as an osmolyte. Several resonances are attributed to mIns, but the most prominent is a doublet of doublets at 3.54ppm. Other resonances are visible, including a triplet at 3.27ppm which overlaps with Tau, a triplet at 3.61ppm and a triplet at 4.05ppm. mIns has been implicated as a marker of low grade tumours, with high grade gliomas having a lower mIns/Cr ratio (109).

Glycine (Gly)

Gly is the simplest amino acid with a single proton as a side chain. Gly is involved in the one carbon cycle, responsible for generating methyl units for cellular processes (87). It is also an end-product of choline degradation. Gly has a single peak at 3.56ppm.

Scyllo-inositol (sIns)

Like mIns, sIns is a hexose sugar and in normal brain exists in a mIns:sIns ratio of approximately 12:1 (110). The concentration of sIns and mIns has been shown to correlate (111), and the two appear to be interconvertable with an epimerase enzyme (112). Little is known about the function of sIns, but there is evidence of anti-convulsant properties (113) and an ability to reduce amyloid-β protein in Alzheimer's patients (114). This metabolite appears as a singlet peak at 3.35ppm.

Serine (Ser)

Ser is an amino acid that, along with glycine, is involved in the one carbon cycle (87). It is observed as a doublet of doublets at 3.84ppm, with other doublet of doublets at 3.94 and 3.98ppm.

1.4.3.1.2 Metabolic stability of resected tissue

To examine the stability of metabolite profiles following resection, Opstad et al acquired HR-MAS on dissected rat brains that had experienced varying lengths of ischemia (time points every 30 mins) at 20°C (115). This work showed that Glc was rapidly and significantly depleted during the initial 30 mins of ischemia, with an accompanying significant increase in Lac and Ala. These are changes that would be expected when a tissue experiences a lack of oxygen. However, during the initial ischemic period, the other quantifiable metabolites except GABA appear to remain stable. There are further significant changes in metabolite concentrations at longer time intervals as the tissue degrades. Prompt snap freezing of tissue prevents further metabolic degradation and, once frozen, metabolite profiles have been shown to remain stable for long periods of time. Jordan et al. demonstrated stable metabolite profiles for prostate cancer tissue stored at -80°C for three years (116). Wu et al observed similar results in prostate tissues, with only Cho not showing a significant correlation between the concentration before and after freezing (117).

1.4.3.2 *In vivo* MRS

An *in vivo* method closely related to NMR can be performed during the patients initial clinical MRI without the need for any further specialised equipment. A region of interest within the brain (voxel) is selected from which metabolite information is acquired. MRS has been performed in children with brain tumours, with many studies assessing its clinical applications. It has shown to be capable of diagnosing common brain tumours with high accuracy (5, 118-120), with prospective evidence that MRS enhances diagnostic and grading accuracy (121). Metabolites quantified using MRS data have been shown to have general prognostic significance (4, 122) and tumour specific prognostic significance (98). MRS can also aid in monitoring disease; metabolite profiles can distinguish between post-treatment changes and tumour progression (123).

However, the low field strength, the line broadening effects of restricted metabolite movement and distance of the receiver coils from the voxel leads to low resolution spectra where metabolites with low abundance are obscured by higher abundance metabolites (**Figure 1.6**). Broad macromolecular and lipid resonances further reduce the ability to identify metabolite peaks. Statistical software packages have been developed to allow quantification of metabolites by fitting the peaks of expected metabolites to the MRS spectrum and minimising the residual.

1.4.3.2.1 Correlations between *ex vivo* HR-MAS and *in vivo* MRS

Given that *in vivo* MRS and HR-MAS both measure metabolite concentrations using the same physical principles, there has been great interest in correlating concentrations from both techniques to establish the extent of agreement between the methodologies. Strong correlations between the methodologies would allow the translation of *ex vivo* findings to non-invasive *in vivo* application.

Tzika et al examined 11 brain tumours from patients that had matching *in vivo* MRS and found that ratios between metabolites correlated between the two methods (124). In this study, HR-MAS determined PCh/tCr and PCh+Cho/tCr was shown to correlate with tCho/tCr determined by *in vivo* MRS. Additionally PCh/NAA and PCh+Cho/NAA as measured by HR-MAS were shown to correlate with *in vivo* determined tCho/NAA.

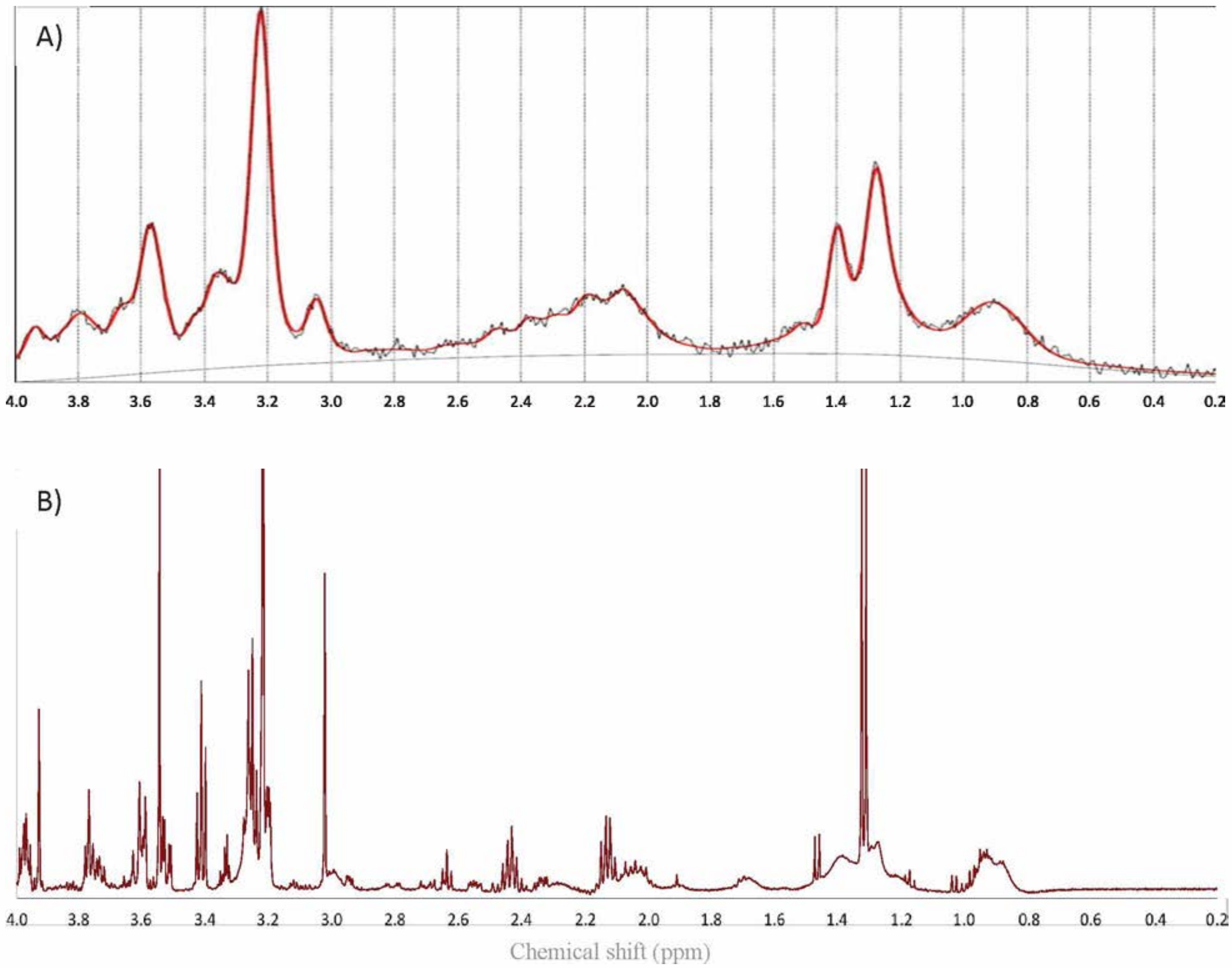

Figure 1.6 – comparison between A) *in vivo* ^{1}H MRS and B) HR-MAS from matched tissue. Notice the increase in resolution, in particular the regions between 2.0ppm and 2.7ppm, the resolution of the choline compounds at 3.2ppm and discrimination of mIns and Gly between 3.5 and 3.6ppm.

Wilson et al. performed a similar study using matched data from 15 patients (6). This study correlated metabolite concentrations instead of ratios, and found significant correlations between Ala, Cr, Gln, Glu, mIns, Lac, Tau, PCh, tCho, Glx, sIns+Tau and mIns+Gly. Opstad et al calculated correlations between *in vivo* MRS of 17 adult gliomas and matched HR-MAS of resected tissue and observed significant correlations between Cr, mIns, NAA, sIns, Glx, tCho, lipids at 1.3ppm and lipids at 0.9ppm (125). In prostate tissue, Selnaes et al observed a significant correlation between the clinically relevant marker tCho+tCr+spermine/Cit (CCS/C) as measured *in vivo* and *ex vivo* (126). In this study, 40 samples from 13 patients were analysed, with the tissue samples being spatially matched to data acquired through Magnetic Resonance Spectroscopic Imaging (MRSI).

1.4.3.3 Mass spectrometry (MS)

MS is the other mainstream platform for metabolomics. The technique measures the mass/charge ratio (m/z ratio) of ions generated from a sample. Many variants exist, but the basic components of a mass spectrometer involve an ion source (for example, electrospray ionisation or matrix assisted laser desorption ionisation), a mass analyser (for example, quadrupole or time of flight) and a detector. The abundance of the ions is plotted on a mass spectrum; the x-axis is the m/z ratio and the y-axis represents the relative abundance of each ion. MS is far more sensitive than NMR, with the ability to detect many more metabolites; however, it requires metabolites to be extracted from the sample, which requires complex sample processing.

As the extracted metabolites exist in a highly complex mixture, MS is often preceded by a metabolite separation step. Such separation procedures include gas chromatography and liquid chromatography. The simplified mixture reduces ion suppression and the retention time from the separation step aids in metabolite identification.

MS has been proposed as a tool in aiding in the management of brain tumours. Agar et al published a proof of principle study that MS performed on resected tissue had the potential to interrogate a tissue sample for delineation (127). The authors noted that lipid species correlated with tumour cell prevalence. Upon further development of this work, Eberlin et al published results demonstrating the ability of Desorption Electrospray Ionization MS (DESI-MS) to classify brain tumours from adults.

MS has the advantage of being able to interrogate the lipid species of a sample. Eberlin et al showed that lipid species were able to classify adult gliomas (128).

Whilst the methodologies from the above studies requires tissue to be prepared on a slide for analysis, technical advances have allowed the development of a handheld probe that allows MS data to be acquired from a tumour without prior resection (129). This technique has been used by Woolman et al to subgroup MB cell lines xenografted to mice (130).

1.4.4 HR-MAS in cancer research

HR-MAS is a valuable and powerful technique for identifying metabolite markers of tumour tissue. Key published literature regarding HR-MAS studies of cancer is reviewed below.

1.4.4.1 Discriminating cancer from benign tissue

In a number of cancers, characteristic changes in metabolism have been identified between malignant and normal tissue. Perhaps the most commonly identified alteration between tumour and normal tissue is an increase in the choline-containing compounds Cho, PCh and GPC as well as Lac (131-140).These metabolites are believed to be related to increases in cell proliferation and glycolytic metabolism. Whilst these markers are seen in most tumours, there are other HR-MAS visible tumour-specific markers for separating normal and malignant tissue. Citrate and spermine are commonly visible in healthy prostate tissue; however, they are less abundant or absent in prostate cancer tissue (133-135, 138, 140).

Paraganglioma/pheochromocytoma are driven in some circumstances by mutations in SDH, which causes detectable accumulation of Suc (99). Similarly, IDH mutated gliomas accumulate detectable levels of 2-hydroxyglutarate (141).

1.4.4.2 Identification of diagnostic markers

After identifying tumour tissue, a pathologist will attempt to diagnose the tumour type, which will inform future treatment in both the short term and long term. The inter-observer variation and qualitative nature of the pathological assessments are potential drawbacks and can cause delays in obtaining a diagnosis. Studies performed in many cancers have demonstrated the ability of HR-MAS to diagnose tumour types. Duarte et al were able to demonstrate differences in metabolite profiles between lung adenocarcinoma, squamous cell carcinoma and carcinoid tumours (132). Discrimination between the different tumour types using biochemical information could improve staging of lung cancers and aid clinical decisions.

A number of studies have published markers of tumour diagnosis in adult brain tumours. Cheng et al were the first to examine brain tumour tissue using HR-MAS and identify differences in metabolite profiles between common tumour types (142). The authors conclude that significant differences in metabolite concentrations can be used to discriminate tumours, but did not perform any validation of the results. Wright et al (143) performed a similar study and identified significant differences in metabolite concentrations between different tumour types. Building on these studies, Poullet et al constructed binary classifiers for grade II or III gliomas, GBM, meningiomas and metastases using several processing and classification algorithms (144). The classification accuracy for the various combinations averaged approximately 90%, although the importance of particular metabolites for classification was not reported. Andronessi et al. also constructed binary classifiers for various adult CNS, metastases from outside the CNS and a normal control group consisting of epileptic tissue (145). A combination of feature selection and linear SVM produced classification accuracies averaging 90%.

In paediatric brain tumours, a study by Tzika et al qualitatively assessed tissue metabolite profiles of 11 brain tumour tissue samples and identified differences between tumour types (124). Cuellar–Baena et al characterised the metabolite profiles of a small cohort of PAs, EPs and MBs and identified differences through a combination of univariate and multivariate analyses. Although no classification analyses were performed in either study, the Cuellar_Baena study highlights the potential of metabolite profiles to discriminate paediatric brain tumours. Wilson et al did perform a classification analysis on 29 paediatric tumours, including PAs, MBs, neuroblastomas, supratentorial PNETs and EPs. The linear discriminant analysis had a cross validated accuracy of 80% (3).

There is a wealth of evidence to support the use of metabolite profiles as a diagnostic aid, but a lack of studies examining the ability of tissue metabolite profiles from a single area of the brain to construct robust classifiers. The technical qualities of HR-MAS would suit a rapid diagnostic application; however, there is limited literature on how the classification accuracy of tissue metabolite profiles compares to current rapid diagnostic testing.

There is also a lack of literature using metabolite profiles to identify how the underlying metabolism of each tumour is altered in terms of metabolic pathways. Madhu et al studied correlations between metabolites in adult brain tumour tissue and in doing so identified repeating correlations (8). The authors speculated this to be the result of the tumours using the same set of biochemical mechanisms. Whilst important correlations are observed between several pools of metabolites, the analysis does not take into account the underlying metabolic pathways through which metabolites are metabolised.

1.4.4.3 Assessing heterogeneity of tumours

HR-MAS acquires data from small samples taken from a larger tumour. It is important to understand how representative the studied samples are of the original tumour. By studying breast cancer tissues, Gogiashvili et al concluded that the inter-tumoural variation is greater than intra-tumoural variation (146). Park et al reached a similar conclusion, that intra-tumoural location does not significantly affect the HR-MAS spectrum. With regards to paediatric tumours, Wilson et al found that the intra tumoural-variation of neuroblastoma samples was significantly smaller than inter-tumoural variation (3).

Multiple samples are rarely obtained from brain tumours; however, Cheng et al conducted a study investigating the heterogeneity in a single GBM, and found the metabolite profiles to be variable (147). This variability was shown to correlate with the degree of necrosis in the sample.

1.4.4.4 Identifying prognostic markers

Beyond diagnosis, prognostic information can be provided by metabolite profiles. Several studies have identified increases in the concentrations of choline-containing compounds, or elevations of ratios with choline-containing compounds in the numerator, as markers of aggressive disease or disease more likely to recur (148-150). Other metabolites have proposed prognostic potential; Pacholczyk-Sienicka et al. identified elevated Tau/Gly and Tau/mIns as prognostic markers in colorectal tumours (151). Interestingly, mIns was also predictive of more aggressive prostate cancer in a study by Vandergrift et al (152). However, in adult brain tumours, whilst Gly does show some ability to predict aggressiveness, mIns is thought to be a marker of positive prognosis (153). Erb et al (154), Righi et al (155) and Elkhaled et al (156) have examined metabolite profiles of adult gliomas. All three studies found that tumour grade could be predicted by metabolite concentrations and, in the case of Elkhaled et al, predict transformation status. Paediatric brain tumours have been examined using *in vivo* MRS and it was shown that high concentrations of Gln and NAA were predictive of better survival whilst high concentrations of sIns and lipids were predictive of poorer survival for these patients (4).

There is a relative lack of studies which examine the prognostic potential of tissue metabolite profiles, and children's brain tumours in particular. The ability to predict the aggressiveness of a brain tumour using metabolite profiles would provide valuable information to clinicians and allow further risk stratification alongside current prognostic indicators.

1.4.4.5 HR-MAS and assessing response to treatment

Metabolite profiles of tissue or cells detected by HR-MAS have been used to assess response to treatment in a range of cancer fields. Lung cancer cell lines exposed to cisplatin had significantly increased triacylglycerides and cholesterol esters (157). The ratio of the lipid resonance at ~1.3ppm to the lipid resonance at ~0.9ppm was significantly increased in treated cells, and this was concluded to result from an increase in the length of fatty acid chains. Furthermore, the ratio of the lipid resonance at ~5.3ppm and the lipid resonance at ~0.9ppm was significantly increased in treated cells, suggesting the lipids in treated cells had a higher degree of unsaturation. The authors also observed significant increases in GPC and sorbitol after treatment, whilst the concentration of amino acids was significantly decreased. Mouse models of BRCA1-positive docetaxel-sensitive and resistant breast cancers were treated with docetaxel, and the metabolite profiles of the tissue were examined to identify markers of treatment resistance (158). All choline compounds were shown to be higher in resistant cell lines whilst Gly, Tau and Cr were lower before treatment. Upon treatment of the sensitive tumours with docetaxel, the authors observed a transient increase in the ratios of the choline compounds to creatine over the first five days of treatment. Although the use of ratios in this study makes it difficult to compare directly, an increase in GPC would agree with Duarte et al (157) as a marker of treatment response. Unfortunately, as lipids are relatively concentrated in breast tissue and highly variable, van Asten et al did not examine lipids as response markers (158).

Changes in metabolite profiles have been observed in prostate cancer tissues when treated with Degralix (159). In this study, significant reductions were seen in tCho and Lac after Degralix treatment, which corresponded with less aggressive histology of the tissue sections. With regards to brain tumours, rat models implanted with BT4C cells have been used to examine the changes in metabolite profiles after induction of apoptosis through gene therapy (160). Upon day 4 of treatment, a significant increase in the concentrations of PCh and GPC was observed, which declined below pre-treatment levels by day 6. Furthermore, Tau concentrations began to decline on day 6, which was shown to correlate with cell density.

1.4.4.6 Correlations between metabolite concentrations and gene expression and/or histological features

The relationship between metabolite concentrations and gene expression or histological markers is of interest for understanding the underlying biology of the metabolome and its clinical application. In prostate tumours, it was shown that clustering of tumours on metabolite profiles corresponded with the expression level of ERG mRNA, and that metabolite concentrations showed significant differences with regards to ERG_{high} and ERG_{low} groups (161). Bertilsson et al demonstrated significant positive correlations between citrate, Cho and GPC and their biosynthetic enzymes.

In the adult brain, Cheng et al investigated the heterogeneity of GBM samples from a single tumour, and correlated the concentration of metabolites with percentage areas of necrosis and tumour (147). Lipids and Lac significantly positively correlated with area of necrosis, whilst the ratio of PCh to Cho correlated with area of tumour in the sample. The finding that lipids are a marker of necrosis is supported by Opstad et al (162). The authors also propose Tau as a marker of apoptosis in glial tumours; the concentration of this metabolite correlated with TUNEL staining in both necrotic and non-necrotic samples. Dali-Youcef et al successfully correlated the expression of histone deacetylases and transcriptional co-factors with grade II and III oligodendrogliomas and GBM (153). The ratio of GPC to PCh significantly correlated positively with the expression of histone deacetylase 4 and SIRT1, whilst correlating negatively with HDAC1. In paediatric brain, the levels of metabolites were shown to correlate with histological features (163). Histological features assessed include apoptosis, percentage of Ki67 positive cells, atypia and neoplastic glial elements.

One benefit of HR-MAS is its non-destructive nature – the sample is retrievable after the metabolite profile has been obtained. Studies have been performed investigating the integrity of post HR-MAS samples with regards to RNA and histology, and correlating metabolite concentrations with gene expression and histological markers. Prostate tissue has been shown to retain both its structure after HR-MAS (164) and the integrity of mRNA (165). Post HR-MAS adult brain tissue was stained with Nile Red to visualise lipid droplets, although the authors did not formally assess the quality of the tissue after HR-MAS (95). Cheng et al examined GBM tissue after HR-MAS and concluded that the tissue staining was suitable for histological examination (147).

1.4.5 Summary

In summary, tissue metabolite profiles are a powerful characterising feature of tumours that have many potential applications to patient management, including diagnosis and prognosis. Whilst there is a wealth of evidence demonstrating the diagnostic potential of metabolite profiles, there is a lack of studies investigating how diagnosis of tumours can be aided by using HR-MAS.

Tissue metabolite profiles have shown prognostic potential in a variety of tumour types but, whilst evidence exists from *in vivo* MRS that metabolites can predict survival for paediatric brain tumour patients, there are few studies examining tumour tissue from these patients to confirm the ability of metabolites to predict survival.

Finally, whilst efforts have been made to examine the biological reasons for the differences in metabolite profiles through correlating metabolite concentrations, there are few studies which have used the prior knowledge of metabolic networks to identify differences in metabolism.

1.5 Objectives

1. To construct diagnostic classifiers using metabolite profiles of cerebellar tumours obtained by HR-MAS ;

2. To compare diagnostic accuracy of metabolite profiles to the accuracy of current rapid intraoperative diagnostic testing;
3. To perform survival analysis using metabolite profiles obtained by HR-MAS to identify metabolites that are predictive of overall survival;
4. To perform survival analysis using metabolite profiles obtained by HR-MAS to identify metabolites that are predictive of progression-free survival in cerebellar PA;
5. To identify metabolic pathways differentially activated by cerebellar tumours using HR-MAS and MS metabolite profiles.

1.6 Organisation of thesis

Chapter 2 contains detailed protocols for acquiring tissue, HR-MAS sample handling and data collection, mass spectrometry sample handling and data collection used in this thesis.

Objectives 1 and 2 are achieved in chapter 3. As discussed above, current rapid intraoperative diagnosis based on qualitative morphological features of tissue samples is limited by overlapping histological features and inter-observer variation. With the prognosis of some tumours, ependymoma in particular, being strongly associated with surgical outcome, improvements in intraoperative diagnosis have the potential to enhance survival. Metabolite profiles, which have diagnostic capability shown in other tumours, can be acquired using HR-MAS in a similar timescale to current histological processing. Combined with classification algorithms, they could help identify histologically ambiguous tumours. Chapter 3 uses metabolite profiles of cerebellar tumours to construct accurate and robust cross-validated classifiers, the accuracy of which are compared to the results of rapid intraoperative classification.

Objective 3 is achieved in chapter 4. Metabolites detected by *in vivo* MRS have been shown to be predictive of overall survival in paediatric brain tumours. However, the low resolution of MRS may obscure other markers predictive of survival. *In vivo* MRS can potentially be optimised to detect other markers of prognosis. In chapter 4, the ability of metabolite concentrations obtained by HR-MAS to predict overall survival in brain tumours from all areas of the brain is investigated using Kaplan-Meier analysis. The survival risk of patients is determined by Hazard Ratios calculated using Cox regression.

Whilst some tumours are associated with poor overall survival, some have very good prognoses; however, often these tumours have variable progression-free survival and require further treatment. In chapter 5, metabolite profiles obtained from cerebellar PA are subjected to a survival analysis to determine the extent to which they can predict progression-free survival and meet objective 4.

As metabolite profiles represent the phenotype of the tumour, differences in metabolite concentrations can identify potential novel therapeutic targets. In chapter 6 a pathway analysis on cerebellar tumours is performed to identify differences in metabolic pathways. Furthermore, the results are confirmed using MS, which increases the metabolome coverage. This analysis achieves objective 5.

Chapter 7 summarises the findings of the thesis, and discusses future work required for translation of the results to clinical practice.

CHAPTER 2: Methods

2.1 HR-MAS

2.1.1 Tissue preparation

Tumour tissue identified by a consultant histopathologist in surgically resected specimens was snap frozen in liquid nitrogen as soon as possible after removal and stored at -80°C. Time from surgical resection to snap freezing following diagnostic processes is estimated to be 25-30 mins. This study has Research Ethical Committee approval (NRES East Midlands-Derby, 04/MRE04/41) and CCLG Biological Studies Committee approval (2015 BS 01). Informed consent was given by the patient's parent or guardian. HR-MAS was performed at the Henry Wellcome Building for Nuclear Magnetic Resonance (HWB-NMR), the Biomolecular NMR Facility at the University of Birmingham. Tissue was cut with a scalpel over dry ice to fit into a 12 µl or 50 µl zirconium rotor (**Figure 2.1**) before being weighed. Data were acquired from tissue samples weighing between 3 and 45mg. The internal standard 3-(Trimethylsilyl)propionic-2,2,3,3-d4 acid sodium salt (TMSP) (Cambridge Biosciences, Cambridge, UK) was added to the sample in a rotor dependent manner. 3 µl of standard was added to 12 µl rotors (final concentration of 2.5 mM) whilst 5 µl of standard was added to 50 µl rotors (final concentration 1 mM). D_2O (Sigma Aldrich, Dorset, UK) was added to completely fill the rotor before it was fully assembled. The sample and rotor were kept cold over dry ice during preparation to prevent tissue degradation. The time from the start of sample preparation to the start of spectral acquisition is approximately 15 mins.

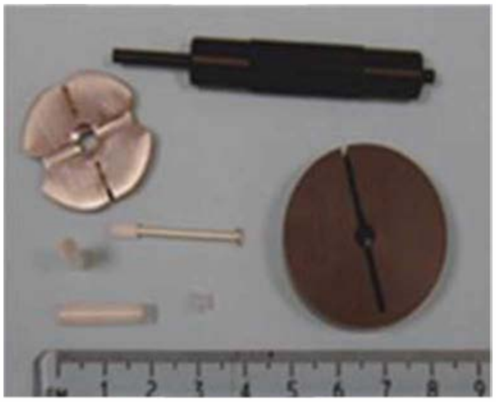

Figure 2.1 – Photograph of HR-MAS rotor components.

2.1.2 HR-MAS acquisition

Spectra were acquired using a Bruker Avance spectrometer (Bruker, Coventry, UK) with a magnetic field strength of 500 MHz fitted with a 4 mm three channel HCD HRMAS z-PFG band probe. The gas flow rate was set to 535 L h^{-1}. The rotor was spun at a temperature of 4°C to prevent metabolic activity and a frequency of 4800 Hz to remove spinning sidebands from the spectra. A NOESY sequence with water presaturation and spoil gradients was used with 2 s presaturation to suppress the water signal, a spectral width of 8000 Hz, acquisition time of 2 s, 32,000 data points, 4 dummy scans, a mixing time of 10 ms, 2 200 µs delay periods for gradient recovery and a repetition time of 4.07 s. No presaturation pulse was applied during the mixing time. Shimming was optimised using a solution of 100 mM lactate in D_20. Tuning and matching were optimised for each sample. The 90° pulse length was optimised for each sample to ensure the highest signal to noise ratio. 256 or 512 averages were acquired for 50 µl and 12 µl rotors respectively. An additional CPMG sequence with an echo time of 285 ms (number of loops = 137) was used to reduce the influence of lipids and macromolecules with short T_2 relaxation times on the spectrum and allow more accurate metabolite identification. Such a long echo time ensures full T_2 relaxation of the lipids and macromolecules, leaving only signals from the long T_2 polar metabolites. Time from the start of sample preparation to the start of spectral acquisition is approximately 15 mins. Post HR-MAS tissue was removed from the rotor and placed into an Eppendorf tube for storage at -80°C.

2.1.2.1 Limitations of the HR-MAS protocol

It is important to consider the limitations of this protocol. Before HR-MAS, the tissue samples experience a varying amount of time between surgical resection and snap freezing, which is likely to cause differences in abundance of some metabolite species such as glucose and lactate.

HR-MAS can cause mechanical degradation of the tissue samples due to high spin speeds. The mechanical damage can increase the concentration of metabolites by releasing previously NMR invisible molecules from macromolecular structures. Data not presented suggests that most metabolites do not significantly differ, with the exception of PCh and GSH, both of which are significantly lower.

The repetition time of the experiment needs to allow for T_1 relaxation of the metabolites in the tissue. Repetition time should be at least 5 times the longest metabolite T_1 relaxation time. Failure to allow long enough relaxation time will cause variable peak area of long T_1 metabolites between scans. Taurine exhibits the longest T_1 relaxation time of metabolites as reported in prostate tissue at 500 MHz at a temperature of 1°C (T_1 mean = 636 ms) (138). Therefore, repetition time should be $> 5 \times 636 = 3180$ ms. The protocol has a repetition time of 4 seconds, and should allow appropriate T_1 relaxation of the metabolites as T_1 relaxation reaches 99.8% for Tau.

There is a short interval between the first 90° pulse and the start of the data acquisition which will allow some T_1 and T_2 relaxation to occur. The NOESY protocol has an effective echo time of approximately 10 ms, which would allow 1.5-3.0% T_1 relaxation and 3-5% T_2 relaxation depending on a metabolites respective T_1/T_2 relaxation time.

The non-polar trimethylsilyl group of the TMSP molecule can interact with lipids in the sample, creating an unknown proportion of NMR invisible TMSP. This can cause over estimation of the concentration of metabolites in the tissue sample. Alternatives to TMSP include a separate volume within the rotor for a quantitative reference, or electronic references such as ERETIC (166) or PULCON (167).

2.1.3 HR-MAS spectra processing

Free Induction Decays were Fourier transformed in Topsin 2.0 (Bruker, Coventry, UK) and the resulting spectra were imported into MestReNova 9.0.1 software suite (Mestrelab Research, Spain). The spectra were manually phased and the chemical shift referenced with respect to TMSP at 0 ppm.

The baseline was automatically corrected using a Whittaker smoother, a penalised least squares approach that can be used to model the baseline (168). From a series of m points y_i sampled at equal intervals of the NMR spectrum, the algorithm creates a new series z that is influenced by two opposing factors. The first factor is recreating *y*, or fidelity, (F) expressed as the sum of squares of the differences between *y* and *z*:

$$F = \sum_{i=1}^{m} (y_i - z_i)^2$$

The second factor smoothness (S) is expressed in terms of the *d*th differences:

$$S = \sum_{i=1}^{m} (\Delta^d z_i)^2$$

The optimum z_i is found by minimising the value of Q, where Q=F+λS. The λ parameter is used to determine the importance of the smoothing factor S. An example of the Whittaker smoother being applied to a spectrum is shown in **Figure 2.2**. To prevent observer bias, the parameters were selected by automated functions built into Mestrenova.

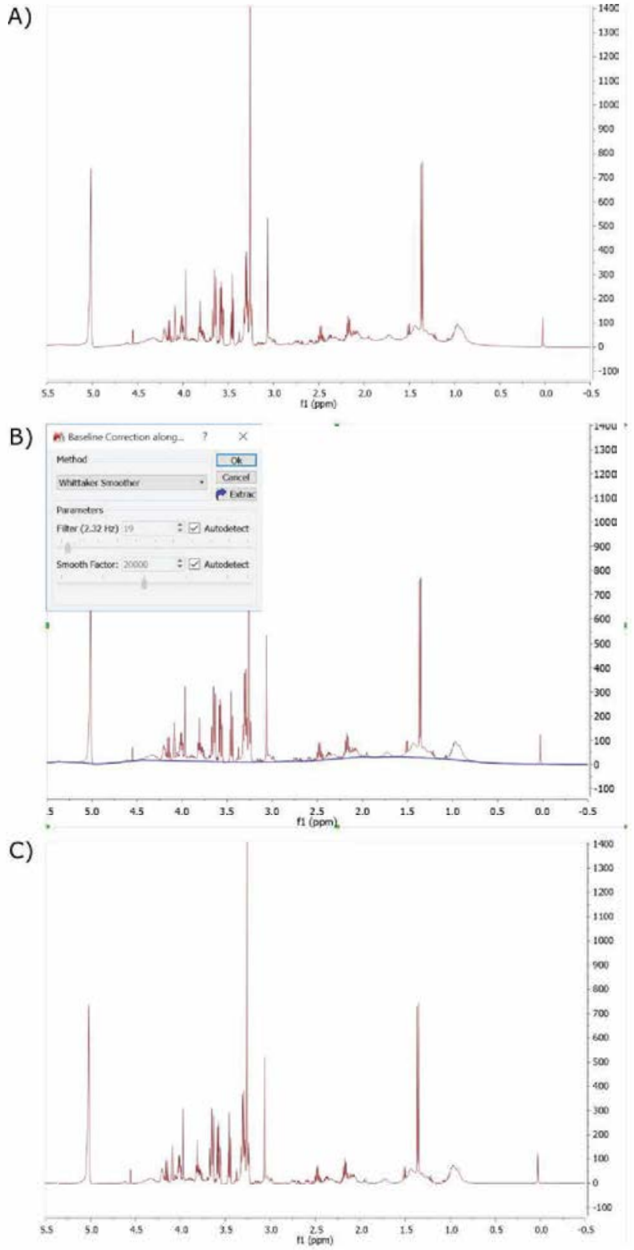

Method
Whittaker Smoother

Filter (2.32 Hz) 19 ☑ Autodetect

Smooth Factor: 20000 ☑ Autodetect

Figure 2.2 – Whittaker smoother as applied to the spectrum of a tumour sample. A) The original spectrum has a baseline that would distort analysis and needs to be removed. B) The Whittaker smoother panel from Mestrenova indicating the interval at which to sample the spectrum and the smoothing factor. C) The spectrum after the baseline has been removed by the Whittaker smoother.

Peaks were picked using the Global Spectral Deconvolution (GSD) algorithm to improve the resolution of areas of the spectrum with overlapping resonances. This algorithm fits a set of Lorentzian or near Lorentzian lines to the peaks in the spectrum whilst ignoring noise. To prevent bias by the observer, the default settings for the GSD algorithm were used. An example of the GSD algorithm as applied to a spectrum is displayed in **Figure 2.3**.

Deconvolved features from the NOESY experiments were quantified by comparing the area of the peaks corresponding to the respective metabolite to the area of the internal standard peak, considering the number of protons contributing to both the metabolite and standard signal. Experimentally acquired chemical shift information from Govindaraju et al.(169) and the Human Metabolome Database (HMDB) (170) were used to confirm signal assignment. Assigned resonances are displayed in **Table 2.1**. The assignments were made using the most separated resonances to reduce assignment errors. However, other resonances were used as a visual aid in determining peak identity. If peaks corresponding to the expected resonances were not visible, then a value of 0 was given for that metabolite. Examples of deconvolved and assigned metabolites can be found in Appendix 1.

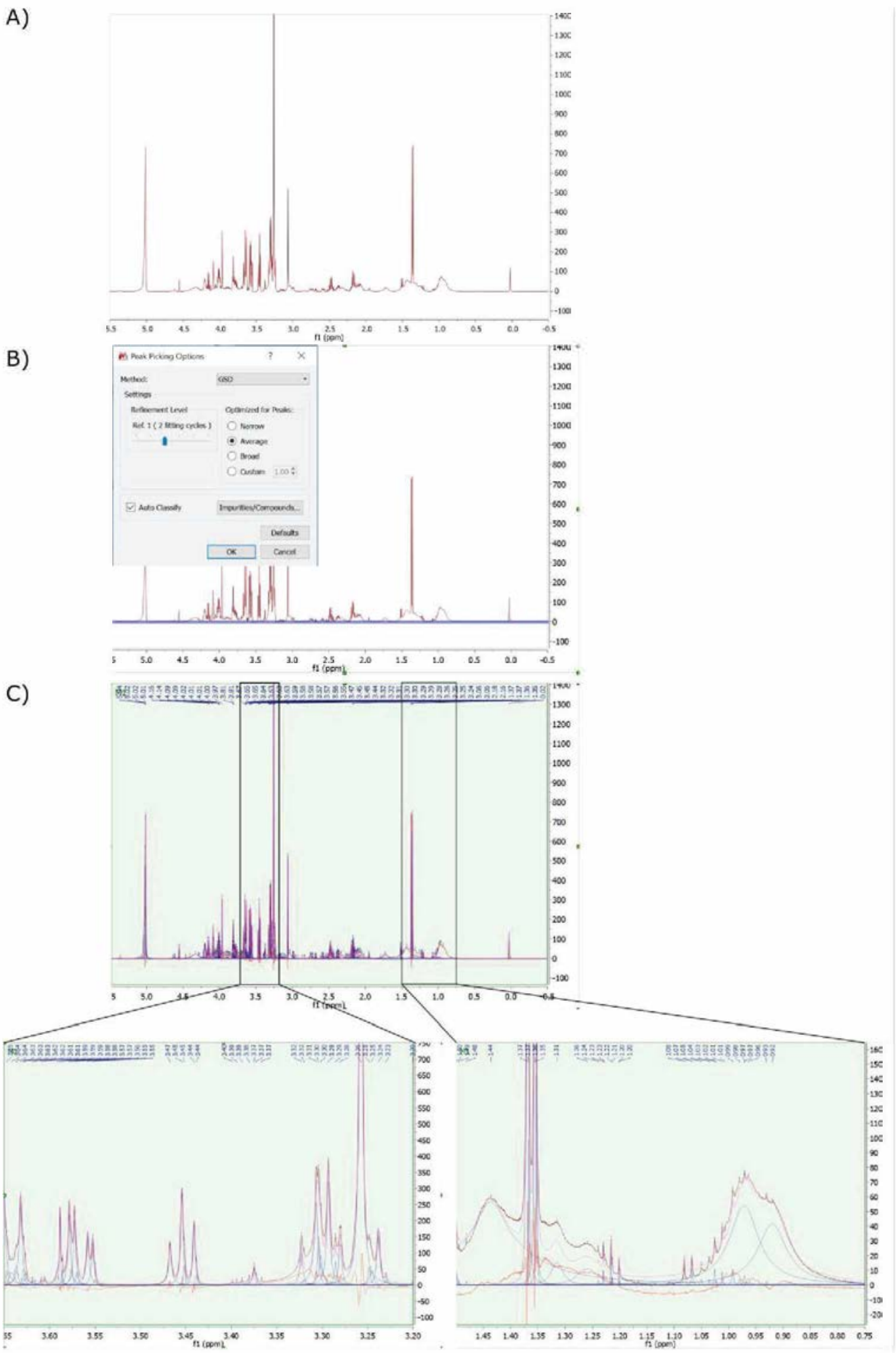

Peak Picking Options

Method: GSD

Settings

Refinement Level: Ref. 1 (2 fitting cycles)

Optimized for Peaks:
○ Narrow
● Average
○ Broad
○ Custom 1.00

☑ Auto Classify

Figure 2.3 – Legend on next page.

Figure 2.3 - GSD as applied to the same spectrum from figure 2.2. A) The baseline removed spectrum from figure 2.2. B) The panel within Mestrenova allowing GSD to be performed on the spectrum. The blue lines across the spectrum indicate thresholds for separating peaks from noise. C) A full deconvolved spectrum with sections expanded showing the regions of 0.75-1.5ppm and 3.2-3.65ppm.

Metabolite	Chemical shift of peak/peaks (ppm)	Number of protons	Peak splitting pattern
Lipids 0.9	0.9	3	Broad singlet
Leu	0.95	3	Triplet
Iso	1.01	3	Doublet
Val	1.05	3	Doublet
Lipids	1.30	2	Broad singlet
Lac	1.32	2	Doublet
Ala	1.47	2	Doublet
Ace	1.92	3	Singlet
NAA	2.01	3	Singlet
Acetone	2.23	6	Singlet
GABA	2.31	2	Triplet
Glu	2.35	2	Multiplet
Suc	2.41	4	Singlet
Gln	2.45	2	Multiplet
GSH	2.55	2	Multiplet
hTau	2.65	2	Triplet
Asp	2.81	2	Doublet of doublets
Cr	3.03	3	Singlet
Cho	3.21	9	Singlet
PCh	3.23	9	Singlet
GPC	3.24	9	Singlet
sIns	3.35	6	Singlet
Tau	3.42	2	Triplet
mIns	3.54	2	Doublet of doublets
Gly	3.56	2	Singlet
Ser	3.84	1	Doublet of doublets
Asc	4.53	1	Doublet
Glc	4.65	1	Doublet

Table 2.1 – The assignments for visible metabolites in HR-MAS spectra of brain. These features are the most easily observable for the metabolites. Whilst other resonances are observable in a spectrum, they are used to confirm an assignment and not for quantification.

2.1.4 HR-MAS quality control

To ensure data quality, HR-MAS spectra were visually assessed against the following criteria. Non-tumour brain tissue is visually different to tumour tissue in that NAA is the predominant peak, with very low levels of choline-containing compounds and lipids. Each spectrum was visually assessed, and any cases displaying these characteristics were excluded from further analysis. Furthermore, spectra were assessed for the following:

1. High signal to noise ratio;
2. Symmetrical TMSP peak at 0ppm;
3. Discrimination of singlets for Cho at 3.21ppm, PCh at 3.23ppm and GPC at 3.24ppm;
4. No contamination of tissue with specimen matrix.

Spectra not meeting these standards were excluded from analysis.

2.1.5 Statistical analysis of HR-MAS data

Quantified metabolite data were imported into the R statistical environment for statistical analysis. Metabolite concentrations of each sample were normalised by dividing each concentration by the sum of non-lipid concentrations in the sample. Morphological properties of the various tumour types, such as cellularity and tissue structure, differ and as such normalisation to sample weight is perhaps not the most adequate normalisation factor. To account for the morphological differences, the metabolite concentrations are normalised to the total sum of the polar metabolites. Lipids are excluded from total sum as areas of necrosis will bias the normalisation factor. Furthermore, as tissue samples were dissected on dry ice and put into the rotors whilst frozen, tissue weight measurements can be skewed by water ice that was frozen with the sample. As normalised metabolite concentrations do not show normal distributions, non-parametric statistical tests in the base stats R library were used to analyse data. Survival analyses were performed using the survival library written in R.

2.2 Mass spectrometry

2.2.1 Metabolite and lipid extraction

Mass spectrometry was performed at the Phenome Centre Birmingham at the University of Birmingham. Tissue was stored at -80°C prior to metabolite extraction. Metabolites and lipids were extracted from pre-weighed tissue using a two-step Bligh and Dyer style biphasic extraction protocol (171, 172) with some modifications. Samples weighing <15 mg were homogenised in 120 µl ice-cold methanol (LC-MS grade, LiChrosolv, Merck) and 48 µl ice-cold water (LC-MS grade, LiChrosolv, Merck) using a bead-based homogeniser (Precellys 24, Stretton Scientific). The homogenate was transferred to a 1.8 ml glass vial, and 120 µl ice-cold chloroform (HPLC grade, HiPerSolv CHROMANORM, VWR) and 60 µl ice-cold water were added before vortexing for 30 s. Samples were set on ice for 10 min and then centrifuged (2500 G, 4°C, 10 min). To complete phase separation, samples were set at room temperature for 5 min. The entire polar and non-polar phases were removed using a Hamilton syringe. Polar extracts were dried using a SpeedVac (Savant SPD111V, Thermo Fisher Scientific) and vapour trap (RVT5105230, Thermo Fisher Scientific), and non-polar extracts were dried under a nitrogen stream (Techne Sample Concentrator FSC400D, Thermo Fisher Scientific). Dried extracts were stored at -80°C until analysis. Samples weighing >15 mg were prepared identically except 560 µl methanol, and 224 µl water were added in the first step, and 560 µl chloroform and 280 µl water were added in the second step. For both preparation methods, the methanol/chloroform/water ratio was identical. Extract blanks were prepared by the same methods in the absence of tissue.

2.2.2 Sample resuspension

Polar extracts were resuspended 3:1 acetonitrile/water (LCMS grade, LiChrosolv, Merck) and non-polar extracts were re-suspended 3:1 propan-2-ol/water (LCMS grade, LiChrosolv, Merck). The utilised volumes of resuspension solvent were normalised to the initial frozen tissue mass. For the group of samples weighing <15mg, the lowest mass sample was resuspended in 50µL and the resuspension volume for other samples was calculated as follows:

([tissue mass of sample] / [tissue mass of smallest sample]) × 50.

For the group of samples weighing >15mg, the lowest mass sample was resuspended in 100µL and the resuspension volume for other samples was calculated as follows:

([tissue mass of sample] / [tissue mass of smallest sample]) × 100.

Following resuspension solvent addition, samples were vortexed for 30 s. Separately for polar and non-polar samples, a pooled QC sample was prepared by combining 50 µl aliquots from resuspended extracts where more than 150 µl total volume was present (40 out of 60 samples). All samples were centrifuged (20,000-g, 4°C, 20 min) and loaded into HPLC vials (VI-04-12-02RVG 300µl Plastic, Chromatography Direct, UK).

2.2.3 Ultra Performance Liquid chromatography-Mass spectrometry (UPLC-MS)

The samples were analysed applying two (UPLC-MS) methods using a Dionex UltiMate 3000 Rapid Separation LC system (Thermo Fisher Scientific, MA, USA) coupled with an electrospray Q Exactive Focus mass spectrometer (Thermo Fisher Scientific, MA, USA). Polar extracts were analysed on an Accucore-150-Amide-HILIC column (100 x 2.1 mm, 2.6 µm, Thermo Fisher Scientific, MA, USA). Mobile phase A consisted of 10 mM ammonium formate and 0.1% formic acid in 95% acetonitrile/water and mobile phase B consisted of 10 mM ammonium formate and 0.1% formic acid in 50% acetonitrile/water. Flow rate was set for 0.50 ml min^{-1} with the following gradient: t=0.0, 1% B; t=1.0, 1% B; t=3.0, 15% B; t=6.0, 50% B; t=9.0, 95% B; t=10.0, 95% B; t=10.5, 1% B; t=14.0, 1% B, all changes were linear with curve = 5. The column temperature was set to 35°C and the injection volume was 2 µl. Data were acquired in positive and negative ionisation modes separately within the mass range of 70 – 1050 m/z at resolution 70,000 (FWHM at m/z 200). Ion source parameters were set as follows: Sheath gas = 53 arbitrary units, Aux gas = 14 arbitrary units, Sweep gas = 3 arbitrary units, Spray Voltage = 3.5kV, Capillary temp. = 269 °C, Aux gas heater temp. = 438°C. Data dependent MS2 in 'Discovery mode' was used for the MS/MS spectra acquisition using the following settings: resolution = 17,500 (FWHM at m/z 200); Isolation width = 3.0 m/z; stepped normalised collision energies (stepped NCE) = 25, 60, 100%. Spectra were acquired in three different mass ranges: 50 – 200 m/z; 200 – 400 m/z; 400 – 1000 m/z.

Non-polar extracts were analysed on a Hypersil GOLD column (100 x 2.1mm, 1.9 µm; Thermo Fisher Scientific, MA, USA). Mobile phase A consisted of 10 mM ammonium formate and 0.1%

formic acid in 60% acetonitrile/water and mobile phase B consisted of 10 mM ammonium formate and 0.1% formic acid in 90% propan-2-ol/water. Flow rate was set for 0.40 mL min^{-1} with the following gradient: t=0.0, 20% B; t=0.5, 20% B, t=8.5, 100% B; t=9.5, 100% B; t=11.5, 20% B; t=14.0, 20% B; all changes were linear with curve = 5. The column temperature was set to 55°C and the injection volume was 2µL. Data were acquired separately in positive and negative ionisation mode, within the mass range of 150 – 2000 m/z at resolution 70,000 (FWHM at m/z 200). Ion source parameters were set as follows: Sheath gas = 50 arbitrary units, Aux gas = 13 arbitrary units, Sweep gas = 3 arbitrary units, Spray Voltage = 3.5kV, Capillary temp. = 263°C, Aux gas heater temp. = 425°C. Data dependent MS2 in 'Discovery mode' was used for the MS/MS spectra acquisition using the following settings: resolution = 17,500 (FWHM at m/z 200); Isolation width = 3.0 m/z; stepped normalised collision energies (stepped NCE) = 20, 50, 80%. Spectra were acquired in three different mass ranges: 200 – 400 m/z; 400 – 700 m/z; 700 – 1500 m/z.

A Thermo ExactiveTune 2.8 SP1 build 2806 was used as instrument control software in both cases and data were acquired in profile mode. Quality control (QC) samples were analysed as the first ten injections and then every seventh injection with two QC samples at the end of the analytical batch. Two blank samples were analysed, the first as the 6th injection and then at the end of each batch.

2.2.4 Raw data processing and metabolite annotation

Raw data acquired in each analytical batch were converted from the instrument-specific format to the mzXML file format applying the open access ProteoWizard software (173). Deconvolution was performed with XCMS software (174) according to the following settings: min peak width of 4 for HILIC and 6 for lipids; max peak width of 30; ppm (12 for HILIC and 14 for lipids); mzdiff (0.001); gapInit (0.5 for HILIC and 0.4 for lipids); gapExtend (2.4); bw (0.25); mzwid (0.01). A data matrix of metabolite features (m/z-retention time pairs) vs. samples was constructed with peak areas provided where the metabolite feature was detected for each sample. Data for the first 8 QC samples were removed from the dataset. The remaining QC samples were applied to filter the data and remove data which were not reproducibly detected. All metabolite features which were detected in less than 60% of samples were removed from the dataset and all metabolite features whose peak area reproducibilities were defined as not acceptable (RSD>30%) were removed from the dataset. Putative annotation of metabolites or metabolite groups was performed by applying the PUTMEDID-LCMS workflows operating in the Taverna workflow environment(175). A 5 ppm mass error and a retention time range of 2 s in feature grouping and molecular formula and metabolite matching was applied. Multiple annotations could be observed for a single detected metabolite feature, as different metabolites can be detected with the same accurate m/z (for example, isomers with the same molecular formula). Also, a single metabolite could be detected as multiple molecules, particularly as a different type of ion (e.g., protonated and sodiated ions). Throughout the coming chapters, the term “metabolite” in the context of mass spectrometry refers to either single metabolites or groups of molecules with the same retention time and the same accurate m/z. All molecules were annotated according to guidelines for reporting of chemical analysis results, specifically to Metabolomics Standards Initiative level 2 (176).

2.3 Acquisition and analysis of genetic data

An independent dataset was identified and downloaded from the Gene Expression Omnibus (GEO), a repository created by the National Centre for Biotechnology Information. The dataset, archived by Henriquez et al, is composed of 73 brain tumour gene expression experiments and given the accession number GSE42656. Data were generated using the IlluminaHT-12 V3.0 expression beadchip. Raw expression was normalised using the interquartile range for each probe and was log2 transformed prior to analysis.

2.4 Gathering clinical data

The pathology and radiology reports for samples from the local tissue bank at Birmingham Children's Hospital were available to view on the hospitals reporting systems. Dates of death were provided by the West Midlands Tumour Registry Office at Birmingham Children's Hospital. For samples from outside centres, information requests were made to the CCLG.

Progression free survival data for PAs was gathered by Dr Neelakshi Ghosh by examining the clinical notes of the patients treated at Birmingham Children's Hospital. Residual tumour following initial resection was measured by Dr Adam Oates.

CHAPTER 3: Metabolic characterisation and classification of paediatric cerebellar tumours using HR-MAS

3.1 Introduction

Techniques for characterising paediatric brain tumours before surgery have become increasingly well developed and can provide a wealth of information (177). However, intraoperative examination of tumour tissue is based on qualitative features visible after staining tumour tissue with H&E. This is subject to technical artefacts, variable quality and inter-observer variability. Tissue metabolite profiles acquired by HR-MAS have potential to improve intraoperative diagnostic accuracy and allow surgeons to obtain optimal surgical results. Cerebellar tumours are common in children, consisting predominantly of MB, EP and PA, and are ideal for testing the classification accuracies of HR-MAS and rapid intraoperative diagnostic testing.

Before surgical excision of a brain tumour, MRI is the predominant imaging modality and gives excellent anatomical and other physical information of a tumour. Nevertheless, the first opportunity to study the tumour directly arises during surgery. The surgeon will remove a piece of the tumour and send it for a histopathological opinion (178). During the initial tissue examination, a pathologist will attempt to provide a diagnosis based on the morphology of the tumour cells as viewed under a microscope after the tissue has been stained with H&E (**Figure 3.1**). This type of examination can be done in the timescale of an operation and provides the neurosurgeon with some information on which to base further surgical management. The pathologist will also examine tissue stained with immunohistochemical stains to further identify a tumour, as well as request relevant genetic testing (179). These examinations take significantly longer than H&E stains, particularly if a second opinion is required and so are reported outside of a surgery.

The intraoperative diagnosis of a tumour has the potential to change how a patient is surgically managed. Different tumour types have different optimum surgical outcomes; currently, the most important prognostic marker for EP is extent of resection (180-183). On the other hand, PAs have very good outcomes even with subtotal resection. Therefore, a surgeon may opt for more aggressive surgical resection if EP is diagnosed. However, current rapid intraoperative diagnosis using H&E staining has variable accuracies reported in the literature (60, 61, 184). For EP, reported accuracies range from 57% to 83%. Low accuracy is usually not attributed to a completely incorrect diagnosis, but the inability to provide a diagnosis beyond the differentiation of the tumour. For example, an EP can be described as a glial tumour. This is not incorrect, but does not give the surgeon important information.

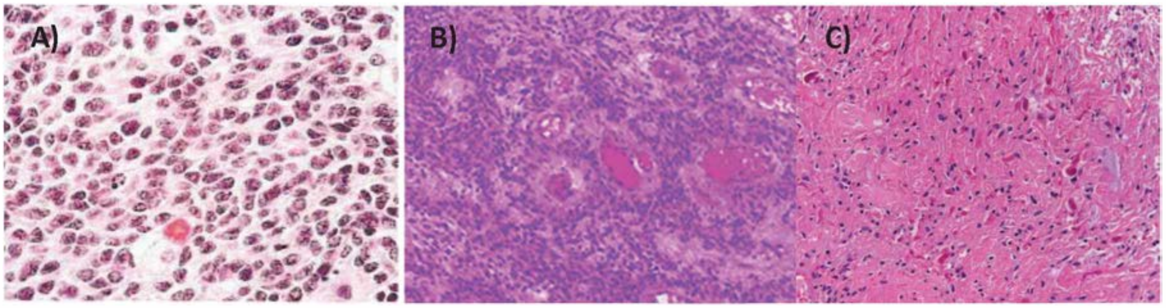

Figure 3.1 – Representative H&E slides of A) MB (185), B) EP (35) and C) PA (21). MB tissue is highly cellular and typically characterised by small, round cells with scant cytoplasm. The cells may form nodules or sheets, or appear anaplastic. EP appear less cellular than MB, although more cellular than normal tissue, and often display perivascular pseudorosettes. EP may show anaplastic features such as necrosis, increased proliferation and cell density. PA are characterised by a biphasic growth pattern of cellular and microcystic regions. The cells

themselves have long, thin cytoplasmic processes. Rosenthal Fibers are commonly seen in these tumours.

Advances in molecular biological techniques have allowed a number of large studies to be performed on paediatric brain tumours. Both gene expression and epigenomic analysis have displayed high classification accuracy. These methods are time consuming and labour intensive and unlikely to provide information in the time limit of an operation.

In vivo MRS has shown that tumours have distinctive metabolite profiles which can provide diagnostic information (3, 5, 120). Unfortunately, *in vivo* MRS suffers from a low signal to noise ratio and poor spectral resolution. HR-MAS has several technical advantages that make it suitable for use as a rapid intraoperative diagnostic aid. Firstly, it is non-destructive; the tissue can be retrieved for further analysis. Secondly, there is no complex sample preparation required. Finally, data can be acquired on the order of minutes, which could allow the spectroscopic findings to influence surgical management. Tissue studies offer an advantage with regards to cohort construction, especially for rarer tumours, in that historic tissue can be used to form a large cohort without the need for large multi-centre studies. HR-MAS has been used with success to examine the metabolite profiles from a range of cancers including prostate (164, 186), breast (187), lung (131, 188) and colon (188) cancers.

In this chapter, tissue metabolite concentrations were used to characterise the metabolite profiles of the most common cerebellar tumours and build a clinically applicable classification model. The classification accuracy was compared to the intraoperative diagnosis for the same tumours to informally compare the two methodologies.

3.2 Methods

3.2.1 Cohort construction

For this retrospective analysis, frozen diagnostic tissue for 24 PAs, 36 MBs, 18 EPs and 5 ATRTs were acquired from Birmingham Children's Hospital and the Children's Cancer and Leukaemia Group (CCLG) tissue banks (**Table 5.1**). All cases originated in the cerebellum and were not exposed to chemotherapy or radiotherapy before surgery. The tissue was snap frozen in liquid nitrogen shortly after resection and stored at -80°C. The final diagnosis for all cases was made following full histopathological examination, including immunohistochemistry where required, and reviewed by multi-disciplinary teams.

3.2.2 Statistical analysis

Normalised metabolite concentrations were subjected to Kruskal Wallis tests to identify metabolites with significantly different concentrations between tumours. Post hoc Dunn tests were used to perform pairwise comparisons.

Hierarchical clustering and PCA were performed on scaled data to visualise data structure. For hierarchical clustering, Euclidean distance was used to calculate the distance metric and Ward's method was used to cluster samples. Euclidean distance is effective in measuring the distance between samples when continuous variables have been scaled, and Ward's clustering algorithm is able to identify spherical clustering with more compact centres based on minimising sum of squares after samples are merged into a cluster. Both methods are well accepted when clustering continuous variables.

3.2.3 Classifier construction

To examine the ability of metabolite profiles to classify EP, MB and PA, principal components accounting for 90% total variation extracted by PCA were used to inform a Linear Discriminant Analysis (LDA) for data classification. This approach allowed the retention of biological information and the identification of metabolites important for tumour assignment. The accuracy and robustness of the constructed classifier was tested using a 10-fold cross validation, in which the data is split into 10 equal folds. The classifier was constructed using 90% of the data, and the remaining 10% was used to test the classifier. This process is repeated until all cases have been tested.

A second LDA classifier was constructed to see how adding ATRTs to the cohort would affect classification accuracies. This second classifier involved two steps; firstly, tumours were classified as embryonal or glial, before assignment of a tumour type. The model was validated using 10-fold cross validation.

Diagnosis	WHO grade	N		Total	Age at diagnosis (months)		Gender		Time in -80°C storage (months)		Rotor size	
		BCH	CCLG		Median	Range	M	F	Median	Range	12ul	50ul
PA	I	24	0	24	120	14-190	11	13	56	25-147	11	13
EP	II/III	8	10	18	32	14-194	13	5	90	13-308	8	10
MB	IV	29	7	36	69	18-210	27	9	54	8-186	13	23
ATRT	IV	5	0	5	2	1 - 55	3	2	46	11-106	1	4

Table 3.1 – a summary of the cohort demographics used for the classification analysis.

3.3 Results

3.3.1 Unsupervised analysis of paediatric cerebellar tumours

Univariate Kruskal Wallis tests identified 15 metabolites with significantly different concentrations between the three main tumour types ($P < 0.05$ Bonferroni corrected) (**Figure 3.2**, **Figure 3.3**, **Table 3.2**). The concentrations of Asc, Asp, PCh, Tau and lipids at 1.3ppm were significantly higher in MB, whilst Glc and sIns concentrations were significantly lower in this tumour group. EP showed significantly higher concentrations of mIns and significantly lower Leu. Gln and hTau concentrations were significantly higher in PA. It was observed that ATRT have significantly lower Cr than the other three tumour types. Furthermore, ATRT display significantly higher GSH than MB and PA.

Multivariate linear regression modelling normalised metabolite concentration as a function of sample weight, storage time, rotor size and diagnosis was performed to identify if any of these variables are confounders in this analysis. Lipids showed a significant relationship with weight in the multivariate analysis (corrected $P < 0.05$). Univariate analysis shows that sample weight accounts for 5% of the total variation in lipids ($R^2 = 0.050$, $P = 0.024$), whilst a univariate analysis with modelling lipids as a function of diagnosis suggests diagnosis accounts for 32% of the total variation ($R2 = 0.32$, $P = 1.83\text{x}10^{-7}$).

Unsupervised hierarchical clustering of EP, MB and PA samples shows the data forms three clusters, with the highest split separating the embryonal tumours from the glial tumours (**Figure 3.4**). Each of the three clusters largely corresponds to a particular tumour type. Upon inclusion of ATRT samples, hierarchical clustering reveals the samples again split into glial and embryonal groups, before broadly splitting again into tumour groups. ATRT samples cluster in a single sub-cluster of embryonal tumours. This suggests that ATRT are more similar to each other than they are to MB samples as a whole.

PCA also shows a glial embryonal split, with ATRT samples grouping within MB samples. A PCA scatterplot shows the second principal component separates embryonal and glial tumours, although beyond this separation there is considerable overlap between the glial tumour types. (**Figure 3.5**). Examination of the loadings for the second principal component identifies the metabolites influencing the separation of embryonal and glial tumours. Metabolites important for glial tumour separation include Gln, GPC, sIns, Glc and Suc. Metabolites important for embryonal tumour separation include PCh, Tau, Asc and Asp. The branched chain amino acids and Ala have the most negative loadings for the first principal component, although the significance of this is unclear.

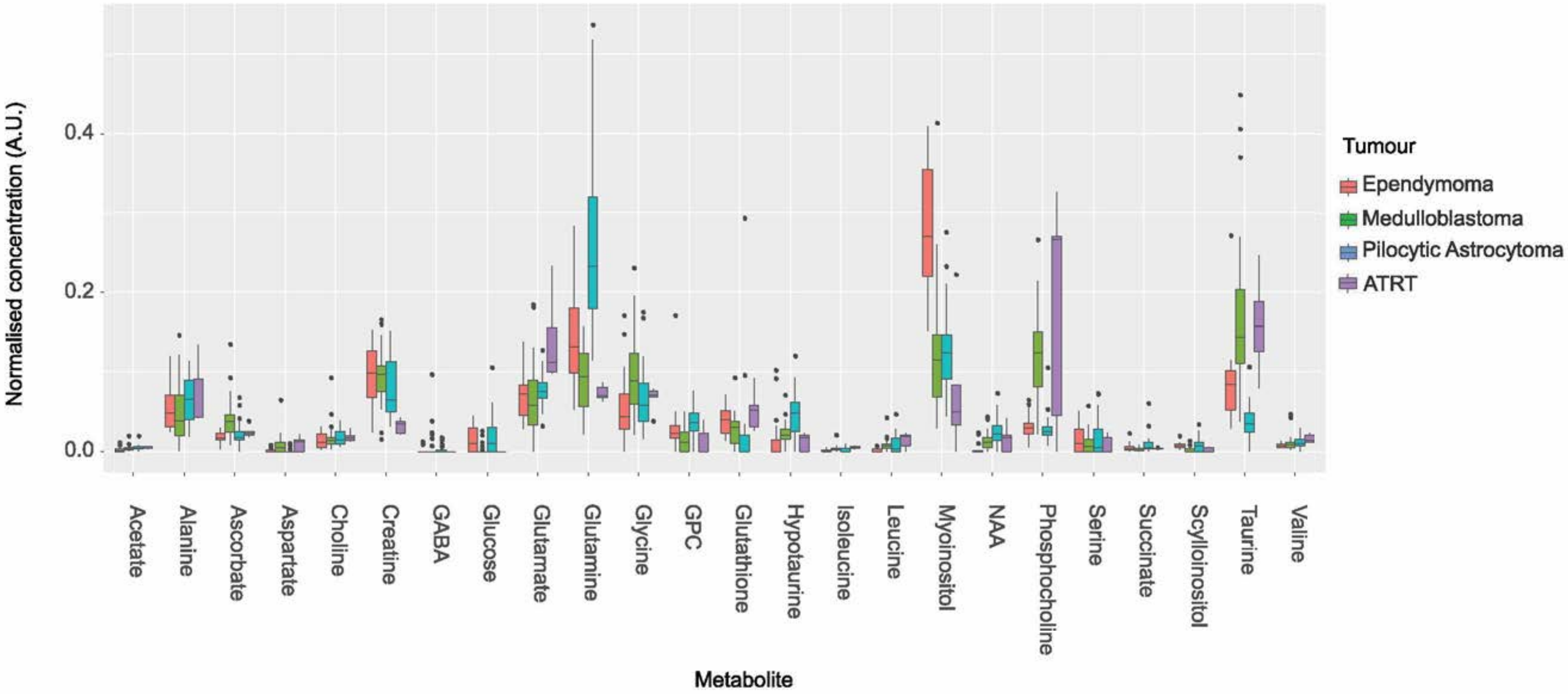

Figure 3.2 – the normalised metabolite concentrations for quantified metabolites obtained from the four most common paediatric cerebellar tumours.

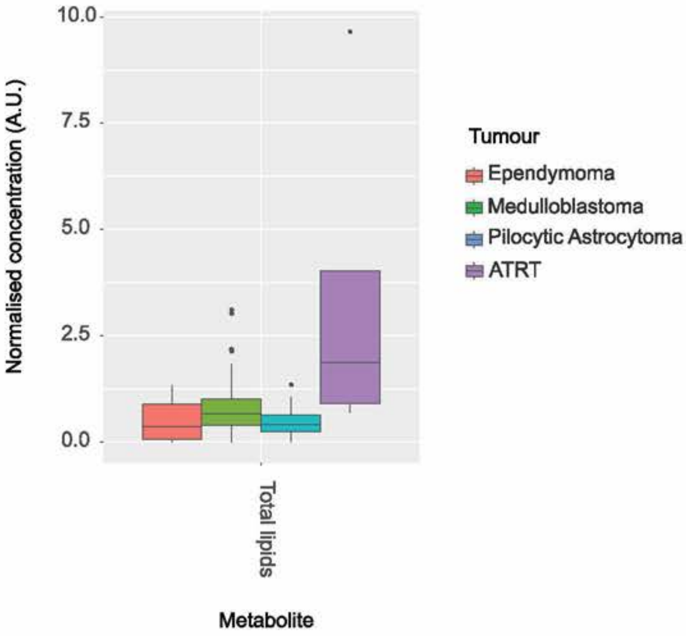

Figure 3.3 – Normalised total lipid concentration for the four most common paediatric cerebellar tumours.

Metabolite	Mean normalised metabolite concentration				Kruskal-Wallis test P-value	Bonferroni corrected P-value	Post hoc Dunn test					
	MB	EP	PA	ATRT			MB vs EP	MB vs PA	MB vs ATRT	EP vs PA	EP vs ATRT	PA vs ATRT
Asc	0.0394	0.0180	0.0219	0.0250	$6.7x10^{-5}$	$1.7x10^{-3}$	$2.5x10^{-5}$	$1.3x10^{-4}$	N.S	N.S	N.S	N.S
Asp	0.0076	0.0014	0.0009	0.0098	$6.4x10^{-5}$	$1.6x10^{-3}$	$1.3x10^{-3}$	$1.5x10^{-5}$	N.S	N.S	$2.5x10-^{2}$	$6.7x10-^{3}$
Cr	0.0939	0.0961	0.0804	0.0320	$1.8x10^{-3}$	$4.5x10^{-2}$	$4.1x10-^{2}$	N.S	$1.8x10^{-4}$	N.S	$3.8x10^{-4}$	$5.6x10-^{3}$
Glc	0.0020	0.0144	0.0185	0.0000	$1.8x10^{-4}$	$4.5x10^{-3}$	$1.5x10-^{3}$	$1.0x10^{-4}$	N.S	N.S	N.S	$4.4x10^{-3}$
Gln	0.0930	0.1390	0.2589	0.0735	$1.2x10^{-9}$	$3.1x10^{-8}$	$1.2x10^{-2}$	$1.6x10^{-10}$	N.S	$6.3x10^{-4}$	$2.3x10^{-2}$	$2.1x10^{-5}$
GPC	0.0136	0.0310	0.0364	0.0125	$4.9x10^{-5}$	$1.2x10^{-3}$	$1.5x10^{-2}$	$2.7x10^{-6}$	N.S	$3.4x10^{-2}$	N.S	$4.8x10^{-3}$
GSH	0.0261	0.0405	0.0233	0.0519	$7.5x10^{-5}$	$1.9x10^{-3}$	$1.4x10^{-2}$	$6.1x10^{-3}$	$3.0x10^{-2}$	$1.7x10^{-5}$	N.S	$7.6X10^{-4}$
hTau	0.0220	0.0174	0.0452	0.0123	$1.9x10^{-4}$	$4.8x10^{-3}$	$2.0x10^{-2}$	$3.3x10^{-3}$	N.S	$1.4x10^{-5}$	N.S	$6.0x10^{-3}$
Leu	0.0082	0.0014	0.0096	0.0138	$2.9x10^{-4}$	$7.2x10^{-3}$	$2.7x10^{-5}$	N.S	N.S	$5.0x10^{-3}$	$1.3x10^{-3}$	N.S
mIns	0.1243	0.2805	0.1283	0.0777	$2.6x10^{-7}$	$6.6x10^{-6}$	$1.2x10^{-7}$	N.S	N.S	$7.2x10^{-6}$	$1.7x10^{-5}$	N.S
NAA	0.0127	0.0036	0.0246	0.0159	$2.6x10^{-6}$	$6.4x10^{-5}$	$5.9x10^{-4}$	$2.7x10^{-3}$	N.S	$4.2x10^{-8}$	$3.0x10^{-2}$	N.S
PCh	0.1212	0.0302	0.0297	0.1814	$1.2x10^{-9}$	$3.1x10^{-8}$	$5.0x10^{-7}$	$4.0x10^{-9}$	N.S	N.S	$5.1x10^{-3}$	$2.1X10^{-3}$
Suc	0.0024	0.0049	0.0099	0.0033	$2.0x10^{-4}$	$5.1x10^{-3}$	$3.3x10^{-2}$	$4.8x10^{-6}$	N.S	$2.1x10^{-2}$	N.S	N.S
sIns	0.0019	0.0072	0.0080	0.0021	$1.7x10^{-5}$	$4.1x10^{-4}$	$1.5x10^{-5}$	$7.3x10^{-5}$	N.S	N.S	$9.5x10^{-3}$	$2.3x10^{-2}$
Tau	0.1672	0.0875	0.0365	0.1594	$9.8x10^{-11}$	$2.5x10^{-9}$	$8.9x10^{-4}$	$5.5x10^{-12}$	N.S	$2.2x10^{-3}$	$3.2x10^{-2}$	$1.0x10^{-4}$

Table 3.2 – Kruskal-Wallis tests identify metabolites with normalised concentrations that differ significantly between the four most common paediatric cerebellar tumour types. Post hoc Dunn tests perform pairwise comparisons and identify which tumours are significantly different to the others for each metabolite.

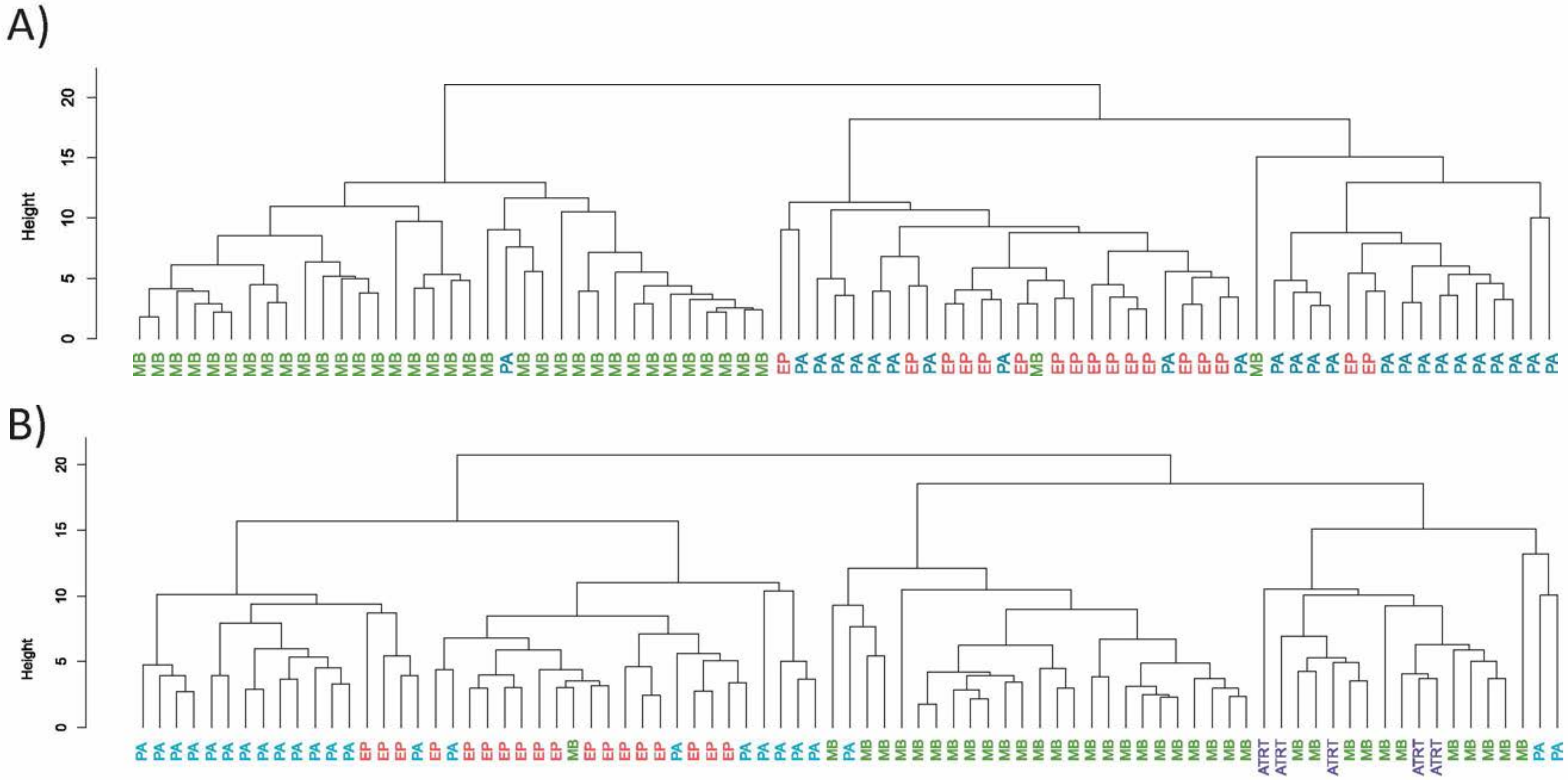

Figure 3.4 – A) Hierarchical clustering of cerebellar MB, EP and PA based on quantified metabolites. B) Hierarchical clustering of MB, ATRT, EP and PA based on quantified metabolites. In these analyses the tumours first separate into glial and embryonal tumours, before broadly separating into tumour type specific clusters. Green – MB, red – EP, blue – PA, purple – ATRT. In both cases, Euclidean distance and Ward's clustering algorithm were used to perform the analysis.

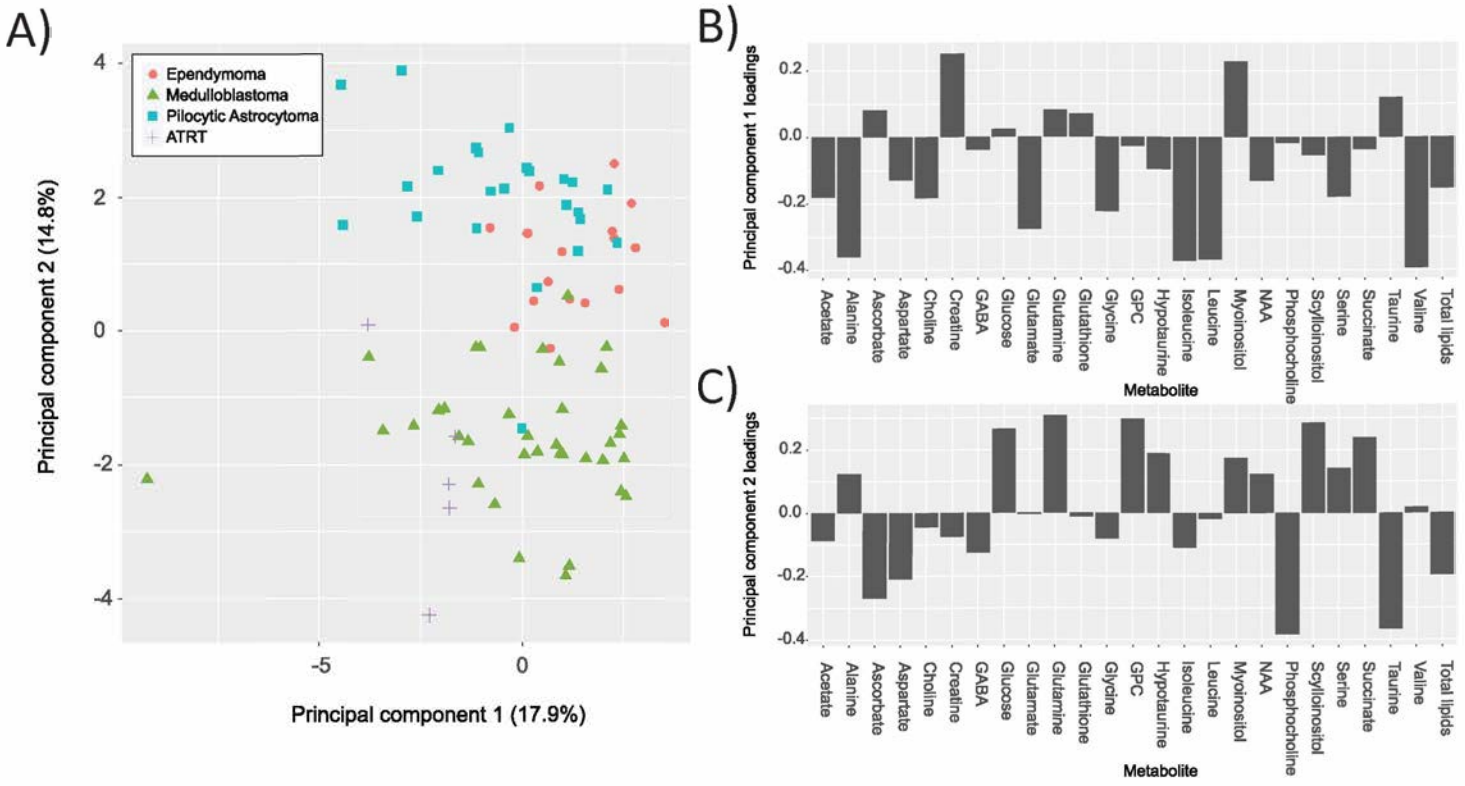

Figure 3.5 – A) The PCA scatterplot shows separation of glial tumours from embryonal tumours along the second principal component, with considerable overlap between tumour types of the same lineage. B) Loadings for the first principal component shows that the branched chain amino acids (Leu, Iso and Val) and Ala are responsible for the large variance in this component. C) Loadings for the second principal component show that Glc, Gln, GPC, hTau, sIns and Suc are important features of glial tumours, whilst Asc, Asp, PCh, Tau and lipids are features of embryonal tumours.

3.3.2 Supervised analysis of paediatric cerebellar tumours

The first linear discrimination model constructed involves the EP, MB and PA samples. The LDA scatterplot shows distinct separation of the three tumour types, and the loadings show which metabolites are responsible for separating the three groups (**Figure 3.6**). MB and PA are separated by the first discriminant, whilst the second discriminant function is responsible for separating EP. Gln, hTau and NAA were the three most important for identifying PAs, whilst Gly, PCh and Tau were the three most important metabolites for MB classification. mIns was the most important metabolite for EP identification. The model was shown to be robust against over-fitting, with classification accuracies of 94% for EP and MB and 92% for PA (**Table 3.3**).

A randomisation of the cohort was performed by randomly assigning 18 EP, 36 MB and 24 PA labels to the data and repeating the classifier cross validation. The classification accuracies for this analysis were 6% for EP, 56% for MB and 17% for PA.

A logistic regression modelling tumour diagnosis as a function of sample weight, storage time and rotor size was performed to identify if these factors alone could diagnose tumour tissue. None of these variables were able to predict tumour diagnosis ($P>0.05$).

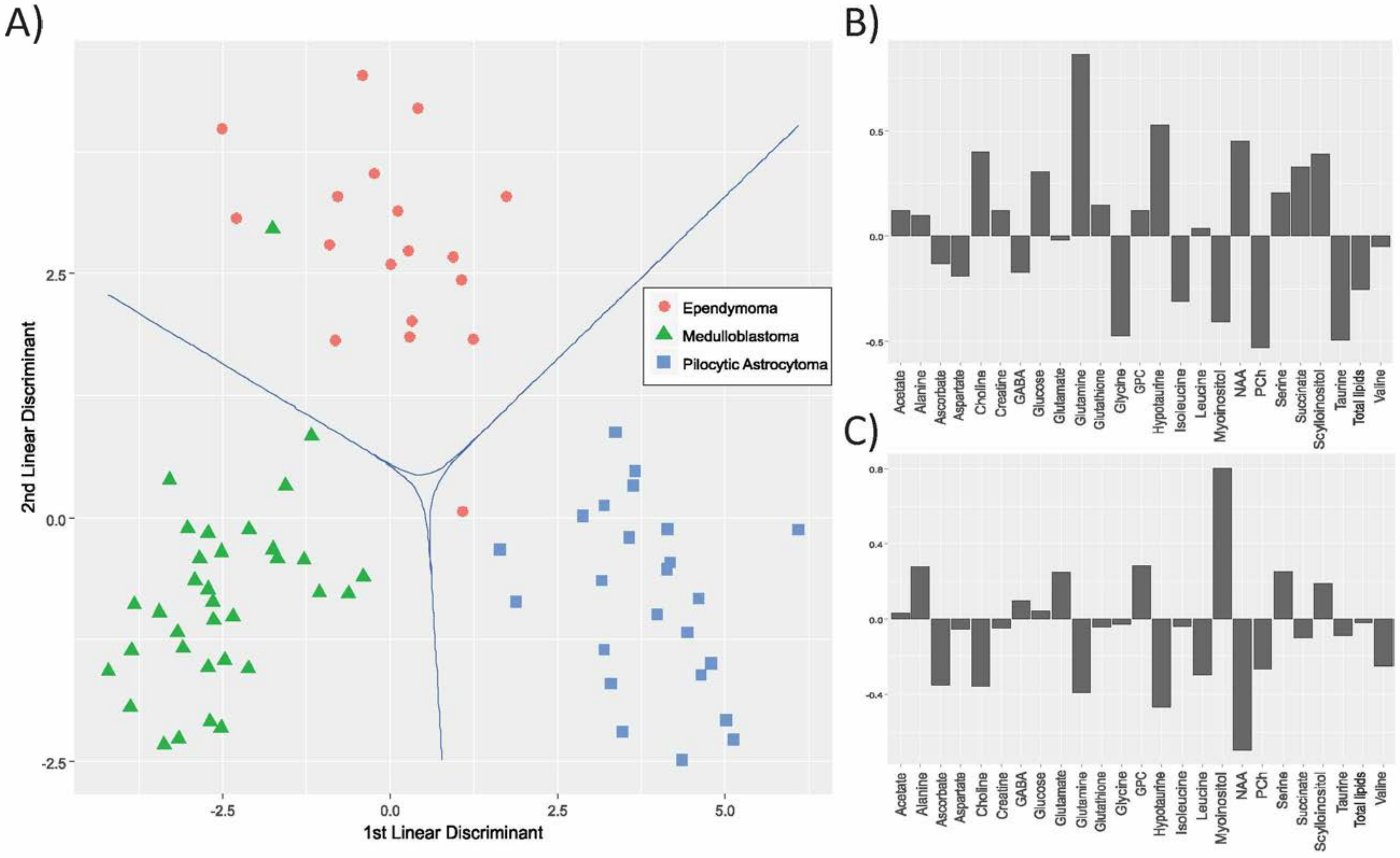

Figure 3.6 – A) Linear discriminant analysis scatterplot with decision boundaries B) The loadings for the first discriminant function identify the most important metabolites for the separation of MB and PA tumour types. C) The second discriminant loadings separate EP from the other two tumour types.

	EP	MB	PA	% accuracy
EP	17	0	1	94.4
MB	1	34	1	94.4
PA	1	1	22	91.7

Table 3.3 – Confusion matrix showing the 10-fold cross validated classification accuracy for the LDA classifier.

3.3.3 Supervised analysis with inclusion of ATRT samples.

There is a large difference in the frequency of ATRT tumours compared to the other tumours types, and this leads to a skew in classification accuracy. When the same approach as the three-way classifier is used, the classification accuracy is 40% for ATRT, 94% for EP, 89% for MB and 88% for PA. A potential solution to this problem is to assign the sample under consideration to either a glial group or embryonal tumours and then assign a tumour diagnosis (**Figure 3.7**). This model returned classification accuracies of 60% for ATRT, 86% for MB, 94% for EP and 92% for PA (**Table 3.4**).

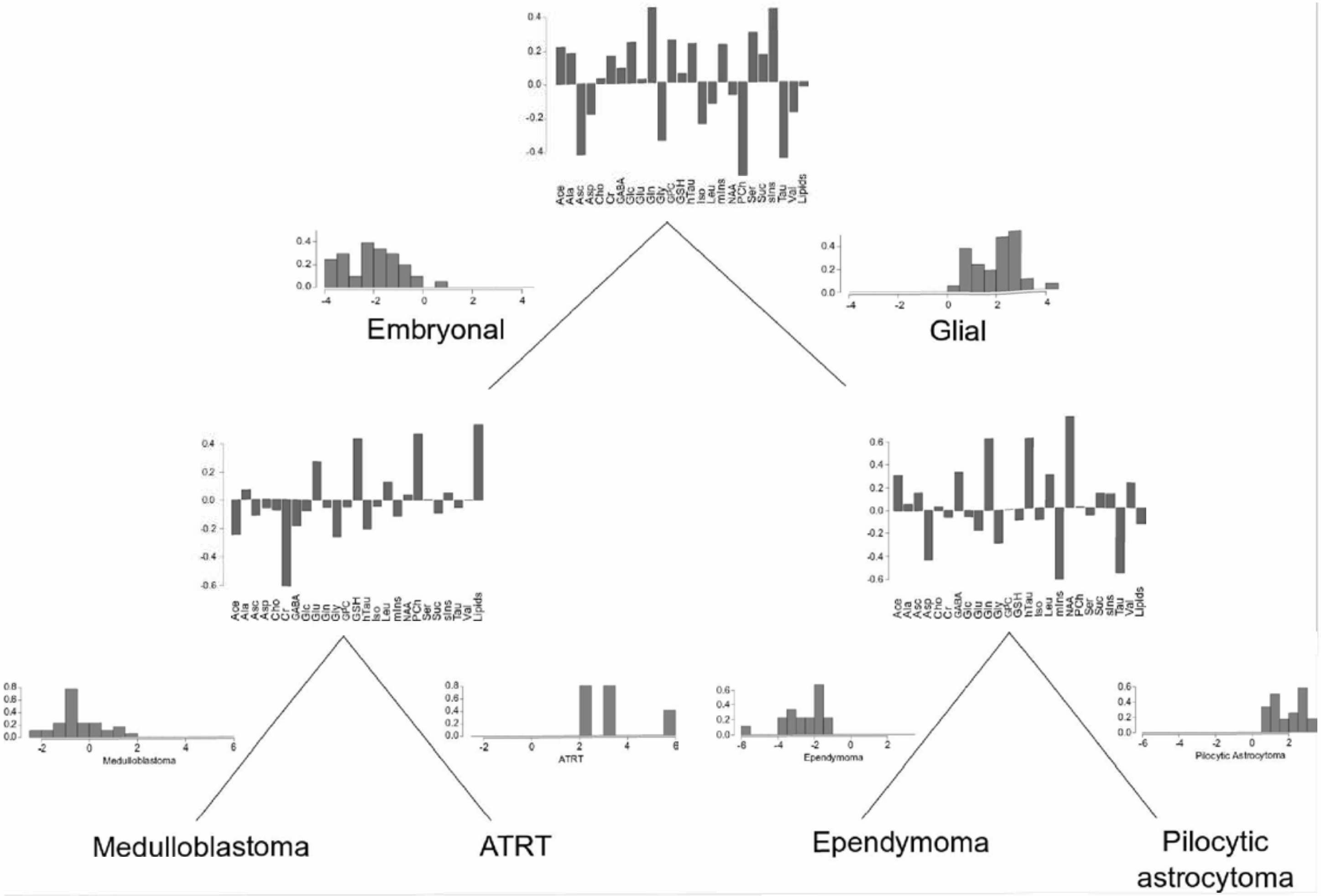

Figure 3.7 – 2 step classification model classification of tumours including ATRTs. First, each tumour is classified as glial or embryonal before being passed to the next step of the branch where it is classified into tumour type. The loadings at each level identify metabolites important for glial or embryonal classification, and tumour type specific classification.

	EP	MB	PA	ATRT	% accuracy
EP	17	0	1	0	94.4%
MB	1	31	0	4	86.1%
PA	1	1	22	0	91.7%
ATRT	1	1	0	3	60%

Table 3.4 – Classification accuracy of the two step classifier. The classification accuracy for PA and EP do not change from the first model. The large difference in class size causes some MB to be classified as ATRT.

3.3.4 Rapid intraoperative diagnosis of cerebellar tumours

The rapid intraoperative diagnosis was compared to the final diagnosis decided upon by the multidisciplinary team (**Table 3.5**). EP had the lowest diagnostic accuracy with 10 of 14 cases (71%) reporting a concordant diagnosis where intra-operative diagnoses were assessed. The remaining 4 cases were partially concordant, being reported as gliomas or low grade gliomas.

The PA group was intermediate in the analysis, with 16 of 18 cases (89%) reporting a concordant diagnosis where an intra-operative diagnosis was given. The remaining 2 cases were diagnosed as a MB and an EP.

MB had the highest rate of concordant diagnoses using rapid intraoperative preparations, with 28 of the 31 cases (90%). Two cases were discordant; one case was thought to represent an astrocytoma whilst the other a low grade glioma. The remaining case was partially concordant as it was diagnosed as a malignant intrinsic tumour.

Of the 5 ATRT cases, 2 (40%) reported a concordant diagnosis. The remaining 3 were partially concordant; two were given with a MB differential diagnosis and one was described as a high grade tumour.

Tumour	**Complete concordant**	**Partial concordance**	**Discordant**	**% accuracy**
EP	10	4	0	71.4%
MB	28	1	2	90.3%
PA	16	0	2	88.9%
ATRT	2	3	0	40%

Table 3.5 – Diagnostic accuracy of current rapid intraoperative diagnostic testing. Complete concordance requires the pathology report to state the tumour type. Partial concordance requires the pathology report to state the lineage, or use a broad term that can include the correct diagnosis. Discordant includes any other answer that doesn't fulfil the previous definitions.

The individual metabolite profile classification results of the partially concordant and discordant cases were reviewed. All partially concordant and discordant PA, EP and MB were correctly classified by the LDA. Of the 3 partially concordant ATRT cases, 1 was correctly classified by the decision tree, whilst 1 was classified as an EP and the other as an MB.

3.4 Discussion

The metabolite profiles of *ex vivo* paediatric cerebellar tumour tissue were shown to be different through univariate statistics and unsupervised analysis, and that they are sufficiently different that robust diagnostic classifiers can be constructed with high rates of diagnostic accuracy. Given the ease of sample handling, the short data acquisition time and potential for automated analysis, the technique could find a role in aiding clinical diagnosis. Although not investigated for the samples in this work, HR-MAS is a non-destructive method and prior studies suggest that post analysis tissue is of suitable quality for subsequent histological and molecular analysis (147, 189). HR-MAS and *in vivo* MRS share the same technical principles, therefore tissue studies such as that presented here can be used to inform and refine non-invasive spectroscopic examination.

3.4.1 Metabolite differences between tumour types

The *ex vivo* spectroscopy provides further evidence for characteristic metabolite profiles of these tumour types. In particular, high mIns in EP tumours, high PCh and Tau in MB and high Gln in PA were important for tumour identification. Previous work has compared the metabolite profiles of paediatric cerebellar tumours and our studies agree on most of the key characteristic metabolite markers (7). This study showed that mIns is higher in concentration in EP than MB, agreeing with in vivo MRS but contrary to the findings reported in Cuellar-Baena et al 2010. This is likely to be a consequence of the larger sample size in this study particularly for EP. Furthermore, our study constructs an accurate and robust classifier with clinical utility and identifies metabolic pathways with different activity.

Whilst there is limited published literature on the metabolite profiles of ATRTs (190), tissue studies have focussed on genomics, epigenomics and transcriptomics (50, 52, 191, 192). This study has shown that ATRT metabolite profiles are similar to MB profiles in that they display high concentrations of Tau and PCh. This is unsurprising given their shared embryonal lineage and high grade; however, this work identifies a significantly lower concentration of Cr in ATRT tissue. The hallmark genetic marker for ATRT is a loss of INI1 expression, as determined through immunohistochemical staining (50, 192). The requirement for immunohistochemical staining inevitably leads to delays with diagnosis for these patients, which, when combined with the aggressive clinical course, leads to a dismal prognosis. A rapid diagnostic test developed using metabolite concentrations would help improve survival rates through quicker identification. Validation of this observation will require a larger cohort as the ATRT group is small.

3.4.2 Classification of paediatric cerebellar brain tumour using metabolite profiles

The decision boundaries clearly separate EP, MB and PA, with only two cases lying outside the decision boundary for their respective tumour type. It is interesting to note that the loadings of the discriminant analysis reflect the findings of the average concentrations of the metabolites discussed previously, confirming that typical metabolite features can be used to separate the three tumour types. The classification algorithm is robust against over-fitting, as demonstrated by the high classification accuracy after 10-fold cross validation. Furthermore, the classification accuracy is far higher than is shown when the tumour labels are randomised.

The 2 step model highlights metabolites responsible for separating MBs and ATRTs. Higher concentrations of Glu, GSH, PCh and lipids are important for ATRT identification. On the other hand, higher Cr concentration is important for MB identification. Whilst the preliminary results for ATRT classification are encouraging, incorporation of rare tumour types may require statistical oversampling methods to compensate for the large differences in tumour frequency (193). On an interesting note, the classification accuracy for PA and EP remain the same when ATRTs are incorporated. Therefore, metabolite profiles are able to confidently identify and separate glial and embryonal tumours, which is important if the tumour in question is a rare entity.

HR-MAS has shown promise for examining tissue from several cancer types (194, 195), and may be used to complement the histological data. Indeed, some work has been published on the use of rapid metabolite profiling and its clinical application in the surgical management of tumours which reported histopathology matching tumour identification in 17 mins (196). With metabolism under the control of the oncogenic drivers, HR-MAS has the potential to identify tumour subgroups in a short time frame, as shown in adults with SDH mutated paragangliomas or pheochromocytomas (99) or IDH mutated gliomas (141). HR-MAS also has the ability to identify novel metabolic subgroups which correlate with histopathological features such as differentiation, necrosis and invasion (163, 197). Whilst this work has not attempted to classify tumours into recognized molecular subgroups, there is evidence that MRS is able to identify the MB molecular subgroup (198) and this warrants further investigation.

3.4.3 Comparison to current rapid intraoperative diagnostic testing

To put the accuracy of the HR-MAS classification into context, a comparison was made with the accuracy of current rapid intraoperative assessment using clinical reports for the tissue used in this analysis. Rapid intraoperative testing consists of smear cytological preparations often complemented by frozen sections stained with H&E to assess the cytological aspect as well as architectural features (178). This method is cheap and rapid, without the need for expensive equipment, and gives reasonably accurate results to guide surgical management decisions.

The results of our analysis broadly agree with published retrospective analyses of rapid intraoperative assessment (61, 199); complete agreement of the rapid intraoperative assessment and final histological diagnosis is achieved in the majority of astrocytoma and MB cases. EP, however, have a higher rate of partial concordance. Currently, the greatest prognostic marker for EP is extent of surgical resection (180-182), therefore it is imperative to identify EP and optimise surgical treatment. Although there were no discordant EP diagnoses by intraoperative assessment in our study, the partially concordant diagnoses could include tumours for which a complete resection is far less important. HR-MAS may aid in the identification of such tumours in real time and improve surgical management when intraoperative H&E assessment is ambiguous. In support of this, the metabolite profiles of the partially concordant and discordant PA, EP and MB were not different from those of their respective tumour types. Metabolite profiles aided in the identification of one of the partially concordant ATRT cases, but not in the other two.

3.5 Conclusion

In conclusion, this chapter has shown that HR-MAS can detect characteristic metabolic profiles from small pieces of fresh frozen biopsy tissue which can be used to build an accurate and clinically relevant classifier, with potential for future development as an intraoperative technique for improved surgical management. As surgeons currently act upon the information provided by an intraoperative assessment of the tissue, any improvement in diagnostic accuracy, or improvement in diagnostic confidence, is useful.

It has been shown that the most concentrated metabolites in brain tumours are quantifiable *in vivo* and correlate with the *ex vivo* spectroscopy (6). Recent technical development of *in vivo* MRS has shown that it is possible to accurately measure the concentration of metabolites with overlapping resonances (200-203). Therefore, the metabolite markers described in this chapter have the potential be to be used as diagnostic markers *in vivo*.

CHAPTER 4: Tissue metabolite concentrations as biomarkers of survival in paediatric brain tumours

4.1 Introduction

Diagnosis is one of the major factors in determining a patients' prognosis. Whilst some brain tumours now have a very good prognosis, others have continued to present a challenge, highlighting the need for new techniques for investigation and management. Identifying novel biomarkers of prognosis would allow more accurate treatment stratification to improve survival rates and reduce long-term morbidity.

A key strategy in optimising the clinical management of children with brain tumours is to identify subgroups that have prognostic significance. This has been particularly successful in MB where molecular subgroups have already been incorporated into the accepted diagnostic classification (15). Whilst most molecular markers have been defined by tumour genetics, there is an increasing interest in tumour metabolism as both a biomarker of prognosis and potential therapeutic target. Mutations in the metabolic enzyme isocitrate dehydrogenase (IDH) acts as a positive prognostic marker in gliomas (204), which has led to novel therapeutic targets being identified (205). The mutated enzyme produces the metabolite 2-hydroxyglutarate which can be detected both in tissue and *in vivo* providing a non-invasive test for this subgroup and illustrating a key advantage for metabolite biomarkers of prognosis.

Whilst the identification of specific prognostic subgroups has advantages, markers that are applicable across multiple tumour types also give clinical value. Histological markers such as Ki67 proliferation index are used, regardless of diagnosis, to assess tumour aggressiveness, and *MYC* status is a marker of poor prognosis used clinically in many different tumour types (206). Specific metabolites have been proposed as markers of prognosis over a range of different children's brain tumours using *in vivo* MRS. In particular, Gln and NAA were found to be markers of good prognosis whilst scyllo-inositol and mobile lipids were markers of poor prognosis (4).

However, performing MRS on typical clinical scanners is associated with a number of limitations, in particular, the relatively small number of metabolites that can be measured accurately and the requirement for sampling of relatively large tumour volumes. HR-MAS can analyse small brain tumour tissue samples to provide quantitative information on a larger number of metabolites (207). HR-MAS has identified prognostic metabolic markers in a number of tumour types including prostate (150), colorectal (151), breast (208), neuroblastoma (209) and pancreatic adenocarcinomas (210). A good agreement has been demonstrated between *in vivo* and *ex vivo* methods (6, 124), providing an indication that HR-MAS-visible metabolites accurately reflect the values present in situ and are potentially observable *in vivo*. The primary aim of this chapter is to identify and measure the concentrations of metabolites in a range of paediatric brain tumours using HR-MAS, and to test the ability of those metabolites to predict survival.

4.2 Methods

4.2.1 Patients

All brain tumour patients presenting at the Birmingham Children's Hospital were eligible to be entered into the study. Patients were accrued between January 1998 and May 2016 and followed up until September 2017. A consensus diagnosis was obtained for each patient by a multidisciplinary team of clinicians that included histopathological diagnosis according to Louis et al 2007 (211). In total, 135 brain tumour samples were released for HR-MAS. Dates of death and clinical information were obtained from the West Midlands Regional Children's Tumour Registry. In contrast to the cohort in chapter 3, which was a multi-centre study limited to tissue from the cerebellum, this chapter includes samples from a single centre (BCH) and from all anatomical sites within the brain. The two cohorts share 27 medulloblastoma, 8 ependymoma, 23 pilocytic astrocytoma and 5 ATRT samples, totalling 63 shared cases. Patients were treated with the protocol appropriate for their respective diagnosis. Broadly, this involved maximal safe surgical resection when the tumour was in a favourable location, with adjuvant radiotherapy and/or chemotherapy if necessary.

4.2.2 Data and statistical analysis

Normalised concentrations between patients alive and deceased at 5 years following diagnosis were compared by non-parametric Kruskal-Wallis tests.

Survival analysis was first performed on the entire cohort. The median concentration for each metabolite was used to determine a cut-off to split the whole cohort into two groups; a high concentration and a low concentration group. A Kaplan-Meier analysis was used to estimate the survival probability of patients in the high and low concentration groups. For this analysis, it was assumed that the events were independent and censoring of patients is uninformative. Log-rank tests were used to test the difference in survival between high and low metabolite concentration groups. Hazard Ratios (HR) for high concentration versus low concentration groups were determined by Cox regression. In a Cox regression, the hazard function is determined by covariates, the impact of which is dependent on the size of respective coefficients. If the HR, defined as the exponential of the covariate multiplied by the coefficient, is greater than 1, then the variable, in this case high metabolite concentration is associated with an increased risk and a shorter survival time. The key assumption of Cox regression is that the hazard of the event in any is a constant multiple of the hazard in any other. This assumption was tested during the analysis in the whole cohort using median metabolite concentration as a cut-off.

Following this, the cohort was split into two, divided by date; an optimisation cohort consisted of tissue collected before June 2006 (n=22) and the validation cohort (n=96) consisted of tissue collected after June 2006 (**Figure 4.1**). The optimisation cohort was used to define an optimum cut-off for each metabolite identified as a significant marker of prognosis from the whole cohort. Optimised metabolite concentration cut-offs were established by minimising the p-value of a log-rank test. To ensure statistical stability, the cut-off was not allowed to be within the top or bottom 20% of the cohort. Optimised metabolite cut-offs were applied to the validation cohort and log-rank tests were used to test the statistical significance of the metabolites as prognostic markers. Kaplan-Meier analyses were used to assess the prognostic significance of clinical factors known to be associated with prognosis, namely diagnosis, grade, age at diagnosis, gender and surgical outcome in the whole cohort and the validation cohort.

Multivariate Cox regression stratified by significant clinical prognostic factors was used to test whether metabolite concentrations were biomarkers of survival independent of confounding variables. Appropriate statistical analyses were used to examine the relationship between significant metabolites and clinical factors.

To further explore the potential of metabolites to predict survival, univariate Cox regression was performed on the whole cohort using the metabolite concentrations as continuous variables.

All analysis was performed using the “stats” and “survival” libraries written for the R software package (212).

Non-parametric Kruskal Wallis tests were used to test for differences in Gln between diagnosis, gender, grade and differentiation (glial versus embryonal).

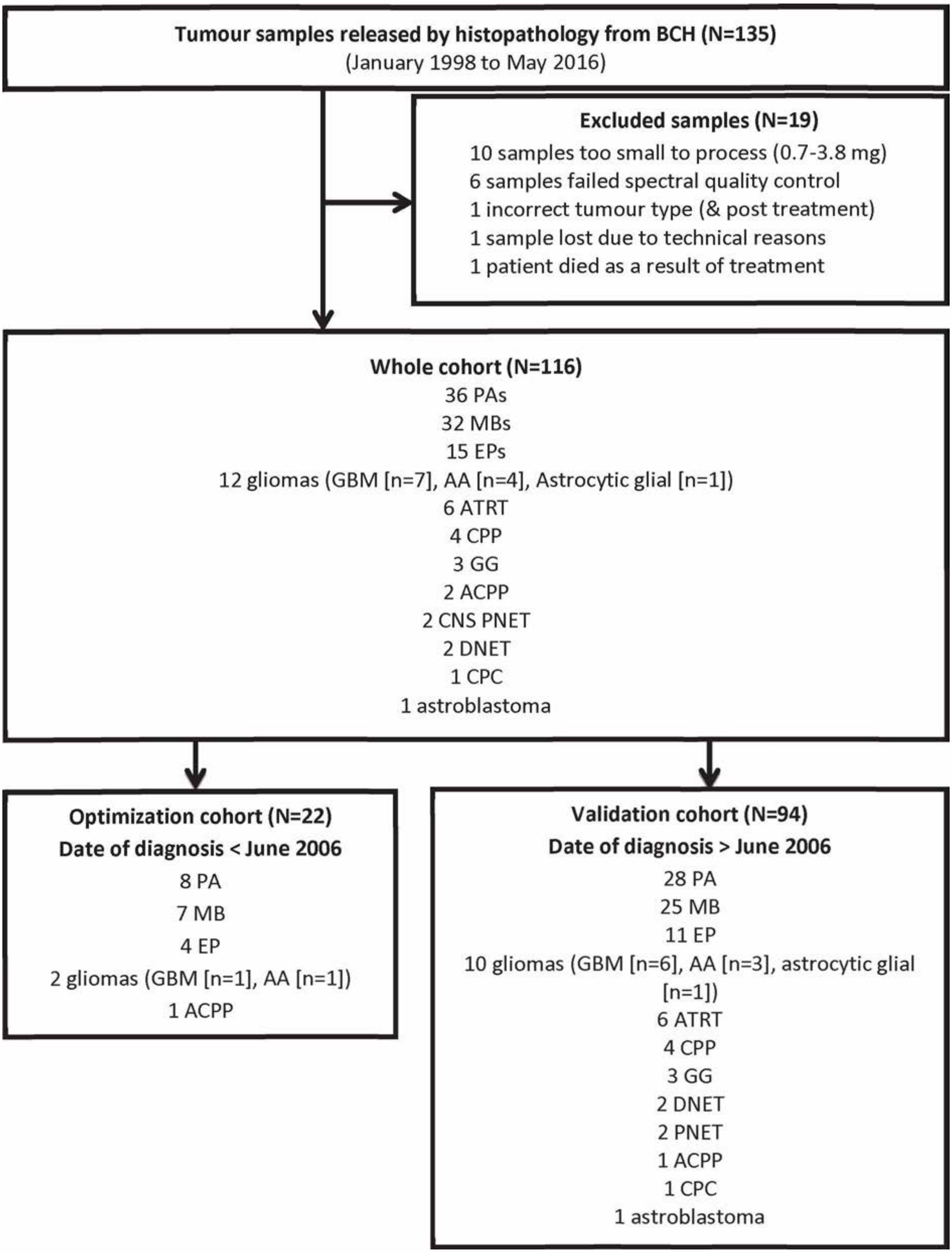

Figure 4.1 – Flowchart for cohort construction and analysis.

4.3 Results

4.3.1 Cohort characteristics

From the 135 tumour samples available, 19 were excluded from the analysis due to quality reasons or cause of death not being from the tumour (**Figure 4.1**). The final cohort consisted of 116 primary pre-treatment CNS tumour samples including 36 PAs, 32 MBs, 15 EPs, 7 GBMs, 6 ATRTs, 4 AAs, 4 CPPs, 3 GGs, 2 ACPPs, 2 DNETs, 2 CNS PNETs, 1 astroblastoma, 1 CPC and 1 astrocytic glial tumour (Table 4.1). As the tumour tissue was requested before the release of the WHO CNS classification 2016, diagnoses are those specified by the WHO CNS classification 2007(211). The diagnosis for a single tumour was ambiguous and so is classed as an 'astro glial tumour' in this chapter. 35 patients died and 81 were alive at the end of the study. The median follow-up time for the whole cohort was 5.3 years.

Table 4.1 – Overall cohort demographics. Diagnoses are those specified in the WHO CNS classification 2007.

	PA	MB	EP	GBM	ATRT	AA	CPP	GG	CNS PNET	ACPP	DNET	CPC	Astro-blastoma	Astrocytic glial tumour	Total
N	36	32	15	7	6	4	4	3	2	2	2	1	1	1	**116**
Number of events	3	13	3	6	4	3	0	0	1	1	0	1	0	0	**35**
Gender (male: female)	18:18	26:6	11:4	5:2	4:2	1:3	4:0	1:2	1:1	1:1	1:1	1:0	0:1	1:0	**75:41**
Mean age at diagnosis (years)	8.30	7.11	5.53	5.68	1.10	10.49	3.40	11.07	7.24	2.95	6.53	5.09	10.18	11.58	**6.91**
Age range (years)	1.16-15.94	1.5-14.55	0.33-16.30	0.03-11.54	0.02-4.61	4.12-15.48	0.36-10.10	8.66-14.86	2.18-12.29	1.62-4.28	5.36-7.70	N/A	N/A	N/A	**0.03-16.30**
Median survival (years)	4.71	1.82	1.68	0.94	0.31	1.54	N/A	N/A	0.94	1.93	N/A	1.39	N/A	N/A	**1.50**

4.3.2 Identification of potential prognostic markers

Initially, the metabolite profiles of those patients alive at five years were compared to those that were deceased at five years (**Figure 4.2**). This analysis identified 6 significantly different metabolites (Kruskal-Wallis P <0.05); Gln was found to be higher in those still alive whilst Acetone, GSH, Tau and lipids at 0.9ppm and 1.3ppm were lower in these patients.

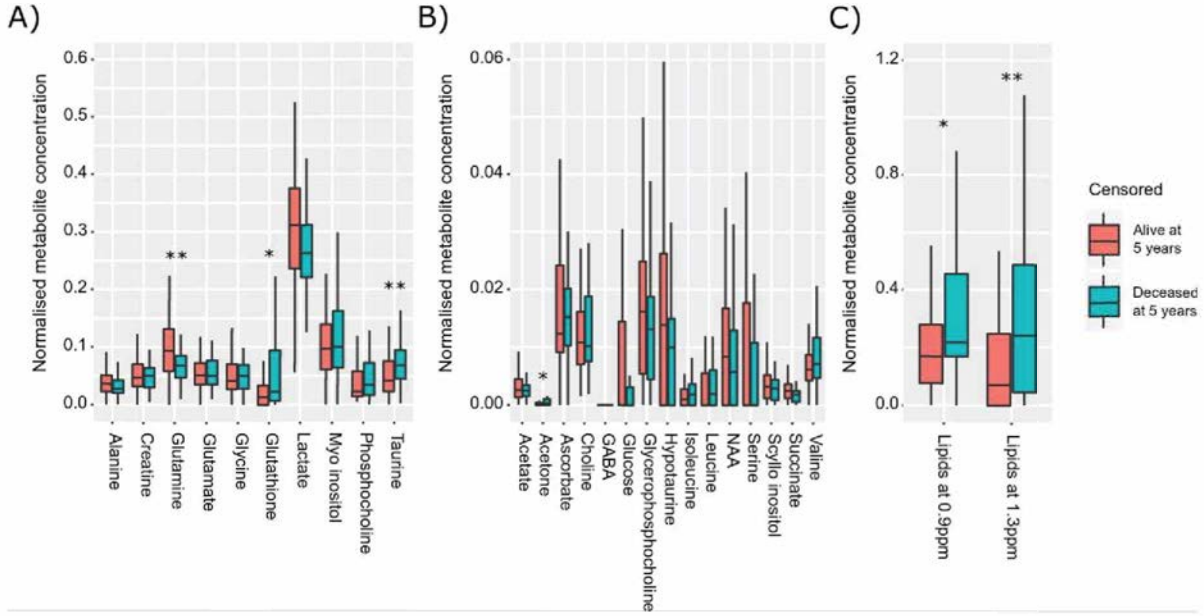

Figure 4.2 – Differences in A) high abundance metabolite concentrations, B) low abundance metabolite concentrations and C) lipid concentrations between patients alive and deceased at 5 years following diagnosis; *, P < 0.05; **, P < 0.01.

In order to identify metabolites that may be prognostic markers, a univariate Cox regression was performed on all metabolites using the entire cohort. The median normalized metabolite concentration was used to define high concentration and low concentration groups for each metabolite. Acetone, Gln, GSH, hTau, Lac, Suc, Tau and lipids at 1.3ppm were found to be significant predictors of survival (**table 4.2, figure 4.3**). Lac was found to violate the proportional hazards assumption for Cox regression and was excluded from the rest of the analysis.

Table 4.2 – Median normalized metabolite concentration values, log-rank P-values and hazard ratios for each metabolite computed using the whole cohort.

Metabolite	Median value	Log-rank P-value	Hazard ratio (95% confidence interval)
Ace	0.0025	0.67	1.15 (0.59-2.24)
Acetone	0	0.02	2.17 (1.12-4.21)
Ala	0.0330	0.17	0.63 (0.32-1.23)
Asc	0.0139	0.11	1.73 (0.88-3.40)
Cho	0.0106	0.55	0.82 (0.42-1.59)
Cr	0.0476	0.70	1.14 (0.59-2.22)
GABA	0	0.21	0.52 (0.18-1.47_
Glc	0	0.15	0.60 (0.29-1.22)
Gln	0.0813	0.04	0.50 (0.25-0.99)
Glu	0.0505	0.84	0.93 (0.48-1.82)
Gly	0.0417	0.57	1.21 (0.62-2.36)
GPC	0.0152	0.07	0.54 (0.27-1.06)
GSH	0.0154	0.02	2.20 (1.10-4.43)
hTau	0.0133	0.03	0.46 (0.23-0.93)
Iso	0.0010	0.38	1.34 (0.69-2.62)
Lac	0.3009	0.01	0.40 (0.20-0.82)
Leu	0.0017	0.88	1.05 (0.54-2.05)
mIns	0.0963	0.63	1.18 (0.60-2.29)
NAA	0.0081	0.07	0.54 (0.27-1.07)
PCh	0.0248	0.06	1.91 (0.96-3.80)
Ser	0	0.56	0.82 (0.42-1.61)
sIns	0.0030	0.10	1.00 (0.51-1.94)
Suc	0.0020	0.04	0.48 (0.24-0.97)
Tau	0.0511	0.01	2.44 (1.19-4.98)
Val	0.0064	0.26	1.46 (0.75-2.85)
Lipids 0.9ppm	0.1821	0.23	1.50 (0.77-2.94)
Lipids 1.3ppm	0.1302	0.02	2.24 (1.11-4.51)

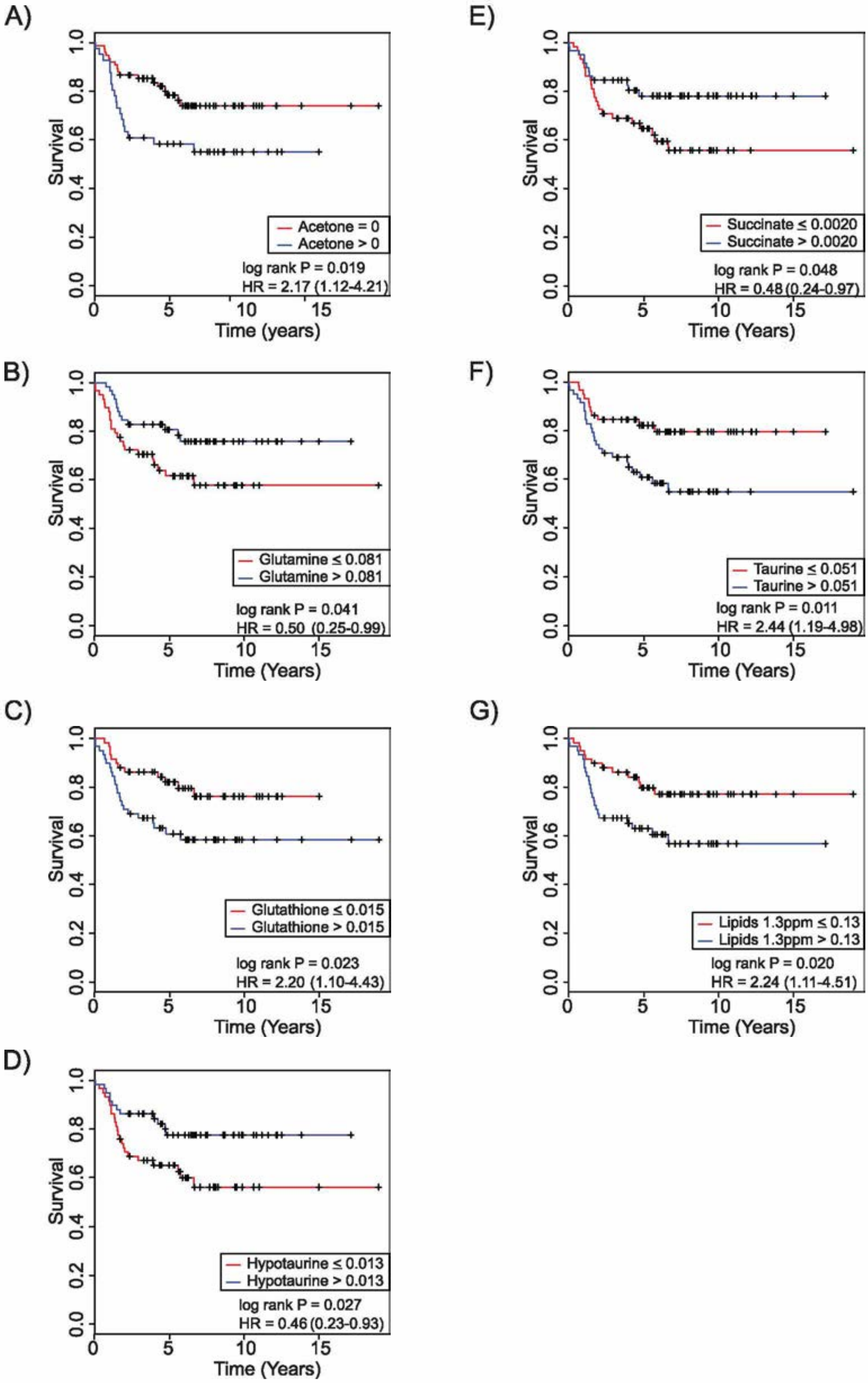

Figure 4.3 – Kaplan-Meier curves, median cut-off values, p-values and hazard ratios for the A) acetone B) Gln, C) GSH, D) hTau, E) Suc, F) Tau and G) lipids at 1.3ppm in the whole cohort.

NAA and sIns have previously been identified as prognostic markers *in vivo* but were not found to be significant in the univariate Cox regression. Optimization of the cut-off value for these metabolites was attempted in the whole cohort, to determine if particularly high or low concentrations of these metabolites act as prognostic markers. The cut-off was not allowed to be within the top or bottom 20% of the whole cohort. A significant threshold for NAA could be determined at 0.0068 ($P<0.05$, HR=0.5 (0.25-0.98)). This cut-off is at the 46th centile. There was no cut-off which gave a significant survival difference for sIns.

A multivariate linear regression was performed was performed modelling normalised metabolite concentration as a function of time in -80°C storage, size of the rotor used, diagnosis and tissue weight. This analysis shows only lipids at 1.3ppm has a relationship with sample weight (corrected $P=0.037$, $R^2=0.27$). Univariate regression of lipids at 1.3ppm as a function of sample weight suggests that sample weight accounts for 4% of the variation of this metabolite ($P=0.017$). Univariate regression of lipids at 1.3ppm and diagnosis shows that diagnosis accounts for over 20% of the variation.

4.3.3 Validation of prognostic markers

Optimal acetone, Gln, GSH, hTau, Suc, Tau and lipids at 1.3ppm cut-offs were determined using the optimization cohort (**figure 4.4**). The optimised cut-offs were applied to the validation cohort in order to test them in a prospective manner. This analysis demonstrated Gln and Tau to be significant prognostic markers (**Figure 4.5**). The hazard ratio for Gln and Tau was determined to be 0.3 (0.10–0.90) and 2.9 (0.97–8.46) respectively, indicating high Gln concentration is a positive prognostic marker whilst high Tau concentration is a negative prognostic marker.

4.3.4 Clinical prognostic markers

Survival analysis was used to test the prognostic significance of diagnosis, grade, age at diagnosis, gender and surgical outcome. Diagnosis was a significant predictor of survival ($P=1.86\times10^{-8}$), with GBM, PNET, ATRT and CPC predicting a worse outcome. All other diagnoses predicted a better outcome. Age at diagnosis was also a significant predictor of survival (P=0.0099) with age greater than 7 years at diagnosis being predictive of a better prognosis (HR=0.39, (0.19-0.82)). Neither gender nor extent of resection were predictors of survival in this cohort (P>0.05).

The same trends are observed in the validation cohort. Diagnosis was a significant predictor of survival ($P=2.79\times10^{-7}$), with GBM, CPC, PNET and ATRT predicting a worse survival. Age greater than 7 years at diagnosis retained significance (P=0.017, HR=0.32. 95% CI 0.12-0.86). Neither gender nor extent of resection was shown to be predictive in the validation cohort.

To account for confounding variables, the validation analysis was repeated using the same optimised concentrations cut-offs following stratification for diagnosis and age at diagnosis. Upon stratification for diagnosis, Gln retained its significance (P=0.021, HR=0.18 (0.04–0.87)) but Tau did not (P>0.05). Upon stratification of the cohort by age (older or young than 7 years at diagnosis), Gln again retained its significance (P=0.045, HR=0.34 (0.12-1.02)), but again, Tau did not (P>0.05).

However, when stratified by differentiation (glial or embryonal) neither Gln nor Tau remain significant, although Gln trends toward significance (Gln P = 0.06, Tau P = 0.1). Furthermore, neither metabolite remains significant when the analysis is stratified by tumour grade (Gln P=0.22 and Tau P=0.41).

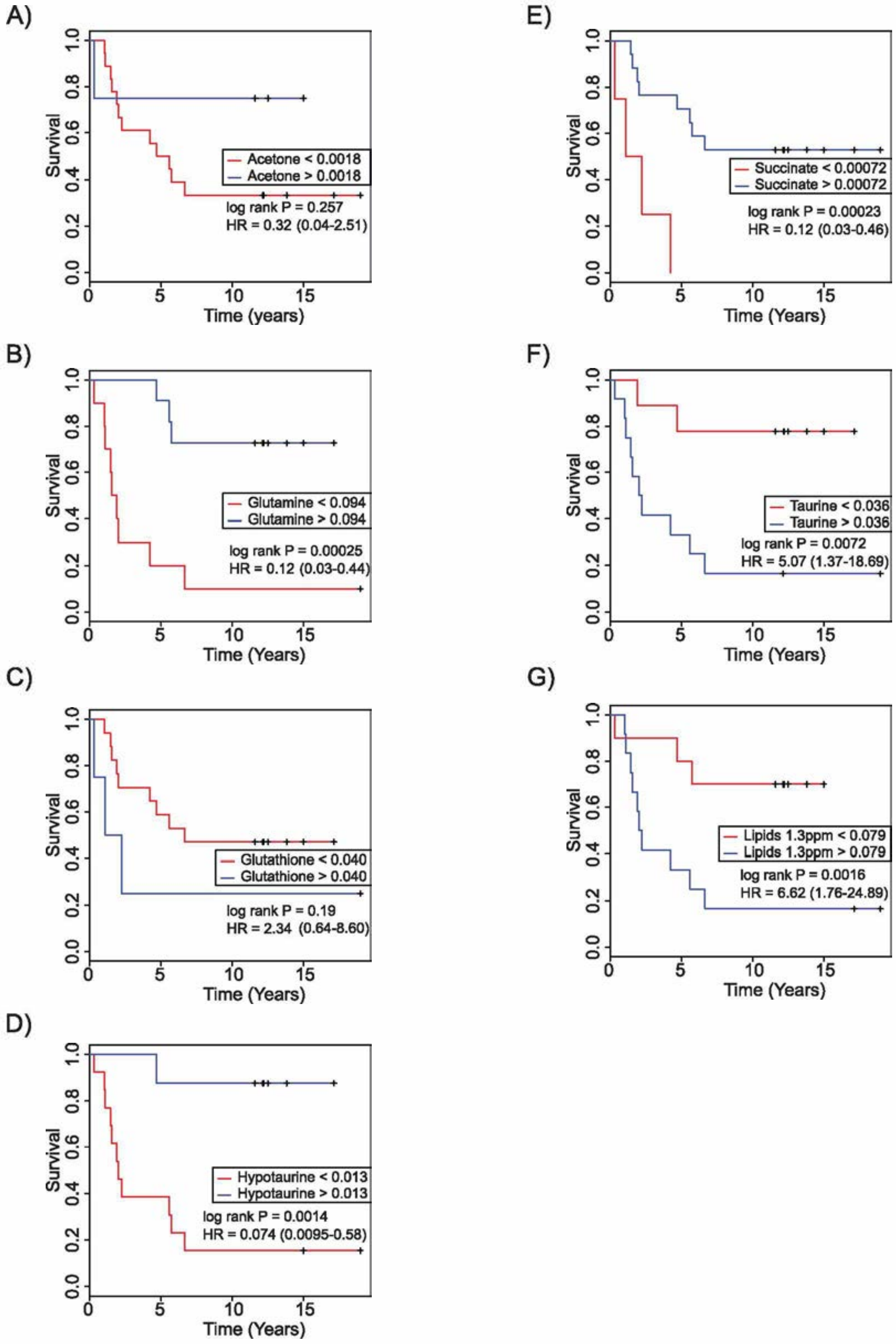

Figure 4.4 - Kaplan-Meier curves, optimum cut-off values, p-values and hazard ratios for A) acetone B) Gln, C) GSH, D) hTau, E) Suc, F) Tau and G) lipids at 1.3ppm in the optimisation cohort.

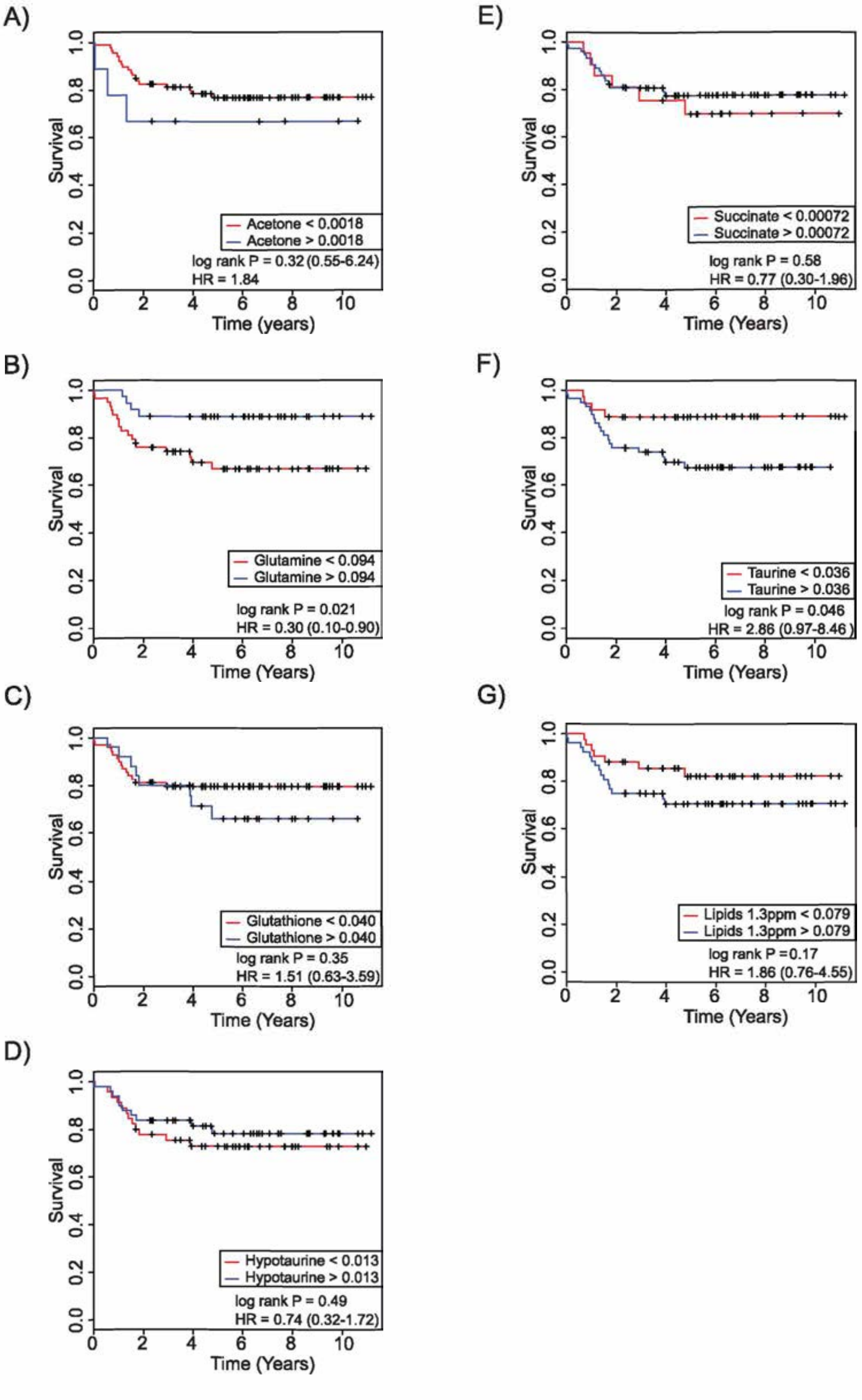

Figure 4.5 - Kaplan-Meier curves, cut-off values, p-values and hazard ratios for A) acetone B) Gln, C) GSH, D) hTau, E) Suc, F) Tau and G) lipids at 1.3ppm in the validation cohort.

4.3.5 Cox regression with continuously variable metabolite concentrations

Cox regression was performed on the whole cohort using continuously variable Gln and Tau concentrations. Gln was again shown to be a positive marker of prognosis ($P=0.020$, $HR=9.504x10^{-5}$ ($4.893x10^{-8}$-0.185)) whilst Tau was shown to be a negative marker of prognosis ($P=0.025$, $HR=122.632$ (1.738-8654)). Gln retained significance upon stratification for diagnosis ($P=0.029$, $HR=5.44x10^{-6}$ ($1.096x10^{-10}$-0.27)) and age at diagnosis ($P=0.049$, $HR=3.34x10^{-4}$ ($1.35x10^{-7}$-0.38)). Tau did not remain significant upon stratification for either variable ($P>0.05$). However, upon stratification for grade or differentiation, neither metabolite was significance ($P>0.05$).

4.3.6 Relationships between other clinical factors and significant metabolic predictors of survival

The relationship between diagnosis and the prognostic markers was examined by performing Kruskal-Wallis tests on the whole cohort. This showed that both Gln and Tau concentration differed significantly with diagnosis (Gln $P=4.8x10^{-7}$, Tau $P=5.6x10^{-9}$). Further examination using a Dunn's post hoc test demonstrates significant differences in Gln concentration between 16 tumour type pairs ($P<0.05$) (**figure 4.6, table 4.4**). A second Dunn's test showed significant differences in Tau concentration between 18 tumour type pairs ($P<0.05$) (**figure 4.7, table 4.5**).

Linear regression between Gln and Tau concentration and age at diagnosis demonstrated significant relationships; however, the coefficients of determination were very low (Gln $R^2=0.046$, Tau $R^2=0.032$) (**figure 4.8**).

The relationship between gender and Gln and Tau was examined despite the lack of prognostic significance of gender in this analysis. There was no difference in Gln concentration between males and females (Mann Whitney U test $P>0.05$) (**Figure 4.9**). Tau was found to be significantly higher in males than females (Mann Whitney U test $P<0.05$) (**figure 4.9**).

Kruskal Wallis tests were also performed examining how normalised Gln and Tau differ with WHO grade and differentiation (glial versus embryonal). Both Gln and Tau varied with grade ($P = 0.006$ and $P = 8.02 \times 10^{-10}$ for Gln and Tau respectively) (**Figure 4.10)**. Dunn tests identified pairwise significant differences for both metabolites between tumour grade. Most importantly, Gln was significantly higher in grade I tumours than grades II, III and IV, whilst Tau was higher in grade IV than in grades II, III and IV.

Both Gln and Tau differed significantly with differentiation, with Gln being significantly higher in glial tumours ($P=0.0006$) and Tau being higher in embryonal tumours ($P=1.15 \times 10^{-10}$) (**Figure 4.11**).

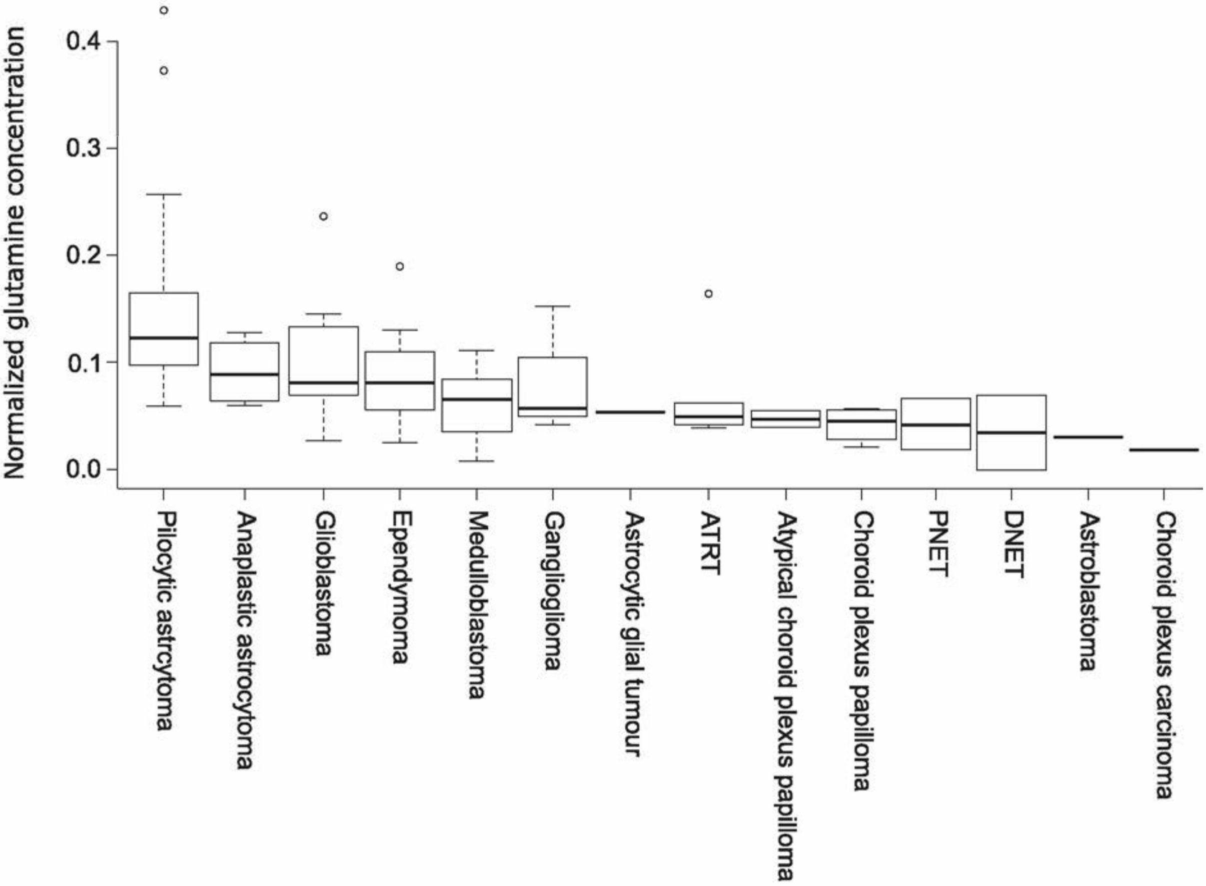

Figure 4.6 – The change in normalised Gln concentration across diagnostic groups. Tumours are ranked by median Gln concentration.

Table 4.3 – Post hoc Dunn tests showing significant differences in Gln with respect to diagnosis. Shaded cells indicate P<0.05.

	AA	Astroblastoma	ACPP	Astrocytic glial tumour	ATRT	CPC	CPP	DNET	EP	GBM	GG	MB	PA	PNET
AA		0.0736	0.0822	0.1658	0.1216	0.051	0.0321	0.0848	0.3577	0.4689	0.3133	0.0886	0.1021	0.0822
Astroblastoma	0.0736		0.367	0.3525	0.211	0.4415	0.39	0.3624	0.0853	0.0592	0.1397	0.1864	0.012	0.367
ACPP	0.0822	0.367		0.4613	0.2904	0.3051	0.4522	0.4941	0.0922	0.059	0.1809	0.2512	0.005	0.5
Astrocytic glial tumour	0.1658	0.3525	0.4613		0.3793	0.2996	0.4209	0.4661	0.197	0.1444	0.2683	0.3579	0.0418	0.4613
ATRT	0.1216	0.211	0.2904	0.3793		0.1597	0.1949	0.2966	0.1282	0.0747	0.2947	0.4662	0.0006	0.2904
CPC	0.051	0.4415	0.3051	0.2996	0.1597		0.3208	0.3008	0.058	0.0395	0.1035	0.1365	0.0069	0.3051
CPP	0.0321	0.39	0.4522	0.4209	0.1949	0.3208		0.4454	0.025	0.0152	0.11	0.1318	0.0001	0.4522
DNET	0.0848	0.3624	0.4941	0.4661	0.2966	0.3008	0.4454		0.0955	0.0612	0.1852	0.2578	0.0053	0.4941
EP	0.3577	0.0853	0.0922	0.197	0.1282	0.058	0.025	0.0955		0.2895	0.3962	0.0515	0.0022	0.0922
GBM	0.4689	0.0592	0.059	0.1444	0.0747	0.0395	0.0152	0.0612	0.2895		0.2711	0.0335	0.0666	0.059
GG	0.3133	0.1397	0.1809	0.2683	0.2947	0.1035	0.11	0.1852	0.3962	0.2711		0.2845	0.0416	0.1809
MB	0.0886	0.1864	0.2512	0.3579	0.4662	0.1365	0.1318	0.2578	0.0515	0.0335	0.2845		0.000	0.2512
PA	0.1021	0.012	0.005	0.0418	0.0006	0.0069	0.0001	0.0053	0.0022	0.0666	0.0416	0.000		0.005
PNET	0.0822	0.367	0.5	0.4613	0.2904	0.3051	0.4522	0.4941	0.0922	0.059	0.1809	0.2512	0.005	

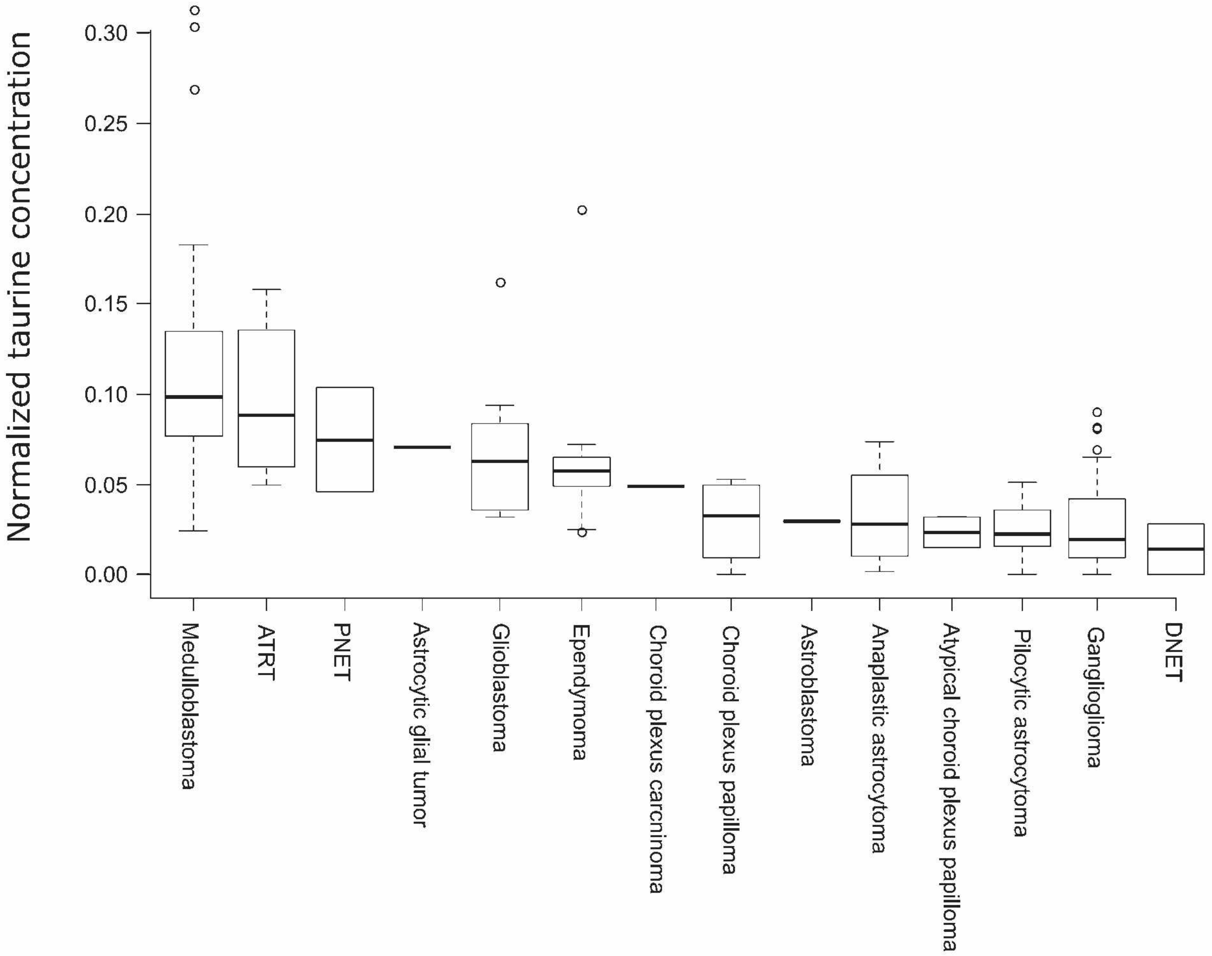

Figure 4.7 – The change in normalised Tau concentration by diagnostic group. Tumours are ranked by median Tau concentration.

Table 4.4 – Post hoc Dunn tests showing significant differences in Tau with respect to diagnosis. Shaded cells indicate P<0.05.

	AA	Astroblastoma	ACPP	Astrocytic glial tumour	ATRT	CPC	CPP	DNET	EP	GBM	GG	MB	PA	PNET
AA		0.4761	0.3245	0.1641	0.0153	0.3279	0.4373	0.2598	0.1053	0.079	0.4139	0.0023	0.3435	0.113
Astroblastoma	0.4761		0.3947	0.2061	0.0879	0.3447	0.4841	0.3443	0.2276	0.1867	0.4658	0.0608	0.443	0.1812
ACPP	0.3245	0.3947		0.1123	0.0142	0.2331	0.3721	0.435	0.0723	0.0553	0.4014	0.0046	0.4012	0.0746
Astrocytic glial tumour	0.1641	0.2061	0.1123		0.3898	0.337	0.1407	0.0889	0.3534	0.4228	0.1378	0.3426	0.0989	0.4855
ATRT	0.0153	0.0879	0.0142	0.3898		0.2031	0.0098	0.0084	0.0763	0.1794	0.0136	0.4029	0.0001	0.3354
CPC	0.3279	0.3447	0.2331	0.337	0.2031		0.2928	0.1943	0.4209	0.3588	0.2826	0.1608	0.2417	0.3266
CPP	0.4373	0.4841	0.3721	0.1407	0.0098	0.2928		0.3032	0.0735	0.056	0.4715	0.0012	0.4242	0.0902
DNET	0.2598	0.3443	0.435	0.0889	0.0084	0.1943	0.3032		0.0468	0.036	0.334	0.0023	0.3173	0.0541
EP	0.1053	0.2276	0.0723	0.3534	0.0763	0.4209	0.0735	0.0468		0.3467	0.0844	0.0053	0.0014	0.3238
GBM	0.079	0.1867	0.0553	0.4228	0.1794	0.3588	0.056	0.036	0.3467		0.0639	0.0687	0.0040	0.4192
GG	0.4139	0.4658	0.4014	0.1378	0.0136	0.2826	0.4715	0.334	0.0844	0.0639		0.0028	0.4693	0.0917
MB	0.0023	0.0608	0.0046	0.3426	0.4029	0.1608	0.0012	0.0023	0.0053	0.0687	0.0028		0.0000	0.2656
PA	0.3435	0.443	0.4012	0.0989	0.0001	0.2417	0.4242	0.3173	0.0014	0.0040	0.4693	0.0000		0.0413
PNET	0.113	0.1812	0.0746	0.4855	0.3354	0.3266	0.0902	0.0541	0.3238	0.4192	0.0917	0.2656	0.0413	

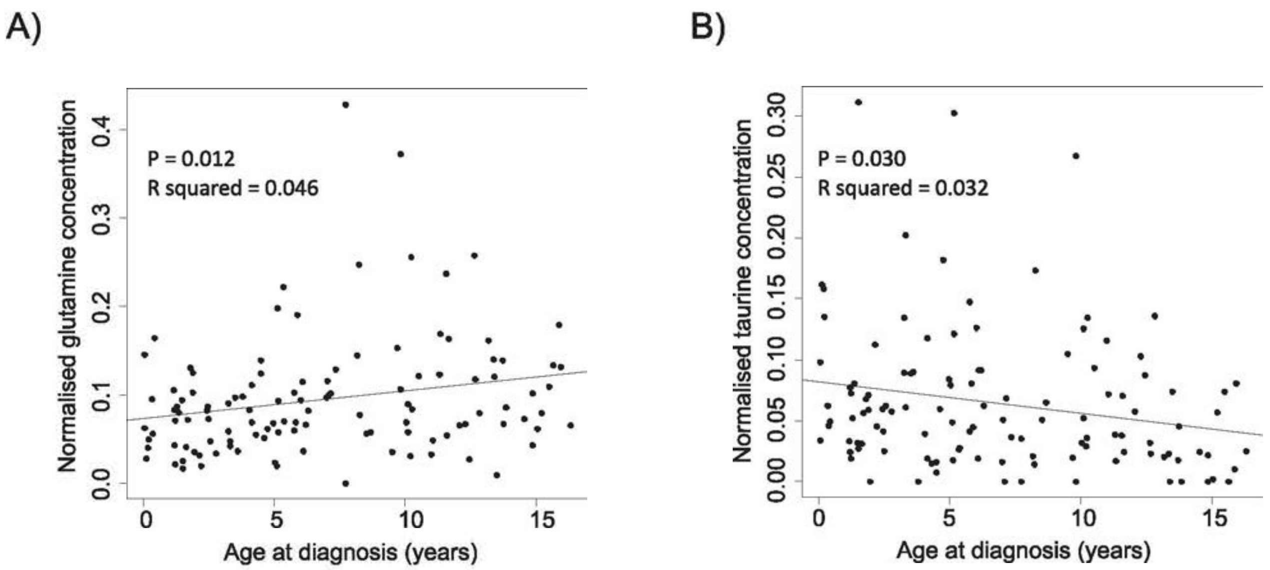

Figure 4.8 – Linear regressions of A) Gln and B) Tau with respect to age at diagnosis. All samples were used in this analysis.

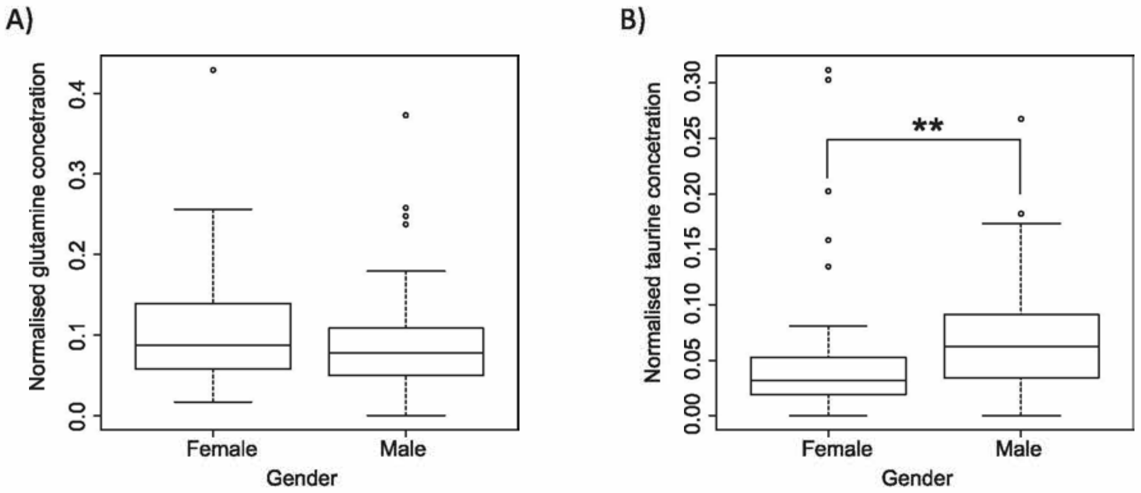

Figure 4.9 – Concentrations of A) Gln and B) Tau with respect to gender. * P < 0.05; ** P < 0.01; *** P < 0.001. All samples were used in this analysis.

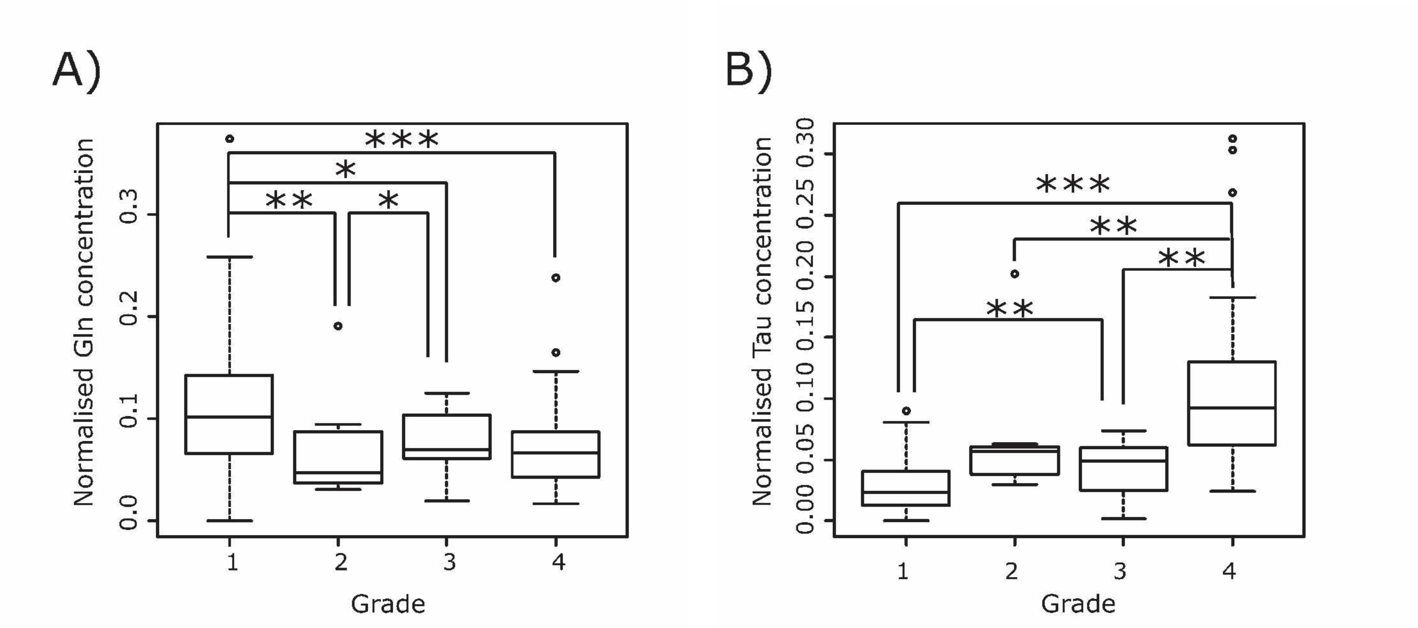

Figure 4.10 – The difference in normalised concentration of A) Gln and B) Tau with respect to WHO grade. All samples were used in this analysis. * P<0.05, ** P<0.01, *** P<0.001

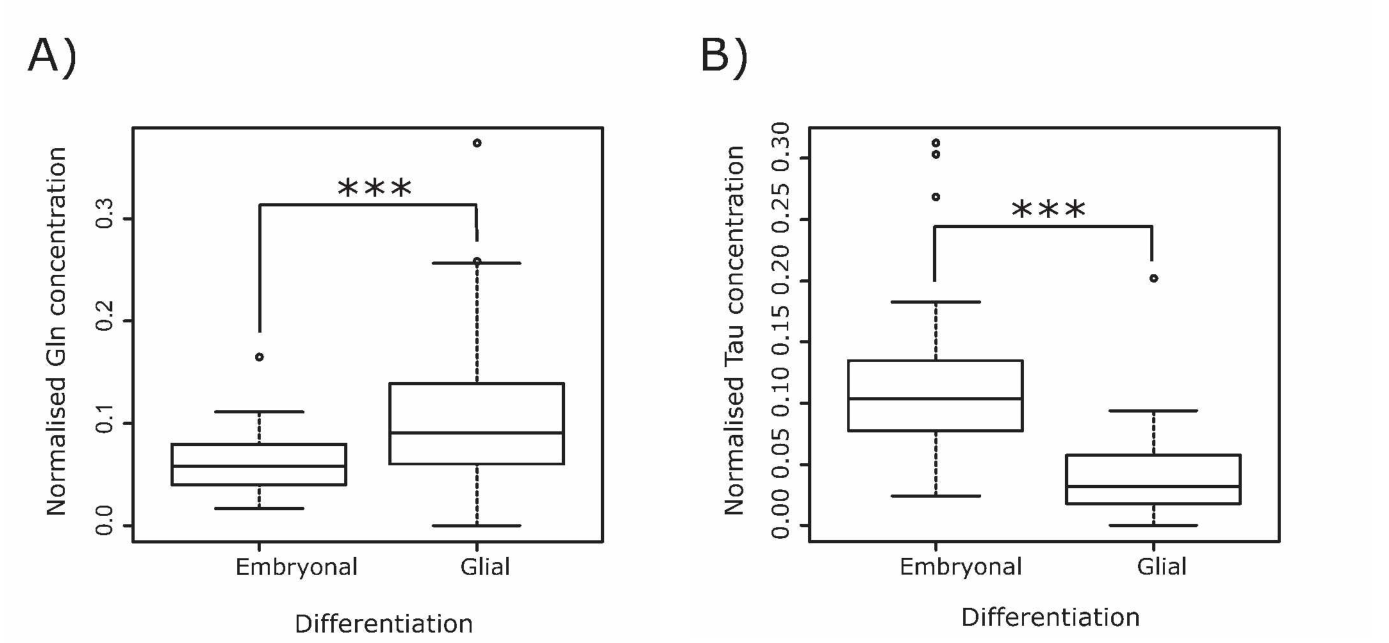

Figure 4.11 – The difference in normalised concentration of A) Gln and B) Tau with respect to differentiation. All samples were used in this analysis. *** P<0.001

4.4 Discussion

This chapter has shown through several survival analyses that the concentration of metabolites measured in fresh frozen diagnostic biopsy tissue from a variety of paediatric brain tumours using HR-MAS varies with disease aggressiveness. It was shown that Gln concentration varies between tumour diagnoses but acts a marker of good prognosis in brain tumours in a manner independent of diagnosis and age at diagnosis. However, when the analysis is stratified by tumour grade or differentiation, prognostic significance is lost. Further analysis with a larger cohort is needed to allow thorough examination of the prognostic ability of all variables considered, clinical and metabolite features, using multivariate models.

Whilst Tau was shown to act as a marker of poor prognosis, the stratified analysis suggests it is also likely to be a marker of embryonal tumours. It was shown that embryonal tumours have significantly higher Tau than most other tumours, and there is *in vivo* MRS evidence that MB tumours have high Tau when compared to other brain tumours (5). Embryonal tumours included in this study have a large bias towards males (32:8 male: female), and this may be responsible for the significant difference in Tau between genders.

Although the regression between Gln concentration and age at diagnosis was shown to be significant, the low R^2 suggests only a small amount of the variation in our data can be explained by age at diagnosis. Brain Gln levels have been shown to increase with age in healthy adult volunteers (213) although the variation in childhood is less well established. We have previously reported *in vivo* Gln concentration as a predictor of good prognosis in paediatric CNS tumours independent of diagnosis (4), and it is encouraging to have this confirmed by *ex vivo* spectroscopy. Gln is poorly resolved at the MR scanner field strength of 1.5T used in that study due to the overlapping of signals from Glu, NAA and macromolecules. Techniques have been developed to improve the accuracy of Gln quantification; 1D MRS techniques include averaging spectra from different echo times (TE) (214), the use of optimal TE's (201, 215, 216), very short TE's (200, 203) and spectral-selective refocusing (202). 2D techniques have also been developed but are not favoured due to the high level of expertise required to ensure reliable results and the time taken to acquire the data (217). There have been recent advances in ultrafast 2D NMR (218), although this is still in its infancy. Overall, there is a realistic prospect that it will be possible to routinely measure tumour Gln levels *in vivo* in the near future.

Gln is the most abundant amino acid in blood plasma and its metabolism has long been known to be important in tumour biology (219); uptake has been shown to increase in brain tumours in order to support cellular bioenergetics and biosynthetic processes needed for proliferation (220). Gln metabolism is under direct control of major transcription factors such as TP53, Myc and Ras (221). Mutations or changes in the regulation of these genes are common in cancers, including brain tumours, and switch the cells' metabolism from oxidative phosphorylation of glucose to energy inefficient glucose fermentation and glutaminolysis (222). This switch to Gln metabolism has been linked to poor prognosis (223), therefore Gln concentration may aid stratification of patients into risk groups and inform treatment decisions. Due to the reliance of some cancers on Gln, the metabolism of this amino acid has been identified as a potential target for treatment (224).

Risk stratification is not the only potential benefit of enhanced metabolite quantification. Progression of disease and response to treatment can be monitored using MRS. Increases in Gln concentration in contralateral white matter are linked to glioblastoma migration (225), whilst reductions in the concentration of PCh and lactate in glioblastoma cell lines have been observed after treatment with mTor and PI3K inhibitors (226), reflecting the observation of a reduced tCho peak in orthotopic glioblastoma mouse models (227).

Whilst acetone, GSH, hTau and Suc were found to be markers of prognosis in the overall cohort, they were not found to be significant in the validation cohort. A larger study is required to examine the value of these metabolites as prognostic markers.

Despite the median NAA cut-off not displaying a significant difference in survival, an optimised cut off could be obtained in the whole cohort. The significance of NAA is likely to be affected by a lack of available frozen tissue from surgically intractable tumours such as optic pathway gliomas, unlike *in vivo* studies, which can non-invasively quantify NAA from such locations. These tumours have been shown to have a high concentration of NAA *in vivo* and a good prognosis (4).

Scyllo-inositol on the other hand, was not shown to be a predictor of survival in this cohort. Similar to NAA, this is likely due to the absence of tumours from inoperable locations biasing the analysis towards only tumours that can be surgically resected. Previous *in vivo* MRS work has identified high concentrations of sIns in brainstem tumours which have a dismal prognosis (4).

Lipids are perhaps the most reported *in vivo* MRS biomarker of prognosis in brain tumours (228-231). In the current study, lipids were a significant biomarker of survival in the whole cohort but not in the validation cohort. This could be a result of different case mix in the *in vivo* and *ex vivo* study cohorts. Lipids *in vivo* may arise from areas of tumour necrosis and it is unlikely that these areas would be used for tissue sampling, thus producing a bias towards lower lipids in the *ex vivo* study. In addition, low grade indolent lesions with low lipids may be included in an *in vivo* study but not have tissue available for an *ex vivo* study. However, technical reasons may also account for the differences between *in vivo* and *ex vivo* results. The NMR visibility of lipids has been shown to be related to temperature; HRMAS of brain tumour tissue has shown a reversible increase in mobile lipid visibility with increasing temperature (232). As a consequence of the low temperature at which the metabolite profiles were acquired, modest differences in low lipid concentration become difficult to detect. Even so, the result from the whole cohort in the current study provides some evidence that lipids act as a negative prognostic marker.

There are examples in the literature for splitting a cohort by time for validation of markers (98). This approach mimics a retrospective/prospective study. However, splitting by time reduces the number of events in the validation cohort, and in an effort to ensure enough power, the cohorts are imbalanced.

The analysis has focused on determining cut-offs that could be applied in a clinical setting to define high and low concentration groups and therefore high and low risk groups. The Cox regression performed on Gln as a continuous variable supports the findings that Gln is a significant predictor of survival and this independent of both diagnosis and age at diagnosis.

Whilst Tau also showed it is a significant predictor before performing a stratified analysis, it again loses significance and so is associated with both diagnosis and age at diagnosis.

4.5 Conclusion

In conclusion, this chapter has demonstrated that Gln concentration acts as a positive predictor of survival, independent of diagnosis and age at diagnosis. Acetone, GSH, hTau, Suc and lipids were also predictors of survival in the whole cohort, although further work is necessary to examine the ability of these metabolites to predict prognosis. It was also shown high Tau is associated with embryonal tumours. The importance of Gln as a predictor of prognosis in children's tumours should lead to its measurement in tumours tissue, the implementation of MRS techniques to accurately measure its concentration non-invasively, and the exploration of novel agents which can alter its metabolism for therapeutic effect.

CHAPTER 5: Tissue metabolite concentrations as biomarkers of progression-free survival in pilocytic astrocytomas

5.1 Introduction

Tissue metabolite profiles were shown in chapter 4 to be predictive of overall survival in a wide range of tumours. However, some tumours have a better clinical course and children rarely die as a result of the tumour. PA is one such tumour type. As previously described, they are slow growing, WHO grade I tumours that occur throughout the CNS, with the largest proportion occurring in the cerebellum (233-235). The overall survival for these tumours is favourable, with 5-year survival reported to be >90%, and progression free survival at 5 years is reported to be >70% (233-235). However, there is difficulty in predicting which tumours are likely to recur following initial surgical resection, especially those in which gross total resection is not attainable.

There are tissue studies that attempt to identify histological features associated with a higher risk of progression. Fernandez et al (235) identify partial resection, location within the optic chiasm, invasion of surrounding tissue and the pilomyxoid variant of PA as negative prognostic markers. Colin et al (234) agree that subtotal resection, location and the pilomyxoid variant are negative prognostic markers. Tibbetts et al (236) and Margraf et al (237) attempted to identify histological markers of progression-free survival, concluding that vascular hyalinisation, oligodendroglioma-like features, calcification, necrosis, and a high MIB-1 labelling index are associated with poorer progression-free survival.

More recently, molecular studies have analysed PAs to identify prognostic markers. The most common genetic alteration in PAs is the BRAF:KIAA1549 fusion, which is considered diagnostic for this tumour type. However, several studies have not shown a difference in survival between patients with BRAF fusions and BRAF wild type. The well characterised BRAF V600E mutation occurs rarely in PA, and is associated with a worse prognosis.

In this chapter, *ex vivo* metabolite profiles of PA are acquired and examined to identify markers of progression-free survival. Such markers are attractive as they are relatively easy to obtain and have the potential to be used *in vivo* to identify higher risk patients, which is important for those with inoperable disease.

5.2 Methods

5.2.1 Cohort

All PA patients presenting at Birmingham Children's Hospital were eligible for entry into this study. Approval was obtained from the research ethics committee and informed consent was given by parents/guardians. A consensus diagnosis was obtained for each patient by a multidisciplinary team of clinicians that included use of histopathological diagnosis according to Louis et al 2007. In total, 18 PA samples were accrued for analysis. Clinical information and date of progression were compiled for each sample by Dr Neelakshi Ghosh. Progression was defined as the date a patient required further treatment beyond initial surgery.

All patients included in this chapter were also included in chapter 3. There were 6 exclusions from the chapter 3 cohort; 3 had no follow-up data, 2 patients were NF1 positive 1 patient had unusual multi focal presentation.

5.2.2 Clinical BRAF testing

Cases passing the aforementioned QC criteria were sent for clinical BRAF testing, performed by the Division of Neuropathology based at University College London Institute of Neurology. Reverse Transcription Polymerase Chain Reaction (RT-PCR) and sequencing of the PCR product was performed on formalin-fixed paraffin-embedded tissue. This technique is designed to detect the 3 most common BRAF:KIAA1549 (KIAA1549 exon 16 and BRAF exon 9, followed by 15-9 and 16-11(20, 23)) fusion genes and the BRAF V600E point mutation. The laboratory is UKAS accredited. Clinical reports were returned to the histopathology department and the patient reports were updated with the BRAF testing result.

5.2.3 Data and statistical analysis

Survival analysis was used to determine the prognostic ability of each metabolite. For each metabolite, an optimum cut-off defining high and low concentration was established by minimising the P-value of log-rank tests. HRs were determined using Cox regression.

Differences in metabolite concentration between BRAF fusion positive versus BRAF fusion negative as well as completely resected versus partially resected were assessed using non-parametric Kruskal Wallis tests.

Unsupervised cluster analysis was used to visualise the relationship of the samples relative to one another and identify any metabolic subgroups. Euclidean distance was used to calculate the dissimilarity matrix and Ward's minimum variance clustering was used to cluster the samples.

Differences in metabolite concentrations between the subgroups were assessed by Kruskal Wallis tests. All statistical analysis was performed in the R statistical environment (238).

5.3 Results

5.3.1 Cohort

The cohort for this chapter consisted of 18 patients diagnosed with a cerebellar PA. All patients had detailed clinical history and BRAF status. Detailed cohort information can be found in **Table 5.1**.

5.3.2 Gln predicts progression free survival in cerebellar PA

Gln has been shown to predict overall survival in a large cohort of tumours. By using the optimised cut off procedure, Gln was shown to be a predictive marker of progression free survival in cerebellar PAs (**Figure 5.1**). The relationship between survival and Gln concentration is as would be expected; higher Gln concentration predicts a reduced risk of progression.

5.3.3 Other metabolic markers of progression free survival

Repeating the analysis on the other quantified metabolites identified Ace, hTau, NAA and lipids at 0.9ppm to have prognostic potential. A higher concentration of these metabolites was associated with a worse prognosis (**Figure 5.2**).

Median and IQR of age at diagnosis (Years)		8.21 (5.38-11.65) years
Gender	Male	9
	Female	9
NF1 status	Negative	18
	Positive	0
BRAF status	BRAF:KIAA1549 16:9	12
	BRAF:KIAA1549 16:11	1
	BRAF:KIAA1549 15:9	1
	Mutation	0
	No identified alteration	4
Extent of resection	Gross total resection	5
	Subtotal Resection	13
	Biopsy	0
Median size of residual (cm^2)		1.8 (1.16-27.87)
Number of patients experiencing progression		5
Median time to progression (Years)		2.09 (2.05-3.18)

Table 5.1 – Detailed cohort information for this chapter.

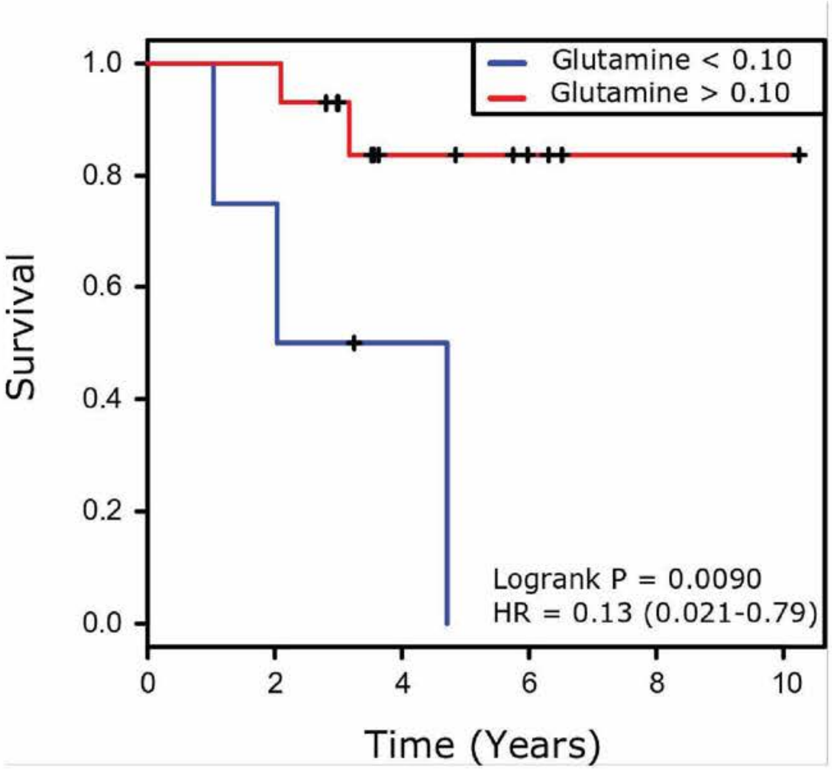

Figure 5.1 – Survival curves for high Gln and low Gln concentration groups.

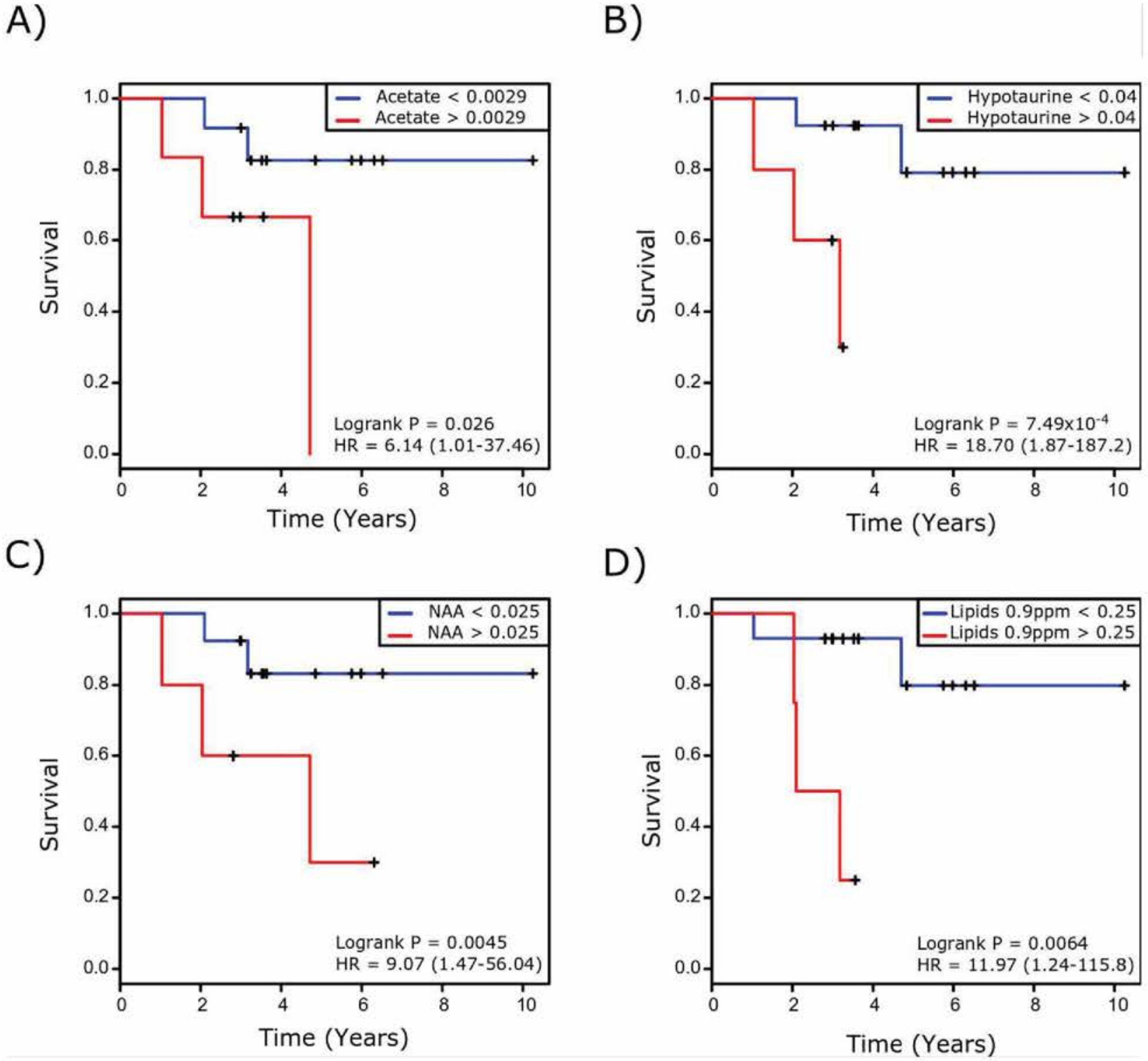

Figure 5.2 – survival curves for A) Ace, B) hTau, C) NAA and D) lipid at 0.9ppm.

5.3.4 Examining the relationship between metabolites and other clinical factors

Kruskal-Wallis tests were performed to test for differences in metabolite concentrations between those cases positive for one of the three most common BRAF fusions and those negative for the most common BRAF fusions No significant differences were identified (P > 0.05), although NAA showed a trend towards lower concentration in BRAF fusion tumours (**Figure 5.3**). Kruskal Wallis tests were also performed to identify if any metabolite concentrations were significantly different between tumours that were completely resected and those that were partially resected. No significant differences were identified (P > 0.05) (**Figure 5.4**).

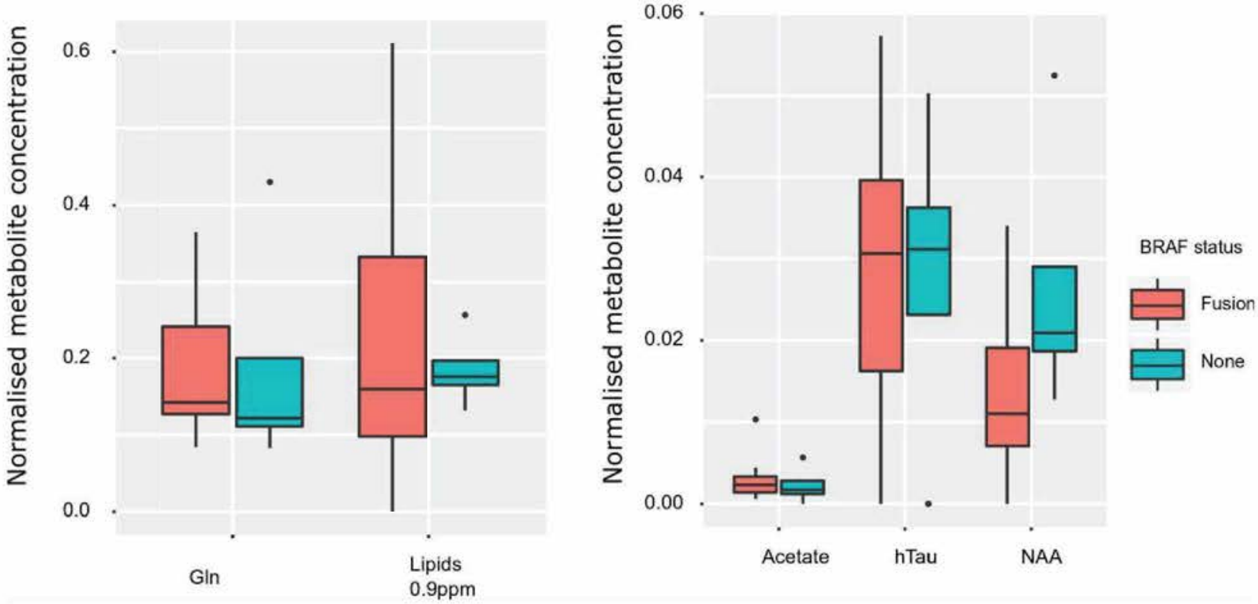

Figure 5.3 – The difference in concentration of prognostic markers with BRAF status.

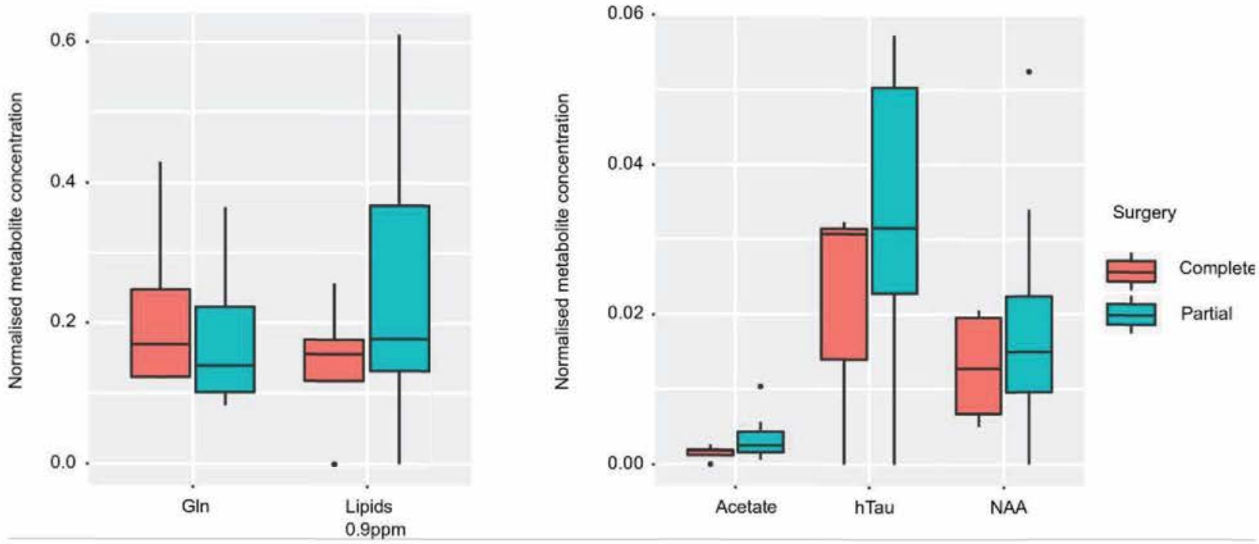

Figure 5.4 – The difference in concentration of prognostic markers with surgical outcome.

5.3.5 Identification of potential metabolic subgroups

Unsupervised cluster analysis of cerebellar PA shows the samples form two separate clusters, termed group 1 and group 2 (**Figure 5.5**). Kruskal-Wallis tests were used to identify metabolites that differed significantly between these two groups. Ala, Asc, Cr, hTau, Iso, Leu, Ser and Val differed significantly between the two clusters (**Figure 5.6**). All three branched chain amino acids were higher in concentration in cluster 1, suggesting a difference in metabolism of these amino acids between these two groups. A trend for poorer PFS was observed for those in cluster 2, but this did not reach statistical significance (**Figure 5.7**). There was no association of between cluster membership and gender, BRAF status (χ^2>0.05) or size of residual (Kruskal-Wallis>0.05).

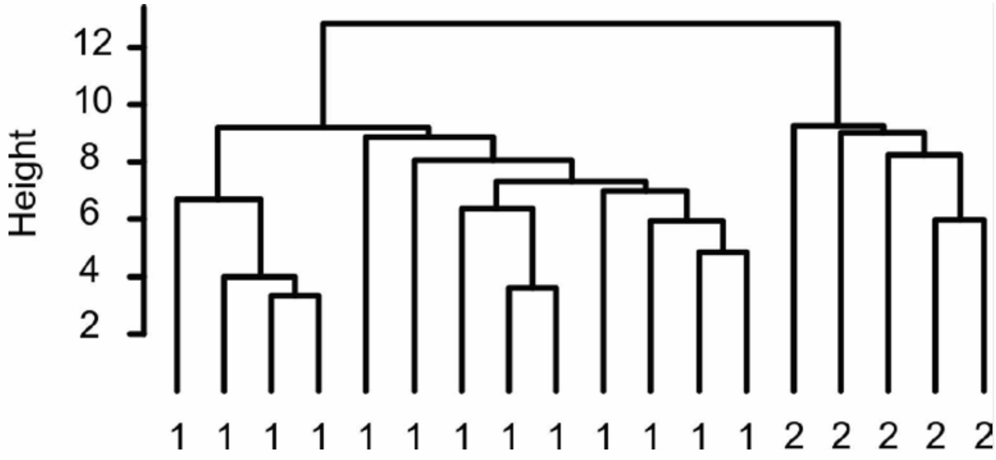

Figure 5.5 – Unsupervised hierarchical clustering shows two potential metabolic subgroups of cerebellar PAs.

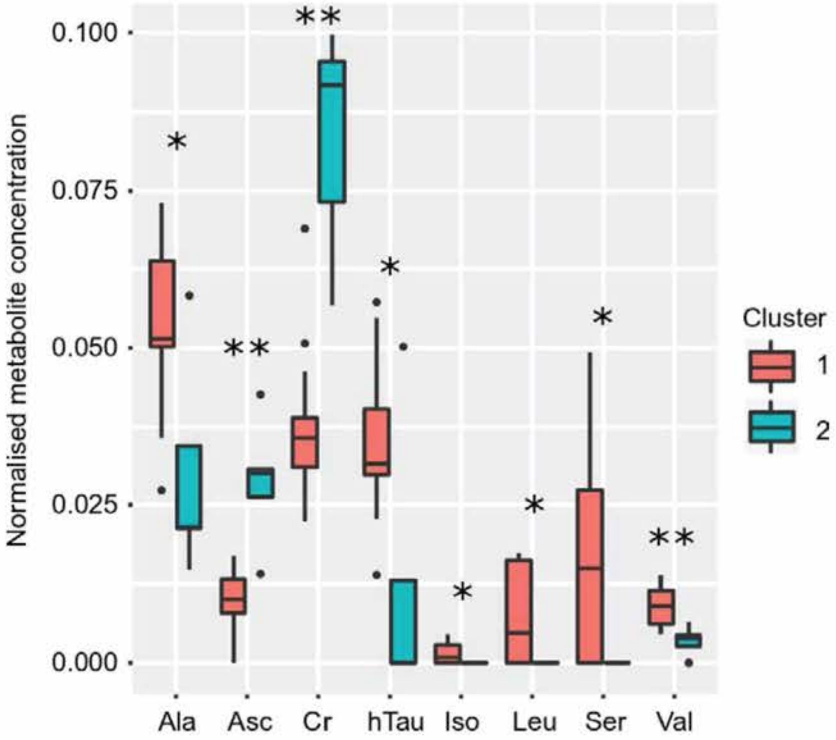

Figure 5.6 – Metabolites demonstrating significant differences in concentration between metabolic subgroups. * $P < 0.05$, ** $P < 0.01$.

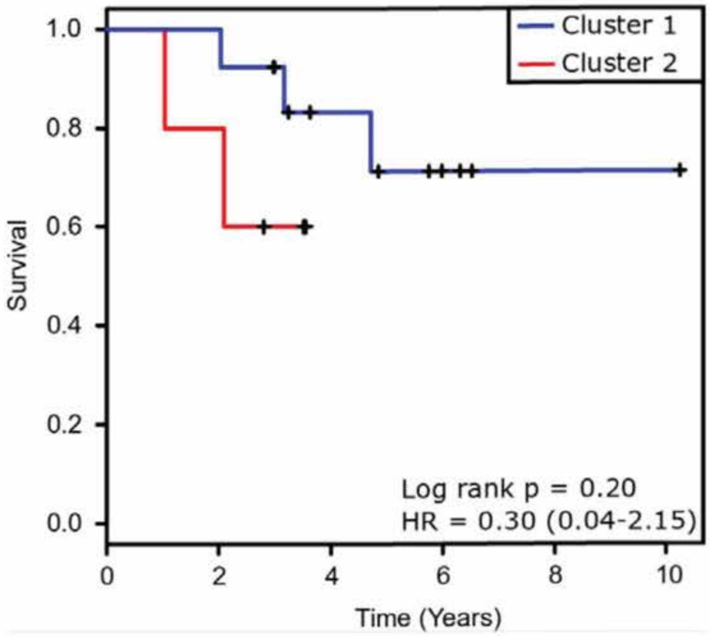

Figure 5.7 – Kaplan-Meier curves for metabolic subgroups of pilocytic astrocytoma.

5.4 Discussion

This chapter has examined the metabolite profiles of paediatric PA tissue and identified metabolites that may act as markers of progression-free survival. Furthermore, by performing unsupervised cluster analysis, two potential metabolic subgroups of cerebellar PA were identified.

Gln was shown to be a prognostic marker, with high Gln concentration indicating a lower risk of progression. This observation mirrors that of chapter 4, where Gln was shown to be a marker of overall survival. Four other metabolites, Ace, hTau, NAA and lipids at 0.9ppm, were shown to have potential prognostic ability. Interestingly, high NAA was shown to predict a higher risk of progression. This is not what would be expected, as NAA has previously been thought of as a positive prognostic marker (4). Explanations for this include a more diffuse growth pattern, entrapping neurons and providing a higher NAA signal. However, there is evidence that NAA concentration does not correlate with entrapped neuronal elements (163). An alternative hypothesis to entrapped neurons involves NAA uptake from the local environment (101). Decreased progression-free survival may be due to an increase in NAA concentration being linked to an increase in growth and decrease in differentiation in *in vitro* studies using glioma-stem-like cells (239).

There is great interest in identifying tumour subgroups, in particular those that have clinical significance. PA methylation (240) and gene expression profiles (241) have been shown to differ with anatomical location, as has the proportion of driver mutations (20, 23). In this chapter, two potential subgroups of cerebellar PA were identified by performing unsupervised cluster analysis using metabolite concentrations. Whilst group membership does not currently show prognostic significance, it does indicate a difference in biology that with further study may be exploitable, with branched chain amino acid metabolism of particular interest. The BCAT1 enzyme has been suggested as a therapeutic target in glioblastoma, where up-regulation of this gene was linked to poorer survival. Wong et al. proposed subgroups of PAs through unsupervised cluster analysis using gene expression data (242); unfortunately the authors did not perform a survival analysis on the cohort, which had a high rate of complete resection.

The analyses in this chapter were performed with a small cohort and so the results are preliminary. Further cases need to be added to the cohort to improve the stability of the analysis and allow for stratification of other markers such as size of residual tumour.

Metabolites with prognostic potential were not shown to significantly differ with BRAF status or extent of surgical resection, indicating that metabolite markers may predict survival independent of these variables.

5.5 Conclusion

In conclusion, metabolites have the potential to predict progression-free survival in cerebellar astrocytomas. High concentrations of Ace, hTau, NAA and lipids at 0.9ppm were predictors of poor progression-free survival, whilst a high concentration of Gln was a marker of better progression-free survival. It is interesting to observe the ablity of Gln to predict a better progression-free survival in a tumour with excellent overall survival. Furthermore, two metabolic subgroups of cerebellar PA are proposed.

This chapter provides evidence that metabolite concentration may aid in deciding the risk of progression in a patient with PA and therefore inform clinicians regarding the treatment or extent of surveillance imaging required to monitor patients. Further study with more cases is required to validate the ability of Gln to predict survival as well as identify the underlying biology of any metabolic subgroups and their prognostic ability.

CHAPTER 6: Metabolic pathway analysis of paediatric brain tumours

6.1 Introduction

The previous chapters have shown how metabolite profiles have potential to inform the clinical management of brain tumour patients through improved prognosis and diagnosis. The rate of improvement of survival for paediatric brain tumour patients has declined in recent decades. Alongside better diagnostic accuracy and risk stratification, further increases in patient survival require the development of novel therapeutic targets and strategies. This chapter describes metabolic pathway analysis on paediatric cerebellar tumours to identify differences in metabolism. Metabolic pathway analysis uses prior knowledge regarding the relationship between metabolites to draw conclusions about how the metabolism of tumours differs and identify potential novel metabolic therapeutic targets.

Paediatric neuro-oncology has embraced the revolution in molecular biology and generated huge amounts of data. These studies have been important for identifying and understanding recurring genetic alterations which drive brain tumour growth. For example, sequencing of tumours has identified recurring mutations in genes within the Sonic Hedgehog (SHH) and Wingless (Wnt) signalling pathways in MB (39, 243-246), and shown that inactivating mutations in *INI1* drive ATRTs (50, 192). More recently epigenomic studies have found that some tumours without recurring genetic mutations have aberrant methylation profiles leading to pathological gene regulation, such as in a subgroup of posterior fossa EPs (247, 248).

Pathway analysis is used to determine which pathways are significantly altered under a given condition. Pathway enrichment has developed from over-representation analysis to gene set enrichment analysis to topological based analysis (249). Topologically- based analyses incorporate prior knowledge on the direction of interactions from curated databases. Such analyses have been used in brain tumour research to identify genetic networks that are significantly different between tumours and tumour types (250, 251).

Whilst pathway analysis has most often been applied to gene expression, there has been an increase in interest in using other data, and both proteomic and metabolomic data can now be analysed using pathway analysis methodologies. Using other omic data to support gene expression studies has some important benefits. Gene expression shows variable correlations with protein expression due to the layers of cellular regulation beyond the transcription of a gene (251), whereas metabolism is the final phenotypic outcome of gene expression and its interaction with the environment.

Cancer cells modify their metabolism to meet their biosynthetic needs. Otto Warburg made the seminal observation of glucose fermentation to lactate by tumour cells, even in the presence of sufficient oxygen (82). This observation led to the development of FDG-PET imaging. Understanding how a tumour alters its metabolism to enable proliferation, and how that differs between different tumours, will allow the development of therapies that target metabolism.

This chapter performs metabolic pathway analysis on paediatric cerebellar tumours to identify differences in metabolism. An initial pathway analysis was performed using metabolite profiles obtained using HR-MAS. The relative lack of sensitivity of this technique means that there are a large number of gaps in the metabolic pathways where the concentrations cannot be measured. Therefore, the other main stream metabolomic technique mass spectrometry was used to increase metabolic pathway coverage. Metabolite concentrations were correlated to determine the extent of agreement between the two methodologies.

6.2 Methods

6.2.1 Cohort

This retrospective study included 60 cases of cerebellar tumours (EP=16, MB=24, PA=20) acquired from Birmingham Children's Hospital and the CCLG tissue banks. The tissue had been previously examined using HR-MAS, and frozen as soon as possible at -80°C after removal from the NMR spectrometer. All cases were included in the cohort for chapter 3, however 9 samples were not available for this analysis; 2 EP and 4 PA post HR-MAS samples were embedded in paraffin. The 24 MB samples are all from the BCH tissue bank, with 5 samples not available for mass spec analysis due to other project needs.

6.2.2 Statistical analysis of UPLC-MS data

Kruskal Wallis tests were used to identify differences in metabolite abundance, and P-values were corrected using Benjamini-Hochberg correction. Features that were significantly different between the tumour types in both the high and low-mass cohorts were passed to a principal component analysis. Correlations were performed between normalised HR-MAS concentrations and normalised UPLC-MS concentrations using Spearman's correlation coefficient. All statistical analyses were performed in the R statistical environment.

6.2.3 Pathway analysis

For the HR-MAS data, the Pathway Analysis module included in the MetaboAnalyst online tool (http://www.metaboanalyst.ca/faces/upload/PathUploadView.xhtml) was used(252). The pathway analysis module combines two analyses, an enrichment analysis and a topological analysis. The enrichment analysis uses a global test to identify differences in pathway activity between tumour types (253). Originally developed for genetic data, it has been shown to be applicable to metabolomic data (254). This test quickly tests if changes in a pathway are related to different conditions; in the case of this work, whether consistent changes in concentrations of metabolites within defined pathways are due to tumour type.

The topological analysis for each pathway uses relative degree centrality. This is the proportion of shortest paths between all pairs of nodes in the pathway that has a detected metabolite along it (255). The relative aspect means that directionality of the pathway is taken into account, with only possible reactions are considered. Therefore, a higher topological score for a pathway indicates that detected metabolites are situated at important nodes within the pathway.

The tumour types were compared in a pairwise manner. The following parameters were used: group label - discrete (classification), ID type - compound name, data format - samples in rows. The compound hit was verified against the query for the name check and no further normalisation was performed. The Homo sapiens (human), Global Test and Relative-betweeness centrality options were selected for the pathway library, pathway enrichment analysis and pathway topology analysis respectively.

The peaks-to-pathway module of MetaboAnalyst was selected for the UPLC-MS pathway analysis (http://www.metaboanalyst.ca/faces/upload/PeakUploadView.xhtml). This module uses the *Mummichog* algorithm, an algorithm designed to analyse high throughput, non-targeted metabolomic data. *Mummichog* requires a list of m/z ratios, significance values and fold changes between conditions to perform a pathway analysis instead of data annotated with compounds. This algorithm refers to the whole list of submitted features as L_{ref}. A user supplied p-value is used to identify significantly different features between the two conditions of study, with significant features forming a list referred to as L_{sig}. A randomised list of features equal in length to L_{sig} is generated from L_{ref}, and mapped to tentative metabolites. Fishers Exact Test (FET) is used to calculate a p-value for each pathway. To construct a null distribution, the previous step is repeated many times to create a list of p-values of all pathways under each permutation. These p-values are modelled as a Gamma distribution and a cumulative distribution function is calculated. Finally, the pathway analysis is performed on the list L_{sig}, with a FET p-value calculated for each pathway, along with a more stringent EASE score, calculated The previously calculated cumulative distribution function is used to adjust the p-value based on the EASE score for each pathway (256). The following parameters were used: Mass accuracy - 5ppm, analytical mode – positive or negative depending on the ionisation mode used for the experiment, P-value cut off – 0.05, pathway library – Homo sapiens [Kegg].

6.2.4 Gene Set Enrichment Analysis

A gene set enrichment analysis (GSEA) was performed using an independent dataset archived in the Gene Expression Omnibus (GEO), a repository curated by the NCBI. GSEA attempts to identify if genes from a particular set tend to occur towards the top or bottom of a list of genes when ranked by their difference in expression between two conditions. This analysis requires defined sets of genes, in the case of this work this is defined by gene products in metabolic pathways. Firstly, an enrichment score is derived by walking down the ranked list of genes using a running-sum statistic which increases when a gene in the pathway of interest is encountered and decreasing when a gene from the pathway isn't encountered. The score is the maximum deviation from 0. Next, the significance of the enrichment score is estimated through permutation of the condition labels to generate the null distribution. Finally, the p-values are adjusted for multiple comparisons (257).

The data for GEO accession number GSE42656 was archived by Henriquez et al 2013 (258) and is comprised of 73 brain tumour gene expression experiments. The data includes gene expression data for 14 PA, 14 EP and 9 MB. The data were acquired using the Illumina HumanHT-12 V3.0 expression beadchip platform. Raw expression data were normalised using the interquartile range for each probe, and prior to analysis was log2 transformed. In a pairwise manner, differences in gene expression were tested using Students t-tests with multiple comparisons being corrected for using Benjamini and Hochberg correction to control the false discovery rate. Genes with an FDR <0.05 were carried forward to a GSEA performed using the Enrichr online tool (259, 260). Fisher's exact test was used to test for significant pathway enrichment for the metabolic pathways identified by the metabolic pathway analysis.

6.3 Results

6.3.1 HR-MAS pathway analysis

Initially, the HR-MAS metabolite concentrations were submitted to MetaboAnalyst for a metabolic pathway analysis. The pathway analysis identified 43 pathways which contained at least one metabolite quantified by HR-MAS, accounting for approximately 25% of all metabolic pathways described by KEGG. The 75th centile included 11 pathways for which the significance was compared in a pairwise manner (Table 6.1). Of these 11 pathways, 5 displayed significant differences in all 3 pairwise comparisons, 5 displayed significant differences for a single tumour type and 1 showed no differences in any comparisons. Glycine, serine and threonine metabolism, glutathione metabolism and glycerophospholipid metabolism were enriched in MBs whilst inositol phosphate , alderate and ascorbate metabolism were enriched in EPs. None of the pathways were enriched in PAs. Although the topology score for pyruvate metabolism was high enough to be included in the list of metabolic pathways, it was not shown to be significantly different between the three tumour types. D-glutamine and D-glutamate metabolism was excluded from the rest of the analysis as it is not possible to distinguish between the enantiomers using HR-MAS. Furthermore, the aminoacyl tRNA biosynthesis pathway was excluded from further analysis as this pathway is reflective of increased protein synthesis and not of metabolic adaptions.

Pathway	Total Compounds	Hits	Relative betweeness centrality	Pairwise pathway analysis FDR		
				MB-EP	EP-PA	MB-PA
Alanine, aspartate and glutamate metabolism	24	7	0.808	0.0136	0.00113	3.31x10^{-10}
Taurine and hypotaurine metabolism	20	4	0.444	0.00582	0.000523	3.89x10^{-8}
Glycine, serine and threonine metabolism	48	5	0.324	0.0216	0.662	0.0193
Glutathione metabolism	38	4	0.256	0.00716	0.662	0.0242
Aminoacyl-tRNA biosynthesis	75	9	0.169	0.00345	0.00113	3.31x10^{-10}
D-Glutamine and D-glutamate metabolism	11	2	0.139	0.0118	0.00113	3.31x10^{-10}
Inositol phosphate metabolism	39	1	0.137	1.12x10^{-7}	2.01x10^{-7}	0.827
Ascorbate and aldarate metabolism	45	2	0.114	1.12x10^{-7}	2.01x10^{-7}	0.403
Pyruvate metabolism	32	1	0.0995	0.233	0.230	0.407
Arginine and proline metabolism	77	5	0.0865	0.0136	0.00113	3.31x10^{-10}
Glycerophospholipid metabolism	39	3	0.0768	1.12x10^{-7}	0.734	4.65x10^{-10}

Table 6.1 – the 11 metabolic pathways in the 75th centile with regards to the topology score (relative betweeness centrality) identified by HR MAS, with pairwise false discovery rate.

6.3.2 UPLC-MS descriptive analysis

The low sensitivity of HR-MAS means there is a low coverage of the metabolome. Even in the alanine, aspartate and glutamate pathway, which had the highest topology score, less than a third of the metabolites could be measured. It was hypothesised that the greater sensitivity of mass spectrometry could increase the metabolome coverage and provide a more complete metabolic pathway analysis.

Using HILIC and lipid assays, metabolism of both polar metabolites and lipids was shown to vary between the three tumour types (**Figure 6.1**). This was seen in both positive and negative ionisation modes in both mass cohorts. After annotation of the data, 266 metabolites were shown to be significantly different (FDR < 0.05) (Table 6.2). Due to multiple potential assignments for each ion, metabolite classes have been assigned. Where more than one metabolite class is present in a potential assignment, it is assigned a mixed class label. A large number of features annotated as glycerophospholipids were significantly different between the three tumour types

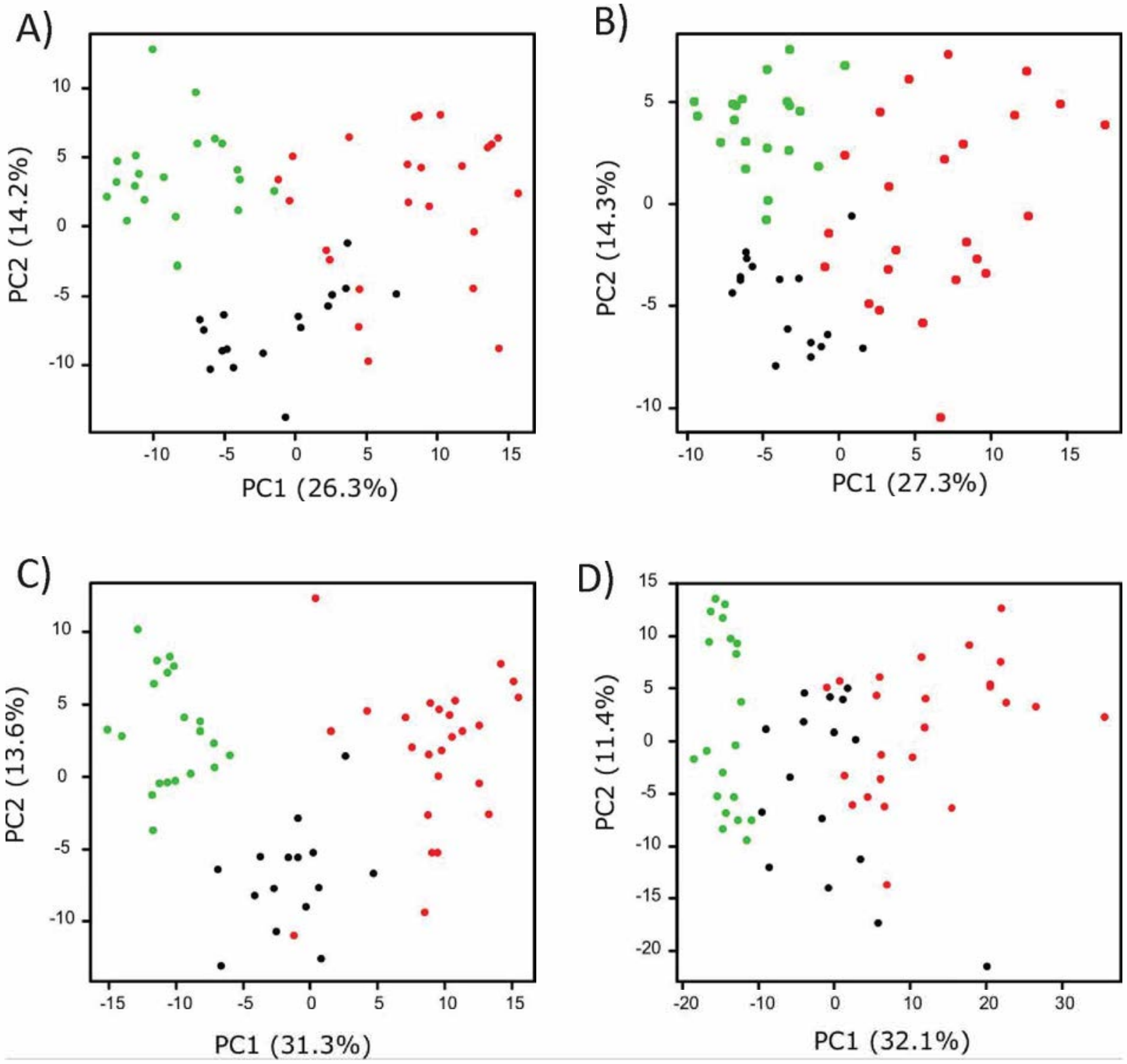

Figure 6.1 – PCA scatterplots for UPLC-MS data. A) HILIC negative mode, B) HILIC positive mode, C) lipids negative mode and D) lipids positive mode. In all cases red points represent MBs, black represent EPs and green represents PAs.

Metabolite class	**Number of significant ions**
Glycerophospholipid	112
Ceramides and sphingolipids	28
Triacylglyceride	28
Other	22
Mixed class	15
Purine, pyrimidine, nucleoside and nucleotide	11
Diacylglyceride	9
Short chain organic acids	8
Carbohydrate metabolism	6
Peptides	6
Fatty acid	3
Fatty esters	3
Cardiolipins	2
N-glycan biosynthesis	2
Vitamin D metabolism	2
Arginine and proline metabolism	1
Aromatic metabolites	1
Cysteine and methionine metabolism	1
Glycerophospholipid metabolism	1
Glycine, serine and threonine metabolism	1
Histidine metabolism	1
Monoacylglyceride	1
Polyamine metabolism	1
Ubiquinone metabolism	1

Table 6.2 – Number of significant metabolites for each metabolite class. Many classes of metabolites showed a number of significantly different m/z features, with glycerophospholipids and lipid species having the largest proportion.

6.3.3 HR-MAS UPLC-MS correlations

To determine the extent of agreement between these two methods, a correlation analysis was performed between metabolites quantified by HR-MAS and candidate m/z features detected by UPLC-MS for both ionisation modes (**Figure 6.2, Figure 6.3**). The metabolites with the highest abundances as measured by HR-MAS (Cr, Gln, Glu, NAA) correlate well with the concentrations determined by UPLC-MS in both positive and negative ionisation modes. The lower abundance metabolites (Asp, GABA, Glc, sIns, Ser) do not correlate so highly. GPC had a surprisingly low correlation, whilst PCh had a consistently negative correlation between HR-MAS and UPLC-MS. There are disagreements in the strength of correlations between ionisation modes for some metabolites, particularly with regards to Ala, Gly, mIns, Leu and Iso.

The differences in correlations between ionisation modes aren't unexpected, as response to ionisation mode is thought to be related to the individual metabolite's chemical properties. Acidic metabolites are thermodynamically more likely to donate than accept a proton, and so they would be better detected in negative mode. The inverse is true for more basic metabolites, for which accepting a proton is more thermodynamically favourable than donating, and so positive mode may be more appropriate.

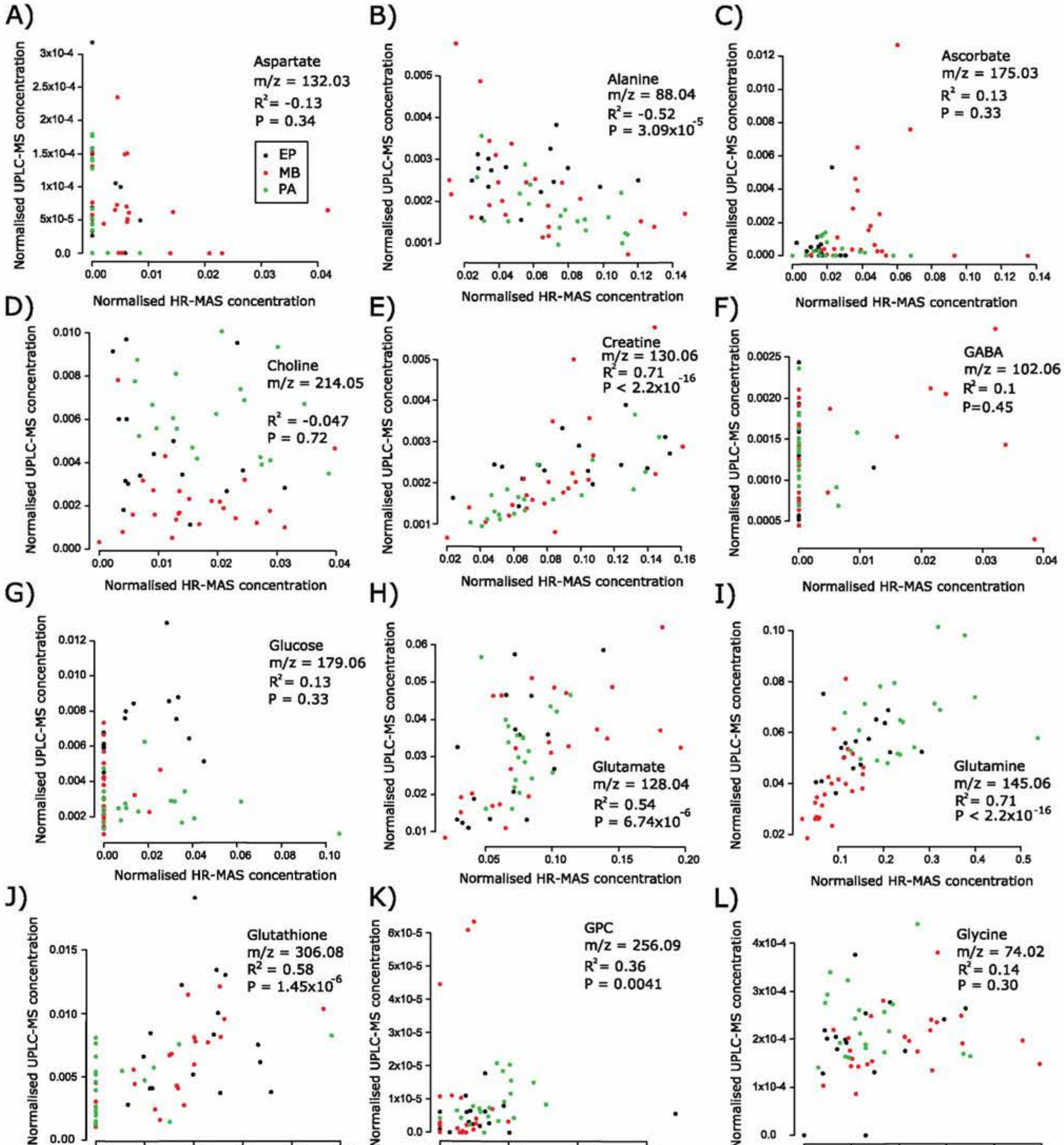

A)
Aspartate
m/z = 132.03
R² = -0.13
P = 0.34
EP
MB
PA
B)
Alanine
m/z = 88.04
R² = -0.52
P = 3.09x10⁻⁵
C)
Ascorbate
m/z = 175.03
R² = 0.13
P = 0.33
D)
Choline
m/z = 214.05
R² = -0.047
P = 0.72
E)
Creatine
m/z = 130.06
R² = 0.71
P < 2.2x10⁻¹⁶
F)
GABA
m/z = 102.06
R² = 0.1
P=0.45
G)
Glucose
m/z = 179.06
R² = 0.13
P = 0.33
H)
Glutamate
m/z = 128.04
R² = 0.54
P = 6.74x10⁻⁶
I)
Glutamine
m/z = 145.06
R² = 0.71
P < 2.2x10⁻¹⁶
J)
Glutathione
m/z = 306.08
R² = 0.58
P = 1.45x10⁻⁶
K)
GPC
m/z = 256.09
R² = 0.36
P = 0.0041
L)
Glycine
m/z = 74.02
R² = 0.14
P = 0.30
Normalised UPLC-MS concentration
Normalised HR-MAS concentration

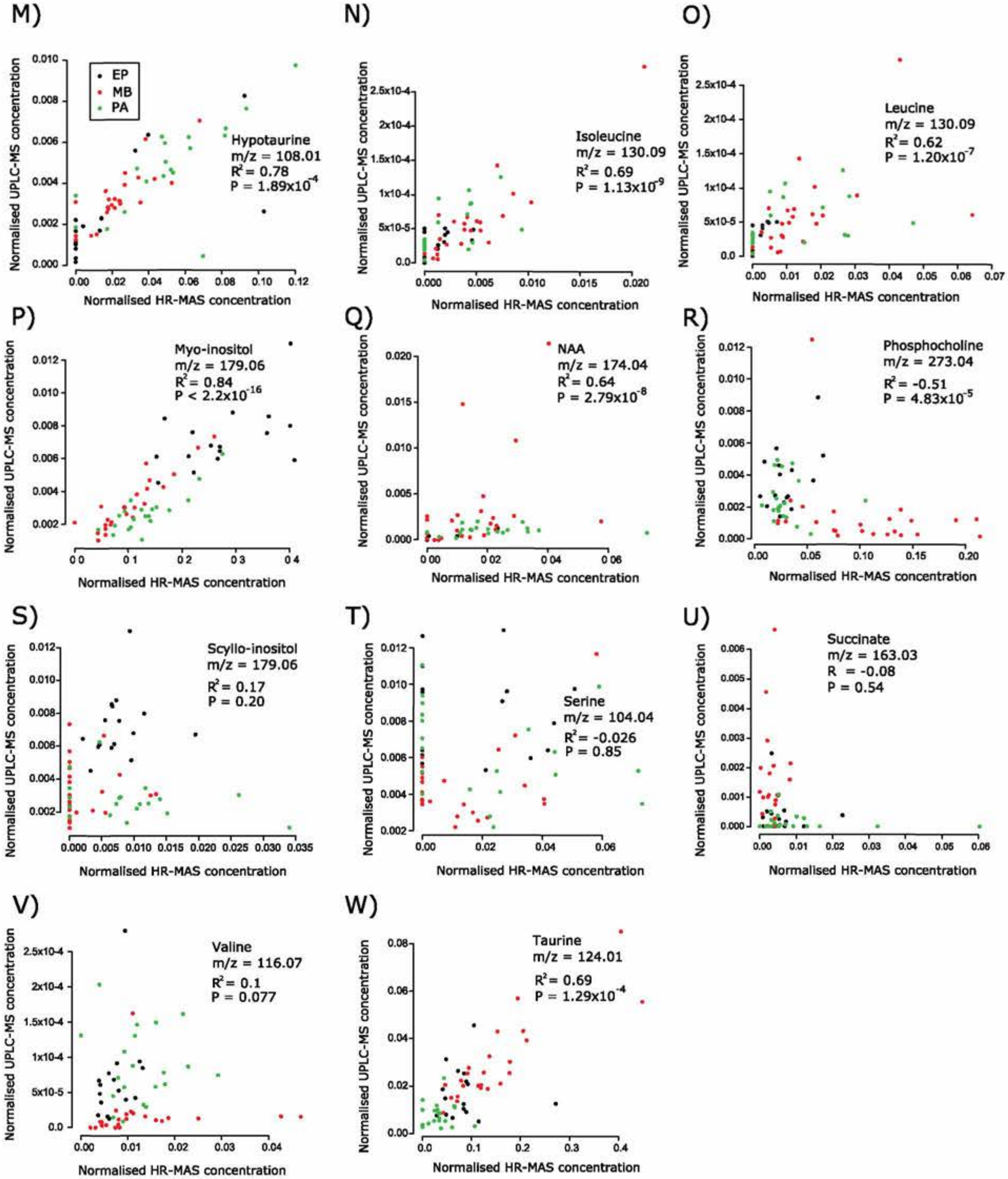

Figure 6.2 – Correlations between normalised concentrations as measured by HR-MAS (x-axis) and negative ionisation mode UPLC-MS (y-axis). Spearman's correlations coefficient is displayed for each metabolite. Red represents MBs, black represents EPs and green represents PAs.

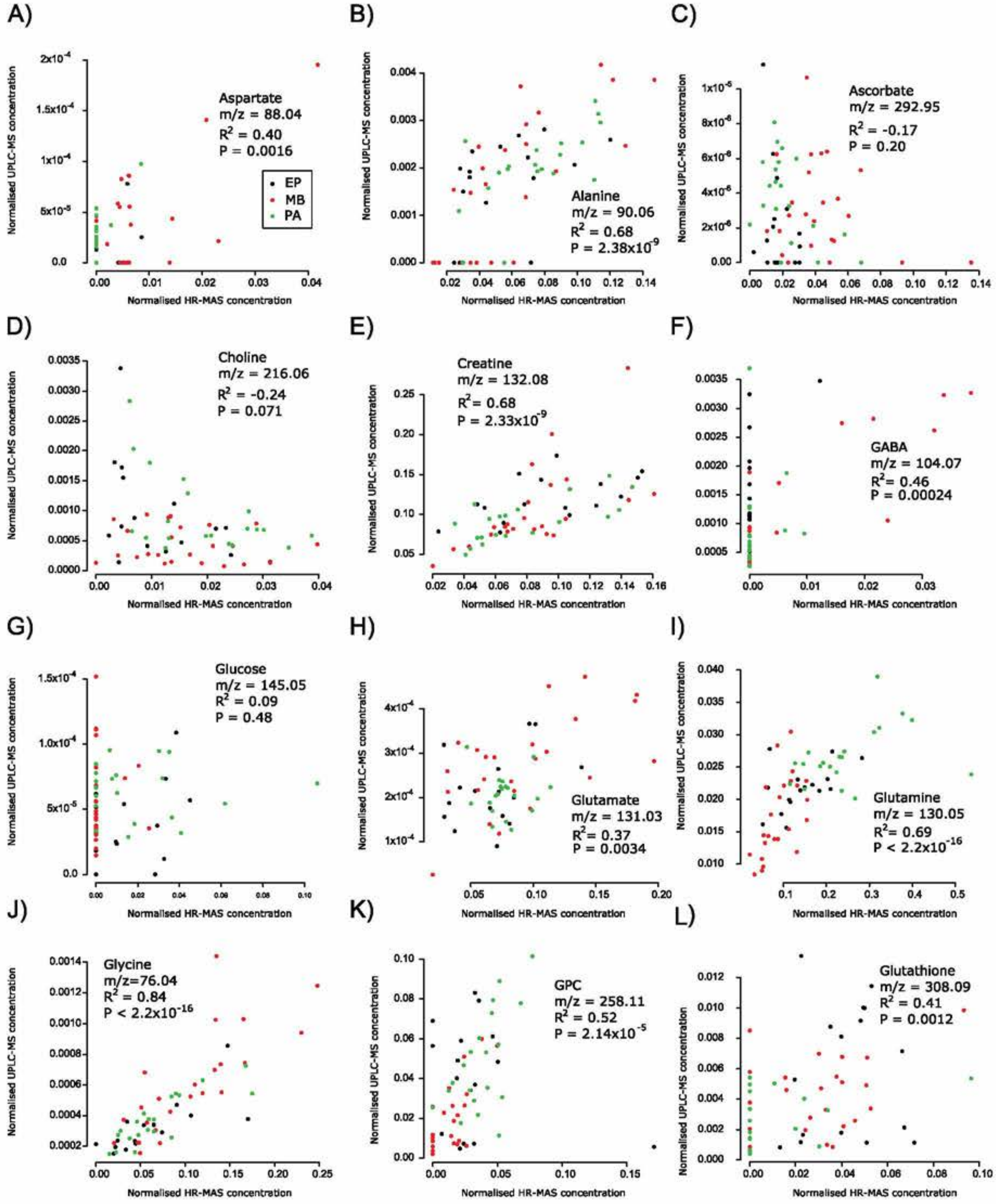
A)
Aspartate
m/z = 88.04
R² = 0.40
P = 0.0016
EP
MB
PA
B)
Alanine
m/z = 90.06
R² = 0.68
P = 2.38x10⁻⁹
C)
Ascorbate
m/z = 292.95
R² = -0.17
P = 0.20
D)
Choline
m/z = 216.06
R² = -0.24
P = 0.071
E)
Creatine
m/z = 132.08
R² = 0.68
P = 2.33x10⁻⁹
F)
GABA
m/z = 104.07
R² = 0.46
P = 0.00024
G)
Glucose
m/z = 145.05
R² = 0.09
P = 0.48
H)
Glutamate
m/z = 131.03
R² = 0.37
P = 0.0034
I)
Glutamine
m/z = 130.05
R² = 0.69
P < 2.2x10⁻¹⁶
J)
Glycine
m/z=76.04
R² = 0.84
P < 2.2x10⁻¹⁶
K)
GPC
m/z = 258.11
R² = 0.52
P = 2.14x10⁻⁵
L)
Glutathione
m/z = 308.09
R² = 0.41
P = 0.0012
Normalised UPLC-MS concentration
Normalised HR-MAS concentration

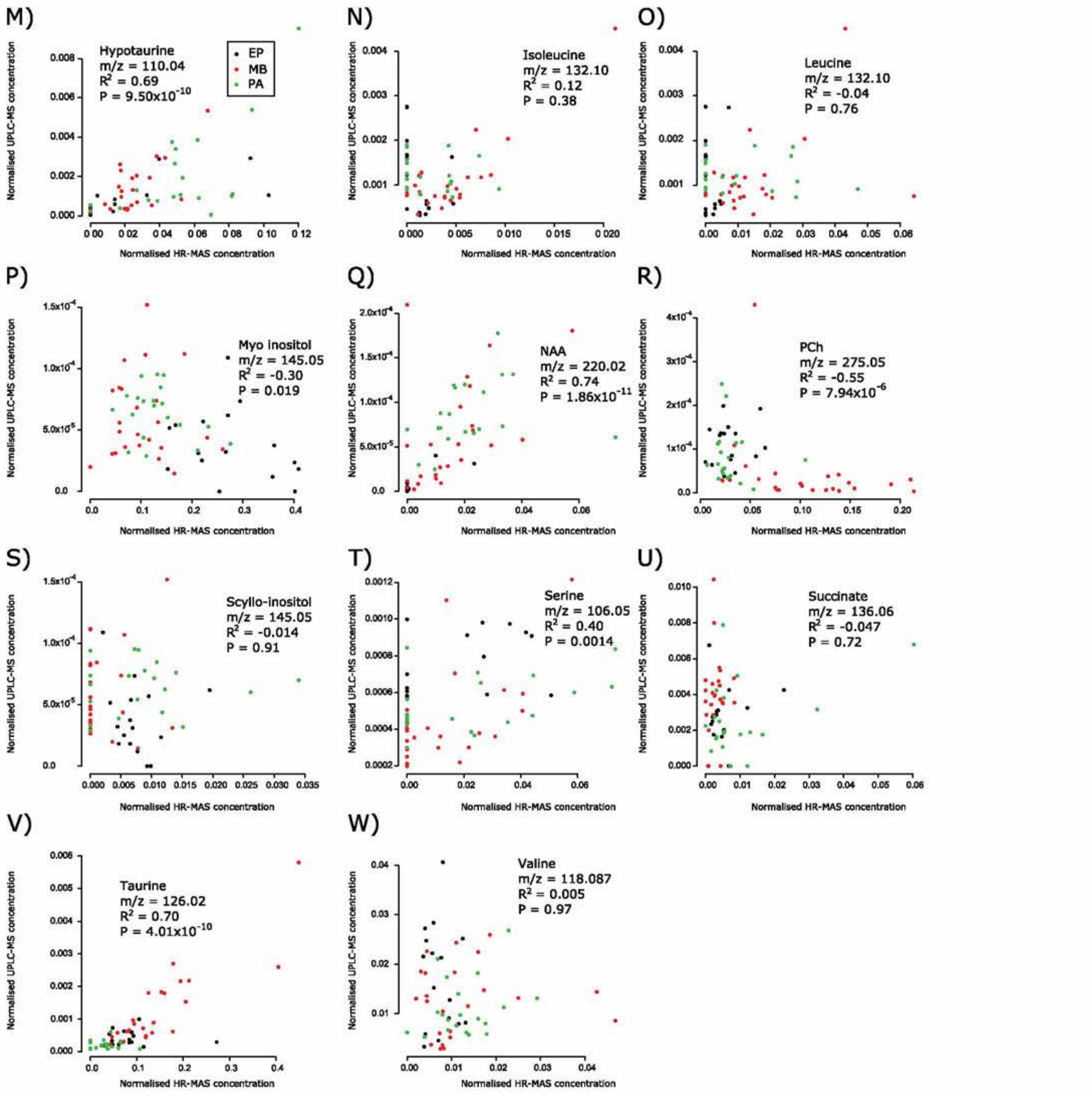

Figure 6.3 – Correlations between normalised concentrations as measured by HR-MAS (x-axis) and positive ionisation mode UPLC-MS (y-axis). Spearmans correlation coefficient is displayed for each metabolite.

6.3.4 UPLC-MS pathway analysis

Pathway analyses were performed by applying the *Mummichog* algorithm to the positive mode UPLC-MS and negative mode UPLC-MS data. The nature of the *Mummichog* algorithm improved the metabolome coverage with regards to HR-MAS (**Figure 6.4**). The negative mode analysis suggests that alanine, aspartate and glutamate metabolism, taurine and hypotaurine metabolism, glycine, serine and threonine metabolism, inositol phosphate metabolism, ascorbate and aldarate metabolism and arginine and proline metabolism are significantly different between the three tumour types. Glutathione metabolism is shown to be significantly different in MBs relative to the other two tumour types. However, glycerophospholipid metabolism was not shown to be significantly different between the tumour types. (**Table 6.3**)

The positive mode analysis agrees that alanine, aspartate and glutamate metabolism and arginine and proline metabolism are significantly different between the three tumour types. The two analyses disagree with regards to the significance of taurine and hypotaurine metabolism and glutathione metabolism, with these metabolic pathways only significantly different between MB and ependymoma. The analysis also suggests glycine, serine and threonine metabolism is significantly different in PA relative to the other two tumour types. Furthermore, glycerophospholipid metabolism was shown to be significantly different between the three tumour types in contrast to the negative mode analysis (**Table 6.4**).

The higher metabolome coverage allows *Mummichog* to further identify pathways with significant differences between the three tumour types. These are contained in Appendix 2.

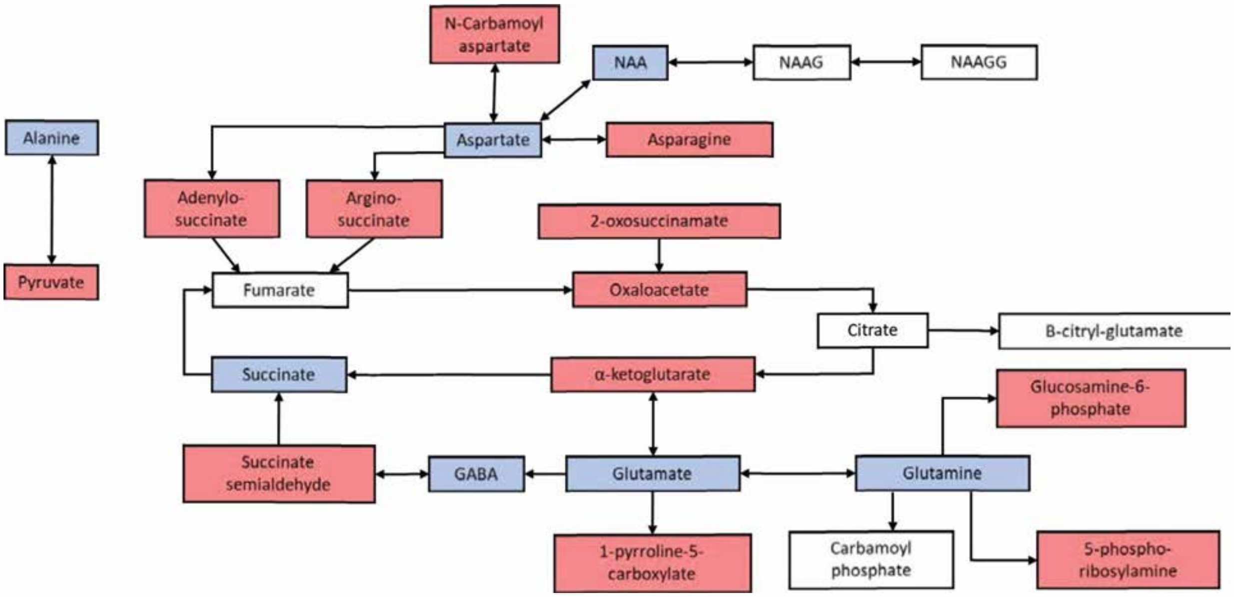

Figure 6.4 – An illustration of the increased metabolome coverage of UPLC-MS. The pathway displayed is the alanine, aspartate and glutamate pathway. Arrows indicate the directionality of reactions. Red highlights metabolites identified by UPLC-MS only, whilst blue highlights metabolites that are detected by both HR-MAS and UPLC-MS. Uncoloured metabolite are not detected by either method; there are no metabolites detected using HR-MAS that are not detected by UPLC-MS in this pathway. Figure adapted from KEGG (261).

Pathway	Pathway total	Hits total	MB-EP		EP-PA		MB-PA	
			Hits sig	P-value	Hits sig	P-value	Hits sig	P-value
Alanine, aspartate and glutamate metabolism	24	22	20	0.003	19	0.002	21	0.003
Taurine and hypotaurine metabolism	20	12	11	0.008	10	0.010	10	0.045
Glycine, serine and threonine metabolism	48	36	30	0.004	26	0.014	30	0.010
Glutathione metabolism	38	14	12	0.013	9	0.112	12	0.025
Inositol phosphate metabolism	39	20	15	0.049	17	0.003	16	0.042
Ascorbate and aldarate metabolism	45	34	30	0.002	32	0.001	32	0.002
Pyruvate metabolism	32	21	17	0.015	18	0.003	19	0.005
Arginine and proline metabolism	77	56	48	0.002	45	0.002	46	0.007
Glycerophospholipid metabolism	39	15	10	0.174	10	0.082	12	0.056

Table 6.3 – Pairwise negative mode UPLC-MS *Mummichog* significance values for the pathways previously identified by the HR-MAS analysis.

Pathway	Pathway total	Hits total	MB-EP		EP-PA		MB-PA	
			Hits sig	P-value	Hits sig	P-value	Hits sig	P-value
Alanine, aspartate and glutamate metabolism	24	19	15	0.007	19	0.002	17	0.005
Taurine and hypotaurine metabolism	20	11	8	0.035	8	0.058	7	0.241
Glycine, serine and threonine metabolism	48	33	21	0.053	25	0.009	25	0.030
Glutathione metabolism	38	18	13	0.019	11	0.171	12	0.179
Inositol phosphate metabolism	39	20	12	0.116	10	0.431	14	0.117
Ascorbate and aldarate metabolism	45	33	15	0.529	20	0.190	25	0.030
Pyruvate metabolism	32	15	10	0.055	13	0.006	14	0.004
Arginine and proline metabolism	77	55	41	0.003	49	0.002	45	0.004
Glycerophospholipid metabolism	39	14	11	0.011	13	0.004	14	0.003

Table 6.4 – Pairwise positive mode UPLC-MS *Mummichog* significance values for the pathways previously identified by the HR-MAS analysis.

6.3.5 Gene set enrichment analysis

GSEA of an independent published dataset was used to determine the genetic basis for the differences in metabolism between the three tumour types. The genetic data shows that differences in expression of genes in the alanine, aspartate and glutamate metabolic pathway are enriched between EP and PA, as are differences in the expression genes in the inositol phosphate pathway. Genes in the glutathione metabolic pathway are enriched between MB and PA (**Table 6.5**).

Pathway	Total pathway genes	MB-EP		EP-PA		MB-PA	
		Hits	FET	Hits	FET	Hits	FET
Alanine, aspartate and glutamate metabolism	35	8	0.680	13	0.049	14	0.385
Arginine and proline metabolism	20	5	0.587	15	0.178	22	0.162
Ascorbate and aldarate metabolism	27	3	0.980	2	0.993	3	0.999
Glutathione metabolism	52	18	0.079	13	0.453	28	0.007
Glycerophospholipid metabolism	95	16	0.979	24	0.382	38	0.259
Glycine, serine and threonine metabolism	40	8	0.820	9	0.621	15	0.497
Inositol phosphate metabolism	71	22	0.154	25	0.017	32	0.080
Taurine and hypotaurine metabolism	11	1	0.958	3	0.498	5	0.366

Table 6.5 – Pathway significance determined by gene expression data from GEO dataset GSE42656. FET – Fisher's exact test.

6.4 Discussion

This chapter has examined the ability of metabolite profiles to provide biological information on how different tumours adapt their metabolism to satisfy their biosynthetic and bioenergetic requirements. Metabolic pathways which are differentially modified in the three tumours types were initially identified using HR-MAS, and further information was acquired using UPLC-MS; a variation on the other mainstream metabolomic technique. The initial pathway analysis using the HR-MAS data identified 43 pathways with the top 25% being taken forward for interpretation. The higher topology scores of these 11 pathways show that the measurable metabolites lie on the shortest paths between the nodes in the directed graphs, and therefore have higher importance than other metabolites.

The results of the UPLC-MS were used to validate the HR-MAS findings. UPLC-MS increased the coverage of the metabolome, detecting a large number of features with significantly different intensities between the three tumour types. The *Mummichog* algorithm, developed to analyse large amounts of mass spectrometry data without prior annotation, was used to perform a pathway analysis on the UPLC-MS data.

Coverage of the pathways was increased in all cases. For the alanine, aspartate and glutamate metabolic pathway, metabolite coverage increased from 7 using HR-MAS to 22 in negative mode UPLC-MS out of a total of 24. Key metabolites displayed a strong positive correlation between the two methods including Gln, Glu and NAA. GABA and Asp did not show significant correlations, whilst a negative correlation was observed for Ala. Whilst GABA and Asp are difficult to quantify using HR-MAS if there are large lipid components or a relatively low SNR, UPLC-MS is able to separate and detect these metabolites. This is demonstrated by the large number of data points at x=0.

Taurine and hypotaurine metabolism coverage increased from 4 using HR-MAS to 12 in negative mode UPLC-MS out of a total of 20 metabolites in the pathway, with strong correlations between the two methods being observed for Tau and hTau.

The metabolite coverage of the glycine, serine and threonine metabolic pathway increased from 5 identified by HR-MAS to 36 identified by negative mode UPLC-MS out of a total of 48 metabolites. Non-significant correlations were observed between the two methods for Gly and Ser. Ser, similarly to GABA and Asp, is difficult to quantify in HR-MAS. The doublet of doublets for Ser is in a crowded region of the HR-MAS spectrum and can be difficult to quantify if Ser is in low abundance. This leads to a large proportion of data points at x=0. Gly, on the other hand, is easily quantified in HR-MAS. Gly has previously shown poor response to electrospray ionisation. This is believed to be due to its relatively low proton affinity, which is the lowest of the amino acids(262).

The metabolite coverage of the glutathione metabolic pathway increased from 4 metabolites detected by HR-MAS to 18 detected by positive mode UPLC-MS out of 38 metabolites. GSH displayed a strong positive correlation between the two methods.

The coverage of the inositol phosphate metabolic pathway increased from 1 metabolite detected using HR-MAS to 20 metabolites detected by UPLC-MS in both ionisation modes. mIns correlated very strongly between HR-MAS and UPLC-MS in negative ionisation mode, but had a weak negative correlation in positive mode.

The metabolite coverage of the ascorbate and aldarate metabolism improved from 2 metabolites identified by HR-MAS to 34 metabolites detected by negative mode UPLC-MS. No significant correlation was observed between HR-MAS and UPLC-MS for Asc.

The coverage of the arginine and proline metabolic pathway increased from 5 metabolites detected by HR-MAS to 56 metabolites detected using negative mode UPLC-MS. Neither arginine nor proline can be quantified using HR-MAS as the peaks are overlapped by more abundant metabolites.

Finally, the glycerophospholipid metabolic pathway had metabolite coverage increased from 3 detected by HR-MAS to 15 detected by negative mode UPLC-MS. Only GPC demonstrated a positive correlation, albeit with a low R^2, between the two methods; Cho did not show a significant correlation, whilst PCh showed a strong negative correlation. This may be due to the extraction protocol; Martínez-bisbal et al (263) demonstrated an average 4.3 fold reduction in the ratios of Cho, PCh and GPC relative to Cr when pre-extraction HR-MAS of brain tumours was compared to post extraction liquid state NMR. This study also showed the ratios between the three choline compounds varied, suggesting the choline concentrations and not the Cr concentration is altered by extracting metabolites. Furthermore, Hao et al observed a poor correlation between Cho measured by liquid state NMR and direct infusion mass spectrometry.

Although the correlations presented in figures 6.2 and 6.3 were produced with candidate m/z features for the metabolite of interest, without tandem mass spectrometry to confirm the identity of prospective metabolites, m/z features can be assigned to multiple metabolites. Retention time can be used to separate m/z features, as mass isomers may have different chemical properties. Furthermore, the m/z features are annotated under some assumptions. Firstly, that ionisation of a metabolite is only associated with the loss or gain of a proton and secondly, that all metabolites are ionised equally efficiently. In reality, some metabolites may fragment during ionisation into smaller ionised fragments, whilst inadequate temporal resolution of the liquid chromatography may lead to several metabolite species eluting at the same time leading to ion suppression as multiple ion species compete for charge. The effect of the matrix on the enhancement or suppression of ion abundance should be considered. Finally, the correlations between HR-MAS and UPLC-MS may be influenced by inaccurate quantification of the HR-MAS data, with metabolite concentrations being affected by small resonances under larger resonances.

Metabolism is gaining wider recognition as a potential targeted therapy. Identifying which pathways different tumours rely upon is the first step in developing these novel therapies.

6.4.1 Alanine, aspartate and glutamate metabolism

The alanine, aspartate and glutamate metabolic pathway was shown to have the highest topology score and was significantly different between the three tumour types using the HR-MAS data. This suggests that the three tumour types are modifying their metabolism differently relative to each other. Alanine, aspartate and glutamate metabolism is an important pathway as it is closely linked to fatty acid biosynthesis, *de novo* nucleotide synthesis, GSH synthesis and the TCA cycle. Gln metabolism can supplement the TCA cycle through conversion to Glu and further deamination to α-ketoglutarate. Glu is also one of three amino acids needed to synthesise GSH. The nitrogen in the amide group can be committed to both purine and pyrimidine synthesis. Up-regulation of Gln catabolising pathways has been linked to more aggressive, higher grade tumours which rely on glutaminolysis to support their increased proliferation(220). Low Gln concentration has been shown in chapter 4 to predict poorer survival, suggesting the tumours have adapted their metabolism to utilise the available Gln and therefore proceed along an aggressive clinical course.

Targeting Gln metabolism has gained interest for tumours that rely on Gln for proliferation, termed Gln-addicted tumours. Glutaminase enzymes GLS1 and GLS2 are under direct control of transcription factors; GLS1 is regulated by c-Myc whilst GLS2 is regulated by p53. Both enzymes convert Gln to Glu as shown in the equation below:

$$\mathrm{Gln} + H_2O \rightarrow \mathrm{Glu} + NH_3$$

Inhibition of the glutaminase enzymes has led to reduced viability of cultured cells (264-266), prevention of tumour formation in a mouse model of Group 3 MB, and to reduction of the size the of tumours in those mice that do develop tumours (267). Other work showed reduced size of tumours in mouse models of hepatocellular carcinoma, with good tolerability and no noticeable off target effects (268).

The results of a phase IIa trial for patients with advanced solid tumours refractory to standard treatments were published by Mueller et al. The treatment combined 6-diazo-5-oxo-L-norleucine (DON) and PEGylated glutaminase. 53% of metastatic colorectal cancer patients were progression free at 3 months, with 29% remaining progression free at 5 months. 83% of patients with lung cancer were progression free at 3 months. 1 metastatic colorectal patient experienced partial response, and an additional patient had stable disease for greater than 12 months. The treatment was well tolerated, with the most common side effects being fatigue in 9.1 %, nausea in 5.5%, vomiting in 3.6% and diarrhoea in 3.6% (269). The NIH is currently supporting 7 clinical trials studying the effect of glutaminase inhibition in a range of cancer types (270); unfortunately, no clinical trials have been set up for brain tumour patients.

6.4.2 Taurine and hypotaurine metabolism

Taurine and hypotaurine metabolism has the second highest topology score, and was shown to be significantly different between all three tumour types. Tau was shown in previous chapters to be a marker of embryonal tumours, whilst hTau was highest in the low grade PAs. Although Tau is transported across the blood brain barrier, it has been shown that neurons and astrocytes are able to synthesise hTau from cysteine via the intermediate sulfinoalanine, or Tau through decarboxylation of cysteic acid (271). No enzyme has so far been identified to catalyse the oxidation of hTau to Tau, and the relatively slow rate of Tau synthesis (272) leads to some uncertainty regarding enzymatic oxidation. Tau has been implicated in various physiological roles throughout the body; it has been shown to have a role in retina development (273), cardiac muscle development , maintenance of osmotic potential (103) and antioxidation (102).

In the brain it has been shown to be important for neuronal stem cell proliferation and neurogenesis (104, 105), the migration of neuronal cells from the external to the internal granular layer in the cerebellum (106, 107) and there is some evidence of action as a neurotransmitter through activation of a variety of receptors.

hTau is a poorly understood metabolite with proposed antioxidant properties. There is evidence that hTau increases invasiveness and proliferation in an *in vitro* GBM model, where it was shown to stabilise HIF expression though inhibition of the α-ketoglutarate binding site on PHD2 (100).

Silencing of cysteine dioxygenase (CDO1), the gene responsible for synthesising the Tau precursor cysteine sulfinic acid from cysteine by shRNA was performed on glioma cell lines. When CDO1 silenced cells were grafted to a mouse model, increased survival was observed when compared to non-CDO1 silenced cell line grafted mice (274).

Tau has been shown to act as an osmolyte, as rats suffering from chronic hyponatremia were shown to have reduced concentrations of Tau compared to healthy controls. Upon correction of hyponatremia, taurine recovers to normal concentrations by day 7 regardless of how quickly the correction is performed (275).

6.4.3 Glycine serine and threonine metabolism

The HR-MAS pathway analysis suggests glycine, serine and threonine metabolism was significantly different in MB compared to the other two tumour types. This pathway is a crucial part of the one-carbon cycle, which maintains a folate pool with many synthetic outputs including methyl units for histone or DNA/RNA methylation, and methylation reactions for phosphatidylcholine head groups (87). This cycle uses a carbon unit from the Ser side chain, converting Ser to Gly. High Gly concentration has been linked to poorer survival in paediatric brain tumours(276), suggesting pathways that generate Gly are up- regulated in aggressive tumours.

The one-carbon cycle is an established therapeutic target, with many drugs targeting enzymes within the cycle. In terms of paediatric brain tumours, gemcitabine and pemetrexed combination therapy was shown to increase the survival time for mice with cortically implanted Group 3 MB cells(277).

6.4.4 Glutathione metabolism

GSH is the major cellular anti-oxidant responsible for scavenging damaging reactive oxygen species. In the brain, GSH is highest in concentration in glial cells. Cells need to maintain a balance between reactive oxygen species and antioxidants to prevent oxidative damage to cellular components. GSH and its metabolism is able to increase resistance to treatment by repairing or reducing cellular damage caused by radiation and chemotherapy (278). Therefore, agents that target the metabolism of GSH are of interest.

The GSH inhibitor L-S,R-buthionine sulfoximine (BSO) has been administered to children with recurrent neuroblastoma following successful trials in adults for with melanoma, ovarian cancer, breast cancer, and small cell carcinoma of the lung(279). The pilot study showed an 18% response rate, demonstrating the utility of inhibiting GSH synthesis.

6.4.5 Inositol phosphate metabolism

Inositol is a six carbon alcohol sugar with nine possible isomers. mIns is the most common isomer, with sIns the second most common. This metabolic pathway appears to be important for ependymomas, where it was shown that mIns concentration is highest.

One of the main functions of mIns is to form a family of phospholipids, with the inositol moiety forming the head group. G-protein coupled receptors initiate a signalling cascade, resulting in the phosphorylation of the carbons at position 3 and 4 of the inositol head group. Phospholipase C cleaves phosphatidylinositol-4,5-diphosphate to form inositol-1,4,5 triphosphate and diacylglycerol, both of which act as secondary messengers. Inositol-1,4,5 triphosphate initiates calcium ion release from the smooth endoplasmic reticulum into the cytosol whilst diacylglycerol activates protein kinase C.

Phosphatidylinositol is also involved in signalling through the action of phosphoinositide 3 kinase (PI3K). In response to receptor activation, PI3K phosphorylates phosphatidylinositol-4,5-biphosphate to phosphatidylinositol-3,4,5-triphosphate, which in turn localises AKT and PDK to the cell membrane. PDK activates AKT the downstream targets of which promote cellular processes including resistance to apoptosis, proliferation, glucose metabolism and cell motility (280). A study by Rogers et al (281) showed that up-regulated signalling through the PI3K pathway was a negative marker of progression free survival for patients with ependymoma, and that inhibition of the pathway reduced the proliferation of ependymoma cell lines. Several clinical trials have used PI3K pathway inhibitors to block the signalling cascade, including some agents that inhibit the phosphorylation of phosphatidylinositol-4,5-biphosphate (282).

Similar to Tau, mIns also acts as an osmolyte and is lower in concentration in rats suffering from hyponatremia. Upon rapid correction, the concentration of mIns has shown to drop before recovering, although normal concentrations weren't reached by day 7. Slow correction again caused a drop in mIns concentration but concentration recovered to normal by day 7 (275).

6.4.6 Aldarate and ascorbate metabolism

Asc is an essential nutrient in humans, with roles including antioxidation, catecholamine synthesis, collagen production, regulation of HIF1α and acting as a modulator of neurotransmission (283). Indeed, the brain and other neuroendocrine tissue have the highest concentration of Asc in the human body. All functions of Asc require the donation of an electron, generating the Asc free radical. The Asc free radical is reduced back to Asc through the action of NADH and NADPH-dependent reductases, or two Asc free radicals dismutate to one molecule of Asc and one molecule of dehydroascorbic acid. Dehydroascorbic acid is unstable in blood and physiological buffers but can be reduced to ascorbic acid through direct interaction with GSH.

Hyperpolarised ^{13}C dehydroascorbic acid has been used to image the oxidative stress of the brain (284). Dehydroascorbic acid is transported into cells through glucose transporters and is rapidly reduced to ascorbic acid when sufficient reducing power is available in the cell. This reduction is observable as the appearance of a peak representing Asc using *in vivo* ^{13}C MRS. The rate of reduction was shown to correlate with brain GSH content; the imaging protocol was repeated following glutathione depletion using diethyl maleate and a significant decrease in the production of Asc was seen. This imaging technique could allow clinicians to determine the extent of oxidative stress in a tissue to determine the aggressiveness of the disease.

Pharmacological Asc has been suggested as a potential agent to sensitise glioblastoma to both chemotherapy and radiotherapy (285). The study demonstrated improved survival of mice with xenografted glioblastoma cells when treated with Asc, radiation and temozolomide.

6.4.7 Arginine and proline metabolism

The arginine and proline metabolic pathway is relatively understudied. It has been shown in the literature that cells with IDH mutations generate Gln-derived proline to rebalance the redox status of these cells (286). Other work has observed similar effects, with patients with IDH mutations displaying a trend towards having higher concentrations of ornithine, arginine and proline in their plasma (287).

Interestingly, proline oxidase is one of only a handful of potential metabolic tumour suppressor genes, which has been shown to be down regulated in renal cancer through inhibition by miR-23b*(288). Proline oxidase in under the regulatory control of p53, and has been shown to promote apoptosis and inhibit tumour growth in colorectal cancer cells (289). Tumours with MYC amplifications were shown to suppress proline oxidase, but increase the expression of proline synthesising enzymes (290). The significance of this is uncertain.

6.4.8 Glycerophospholipid metabolism

Glycerophospholipid metabolism is primarily responsible for synthesizing components for cellular and organelle membranes. Alteration in Cho metabolism is a hallmark of malignancies

(83). In brain tumours, increased concentration of Cho-containing compounds, as detected by *in vivo* ^{1}H MRS, have been associated with higher grade (291). In addition, ^{31}P MRS has identified alterations in the ratios of phosphorylated Cho metabolites between normal tissue and brain tumours (292). This is supported by *ex vivo* work, where it was shown that PCh concentration correlated with grade, phospholipase C and choline kinase β expression (155). These factors influencing synthesis may explain the observed increase in PCh concentration in MB tissue.

As well as meeting the cell's biosynthetic needs, this pathway is involved in intracellular signalling. The action of phosphatidylcholine-specific phospholipase C generates diacylglycerol and a free PCh head whilst phospholipase D generate a free Cho head group and phosphatidic acid. Phosphatidic acid has been shown to promote anchorage-free proliferation in cell line models (293).

GPC has another function as an osmolyte. Similar to Tau and mIns, GPC is reduced in concentration in the brain of rats suffering from chronic hyponatremia. Upon correction, whether rapid or slow, GPC reaches normal concentrations far quicker than either Tau or mIns, reaching normal levels by day 1 after correction (275).

6.4.9 Gene set enrichment analysis

Metabolism is partly under the influence of gene expression, and so a gene set enrichment analysis was performed to investigate the significance of gene expression with regards to the identified metabolic pathways. Whilst this analysis does support some of the findings, it is known that the relationship between gene expression and metabolite concentration is not linear, and involves several layers of regulation through miRNA expression and protein post-translational modifications.

6.5 Conclusion

In conclusion, this chapter has identified a list of metabolic pathways that are remodelled in the three most common paediatric cerebellar tumours. Pathways were initially identified using HR-MAS, before the same samples were analysed using UPLC-MS, utilising the latter technique's greater sensitivity to improve the metabolome coverage. Many high abundance metabolites displayed strong positive correlations between the two methods, whilst others correlated less strongly. UPLC-MS identified other pathways that may be of clinical use. Interfering with tumour metabolism is a potential avenue for targeted therapies, with some already being used clinically. Spectroscopy can detect important metabolites in these pathways and has promise in identifying which patients could benefit from metabolic therapies.

CHAPTER 7: Conclusions and future work

7.1 Conclusions

This thesis has sought to demonstrate the benefits of tissue metabolite profiles acquired by HR-MAS in the management of paediatric brain tumour patients.

It was shown that metabolite profiles acquired by HR-MAS from resected tissue can be used to construct accurate classifiers for cerebellar brain tumours. Additionally, in a comparison with current rapid intraoperative diagnostic testing, it was shown for the first time that HR-MAS can aid in the diagnosis of histologically ambiguous tumours.

Metabolite profiles acquired by HR-MAS can also identify tumours likely to follow an aggressive course by measuring the concentration of Gln in resected tissue. Gln was shown to be a prognostic marker for overall survival in a mixed cohort of tumours and a positive prognostic marker for progression free survival in cerebellar PA.

Differences in metabolite profiles were used to identify differences in metabolism between the three most common brain tumours which are potentially targetable. These results were supported by both UPLC-MS, which increased the metabolome coverage with its greater sensitivity, and by gene expression data acquired from an independent archived dataset.

The conclusions drawn from this work and future directions include:

1) Metabolite profiles from resected tumour tissue can be used to accurately and robustly classify common brain tumours when combined with machine learning techniques. Gln, hTau and NAA were important for identifying PA, whilst PCh, Tau and Gly were important for MB classification and mIns was the most important metabolite for EP

identification. As *in vivo* MRS improves, especially with higher field strength scanners becoming more widely available and pulse sequences being developed, the markers identified in this work could be translated to in *vivo* MRS. Therefore, metabolites not currently included in basis sets, such as hTau, should be added and the ability to estimate its concentration examined by phantom and volunteer studies.

2) The technical qualities of HR-MAS, fast data acquisition, high quality metabolite profiles and retrieval of tissue after acquisition would make it suitable for development as a rapid intraoperative diagnostic aid. In a comparison with current intraoperative histological diagnosis, HR-MAS was shown to increase diagnostic accuracy of ependymoma by over 20%. Future work will involve incorporating rarer tumour types into the classifier algorithm from other sites in the brain and performing prospective analyses using HR-MAS acquired metabolite profiles.
3) Metabolites, in particular Gln, have prognostic potential which could be assessed at the same time as diagnostic testing. This work was performed on a mixed cohort, which was stratified according to diagnosis. The analysis was validated using an independent testing cohort to ensure the robustness of the defined marker. Whilst diagnosis is the biggest confounder in this analysis, further analysis with added cases should be performed to allow further stratification for treatment received by the patients. This should include both general treatment outcomes, such as extent of surgical resection, but also tumour specific treatment, such as chemotherapy regimens and any radiotherapy given to the patients. The most effective way of achieving this would be to incorporate the technique

into multi-centre clinical trials of treatment which are well established in children's cancer.

4) Gln may predict more aggressive disease in PA, with low Gln predicting a higher risk of progression. This supports the above finding of high Gln as a predictor of better overall survival. Cohort expansion is required to account for confounding variables, size of residual tumour being the obvious variable. Furthermore, the effect of the different BRAF:KIAA1549 fusions, as well as rarer fusion genes (QKI/NACC2:NTRK, SRGAP3:RAF1) and point mutations needs to be taken into account. Incorporation of PA from other anatomical regions of the brain would improve the ability to predict progression free survival for these tumours, although these tumours can be treated differently to cerebellar PA if they are in a surgically inaccessible location.
5) It was proposed in chapter 5 that there are two potential metabolic subgroups of cerebellar PA. The metabolite profiles of these tumours implies altered metabolism of branched chain amino acids alongside other differences. Further elucidation of these potential subgroups is required, and any prognostic or therapeutic potential examined by increasing the sample size.
6) Tissue metabolite profiles acquired by HR-MAS can identify differences in how tumours use their biochemical resources, and this could be used to identify novel metabolic therapeutic targets. These results are supported by both UPLC-MS on post HR-MAS tissue and genetic pathway analysis on an independent archived dataset. Translation of

these findings into treatments requires development of accurate preclinical models that are representative of the human diseases and well-designed multi-centre trials.

7) In agreement with other published literature, UPLC-MS relative abundances were shown to correlate with high abundance metabolites quantified by HR-MAS. A drawback of UPLC-MS is the difficulty in annotating large datasets; however, the development of advanced statistical methodologies is starting to overcome this limitation. Combining the methodologies may help with identification of unknown features from either technique.

There are some limitations that should be considered. Brain tumours are rare and it is difficult to build large cohorts for analysis. As such, the retrospective classification study presented in chapter 3 focuses primarily on the three most common tumour types. A lack of tissue from other rarer diagnoses prevents construction of comprehensive classifiers. This lack of tissue for less common brain tumours also affects survival analysis, as it reduces the power of survival analyses to account for the effect of diagnosis on survival. To compound the issue, prognostic tumour subgroups, such as the four medulloblastoma subgroups, are being identified using large international cohorts. HR-MAS is limited in its sensitivity, allowing quantification of a relatively low number of metabolites. An untargeted mass spectrometry analysis was performed to compensate for the low sensitivity which detected many thousands of features; however, the inability to confidently assign single metabolite assignments to these features hampers the ability to draw biological conclusions.

There are challenges that need to be overcome for adoption of HR-MAS into routine clinical use.

Firstly, spectrometers utilising electromagnets to achieve high field strengths similar to those used in this thesis are physically large and require cryogenic gases to function. If adopted, pathology departments will have to arrange space for a spectrometer and its maintenance or have access to an institute in very close proximity with a spectrometer. Desktop spectrometers are manufactured using relatively low field strengths generated by permanent magnets; but whether they allow adequate analysis of tissue samples or if there is a drive to develop HR-MAS probes for these spectrometers is uncertain.

Secondly, optimal pulse sequence parameters will need to be developed, validated and standardised to allow routine clinical use.

Thirdly, a large repository of cases is required against which clinical cases can be assessed. Multicentre databases have been created to store spectroscopic data; INTERPRET gathered in vivo spectroscopic data and developed a decision support system, whilst its successor eTUMOUR gathered ex vivo spectroscopy alongside in vivo MRS and genetic data. Such repositories will be essential to further the study of rare diseases such as paediatric brain tumours.

Finally, pathologists will need to be trained in interpreting metabolite data. A similar process is underway with *in vivo* MRS, with radiologists being trained to interpret spectroscopic data to aid in diagnosis of tumours and monitoring disease.

Whilst there are a number of challenges facing the adoption of HR-MAS, there is a wealth of evidence demonstrating its ability to aid in patient care, some of which has been presented in this thesis. Furthermore, it provides a direct link between pathological and radiological examination, as translation of *ex vivo* HR-MAS to *in vivo* MRS is a scenario not possible with other metabolic platforms.

With all the results considered, these works provide strong evidence supporting the inclusion of tissue metabolite profiles in the clinical workflow for paediatric brain tumours. Through more accurate rapid diagnosis, identification of tumours displaying aggressive metabolic profiles and the development of novel treatments targeted at identified pathways, survival of children with brain tumours could be significantly improved.

8.0 References

1. Wolfe I, Donkin A, Marmot M, Macfarlane A, Cass H, Viner R. UK child survival in a European context: recommendations for a national Countdown Collaboration. Archives of disease in childhood. 2015;100(10):907-14.

2. Hanahan D, Weinberg RA. Hallmarks of cancer: the next generation. Cell. 2011;144(5):646-74.

3. Wilson M, Davies NP, Brundler M-A, McConville C, Grundy RG, Peet AC. High resolution magic angle spinning 1H NMR of childhood brain and nervous system tumours. Molecular Cancer. 2009;8:6-.

4. Wilson M, Cummins CL, Macpherson L, Sun Y, Natarajan K, Grundy RG, et al. Magnetic resonance spectroscopy metabolite profiles predict survival in paediatric brain tumours. European journal of cancer. 2013;49(2):457-64.

5. Davies NP, Wilson M, Harris LM, Natarajan K, Lateef S, Macpherson L, et al. Identification and characterisation of childhood cerebellar tumours by in vivo proton MRS. NMR in biomedicine. 2008;21(8):908-18.

6. Wilson M, Davies NP, Grundy RG, Peet AC. A quantitative comparison of metabolite signals as detected by in vivo MRS with ex vivo 1H HR-MAS for childhood brain tumours. NMR in biomedicine. 2009;22(2):213-9.

7. Cuellar-Baena S, Morales JM, Martinetto H, Calvar J, Sevlever G, Castellano G, et al. Comparative metabolic profiling of paediatric ependymoma, medulloblastoma and pilocytic astrocytoma. International journal of molecular medicine. 2010;26(6):941-8.

8. Madhu B, Jauhiainen A, McGuire S, Griffiths JR. Exploration of human brain tumour metabolism using pairwise metabolite-metabolite correlation analysis (MMCA) of HR-MAS 1H NMR spectra. PloS one. 2017;12(10):e0185980.

9. Ostrom QT, de Blank PM, Kruchko C, Petersen CM, Liao P, Finlay JL, et al. Alex's Lemonade Stand Foundation Infant and Childhood Primary Brain and Central Nervous System Tumors Diagnosed in the United States in 2007–2011. Neuro Oncol. 2015;16(Suppl 10):x1-x36.

10. Bleeker FE, Hopman SM, Merks JH, Aalfs CM, Hennekam RC. Brain tumors and syndromes in children. Neuropediatrics. 2014;45(3):137-61.

11. Grobner SN, Worst BC, Weischenfeldt J, Buchhalter I, Kleinheinz K, Rudneva VA, et al. The landscape of genomic alterations across childhood cancers. Nature. 2018;555(7696):321-7.

12. Johnson KJ, Cullen J, Barnholtz-Sloan JS, Ostrom QT, Langer CE, Turner MC, et al. Childhood Brain Tumor Epidemiology: A Brain Tumor Epidemiology Consortium Review. Cancer epidemiology, biomarkers & prevention. 2014;23(12):2716-36.

13. Cancer Research UK [Available from: http://www.cancerresearchuk.org/health-professional/cancer-statistics/childrens-cancers.

14. PDQ Pediatric Treatment Editorial Board. Childhood Central Nervous System Atypical Teratoid/Rhabdoid Tumor Treatment (PDQ®): Patient Version. In: (US) BMNCI, editor. 2008.

15. Louis DN, Perry A, Reifenberger G, von Deimling A, Figarella-Branger D, Cavenee WK, et al. The 2016 World Health Organization Classification of Tumors of the Central Nervous System: a summary. Acta neuropathologica. 2016;131(6):803-20.

16. Rodriguez FJ, Scheithauer BW, Burger PC, Jenkins S, Giannini C. Anaplasia in pilocytic astrocytoma predicts aggressive behavior. The American journal of surgical pathology. 2010;34(2):147-60.

17. Rodriguez FJ, Perry A, Gutmann DH, Neill BP, Leonard J, Bryant S, et al. Gliomas in Neurofibromatosis Type 1: A Clinicopathologic Study of 100 Patients. Journal of Neuropathology & Experimental Neurology. 2008;67(3):240.

18. Listernick R, Charrow J, Greenwald M, Mets M. Natural history of optic pathway tumors in children with neurofibromatosis type 1: a longitudinal study. The Journal of pediatrics. 1994;125(1):63-6.

19. Jones DT, Kocialkowski S, Liu L, Pearson DM, Backlund LM, Ichimura K, et al. Tandem duplication producing a novel oncogenic BRAF fusion gene defines the majority of pilocytic astrocytomas. Cancer research. 2008;68(21):8673-7.

20. Zhang J, Wu G, Miller CP, Tatevossian RG, Dalton JD, Tang B, et al. Whole-genome sequencing identifies genetic alterations in pediatric low-grade gliomas. Nature genetics. 2013;45(6):602-12.

21. Collins VP, Jones DT, Giannini C. Pilocytic astrocytoma: pathology, molecular mechanisms and markers. Acta neuropathologica. 2015;129(6):775-88.

22. Janzarik WG, Kratz CP, Loges NT, Olbrich H, Klein C, Schäfer T, et al. Further Evidence for a Somatic KRAS Mutation in a Pilocytic Astrocytoma. Neuropediatrics. 2007;38(02):61-3.

23. Jones DT, Hutter B, Jager N, Korshunov A, Kool M, Warnatz HJ, et al. Recurrent somatic alterations of FGFR1 and NTRK2 in pilocytic astrocytoma. Nature genetics. 2013;45(8):927-32.

24. Jones DTW, Kocialkowski S, Liu L, Pearson DM, Ichimura K, Collins VP. Oncogenic RAF1 rearrangement and a novel BRAF mutation as alternatives to KIAA1549:BRAF fusion in activating the MAPK pathway in pilocytic astrocytoma. Oncogene. 2009;28(20):2119-23.

25. Packer RJ, Pfister S, Bouffet E, Avery R, Bandopadhayay P, Bornhorst M, et al. Pediatric low-grade gliomas: implications of the biologic era. Neuro Oncol. 2017;19(6):750-61.

26. Jones C, Karajannis MA, Jones DTW, Kieran MW, Monje M, Baker SJ, et al. Pediatric high-grade glioma: biologically and clinically in need of new thinking. Neuro-Oncology. 2017;19(2):153-61.

27. Seidel C, von Bueren AO, Bojko S, Hoffmann M, Pietsch T, Gielen GH, et al. Concurrent radiotherapy with temozolomide vs. concurrent radiotherapy with a cisplatinum-based polychemotherapy regimen. Strahlentherapie und Onkologie. 2018;194(3):215-24.

28. Xu W, Yang H, Liu Y, Yang Y, Wang P, Kim S-H, et al. Oncometabolite 2-hydroxyglutarate is a competitive inhibitor of α-ketoglutarate-dependent dioxygenases. Cancer cell. 2011;19(1):17-30.

29. Mörén L, Perryman R, Crook T, Langer JK, Oneill K, Syed N, et al. Metabolomic profiling identifies distinct phenotypes for ASS1 positive and negative GBM. BMC cancer. 2018;18(1):167-.

30. Syed N, Langer J, Janczar K, Singh P, Lo Nigro C, Lattanzio L, et al. Epigenetic status of argininosuccinate synthetase and argininosuccinate lyase modulates autophagy and cell death in glioblastoma. Cell death & disease. 2013;4(1):e458-e.

31. Marjon K, Cameron MJ, Quang P, Clasquin MF, Mandley E, Kunii K, et al. MTAP Deletions in Cancer Create Vulnerability to Targeting of the MAT2A/PRMT5/RIOK1 Axis. Cell reports. 2016;15(3):574-87.

32. Avila MaA, García-Trevijano ER, Lu SC, Corrales FJ, Mato JM. Methylthioadenosine. The International Journal of Biochemistry & Cell Biology. 2004;36(11):2125-30.

33. Kryukov GV, Wilson FH, Ruth JR, Paulk J, Tsherniak A, Marlow SE, et al. MTAP deletion confers enhanced dependency on the PRMT5 arginine methyltransferase in cancer cells. Science. 2016;351(6278):1214-8.

34. McGuire CS, Sainani KL, Fisher PG. Both location and age predict survival in ependymoma: a SEER study. Pediatric blood & cancer. 2009;52(1):65-9.

35. Kilday J-P, Rahman R, Dyer S, Ridley L, Lowe J, Coyle B, et al. Pediatric Ependymoma: Biological Perspectives. Molecular Cancer Research. 2009;7(6):765-86.

36. Pajtler KW, Witt H, Sill M, Jones DTW, Hovestadt V, Kratochwil F, et al. Molecular Classification of Ependymal Tumors across All CNS Compartments, Histopathological Grades, and Age Groups. Cancer cell. 2015;27(5):728-43.

37. Pajtler KW, Mack SC, Ramaswamy V, Smith CA, Witt H, Smith A, et al. The current consensus on the clinical management of intracranial ependymoma and its distinct molecular variants. Acta neuropathologica. 2017;133(1):5-12.

38. Rickert CH, Paulus W. Epidemiology of central nervous system tumors in childhood and adolescence based on the new WHO classification. Child's nervous system : ChNS : official journal of the International Society for Pediatric Neurosurgery. 2001;17(9):503-11.

39. Taylor MD, Northcott PA, Korshunov A, Remke M, Cho YJ, Clifford SC, et al. Molecular subgroups of medulloblastoma: the current consensus. Acta neuropathologica. 2012;123(4):465-72.

40. Ellison DW, Dalton J, Kocak M, Nicholson SL, Fraga C, Neale G, et al. Medulloblastoma: clinicopathological correlates of SHH, WNT, and non-SHH/WNT molecular subgroups. Acta neuropathologica. 2011;121(3):381-96.

41. Ellison DW, Kocak M, Dalton J, Megahed H, Lusher ME, Ryan SL, et al. Definition of disease-risk stratification groups in childhood medulloblastoma using combined clinical, pathologic, and molecular variables. Journal of clinical oncology. 2011;29(11):1400-7.

42. Ellison DW, Onilude OE, Lindsey JC, Lusher ME, Weston CL, Taylor RE, et al. beta-Catenin status predicts a favorable outcome in childhood medulloblastoma: the United Kingdom Children's Cancer Study Group Brain Tumour Committee. Journal of clinical oncology. 2005;23(31):7951-7.

43. Kool M, Korshunov A, Remke M, Jones DTW, Schlanstein M, Northcott PA, et al. Molecular subgroups of medulloblastoma: an international meta-analysis of transcriptome, genetic aberrations, and clinical data of WNT, SHH, Group 3, and Group 4 medulloblastomas. Acta neuropathologica. 2012;123(4):473-84.

44. Zhukova N, Ramaswamy V, Remke M, Pfaff E, Shih DJ, Martin DC, et al. Subgroup-specific prognostic implications of TP53 mutation in medulloblastoma. Journal of clinical oncology. 2013;31(23):2927-35.

45. Robinson GW, Rudneva VA, Buchhalter I, Billups CA, Waszak SM, Smith KS, et al. Risk-adapted therapy for young children with medulloblastoma (SJYC07): therapeutic and molecular outcomes from a multicentre, phase 2 trial. The Lancet Oncology. 2018;19(6):768-84.

46. Camara-Costa H, Resch A, Kieffer V, Lalande C, Poggi G, Kennedy C, et al. Neuropsychological Outcome of Children Treated for Standard Risk Medulloblastoma in the PNET4 European Randomized Controlled Trial of Hyperfractionated Versus Standard Radiation Therapy and Maintenance Chemotherapy. International journal of radiation oncology, biology, physics. 2015;92(5):978-85.

47. Ottensmeier H, Zimolong B, Wolff JE, Ehrich J, Galley N, von Hoff K, et al. Neuropsychological short assessment of disease- and treatment-related intelligence deficits in children with brain tumours. European journal of paediatric neurology. 2015;19(3):298-307.

48. Bartelheim K, Nemes K, Seeringer A, Kerl K, Buechner J, Boos J, et al. Improved 6-year overall survival in AT/RT – results of the registry study Rhabdoid 2007. Cancer Medicine. 2016;5(8):1765-75.

49. Parwani AV, Stelow EB, Pambuccian SE, Burger PC, Ali SZ. Atypical teratoid/rhabdoid tumor of the brain. Cancer Cytopathology. 2005;105(2):65-70.

50. Biegel JA, Zhou JY, Rorke LB, Stenstrom C, Wainwright LM, Fogelgren B. Germ-line and acquired mutations of INI1 in atypical teratoid and rhabdoid tumors. Cancer research. 1999;59(1):74-9.

51. Buscariollo DL, Park HS, Roberts KB, Yu JB. Survival outcomes in atypical teratoid rhabdoid tumor for patients undergoing radiotherapy in a Surveillance, Epidemiology, and End Results analysis. Cancer. 2011;118(17):4212-9.

52. Johann PD, Erkek S, Zapatka M, Kerl K, Buchhalter I, Hovestadt V, et al. Atypical Teratoid/Rhabdoid Tumors Are Comprised of Three Epigenetic Subgroups with Distinct Enhancer Landscapes. Cancer cell. 2016;29(3):379-93.

53. Ostrom QT, Gittleman H, Liao P, Vecchione-Koval T, Wolinsky Y, Kruchko C, et al. CBTRUS Statistical Report: Primary brain and other central nervous system tumors diagnosed in the United States in 2010–2014. Neuro Oncol. 2017;19(suppl_5):v1-v88.

54. Nicholson HS, Kretschmar CS, Krailo M, Bernstein M, Kadota R, Fort D, et al. Phase 2 study of temozolomide in children and adolescents with recurrent central nervous system tumors: a report from the Children's Oncology Group. Cancer. 2007;110(7):1542-50.

55. Wilne SH, Dineen RA, Dommett RM, Chu TP, Walker DA. Identifying brain tumours in children and young adults. BMJ (Clinical research ed). 2013;347:f5844.

56. Somerset HL, Kleinschmidt-DeMasters BK. Approach to the intraoperative consultation for neurosurgical specimens. Advances in anatomic pathology. 2011;18(6):446-9.

57. Ansorge O. The neuropathological approach to the diagnosis of brain tumours. Diagnostic Histopathology. 2011;17(11):465-75.

58. Adesina AM. Frozen Section Diagnosis of Pediatric Brain Tumors. Surgical pathology clinics. 2010;3(3):769-96.

59. Roessler K, Dietrich W Fau - Kitz K, Kitz K. High diagnostic accuracy of cytologic smears of central nervous system tumors. A 15-year experience based on 4,172 patients. Acta Cytol. 2002;46(0001-5547 (Print)):667-74.

60. Goel D, Sundaram C Fau - Paul TR, Paul Tr Fau - Uppin SG, Uppin Sg Fau - Prayaga AK, Prayaga Ak Fau - Panigrahi MK, Panigrahi Mk Fau - Purohit AK, et al. Intraoperative cytology (squash smear) in

neurosurgical practice - pitfalls in diagnosis experience based on 3057 samples from a single institution. Cytopathology. 2007;18(0956-5507 (Print)):300-8.

61. Krishnani N, Kumari N Fau - Behari S, Behari S Fau - Rana C, Rana C Fau - Gupta P, Gupta P. Intraoperative squash cytology: accuracy and impact on immediate surgical management of central nervous system tumours. Cytopathology. 2012(1365-2303).

62. Rausch T, Jones DT, Zapatka M, Stutz AM, Zichner T, Weischenfeldt J, et al. Genome sequencing of pediatric medulloblastoma links catastrophic DNA rearrangements with TP53 mutations. Cell. 2012;148(1-2):59-71.

63. Schwartzentruber J, Korshunov A, Liu XY, Jones DT, Pfaff E, Jacob K, et al. Driver mutations in histone H3.3 and chromatin remodelling genes in paediatric glioblastoma. Nature. 2012;482(7384):226-31.

64. Parker M, Mohankumar KM, Punchihewa C, Weinlich R, Dalton JD, Li Y, et al. C11orf95-RELA fusions drive oncogenic NF-kappaB signalling in ependymoma. Nature. 2014;506(7489):451-5.

65. Sturm D, Orr Brent A, Toprak Umut H, Hovestadt V, Jones David TW, Capper D, et al. New Brain Tumor Entities Emerge from Molecular Classification of CNS-PNETs. Cell. 2016;164(5):1060-72.

66. Capper D, Jones DTW, Sill M, Hovestadt V, Schrimpf D, Sturm D, et al. DNA methylation-based classification of central nervous system tumours. Nature. 2018;555(7697):469-74.

67. Archer TC, Ehrenberger T, Mundt F, Gold MP, Krug K, Mah CK, et al. Proteomics, Post-translational Modifications, and Integrative Analyses Reveal Molecular Heterogeneity within Medulloblastoma Subgroups. Cancer cell. 2018;34(3):396-410.e8.

68. Morrish F, Isern N, Sadilek M, Jeffrey M, Hockenbery DM. c-Myc activates multiple metabolic networks to generate substrates for cell-cycle entry. Oncogene. 2009;28(27):2485-91.

69. Koufaris C, Valbuena GN, Pomyen Y, Tredwell GD, Nevedomskaya E, Lau CH, et al. Systematic integration of molecular profiles identifies miR-22 as a regulator of lipid and folate metabolism in breast cancer cells. Oncogene. 2015;35:2766.

70. Hall Z, Ament Z, Wilson CH, Burkhart DL, Ashmore T, Koulman A, et al. Myc Expression Drives Aberrant Lipid Metabolism in Lung Cancer. Cancer research. 2016;76(16):4608-18.

71. Huppi PS, Posse S, Lazeyras F, Burri R, Bossi E, Herschkowitz N. Magnetic resonance in preterm and term newborns: 1H-spectroscopy in developing human brain. Pediatr Res. 1991;30(6):574-8.

72. Kreis R, Ernst T, Ross BD. Development of the human brain: in vivo quantification of metabolite and water content with proton magnetic resonance spectroscopy. Magnetic resonance in medicine. 1993;30(4):424-37.

73. Pouwels PJW, Brockmann K, Kruse B, Wilken B, Wick M, Hanefeld F, et al. Regional Age Dependence of Human Brain Metabolites from Infancy to Adulthood as Detected by Quantitative Localized Proton MRS. Pediatric Research. 1999;46:474.

74. Darmanis S, Sloan SA, Zhang Y, Enge M, Caneda C, Shuer LM, et al. A survey of human brain transcriptome diversity at the single cell level. Proceedings of the National Academy of Sciences of the United States of America. 2015;112(23):7285-90.

75. Herrero-Mendez A, Almeida A, Fernández E, Maestre C, Moncada S, Bolaños JP. The bioenergetic and antioxidant status of neurons is controlled by continuous degradation of a key glycolytic enzyme by APC/C–Cdh1. Nature cell biology. 2009;11:747.

76. Barros LF, Courjaret R, Jakoby P, Loaiza A, Lohr C, Deitmer JW. Preferential transport and metabolism of glucose in Bergmann glia over Purkinje cells: A multiphoton study of cerebellar slices. Glia. 2009;57(9):962-70.

77. Pellerin L, Magistretti PJ. Glutamate uptake into astrocytes stimulates aerobic glycolysis: a mechanism coupling neuronal activity to glucose utilization. Proceedings of the National Academy of Sciences. 1994;91(22):10625.

78. Itoh Y, Esaki T, Shimoji K, Cook M, Law MJ, Kaufman E, et al. Dichloroacetate effects on glucose and lactate oxidation by neurons and astroglia in vitro and on glucose utilization by brain in vivo. Proceedings of the National Academy of Sciences. 2003;100(8):4879.

79. Erecińska M, Silver IA. Metabolism and role of glutamate in mammalian brain. Progress in Neurobiology. 1990;35(4):245-96.

80. Nicholls DG. The glutamatergic nerve terminal. European journal of biochemistry / FEBS. 1993;212(3):613-31.

81. Rowley NM, Madsen KK, Schousboe A, Steve White H. Glutamate and GABA synthesis, release, transport and metabolism as targets for seizure control. Neurochemistry International. 2012;61(4):546-58.

82. Warburg O. On the origin of cancer cells. Science. 1956;123(3191):309-14.

83. Glunde K, Bhujwalla ZM, Ronen SM. Choline metabolism in malignant transformation. Nature reviews Cancer. 2011;11(12):835-48.

84. Tonjes M, Barbus S, Park YJ, Wang W, Schlotter M, Lindroth AM, et al. BCAT1 promotes cell proliferation through amino acid catabolism in gliomas carrying wild-type IDH1. Nature medicine. 2013;19(7):901-8.

85. Marquez J, Alonso FJ, Mates JM, Segura JA, Martin-Rufian M, Campos-Sandoval JA. Glutamine Addiction In Gliomas. Neurochemical research. 2017;42(6):1735-46.

86. Amelio I, Cutruzzolá F, Antonov A, Agostini M, Melino G. Serine and glycine metabolism in cancer. Trends in Biochemical Sciences. 2014;39(4):191-8.

87. Locasale JW. Serine, glycine and the one-carbon cycle: cancer metabolism in full circle. Nature reviews Cancer. 2013;13(8):572-83.

88. Gault CR, Obeid LM, Hannun YA. An overview of sphingolipid metabolism: from synthesis to breakdown. Advances in experimental medicine and biology. 2010;688:1-23.

89. Glade MJ, Smith K. Phosphatidylserine and the human brain. Nutrition. 2015;31(6):781-6.

90. Martin DD, Robbins ME, Spector AA, Wen BC, Hussey DH. The fatty acid composition of human gliomas differs from that found in nonmalignant brain tissue. Lipids. 1996;31(12):1283-8.

91. Guo D, Prins RM, Dang J, Kuga D, Iwanami A, Soto H, et al. EGFR signaling through an Akt-SREBP-1-dependent, rapamycin-resistant pathway sensitizes glioblastomas to antilipogenic therapy. Science signaling. 2009;2(101):ra82-ra.

92. Guo D, Hildebrandt IJ, Prins RM, Soto H, Mazzotta MM, Dang J, et al. The AMPK agonist AICAR inhibits the growth of EGFRvIII-expressing glioblastomas by inhibiting lipogenesis. Proceedings of the National Academy of Sciences of the United States of America. 2009;106(31):12932-7.

93. McKay RT. How the 1D-NOESY suppresses solvent signal in metabonomics NMR spectroscopy: An examination of the pulse sequence components and evolution. Concepts in Magnetic Resonance Part A. 2011;38A(5):197-220.

94. Zheng G, Price WS. Solvent signal suppression in NMR. Progress in Nuclear Magnetic Resonance Spectroscopy. 2010;56(3):267-88.

95. Opstad KS, Bell BA, Griffiths JR, Howe FA. An investigation of human brain tumour lipids by high-resolution magic angle spinning 1H MRS and histological analysis. NMR in biomedicine. 2008;21(7):677-85.

96. Astrakas LG, Zurakowski D, Tzika AA, Zarifi MK, Anthony DC, De Girolami U, et al. Noninvasive magnetic resonance spectroscopic imaging biomarkers to predict the clinical grade of pediatric brain tumors. Clinical cancer research. 2004;10(24):8220-8.

97. Felig P. The glucose-alanine cycle. Metabolism: clinical and experimental. 1973;22(2):179-207.

98. Wilson M, Gill SK, MacPherson L, English M, Arvanitis TN, Peet AC. Noninvasive detection of glutamate predicts survival in pediatric medulloblastoma. Clinical cancer research. 2014;20(17):4532-9.

99. Imperiale A, Moussallieh F-M, Roche P, Battini S, Cicek AE, Sebag F, et al. Metabolome Profiling by HRMAS NMR Spectroscopy of Pheochromocytomas and Paragangliomas Detects SDH Deficiency: Clinical and Pathophysiological Implications. Neoplasia. 2015;17(1):55-65.

100. Gao P, Yang C, Nesvick CL, Feldman MJ, Sizdahkhani S, Liu H, et al. Hypotaurine evokes a malignant phenotype in glioma through aberrant hypoxic signaling. Oncotarget. 2016;7(12):15200-14.

101. Moffett JR, Ross B, Arun P, Madhavarao CN, Namboodiri AMA. N-Acetylaspartate in the CNS: from neurodiagnostics to neurobiology. Progress in neurobiology. 2007;81(2):89-131.

102. Chen G, Nan C, Tian J, Jean-Charles P, Li Y, Weissbach H, et al. Protective effects of taurine against oxidative stress in the heart of MsrA knockout mice. Journal of cellular biochemistry. 2012;113(11):3559-66.

103. Huxtable RJ. Physiological actions of taurine. Physiological reviews. 1992;72(1):101-63.

104. Hernandez-Benitez R, Pasantes-Morales H, Saldana IT, Ramos-Mandujano G. Taurine stimulates proliferation of mice embryonic cultured neural progenitor cells. Journal of neuroscience research. 2010;88(8):1673-81.

105. Hernandez-Benitez R, Ramos-Mandujano G, Pasantes-Morales H. Taurine stimulates proliferation and promotes neurogenesis of mouse adult cultured neural stem/progenitor cells. Stem cell research. 2012;9(1):24-34.

106. Maar T, Moran J, Schousboe A, Pasantes-Morales H. Taurine deficiency in dissociated mouse cerebellar cultures affects neuronal migration. International journal of developmental neuroscience : the official journal of the International Society for Developmental Neuroscience. 1995;13(5):491-502.

107. Sturman JA, Moretz RC, French JH, Wisniewski HM. Taurine deficiency in the developing cat: persistence of the cerebellar external granule cell layer. Journal of neuroscience research. 1985;13(3):405-16.

108. Panigrahy A, Krieger MD, Gonzalez-Gomez I, Liu X, McComb JG, Finlay JL, et al. Quantitative short echo time 1H-MR spectroscopy of untreated pediatric brain tumors: preoperative diagnosis and characterization. AJNR American journal of neuroradiology. 2006;27(3):560-72.

109. Castillo M, Smith JK, Kwock L. Correlation of Myo-inositol Levels and Grading of Cerebral Astrocytomas. American Journal of Neuroradiology. 2000;21(9):1645-9.

110. Michaelis T, Helms G, Merboldt KD, Hanicke W, Bruhn H, Frahm J. Identification of Scyllo-inositol in proton NMR spectra of human brain in vivo. NMR in biomedicine. 1993;6(1):105-9.

111. Kaiser LG, Schuff N, Cashdollar N, Weiner MW. Scyllo-inositol in normal aging human brain: 1H magnetic resonance spectroscopy study at 4 Tesla. NMR in biomedicine. 2005;18(1):51-5.

112. Hipps PP, Holland WH, Sherman WR. Interconversion of myo- and scyllo-inositol with simultaneous formation of neo-inositol by an NADP+ dependent epimerase from bovine brain. Biochemical and Biophysical Research Communications. 1977;77(1):340-6.

113. Nozadze M, Mikautadze E, Lepsveridze E, Mikeladze E, Kuchiashvili N, Kiguradze T, et al. Anticonvulsant activities of myo-inositol and scyllo-inositol on pentylenetetrazol induced seizures. Seizure. 2011;20(2):173-6.

114. McLaurin J, Golomb R, Jurewicz A, Antel JP, Fraser PE. Inositol stereoisomers stabilize an oligomeric aggregate of Alzheimer amyloid beta peptide and inhibit abeta -induced toxicity. The Journal of biological chemistry. 2000;275(24):18495-502.

115. Opstad KS, Bell BA, Griffiths JR, Howe FA. An assessment of the effects of sample ischaemia and spinning time on the metabolic profile of brain tumour biopsy specimens as determined by high-resolution magic angle spinning (1)H NMR. NMR in biomedicine. 2008;21(10):1138-47.

116. Jordan KW, He W, Halpern EF, Wu CL, Cheng LL. Evaluation of Tissue Metabolites with High Resolution Magic Angle Spinning MR Spectroscopy Human Prostate Samples After Three-Year Storage at -80 degrees C. Biomarker Insights. 2007;2:147-54.

117. Wu CL, Taylor JL, He W, Zepeda AG, Halpern EF, Bielecki A, et al. Proton high-resolution magic angle spinning NMR analysis of fresh and previously frozen tissue of human prostate. Magnetic resonance in medicine. 2003;50(6):1307-11.

118. Harris LM, Davies N, MacPherson L, Foster K, Lateef S, Natarajan K, et al. The use of short-echo-time 1H MRS for childhood cerebellar tumours prior to histopathological diagnosis. Pediatric Radiology. 2007;37(11):1101-9.

119. Harris LM, Davies NP, Wilson S, MacPherson L, Natarajan K, English MW, et al. Short echo time single voxel 1H magnetic resonance spectroscopy in the diagnosis and characterisation of pineal tumours in children. Pediatric blood & cancer. 2011;57(6):972-7.

120. Vicente J, Fuster-Garcia E, Tortajada S, Garcia-Gomez JM, Davies N, Natarajan K, et al. Accurate classification of childhood brain tumours by in vivo (1)H MRS - a multi-centre study. European journal of cancer. 2013;49(3):658-67.

121. Julia-Sape M, Coronel I, Majos C, Candiota AP, Serrallonga M, Cos M, et al. Prospective diagnostic performance evaluation of single-voxel 1H MRS for typing and grading of brain tumours. NMR in biomedicine. 2012;25(4):661-73.

122. Davies NP, Wilson M, Natarajan K, Sun Y, MacPherson L, Brundler MA, et al. Non-invasive detection of glycine as a biomarker of malignancy in childhood brain tumours using in-vivo 1H MRS at 1.5 tesla confirmed by ex-vivo high-resolution magic-angle spinning NMR. NMR in biomedicine. 2010;23(1):80-7.

123. Fink JR, Carr RB, Matsusue E, Iyer RS, Rockhill JK, Haynor DR, et al. Comparison of 3 Tesla proton MR spectroscopy, MR perfusion and MR diffusion for distinguishing glioma recurrence from posttreatment effects. Journal of magnetic resonance imaging. 2012;35(1):56-63.

124. Tzika A, Cheng L, Goumnerova L, Madsen J, Zurakowski D, Astrakas L, et al. Biochemical characterization of pediatric brain tumors by using in vivo and ex vivo magnetic resonance spectroscopy. Journal of neurosurgery. 2002;96(6):1023-31.

125. Opstad KS, Wright AJ, Bell BA, Griffiths JR, Howe FA. Correlations between in vivo (1)H MRS and ex vivo (1)H HRMAS metabolite measurements in adult human gliomas. Journal of magnetic resonance imaging. 2010;31(2):289-97.

126. Selnaes KM, Gribbestad IS, Bertilsson H, Wright A, Angelsen A, Heerschap A, et al. Spatially matched in vivo and ex vivo MR metabolic profiles of prostate cancer -- investigation of a correlation with Gleason score. NMR in biomedicine. 2013;26(5):600-6.

127. Agar NY, Golby AJ, Ligon KL, Norton I, Mohan V, Wiseman JM, et al. Development of stereotactic mass spectrometry for brain tumor surgery. Neurosurgery. 2011;68(2):280-89; discussion 90.

128. Eberlin LS, Norton I, Dill AL, Golby AJ, Ligon KL, Santagata S, et al. Classifying Human Brain Tumors by Lipid Imaging with Mass Spectrometry. Cancer research. 2012;72(3):645-54.

129. Zhang J, Rector J, Lin JQ, Young JH, Sans M, Katta N, et al. Nondestructive tissue analysis for ex vivo and in vivo cancer diagnosis using a handheld mass spectrometry system. Sci Transl Med. 2017;9(406).

130. Woolman M, Ferry I, Kuzan-Fischer C M, Wu M, Zou J, Kiyota T, et al. Rapid determination of medulloblastoma subgroup affiliation with mass spectrometry using a handheld picosecond infrared laser desorption probe. Chemical Science. 2017;8(9):6508-19.

131. Rocha CM, Barros AS, Gil AM, Goodfellow BJ, Humpfer E, Spraul M, et al. Metabolic profiling of human lung cancer tissue by 1H high resolution magic angle spinning (HRMAS) NMR spectroscopy. Journal of proteome research. 2010;9(1):319-32.

132. Duarte IF, Rocha CM, Barros AS, Gil AM, Goodfellow BJ, Carreira IM, et al. Can nuclear magnetic resonance (NMR) spectroscopy reveal different metabolic signatures for lung tumours? Virchows Archiv : an international journal of pathology. 2010;457(6):715-25.

133. Swanson MG, Vigneron DB, Tabatabai ZL, Males RG, Schmitt L, Carroll PR, et al. Proton HR-MAS spectroscopy and quantitative pathologic analysis of MRI/3D-MRSI-targeted postsurgical prostate tissues. Magnetic resonance in medicine. 2003;50(5):944-54.

134. Burns MA, He W, Wu CL, Cheng LL. Quantitative pathology in tissue MR spectroscopy based human prostate metabolomics. Technology in cancer research & treatment. 2004;3(6):591-8.

135. Stenman K, Stattin P, Stenlund H, Riklund K, Grobner G, Bergh A. H HRMAS NMR Derived Biomarkers Related to Tumor Grade, Tumor Cell Fraction, and Cell Proliferation in Prostate Tissue Samples. Biomarker Insights. 2011;6:39-47.

136. Jimenez B, Mirnezami R, Kinross J, Cloarec O, Keun HC, Holmes E, et al. 1H HR-MAS NMR spectroscopy of tumor-induced local metabolic "field-effects" enables colorectal cancer staging and prognostication. Journal of proteome research. 2013;12(2):959-68.

137. Mirnezami R, Jimenez B, Li JV, Kinross JM, Veselkov K, Goldin RD, et al. Rapid diagnosis and staging of colorectal cancer via high-resolution magic angle spinning nuclear magnetic resonance (HR-MAS NMR) spectroscopy of intact tissue biopsies. Annals of surgery. 2014;259(6):1138-49.

138. Swanson MG, Zektzer AS, Tabatabai ZL, Simko J, Jarso S, Keshari KR, et al. Quantitative analysis of prostate metabolites using 1H HR-MAS spectroscopy. Magnetic resonance in medicine. 2006;55(6):1257-64.

139. Tessem MB, Swanson MG, Keshari KR, Albers MJ, Joun D, Tabatabai ZL, et al. Evaluation of lactate and alanine as metabolic biomarkers of prostate cancer using 1H HR-MAS spectroscopy of biopsy tissues. Magnetic resonance in medicine. 2008;60(3):510-6.

140. van Asten JJ, Cuijpers V, Hulsbergen-van de Kaa C, Soede-Huijbregts C, Witjes JA, Verhofstad A, et al. High resolution magic angle spinning NMR spectroscopy for metabolic assessment of cancer presence and Gleason score in human prostate needle biopsies. Magma. 2008;21(6):435-42.

141. Elkhaled A, Jalbert LE, Phillips JJ, Yoshihara HAI, Parvataneni R, Srinivasan R, et al. Magnetic Resonance of 2-Hydroxyglutarate in IDH1-Mutated Low-Grade Gliomas. Science translational medicine. 2012;4(116):116ra5-ra5.

142. Cheng LL, Chang IW, Louis DN, Gonzalez RG. Correlation of high-resolution magic angle spinning proton magnetic resonance spectroscopy with histopathology of intact human brain tumor specimens. Cancer research. 1998;58(9):1825-32.

143. Wright A, Fellows GA, Griffiths JR, Wilson M, Bell BA, Howe FA. Ex-vivo HRMAS of adult brain tumours: metabolite quantification and assignment of tumour biomarkers. Molecular Cancer 2010;9:66.

144. Poullet JB, Martinez-Bisbal MC, Valverde D, Monleon D, Celda B, Arus C, et al. Quantification and classification of high-resolution magic angle spinning data for brain tumor diagnosis. Conference

proceedings : Annual International Conference of the IEEE Engineering in Medicine and Biology Society. 2007;2007:5407-10.

145. Andronesi OC, Blekas KD, Mintzopoulos D, Astrakas L, Black PM, Tzika AA. Molecular classification of brain tumor biopsies using solid-state magic angle spinning proton magnetic resonance spectroscopy and robust classifiers. International Journal of Oncology. 2008;33(5):1017-25.

146. Gogiashvili M, Horsch S, Marchan R, Gianmoena K, Cadenas C, Tanner B, et al. Impact of intratumoral heterogeneity of breast cancer tissue on quantitative metabolomics using high-resolution magic angle spinning (1) H NMR spectroscopy. NMR in biomedicine. 2018;31(2).

147. Cheng LL, Anthony DC, Comite AR, Black PM, Tzika AA, Gonzalez RG. Quantification of microheterogeneity in glioblastoma multiforme with ex vivo high-resolution magic-angle spinning (HRMAS) proton magnetic resonance spectroscopy. Neuro Oncol. 2000;2(2):87-95.

148. Zhang VY, Westphalen A, Delos Santos L, Tabatabai ZL, Shinohara K, Vigneron DB, et al. The Role of Metabolic Imaging in Radiation Therapy of Prostate Cancer. NMR in biomedicine. 2014;27(1):10.1002/nbm.3007.

149. Braadland PR, Giskeodegard G, Sandsmark E, Bertilsson H, Euceda LR, Hansen AF, et al. Ex vivo metabolic fingerprinting identifies biomarkers predictive of prostate cancer recurrence following radical prostatectomy. British journal of cancer. 2017;117(11):1656-64.

150. Giskeodegard GF, Bertilsson H, Selnaes KM, Wright AJ, Bathen TF, Viset T, et al. Spermine and citrate as metabolic biomarkers for assessing prostate cancer aggressiveness. PloS one. 2013;8(4):e62375.

151. Pacholczyk-Sienicka B, Fabianska A, Pasz-Walczak G, Kordek R, Jankowski S. Prediction of survival for patients with advanced colorectal cancer using (1) H High-resolution magic angle spinning nuclear MR spectroscopy. Journal of magnetic resonance imaging. 2015;41(6):1669-74.

152. Vandergrift LA, Decelle EA, Kurth J, Wu S, Fuss TL, DeFeo EM, et al. Metabolomic Prediction of Human Prostate Cancer Aggressiveness: Magnetic Resonance Spectroscopy of Histologically Benign Tissue. Scientific reports. 2018;8(1):4997.

153. Dali-Youcef N, Froelich S, Moussallieh FM, Chibbaro S, Noel G, Namer IJ, et al. Gene expression mapping of histone deacetylases and co-factors, and correlation with survival time and 1H-HRMAS metabolomic profile in human gliomas. Scientific reports. 2015;5:9087.

154. Erb G, Elbayed K, Piotto M, Raya J, Neuville A, Mohr M, et al. Toward improved grading of malignancy in oligodendrogliomas using metabolomics. Magnetic resonance in medicine. 2008;59(5):959-65.

155. Righi V, Roda JM, Paz J, Mucci A, Tugnoli V, Rodriguez-Tarduchy G, et al. 1H HR-MAS and genomic analysis of human tumor biopsies discriminate between high and low grade astrocytomas. NMR in biomedicine. 2009;22(6):629-37.

156. Elkhaled A, Jalbert L, Constantin A, Yoshihara HA, Phillips JJ, Molinaro AM, et al. Characterization of metabolites in infiltrating gliomas using ex vivo (1)H high-resolution magic angle spinning spectroscopy. NMR in biomedicine. 2014;27(5):578-93.

157. Duarte IF, Ladeirinha AF, Lamego I, Gil AM, Carvalho L, Carreira IM, et al. Potential markers of cisplatin treatment response unveiled by NMR metabolomics of human lung cells. Molecular pharmaceutics. 2013;10(11):4242-51.

158. van Asten JJ, Vettukattil R, Buckle T, Rottenberg S, van Leeuwen F, Bathen TF, et al. Increased levels of choline metabolites are an early marker of docetaxel treatment response in BRCA1-mutated mouse mammary tumors: an assessment by ex vivo proton magnetic resonance spectroscopy. Journal of translational medicine. 2015;13:114.

159. Madhu B, Shaw GL, Warren AY, Neal DE, Griffiths JR. Response of Degarelix treatment in human prostate cancer monitored by HR-MAS (1)H NMR spectroscopy. Metabolomics. 2016;12:120.

160. Valonen PK, Griffin JL, Lehtimäki KK, Liimatainen T, Nicholson JK, Gröhn OHJ, et al. High-resolution magic-angle-spinning 1H NMR spectroscopy reveals different responses in choline-containing metabolites upon gene therapy-induced programmed cell death in rat brain glioma. NMR in biomedicine. 2005;18(4):252-9.

161. Hansen AF, Sandsmark E, Rye MB, Wright AJ, Bertilsson H, Richardsen E, et al. Presence of TMPRSS2-ERG is associated with alterations of the metabolic profile in human prostate cancer. Oncotarget. 2016;7(27):42071-85.

162. Opstad KS, Bell BA, Griffiths JR, Howe FA. Taurine: a potential marker of apoptosis in gliomas. British journal of cancer. 2009;100(5):789-94.

163. Orphanidou-Vlachou E, Kohe SE, Brundler MA, MacPherson L, Sun Y, Davies N, et al. Metabolite Levels in Paediatric Brain Tumours Correlate with Histological Features. Pathobiology : journal of immunopathology, molecular and cellular biology. 2018.

164. Cheng LL, Wu C-l, Smith MR, Gonzalez RG. Non-destructive quantitation of spermine in human prostate tissue samples using HRMAS 1H NMR spectroscopy at 9.4 T. FEBS Letters. 2001;494(1–2):112-6.

165. Santos CF, Kurhanewicz J, Tabatabai ZL, Simko JP, Keshari KR, Gbegnon A, et al. Metabolic, pathologic, and genetic analysis of prostate tissues: quantitative evaluation of histopathologic and mRNA integrity after HR-MAS spectroscopy. NMR in biomedicine. 2010;23(4):391-8.

166. Akoka S, Barantin L, Trierweiler M. Concentration Measurement by Proton NMR Using the ERETIC Method. Analytical chemistry. 1999;71(13):2554-7.

167. Wider G, Dreier L. Measuring Protein Concentrations by NMR Spectroscopy. Journal of the American Chemical Society. 2006;128(8):2571-6.

168. Cobas C. Applications of the Whittaker smoother in NMR spectroscopy. Magnetic Resonance in Chemistry. 2018;56(12):1140-8.

169. Govindaraju V, Young K, Maudsley AA. Proton NMR chemical shifts and coupling constants for brain metabolites. NMR in biomedicine. 2000;13(3):129-53.

170. Wishart DS, Jewison T, Guo AC, Wilson M, Knox C, Liu Y, et al. HMDB 3.0--The Human Metabolome Database in 2013. Nucleic acids research. 2013;41(Database issue):D801-7.

171. Wu H, Southam AD, Hines A, Viant MR. High-throughput tissue extraction protocol for NMR- and MS-based metabolomics. Analytical biochemistry. 2008;372(2):204-12.

172. Bligh EG, Dyer WJ. A rapid method of total lipid extraction and purification. Canadian journal of biochemistry and physiology. 1959;37(8):911-7.

173. Kessner D, Chambers M, Burke R, Agus D, Mallick P. ProteoWizard: open source software for rapid proteomics tools development. Bioinformatics. 2008;24(21):2534-6.

174. Smith CA, Want EJ, O'Maille G, Abagyan R, Siuzdak G. XCMS: processing mass spectrometry data for metabolite profiling using nonlinear peak alignment, matching, and identification. Analytical chemistry. 2006;78(3):779-87.

175. Brown M, Wedge DC, Goodacre R, Kell DB, Baker PN, Kenny LC, et al. Automated workflows for accurate mass-based putative metabolite. Bioinformatics. 2011;27(8):1108-12.

176. Sumner LW, Amberg A, Barrett D, Beale MH, Beger R, Daykin CA, et al. Proposed minimum reporting standards for chemical analysis Chemical Analysis Working Group (CAWG) Metabolomics Standards Initiative (MSI). Metabolomics. 2007;3(3):211-21.

177. Panigrahy A, Bluml S. Neuroimaging of pediatric brain tumors: from basic to advanced magnetic resonance imaging (MRI). Journal of child neurology. 2009;24(11):1343-65.

178. Mitra S, Kumar M, Sharma V, Mukhopadhyay D. Squash preparation: A reliable diagnostic tool in the intraoperative diagnosis of central nervous system tumors. Journal of cytology / Indian Academy of Cytologists. 2010;27(3):81-5.

179. Chiang JCH, Ellison DW. Molecular pathology of paediatric central nervous system tumours. The Journal of pathology. 2016;241(2):159-72.

180. Bouffet E, Perilongo G, Canete A, Massimino M. Intracranial ependymomas in children: a critical review of prognostic factors and a plea for cooperation. Medical and pediatric oncology. 1998;30(6):319-29; discussion 29-31.

181. Horn B, Heideman R, Geyer R, Pollack I, Packer R, Goldwein J, et al. A multi-institutional retrospective study of intracranial ependymoma in children: identification of risk factors. Journal of pediatric hematology/oncology. 1999;21(3):203-11.

182. Robertson PL, Zeltzer PM, Boyett JM, Rorke LB, Allen JC, Geyer JR, et al. Survival and prognostic factors following radiation therapy and chemotherapy for ependymomas in children: a report of the Children's Cancer Group. Journal of neurosurgery. 1998;88(4):695-703.

183. Tihan T, Zhou T, Holmes E, Burger PC, Ozuysal S, Rushing EJ. The prognostic value of histological grading of posterior fossa ependymomas in children: a Children's Oncology Group study and a review of prognostic factors. Modern pathology. 2008;21(2):165-77.

184. Jaiswal S, Vij M, Jaiswal AK, Behari S. Intraoperative squash cytology of central nervous system lesions: a single center study of 326 cases. Diagnostic cytopathology. 2012;40(2):104-12.

185. Eberhart CG, Kepner JL, Goldthwaite PT, Kun LE, Duffner PK, Friedman HS, et al. Histopathologic grading of medulloblastomas. Cancer. 2002;94(2):552-60.

186. Stenman K, Stattin P, Stenlund H, Riklund K, Gröbner G, Bergh A. (1)H HRMAS NMR Derived Biomarkers Related to Tumor Grade, Tumor Cell Fraction, and Cell Proliferation in Prostate Tissue Samples. Biomarker Insights. 2011;6:39-47.

187. Choi JS, Yoon D, Koo JS, Kim S, Park VY, Kim EK, et al. Magnetic resonance metabolic profiling of estrogen receptor-positive breast cancer: correlation with currently used molecular markers. Oncotarget. 2017;8(38):63405-16.

188. Righi V, Durante C, Cocchi M, Calabrese C, Di Febo G, Lecce F, et al. Discrimination of healthy and neoplastic human colon tissues by ex vivo HR-MAS NMR spectroscopy and chemometric analyses. Journal of proteome research. 2009;8(4):1859-69.

189. Tzika AA, Astrakas L, Cao H, Mintzopoulos D, Andronesi OC, Mindrinos M, et al. Combination of high-resolution magic angle spinning proton magnetic resonance spectroscopy and microscale genomics to type brain tumor biopsies. International journal of molecular medicine. 2007;20(2):199-208.

190. Bruggers CS, Moore K. Magnetic resonance imaging spectroscopy in pediatric atypical teratoid rhabdoid tumors of the brain. Journal of pediatric hematology/oncology. 2014;36(6):e341-5.

191. Chakravadhanula M, Hampton CN, Chodavadia P, Ozols V, Zhou L, Catchpoole D, et al. Wnt pathway in atypical teratoid rhabdoid tumors. Neuro Oncol. 2015;17(4):526-35.

192. Versteege I, Sevenet N, Lange J, Rousseau-Merck MF, Ambros P, Handgretinger R, et al. Truncating mutations of hSNF5/INI1 in aggressive paediatric cancer. Nature. 1998;394(6689):203-6.

193. Zarinabad N, Wilson M, Gill SK, Manias KA, Davies NP, Peet AC. Multiclass imbalance learning: Improving classification of pediatric brain tumors from magnetic resonance spectroscopy. Magnetic resonance in medicine. 2017;77(6):2114-24.

194. Decelle EA, Cheng LL. High-resolution magic angle spinning 1H MRS in prostate cancer. NMR in biomedicine. 2014;27(1):90-9.

195. Sitter B, Lundgren S, Bathen TF, Halgunset J, Fjosne HE, Gribbestad IS. Comparison of HR MAS MR spectroscopic profiles of breast cancer tissue with clinical parameters. NMR in biomedicine. 2006;19(1):30-40.

196. Piotto M, Moussallieh F-M, Neuville A, Bellocq J-P, Elbayed K, Namer IJ. Towards real-time metabolic profiling of a biopsy specimen during a surgical operation by 1H high resolution magic angle spinning nuclear magnetic resonance: a case report. Journal of Medical Case Reports. 2012;6(1):22.

197. Kohe S, Brundler MA, Jenkinson H, Parulekar M, Wilson M, Peet AC, et al. Metabolite profiling in retinoblastoma identifies novel clinicopathological subgroups. British journal of cancer. 2015;113(8):1216-24.

198. Bluml S, Margol AS, Sposto R, Kennedy RJ, Robison NJ, Vali M, et al. Molecular subgroups of medulloblastoma identification using noninvasive magnetic resonance spectroscopy. Neuro Oncol. 2016;18(1):126-31.

199. Roessler K, Dietrich W Fau - Kitz K, Kitz K. High diagnostic accuracy of cytologic smears of central nervous system tumors. A 15-year experience based on 4,172 patients. Acta Cytologica. 2002;46(4):667-74.

200. Wijtenburg SA, Knight-Scott J. Very short echo time improves the precision of glutamate detection at 3T in 1H magnetic resonance spectroscopy. Journal of magnetic resonance imaging. 2011;34(3):645-52.

201. Yang S, Hu J, Kou Z, Yang Y. Spectral simplification for resolved glutamate and glutamine measurement using a standard STEAM sequence with optimized timing parameters at 3, 4, 4.7, 7, and 9.4T. Magnetic resonance in medicine. 2008;59(2):236-44.

202. Choi C, Coupland NJ, Bhardwaj PP, Malykhin N, Gheorghiu D, Allen PS. Measurement of brain glutamate and glutamine by spectrally-selective refocusing at 3 Tesla. Magnetic resonance in medicine. 2006;55(5):997-1005.

203. Mekle R, Mlynarik V, Gambarota G, Hergt M, Krueger G, Gruetter R. MR spectroscopy of the human brain with enhanced signal intensity at ultrashort echo times on a clinical platform at 3T and 7T. Magnetic resonance in medicine. 2009;61(6):1279-85.

204. Combs SE, Rieken S, Wick W, Abdollahi A, von Deimling A, Debus J, et al. Prognostic significance of IDH-1 and MGMT in patients with glioblastoma: One step forward, and one step back? Radiation Oncology. 2011;6:115-9.

205. Rohle D, Popovici-Muller J, Palaskas N, Turcan S, Grommes C, Campos C, et al. An Inhibitor of Mutant IDH1 Delays Growth and Promotes Differentiation of Glioma Cells. Science. 2013;340(6132):626-30.

206. Hutter S, Bolin S, Weishaupt H, Swartling FJ. Modeling and Targeting MYC Genes in Childhood Brain Tumors. Genes. 2017;8(4):107.

207. Griffin JL, Shockcor JP. Metabolic profiles of cancer cells. Nature reviews Cancer. 2004;4(7):551-61.

208. Giskeodegard GF, Lundgren S, Sitter B, Fjosne HE, Postma G, Buydens LM, et al. Lactate and glycine-potential MR biomarkers of prognosis in estrogen receptor-positive breast cancers. NMR in biomedicine. 2012;25(11):1271-9.

209. Imperiale A, Elbayed K, Moussallieh FM, Neuville A, Piotto M, Bellocq JP, et al. Metabolomic pattern of childhood neuroblastoma obtained by (1)H-high-resolution magic angle spinning (HRMAS) NMR spectroscopy. Pediatric blood & cancer. 2011;56(1):24-34.

210. Battini S, Faitot F, Imperiale A, Cicek AE, Heimburger C, Averous G, et al. Metabolomics approaches in pancreatic adenocarcinoma: tumor metabolism profiling predicts clinical outcome of patients. BMC medicine. 2017;15(1):56.

211. Louis DN, Ohgaki H, Wiestler OD, Cavenee WK, Burger PC, Jouvet A, et al. The 2007 WHO Classification of Tumours of the Central Nervous System. Acta neuropathologica. 2007;114(2):97-109.

212. Team RC. R: A Language and Environment for Statistical Computing. R Foundation for Statistical Computing, Vienna, Austria. 2015.

213. Kaiser LG, Schuff N, Cashdollar N, Weiner MW. Age-related glutamate and glutamine concentration changes in normal human brain: (1)H MR spectroscopy study at 4 T. Neurobiology of aging. 2005;26(5):665-72.

214. Hurd R, Sailasuta N, Srinivasan R, Vigneron DB, Pelletier D, Nelson SJ. Measurement of brain glutamate using TE-averaged PRESS at 3T. Magnetic resonance in medicine. 2004;51(3):435-40.

215. Schubert F, Gallinat J, Seifert F, Rinneberg H. Glutamate concentrations in human brain using single voxel proton magnetic resonance spectroscopy at 3 Tesla. NeuroImage. 2004;21(4):1762-71.

216. Mullins PG, Chen H, Xu J, Caprihan A, Gasparovic C. Comparative reliability of proton spectroscopy techniques designed to improve detection of J-coupled metabolites. Magnetic resonance in medicine. 2008;60(4):964-9.

217. Ramadan S, Lin A, Stanwell P. Glutamate and Glutamine: A Review of In Vivo MRS in the Human Brain. NMR in biomedicine. 2013;26(12):10.1002/nbm.3045.

218. Akoka S, Giraudeau P. Fast hybrid multi-dimensional NMR methods based on ultrafast 2D NMR. Magnetic resonance in chemistry. 2015;53(11):986-94.

219. DeBerardinis RJ, Lum JJ, Hatzivassiliou G, Thompson CB. The Biology of Cancer: Metabolic Reprogramming Fuels Cell Growth and Proliferation. Cell metabolism. 2008;7(1):11-20.

220. DeBerardinis RJ, Mancuso A, Daikhin E, Nissim I, Yudkoff M, Wehrli S, et al. Beyond aerobic glycolysis: Transformed cells can engage in glutamine metabolism that exceeds the requirement for protein and nucleotide synthesis. Proceedings of the National Academy of Sciences. 2007;104(49):19345-50.

221. Kim MH, Kim H. Oncogenes and Tumor Suppressors Regulate Glutamine Metabolism in Cancer Cells. Journal of Cancer Prevention. 2013;18(3):221-6.

222. Elstrom RL, Bauer DE, Buzzai M, Karnauskas R, Harris MH, Plas DR, et al. Akt Stimulates Aerobic Glycolysis in Cancer Cells. Cancer research. 2004;64(11):3892.

223. Yang L, Moss T, Mangala LS, Marini J, Zhao H, Wahlig S, et al. Metabolic shifts toward glutamine regulate tumor growth, invasion and bioenergetics in ovarian cancer. Molecular Systems Biology. 2014;10(5):728.

224. Shelton LM, Huysentruyt LC, Seyfried TN. Glutamine targeting inhibits systemic metastasis in the VM-M3 murine tumor model. International journal of cancer. 2010;127(10):2478-85.

225. Kallenberg K, Bock HC, Helms G, Jung K, Wrede A, Buhk JH, et al. Untreated glioblastoma multiforme: increased myo-inositol and glutamine levels in the contralateral cerebral hemisphere at proton MR spectroscopy. Radiology. 2009;253(3):805-12.

226. Venkatesh HS, Chaumeil MM, Ward CS, Haas-Kogan DA, James CD, Ronen SM. Reduced phosphocholine and hyperpolarized lactate provide magnetic resonance biomarkers of PI3K/Akt/mTOR inhibition in glioblastoma. Neuro Oncol. 2012;14(3):315-25.

227. Koul D, Shen R, Kim YW, Kondo Y, Lu Y, Bankson J, et al. Cellular and in vivo activity of a novel PI3K inhibitor, PX-866, against human glioblastoma. Neuro Oncol. 2010;12(6):559-69.

228. Opstad KS, Ladroue C, Bell BA, Griffiths JR, Howe FA. Linear discriminant analysis of brain tumour (1)H MR spectra: a comparison of classification using whole spectra versus metabolite quantification. NMR in biomedicine. 2007;20(8):763-70.

229. Wright AJ, Fellows G, Byrnes TJ, Opstad KS, McIntyre DJ, Griffiths JR, et al. Pattern recognition of MRSI data shows regions of glioma growth that agree with DTI markers of brain tumor infiltration. Magnetic resonance in medicine. 2009;62(6):1646-51.

230. Calvar JA, Meli FJ, Romero C, Calcagno ML, Yanez P, Martinez AR, et al. Characterization of brain tumors by MRS, DWI and Ki-67 labeling index. Journal of neuro-oncology. 2005;72(3):273-80.

231. Majos C, Alonso J, Aguilera C, Serrallonga M, Perez-Martin J, Acebes JJ, et al. Proton magnetic resonance spectroscopy ((1)H MRS) of human brain tumours: assessment of differences between tumour types and its applicability in brain tumour categorization. European radiology. 2003;13(3):582-91.

232. Valverde-Saubi D, Candiota AP, Molins MA, Feliz M, Godino O, Davila M, et al. Short-term temperature effect on the HRMAS spectra of human brain tumor biopsies and their pattern recognition analysis. Magma. 2010;23(4):203-15.

233. Burkhard C, Di Patre PL, Schuler D, Schuler G, Yasargil MG, Yonekawa Y, et al. A population-based study of the incidence and survival rates in patients with pilocytic astrocytoma. Journal of neurosurgery. 2003;98(6):1170-4.

234. Colin C, Padovani L, Chappe C, Mercurio S, Scavarda D, Loundou A, et al. Outcome analysis of childhood pilocytic astrocytomas: a retrospective study of 148 cases at a single institution. Neuropathology and applied neurobiology. 2013;39(6):693-705.

235. Fernandez C, Figarella-Branger D, Girard N, Bouvier-Labit C, Gouvernet J, Paz Paredes A, et al. Pilocytic astrocytomas in children: prognostic factors--a retrospective study of 80 cases. Neurosurgery. 2003;53(3):544-53; discussion 54-5.

236. Tibbetts KM, Emnett RJ, Gao F, Perry A, Gutmann DH, Leonard JR. Histopathologic predictors of pilocytic astrocytoma event-free survival. Acta neuropathologica. 2009;117(6):657.

237. Margraf LR, Gargan L, Butt Y, Raghunathan N, Bowers DC. Proliferative and metabolic markers in incompletely excised pediatric pilocytic astrocytomas—an assessment of 3 new variables in predicting clinical outcome. Neuro Oncol. 2011;13(7):767-74.

238. Team RC. R: A Language and Environment for Statistical Computing. R Foundation for Statistical Computing, Vienna, Austria2015.

239. Long PM, Moffett JR, Namboodiri AMA, Viapiano MS, Lawler SE, Jaworski DM. N-acetylaspartate (NAA) and N-acetylaspartylglutamate (NAAG) promote growth and inhibit differentiation of glioma stem-like cells. The Journal of biological chemistry. 2013;288(36):26188-200.

240. Sexton-Oates A, Dodgshun A, Hovestadt V, Jones DTW, Ashley DM, Sullivan M, et al. Methylation profiling of paediatric pilocytic astrocytoma reveals variants specifically associated with tumour location and predictive of recurrence. Molecular Oncology. 2018;12(8):1219-32.

241. Zakrzewski K, Jarząb M, Pfeifer A, Oczko-Wojciechowska M, Jarząb B, Liberski PP, et al. Transcriptional profiles of pilocytic astrocytoma are related to their three different locations, but not to radiological tumor features. BMC Cancer. 2015;15(1):778.

242. Wong K-K, Chang Y-M, Tsang YTM, Perlaky L, Su J, Adesina A, et al. Expression Analysis of Juvenile Pilocytic Astrocytomas by Oligonucleotide Microarray Reveals Two Potential Subgroups. Cancer research. 2005;65(1):76.

243. Huang H, Mahler-Araujo BM, Sankila A, Chimelli L, Yonekawa Y, Kleihues P, et al. APC mutations in sporadic medulloblastomas. The American journal of pathology. 2000;156(2):433-7.

244. Koch A, Waha A, Tonn JC, Sorensen N, Berthold F, Wolter M, et al. Somatic mutations of WNT/wingless signaling pathway components in primitive neuroectodermal tumors. International journal of cancer. 2001;93(3):445-9.

245. Taylor MD, Liu L Fau - Raffel C, Raffel C Fau - Hui C-c, Hui Cc Fau - Mainprize TG, Mainprize Tg Fau - Zhang X, Zhang X Fau - Agatep R, et al. Mutations in SUFU predispose to medulloblastoma. Nature genetics. 2002(1061-4036 (Print)).

246. Vorechovsky I, Tingby O Fau - Hartman M, Hartman M Fau - Stromberg B, Stromberg B Fau - Nister M, Nister M Fau - Collins VP, Collins Vp Fau - Toftgard R, et al. Somatic mutations in the human homologue of Drosophila patched in primitive neuroectodermal tumours. Oncogene. 1997(0950-9232 (Print)).

247. Wani K, Armstrong Ts Fau - Vera-Bolanos E, Vera-Bolanos E Fau - Raghunathan A, Raghunathan A Fau - Ellison D, Ellison D Fau - Gilbertson R, Gilbertson R Fau - Vaillant B, et al. A prognostic gene expression signature in infratentorial ependymoma. Acta neuropathologica. 2012(1432-0533 (Electronic)).

248. Witt H, Mack Sc Fau - Ryzhova M, Ryzhova M Fau - Bender S, Bender S Fau - Sill M, Sill M Fau - Isserlin R, Isserlin R Fau - Benner A, et al. Delineation of two clinically and molecularly distinct subgroups of posterior fossa ependymoma. Cancer cell. 2011(1878-3686 (Electronic)).

249. Khatri P, Sirota M, Butte AJ. Ten Years of Pathway Analysis: Current Approaches and Outstanding Challenges. PLoS Computational Biology. 2012;8(2):e1002375.

250. Picard D, Miller S, Hawkins CE, Bouffet E, Rogers HA, Chan TSY, et al. Integrative genomic analyses identify LIN28 and OLIG2 as markers of survival and metastatic potential in childhood central nervous system primitive neuro-ectodermal brain tumours. The lancet oncology. 2012;13(8):838-48.

251. Torchia J, Picard D, Lafay-Cousin L, Hawkins CE, Kim SK, Letourneau L, et al. Molecular subgroups of atypical teratoid rhabdoid tumours in children: an integrated genomic and clinicopathological analysis. The Lancet Oncology. 2015;16(5):569-82.

252. Chong J, Soufan O, Li C, Caraus I, Li S, Bourque G, et al. MetaboAnalyst 4.0: towards more transparent and integrative metabolomics analysis. Nucleic acids research. 2018:gky310-gky.

253. Goeman JJ, van de Geer SA, de Kort F, van Houwelingen HC. A global test for groups of genes: testing association with a clinical outcome. Bioinformatics. 2004;20(1):93-9.

254. Hendrickx DM, Hoefsloot HCJ, Hendriks MMWB, Canelas AB, Smilde AK. Global test for metabolic pathway differences between conditions. Analytica Chimica Acta. 2012;719:8-15.

255. Brandes U. On variants of shortest-path betweenness centrality and their generic computation. Social Networks. 2008;30(2):136-45.

256. Li S, Park Y, Duraisingham S, Strobel FH, Khan N, Soltow QA, et al. Predicting Network Activity from High Throughput Metabolomics. PLoS Computational Biology. 2013;9(7).

257. Subramanian A, Tamayo P, Mootha VK, Mukherjee S, Ebert BL, Gillette MA, et al. Gene set enrichment analysis: A knowledge-based approach for interpreting genome-wide expression profiles. Proceedings of the National Academy of Sciences. 2005;102(43):15545.

258. Henriquez NV, Forshew T, Tatevossian R, Ellis M, Richard-Loendt A, Rogers H, et al. Comparative expression analysis reveals lineage relationships between human and murine gliomas and a dominance of glial signatures during tumor propagation in vitro. Cancer research. 2013;73(18):5834-44.

259. Chen EY, Tan CM, Kou Y, Duan Q, Wang Z, Meirelles GV, et al. Enrichr: interactive and collaborative HTML5 gene list enrichment analysis tool. BMC bioinformatics. 2013;14:128.

260. Kuleshov MV, Jones MR, Rouillard AD, Fernandez NF, Duan Q, Wang Z, et al. Enrichr: a comprehensive gene set enrichment analysis web server 2016 update. Nucleic acids research. 2016;44(Web Server issue):W90-7.

261. Alanine, aspartate and glutamate metabolism: KEGG; 2018 [A graphical representation of the alanine, aspartate and glutamate metabolic pathway.]. Available from: https://www.genome.jp/kegg-bin/show_pathway?hsa00250.

262. Hermans J, Ongay S, Markov V, Bischoff R. Physicochemical Parameters Affecting the Electrospray Ionization Efficiency of Amino Acids after Acylation. Analytical chemistry. 2017;89(17):9159-66.

263. Martinez-Bisbal MC, Marti-Bonmati L, Piquer J, Revert A, Ferrer P, Llacer JL, et al. 1H and 13C HR-MAS spectroscopy of intact biopsy samples ex vivo and in vivo 1H MRS study of human high grade gliomas. NMR in biomedicine. 2004;17(4):191-205.

264. Katt WP, Ramachandran S, Erickson JW, Cerione RA. Dibenzophenanthridines as inhibitors of glutaminase C and cancer cell proliferation. Molecular cancer therapeutics. 2012;11(6):1269-78.

265. Lee Y-Z, Yang C-W, Chang H-Y, Hsu H-Y, Chen I-S, Chang H-S, et al. Discovery of selective inhibitors of Glutaminase-2, which inhibit mTORC1, activate autophagy and inhibit proliferation in cancer cells. Oncotarget. 2014;5(15):6087-101.

266. Dranoff G, Elion GB, Friedman HS, Campbell GL, Bigner DD. Influence of glutamine on the growth of human glioma and medulloblastoma in culture. Cancer research. 1985;45(9):4077-81.

267. MEDULLOBLASTOMA. Neuro-Oncology; 2014.

268. Xiang Y, Stine ZE, Xia J, Lu Y, O'Connor RS, Altman BJ, et al. Targeted inhibition of tumor-specific glutaminase diminishes cell-autonomous tumorigenesis. The Journal of clinical investigation. 2015;125(6):2293-306.

269. Mueller C, Al-Batran S, Jaeger E, Schmidt B, Bausch M, Unger C, et al. A phase IIa study of PEGylated glutaminase (PEG-PGA) plus 6-diazo-5-oxo-L-norleucine (DON) in patients with advanced refractory solid tumors. Journal of Clinical Oncology. 2008;26(15_suppl):2533-.

270. Health NIo. Clinical Trials Using Glutaminase Inhibitor CB-839 [Available from: https://www.cancer.gov/about-cancer/treatment/clinical-trials/intervention/glutaminase-inhibitor-cb-839.

271. Vitvitsky V, Garg SK, Banerjee R. Taurine biosynthesis by neurons and astrocytes. The Journal of biological chemistry. 2011;286(37):32002-10.

272. Brand A, Richter-Landsberg C, Leibfritz D. Metabolism of acetate in rat brain neurons, astrocytes and cocultures: metabolic interactions between neurons and glia cells, monitored by NMR spectroscopy. Cellular and molecular biology. 1997;43(5):645-57.

273. Lombardini JB. Effects of ATP and taurine on calcium uptake by membrane preparations of the rat retina. Journal of neurochemistry. 1983;40(2):402-6.

274. Prabhu A, Sarcar B, Kahali S, Yuan Z, Johnson JJ, Adam K-P, et al. Cysteine Catabolism: A Novel Metabolic Pathway Contributing to Glioblastoma Growth. Cancer research. 2014;74(3):787-96.

275. Lien YH, Shapiro JI, Chan L. Study of brain electrolytes and organic osmolytes during correction of chronic hyponatremia. Implications for the pathogenesis of central pontine myelinolysis. The Journal of clinical investigation. 1991;88(1):303-9.

276. Babourina-Brooks B, Kohe S, Gill SK, MacPherson L, Wilson M, Davies NP, et al. Glycine: a non-invasive imaging biomarker to aid magnetic resonance spectroscopy in the prediction of survival in paediatric brain tumours. Oncotarget. 2018;9(27):18858-68.

277. Morfouace M, Shelat A, Jacus M, Freeman BB, Turner D, Robinson S, et al. Pemetrexed and gemcitabine as combination therapy for the treatment of Group3 medulloblastoma. Cancer cell. 2014;25(4):516-29.

278. Bansal A, Simon MC. Glutathione metabolism in cancer progression and treatment resistance. The Journal of Cell Biology. 2018;217(7):2291.

279. Anderson CP, Matthay KK, Perentesis JP, Neglia JP, Bailey HH, Villablanca JG, et al. Pilot study of intravenous melphalan combined with continuous infusion L-S,R-buthionine sulfoximine for children with recurrent neuroblastoma. Pediatric blood & cancer. 2015;62(10):1739-46.

280. Liu P, Cheng H, Roberts TM, Zhao JJ. Targeting the phosphoinositide 3-kinase (PI3K) pathway in cancer. Nature reviews Drug discovery. 2009;8(8):627-44.

281. Rogers HA, Mayne C, Chapman RJ, Kilday J-P, Coyle B, Grundy RG. PI3K Pathway Activation Provides a Novel Therapeutic Target for Pediatric Ependymoma and Is an Independent Marker of Progression-Free Survival. Clinical Cancer Research. 2013;19(23):6450.

282. Wen PY, Lee EQ, Reardon DA, Ligon KL, Alfred Yung WK. Current clinical development of PI3K pathway inhibitors in glioblastoma. Neuro-Oncology. 2012;14(7):819-29.

283. Harrison FE, May JM. Vitamin C function in the brain: vital role of the ascorbate transporter SVCT2. Free radical biology & medicine. 2009;46(6):719-30.

284. Qin H, Carroll VN, Sriram R, Villanueva-Meyer JE, von Morze C, Wang ZJ, et al. Imaging glutathione depletion in the rat brain using ascorbate-derived hyperpolarized MR and PET probes. Scientific reports. 2018;8(1):7928.

285. Schoenfeld JD, Sibenaller ZA, Mapuskar KA, Wagner BA, Cramer-Morales KL, Furqan M, et al. O2(-) and H2O2-Mediated Disruption of Fe Metabolism Causes the Differential Susceptibility of NSCLC and GBM Cancer Cells to Pharmacological Ascorbate. Cancer cell. 2017;31(4):487-500.e8.

286. Hollinshead KER, Munford H, Eales KL, Bardella C, Li C, Escribano-Gonzalez C, et al. Oncogenic IDH1 Mutations Promote Enhanced Proline Synthesis through PYCR1 to Support the Maintenance of Mitochondrial Redox Homeostasis. Cell reports. 2018;22(12):3107-14.

287. Zhao H, Heimberger AB, Lu Z, Wu X, Hodges TR, Song R, et al. Metabolomics profiling in plasma samples from glioma patients correlates with tumor phenotypes. Oncotarget. 2016;7(15):20486-95.

288. Liu W, Zabirnyk O, Wang H, Shiao YH, Nickerson ML, Khalil S, et al. MicroRNA-23b* targets proline oxidase, a mitochondrial tumor suppressor protein in renal cancer. Oncogene. 2010;29(35):4914-24.

289. Liu Y, Borchert GL, Surazynski A, Phang JM. Proline oxidase, a p53-induced gene, targets COX-2/PGE2 signaling to induce apoptosis and inhibit tumor growth in colorectal cancers. Oncogene. 2008;27(53):6729-37.

290. Liu W, Le A, Hancock C, Lane AN, Dang CV, Fan TW, et al. Reprogramming of proline and glutamine metabolism contributes to the proliferative and metabolic responses regulated by oncogenic transcription factor c-MYC. Proc Natl Acad Sci U S A. 2012;109(23):8983-8.

291. Hourani R, Horska A, Albayram S, Brant LJ, Melhem E, Cohen KJ, et al. Proton magnetic resonance spectroscopic imaging to differentiate between nonneoplastic lesions and brain tumors in children. Journal of magnetic resonance imaging. 2006;23(2):99-107.

292. Novak J, Wilson M, Macpherson L, Arvanitis TN, Davies NP, Peet AC. Clinical protocols for (3)(1)P MRS of the brain and their use in evaluating optic pathway gliomas in children. European journal of radiology. 2014;83(2):e106-12.

293. Ahn BH, Kim SY, Kim EH, Choi KS, Kwon TK, Lee YH, et al. Transmodulation between phospholipase D and c-Src enhances cell proliferation. Molecular and cellular biology. 2003;23(9):3103-15.

Appendix 1 – Deconvolved spectrum and assigned metabolites

0.8ppm – 1.10ppm

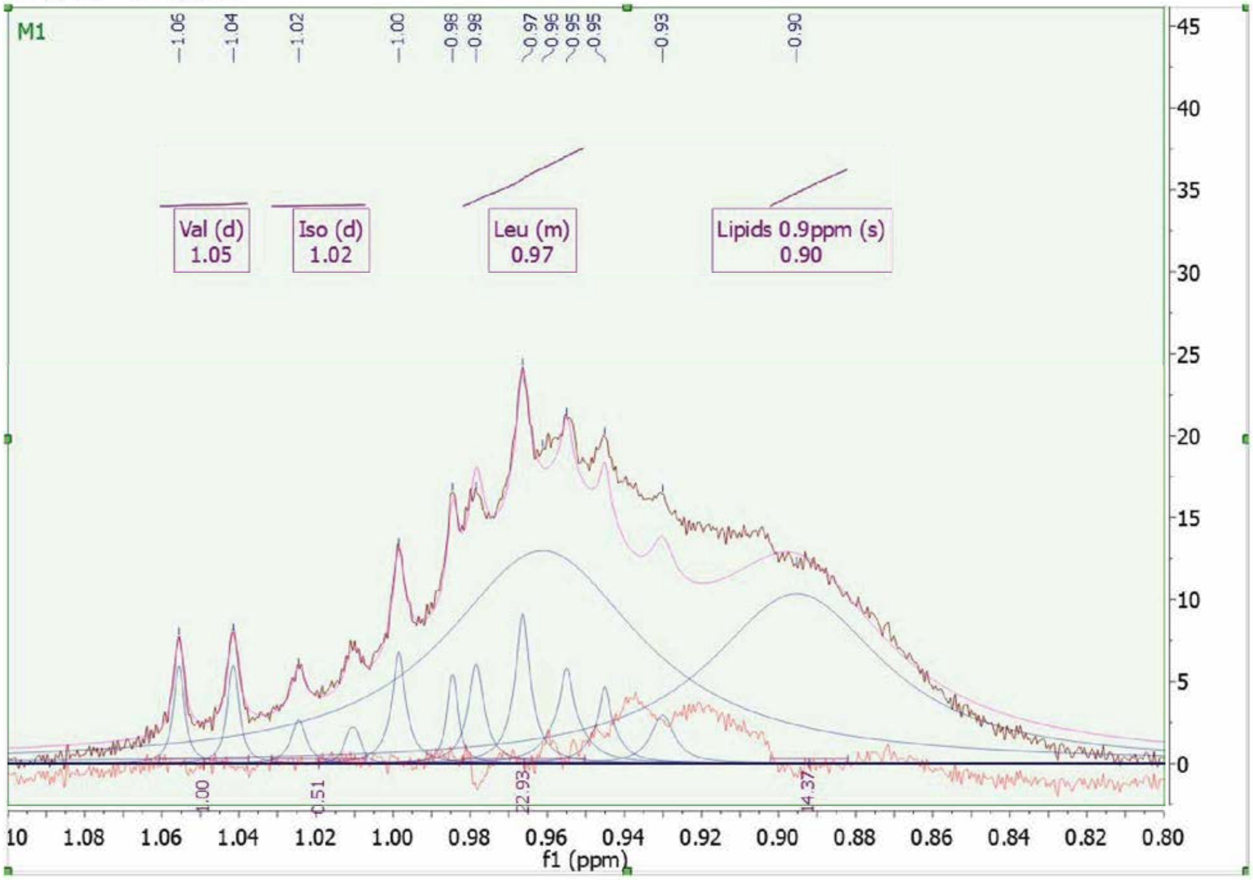

Deconvolution of the spectral region between 0.8ppm and 1.10ppm. All three branched chain amino acids can be assigned, as well as the lipids contributing to the broad resonance at 0.9ppm.

1.15pm – 1.55ppm

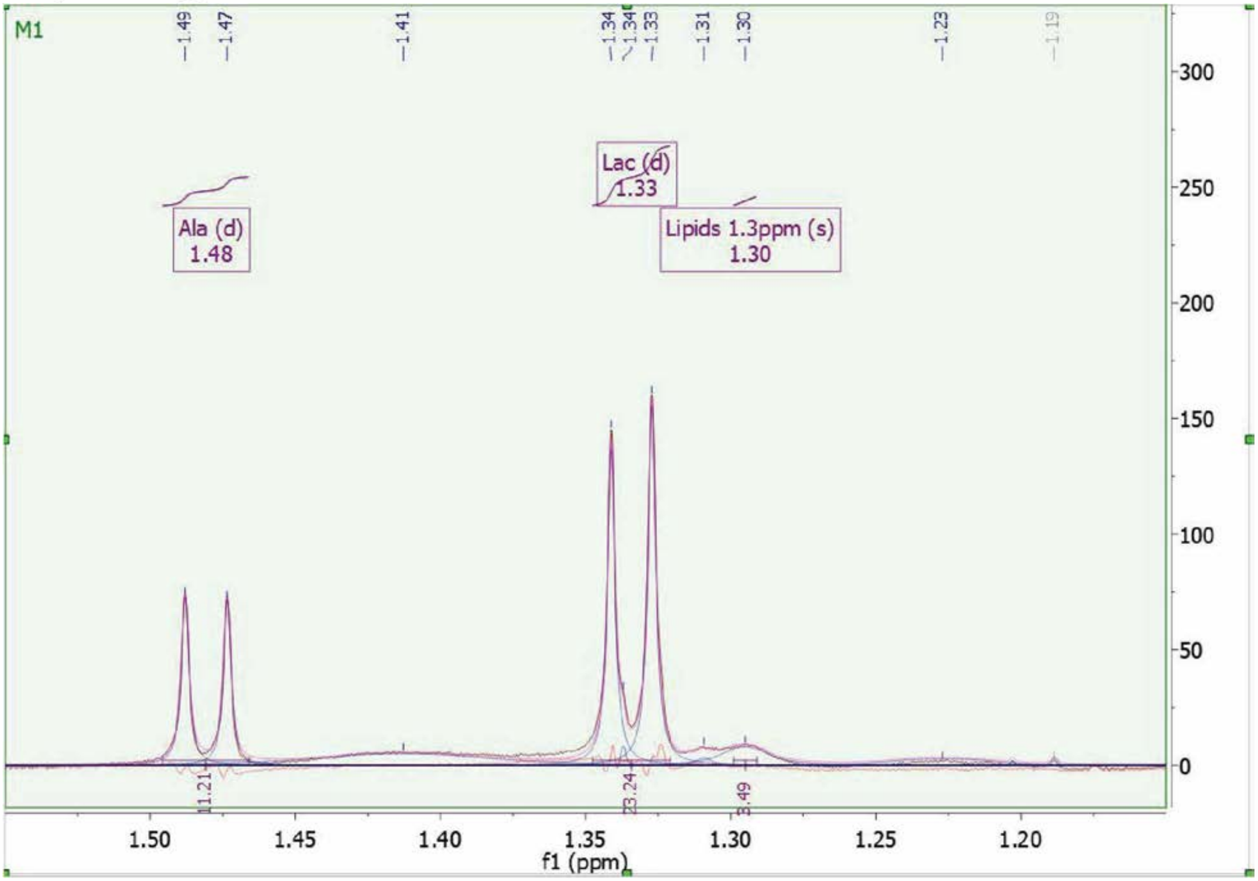

Deconvolution of the spectral region between 1.15ppm and 1.55ppm. Both Lac and Ala can be assigned, as well as the lipids contributing to the broad resonance at 1.2ppm.

1.80ppm – 2.20ppm

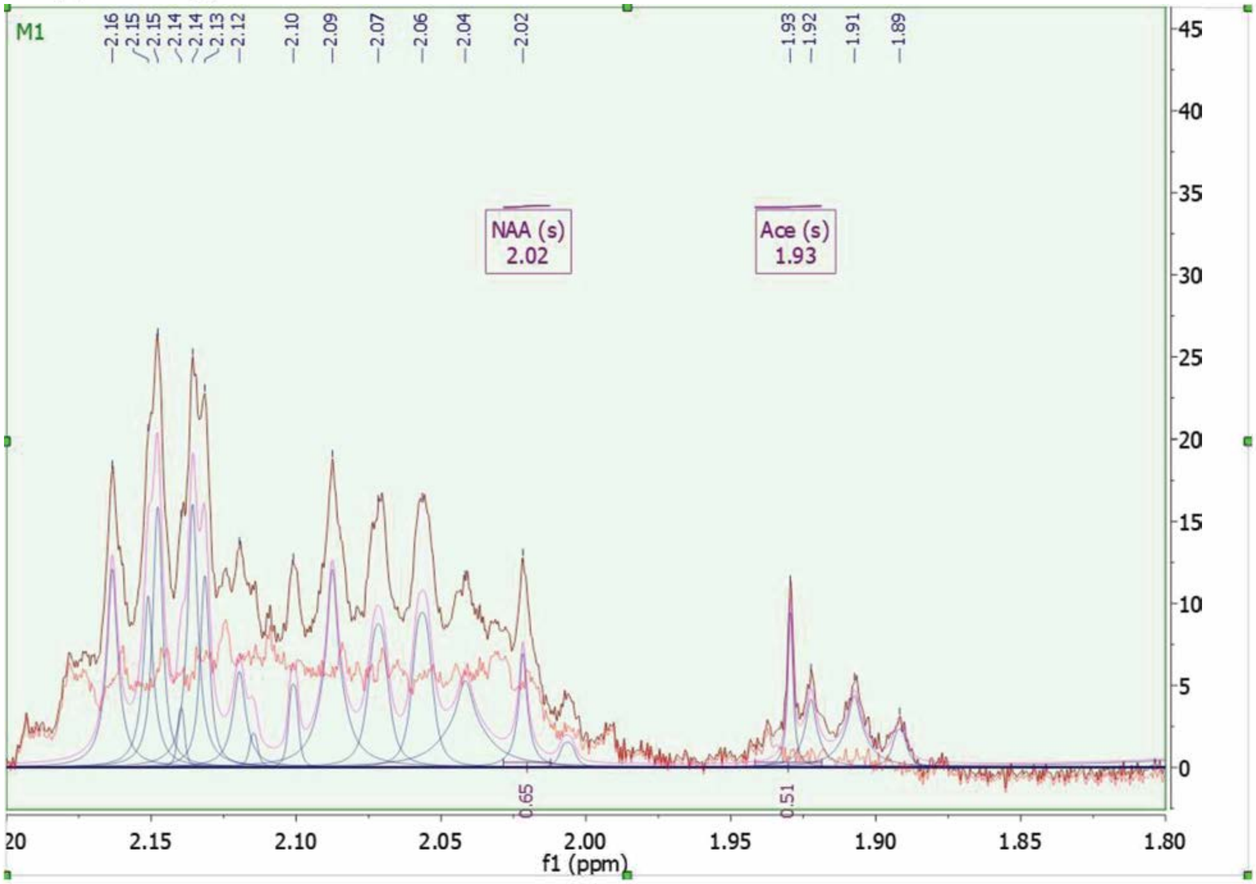

Deconvolution of the spectral region between 1.80ppm and 2.20ppm. Both Ace and NAA can be assigned. The complex region to the left of NAA is the overlapping resonances primarily from Gln and Glu.

2.20ppm – 2.50ppm

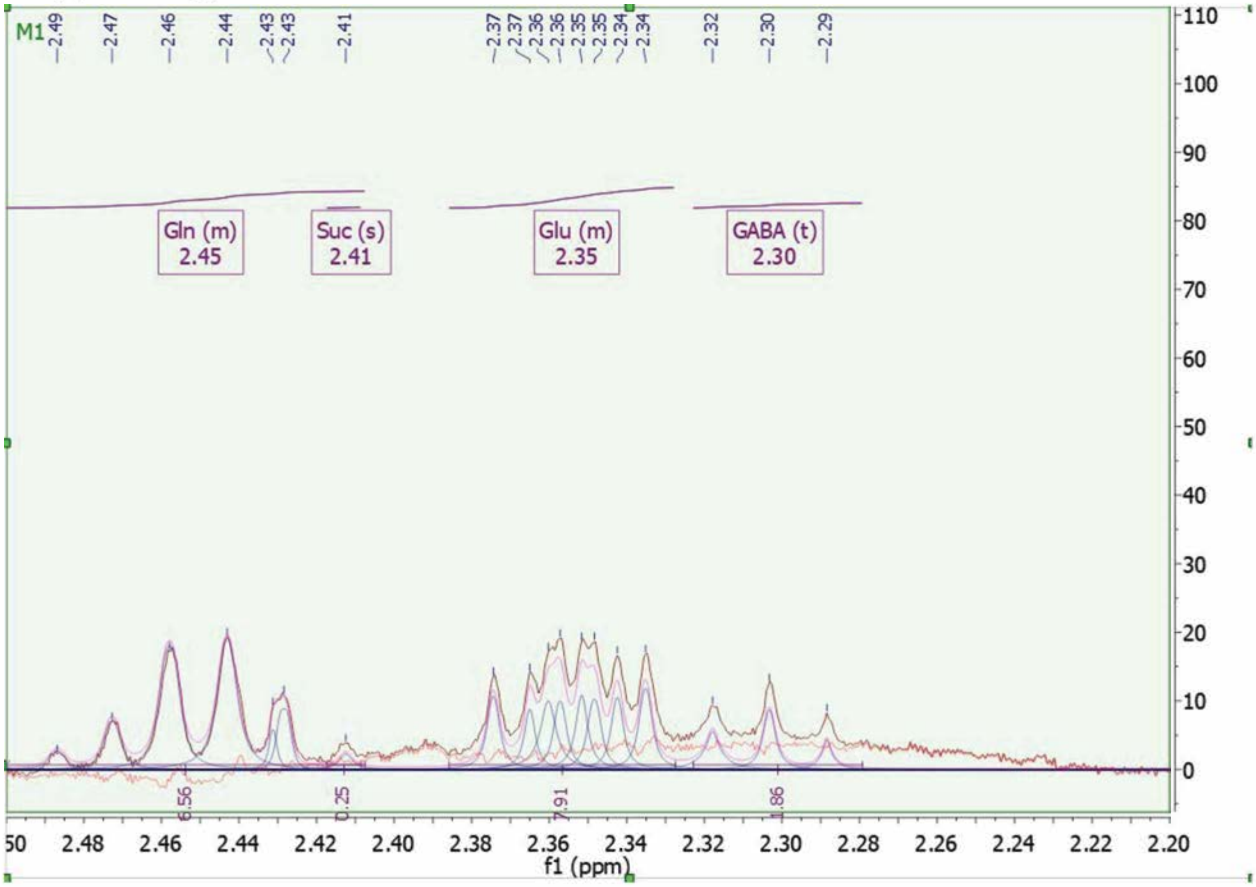

Deconvolution of the spectral region between 2.20ppm and 2.50ppm. The GABA triplet, both Gln and Glu multiplets and the Suc singlet can be assigned. A singlet for acetone is not present in the deconvoluted spectrum, as there is no singlet at 2.23ppm

2.50ppm – 2.90ppm

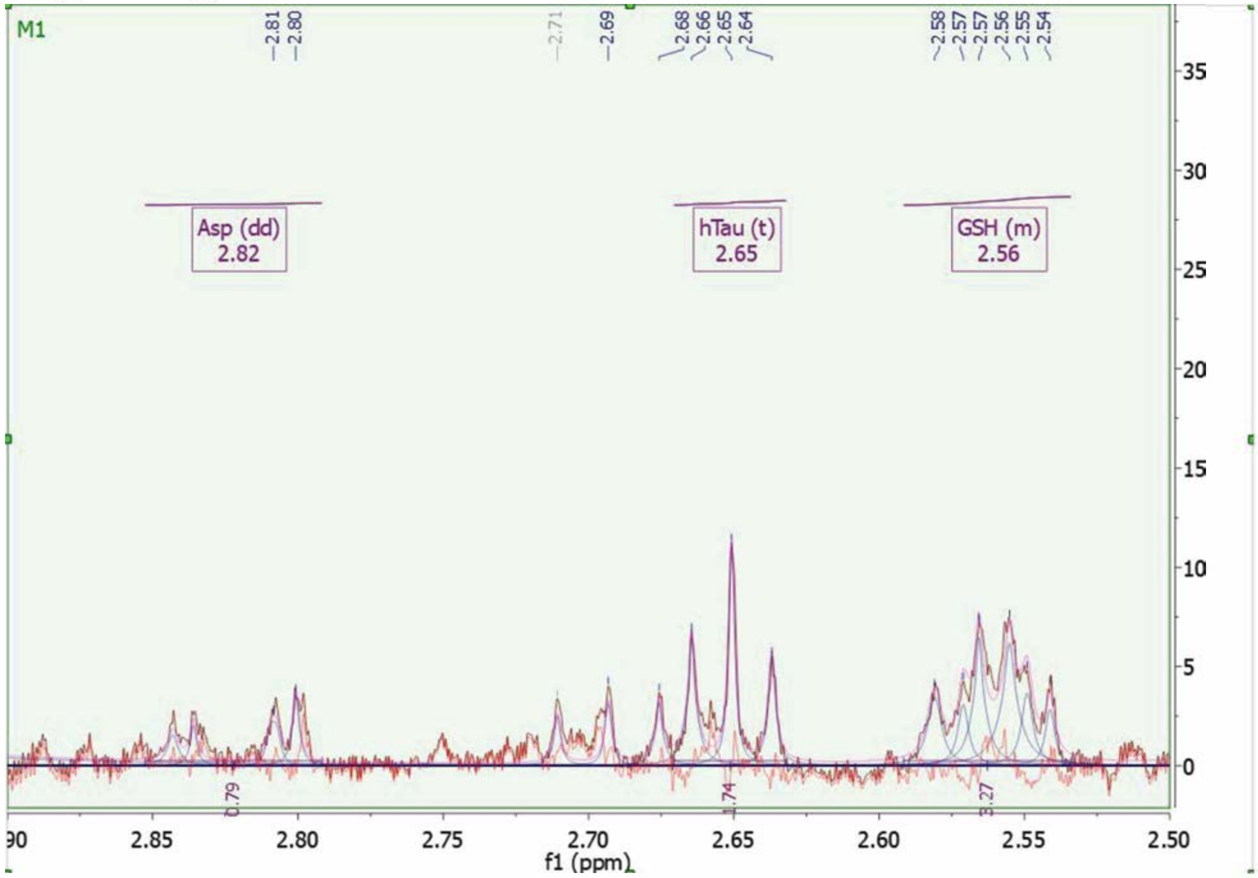

Deconvolution of the spectral region between 2.50ppm and 2.90ppm. The GSH multiplet, hTau triplet and Asp doublet of doublets can be assigned.

2.90ppm – 3.30ppm

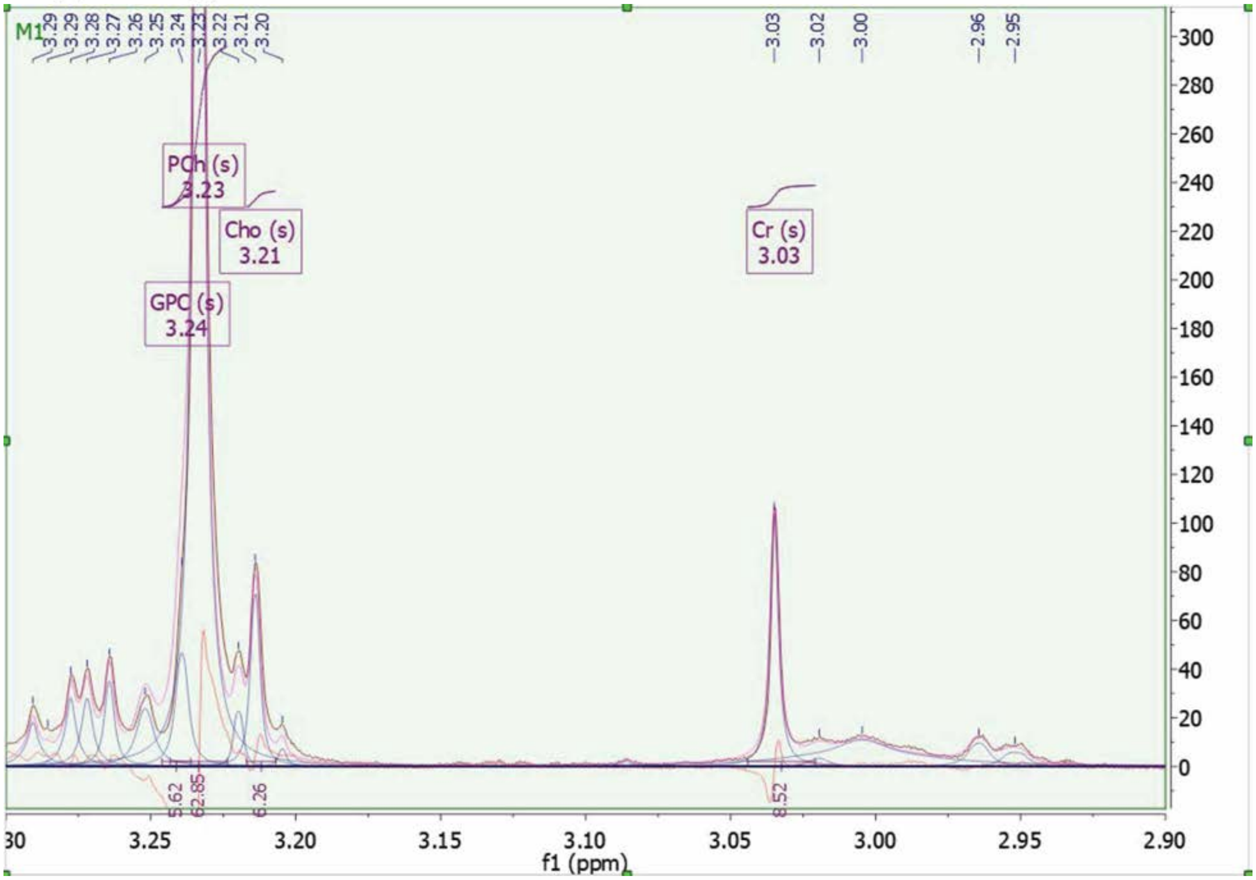

Deconvolution of the spectral region between 2.90ppm and 3.30ppm. The singlets for Cr, Cho, PCh and GPC are all assigned.

3.30ppm – 3.70ppm

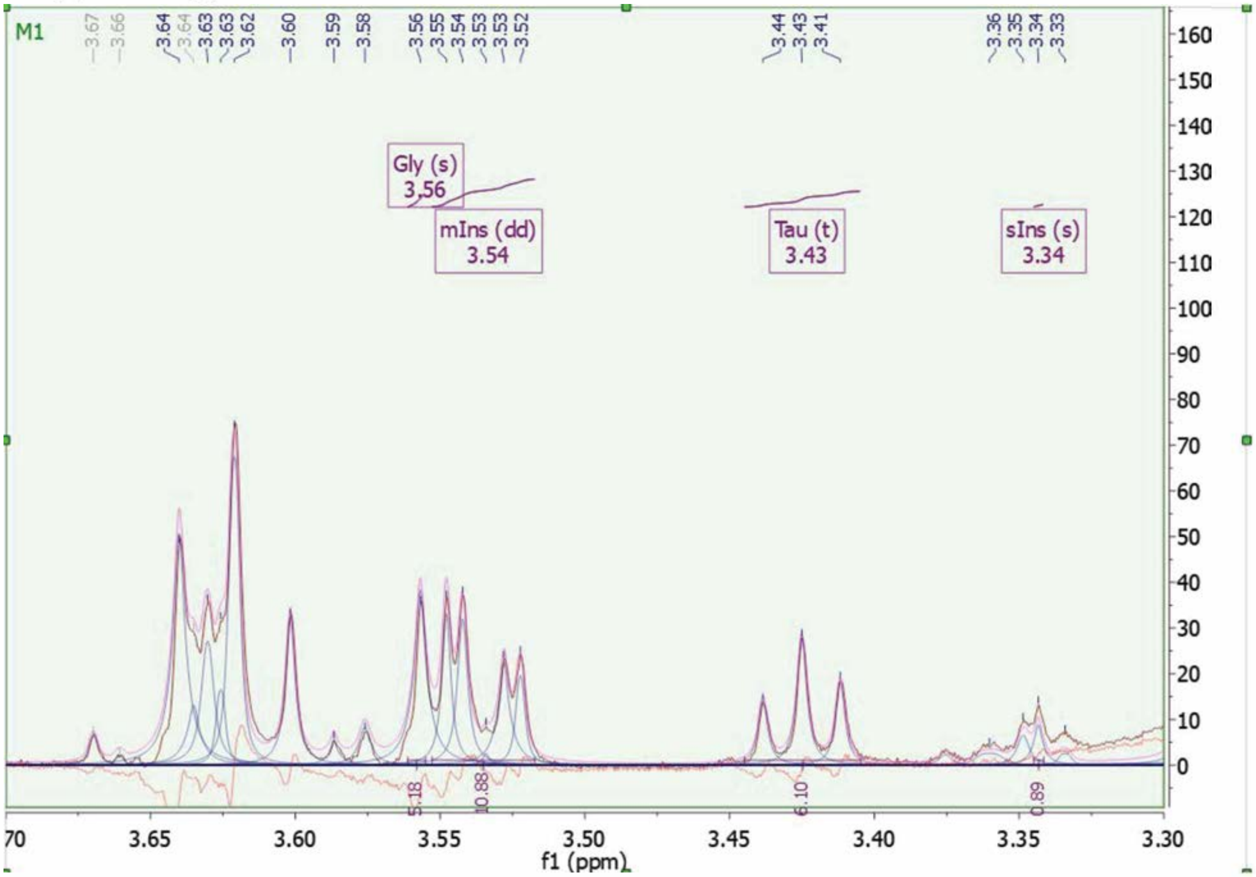

Deconvolution of the spectral region between 3.30ppm and 3.70ppm. The sIns singlet, Tau triplet, mIns doublet of doublets and Gly singlet are assigned.

3.70ppm – 4.00ppm

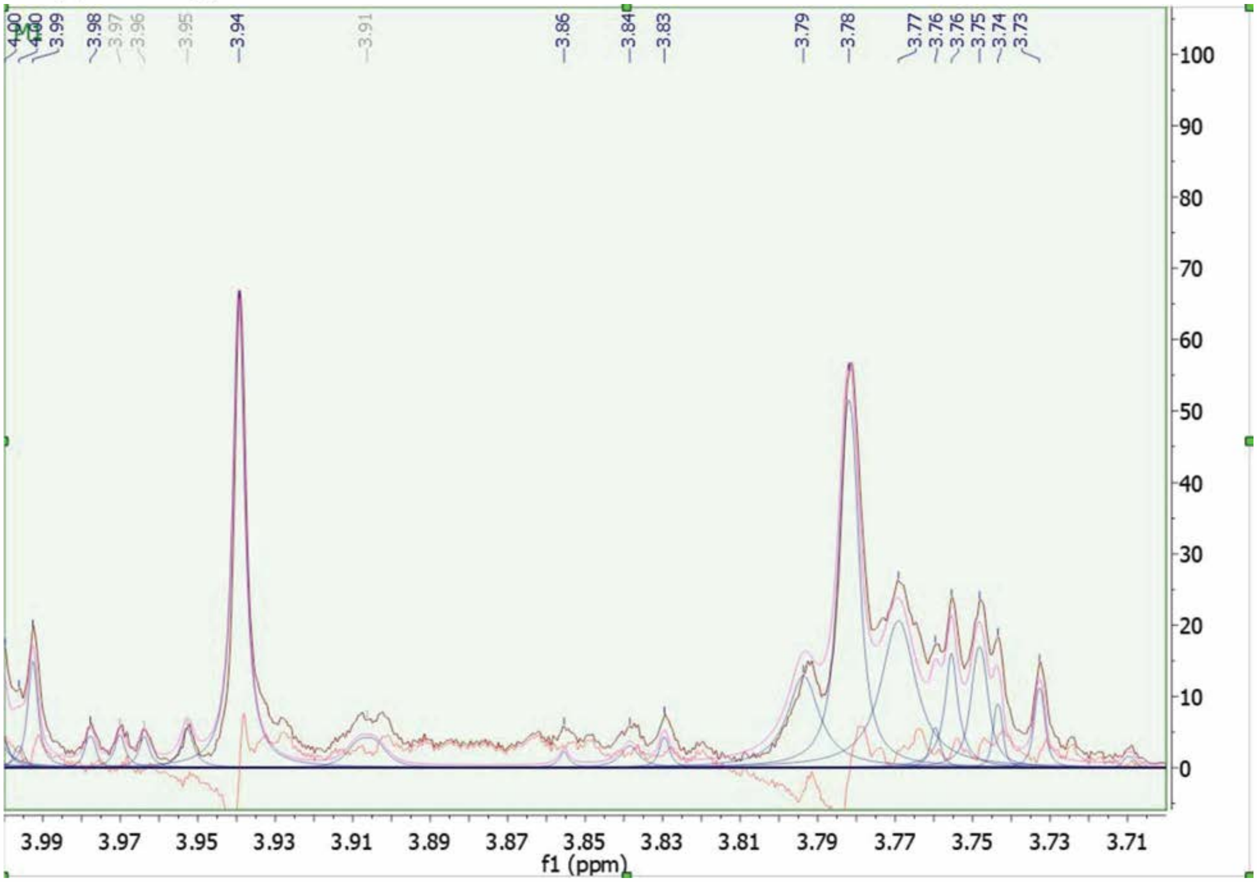

Deconvolution of the spectral region between 3.70ppm and 4.00ppm. The Ser doublet of doublets centred at 3.84ppm has not been deconvoluted and is not assigned.

4.00ppm – 4.70ppm

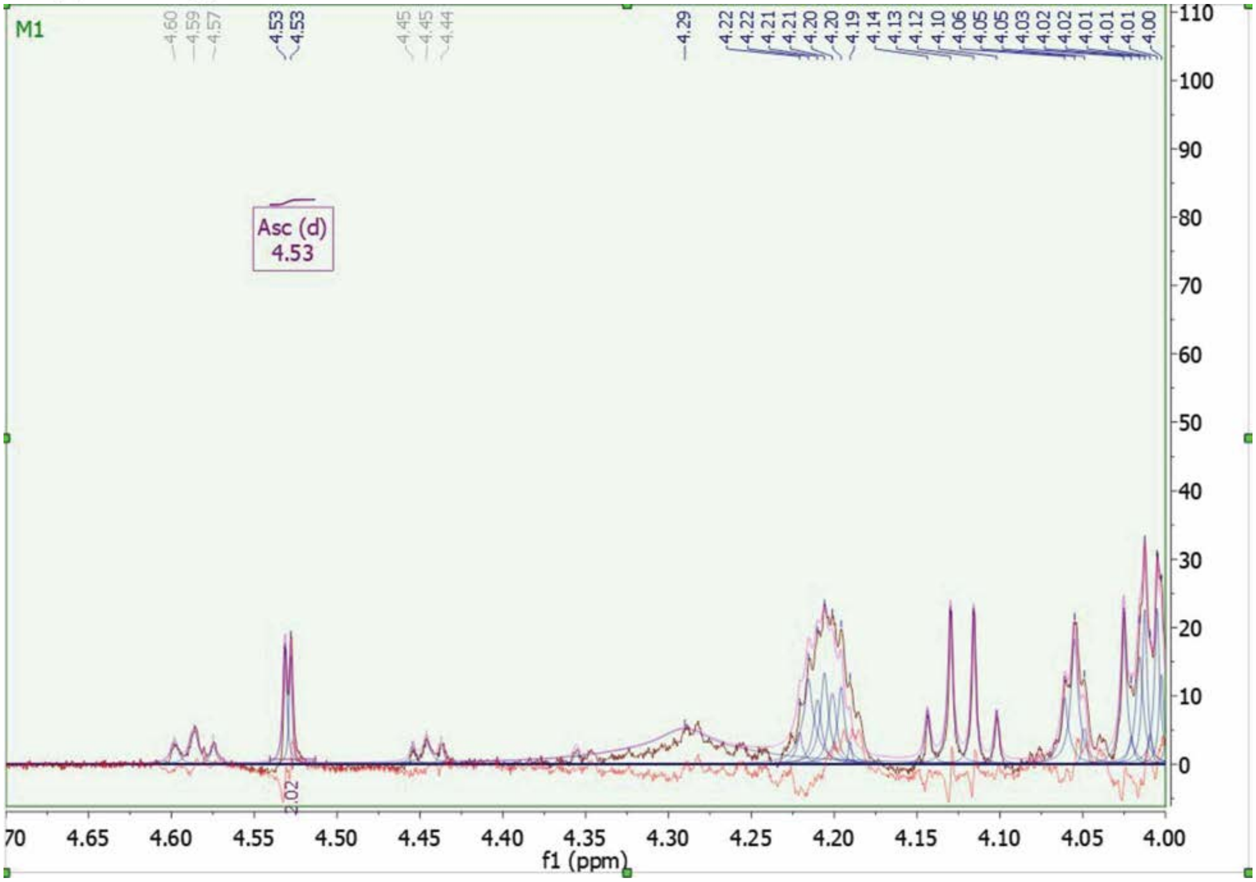

Deconvolution of the spectral region between 4.00ppm and 4.70ppm. The Asc doublet has been assigned, but the Glc doublet at 4.65 is not present and is not assigned.

Appendix 2 – Full results of the UPLC-MS metabolic pathway analysis

HILIC negative mode

	Pathway total	MB-EP			MB-PA			EP-PA		
		Hits.total	Hits.sig	Adjusted P-value	Hits.total	Hits.sig	Adjusted P-value	Hits.total	Hits.sig	Adjusted P-value
Alanine, aspartate and glutamate metabolism	24	22	20	0.0030	22	21	0.0028	22	19	0.0024
Amino sugar and nucleotide sugar metabolism	88	60	38	0.3516	60	54	0.0021	60	47	0.0021
Aminoacyl-tRNA biosynthesis	75	22	22	0.0019	22	19	0.0104	22	16	0.0220
Arachidonic acid metabolism	62	10	3	0.7670	10	7	0.2146	10	4	0.5100
Arginine and proline metabolism	77	56	48	0.0021	56	46	0.0074	56	45	0.0018
Ascorbate and aldarate metabolism	45	34	30	0.0024	34	32	0.0022	34	32	0.0014
beta-Alanine metabolism	28	17	15	0.0062	17	16	0.0046	17	14	0.0059
Biotin metabolism	11	5	5	0.0250	5	5	0.0386	5	4	0.0717
Butanoate metabolism	40	25	24	0.0020	25	22	0.0062	25	19	0.0097
Caffeine metabolism	21	3	2	0.3387	3	2	0.3958	3	3	0.0525
Citrate cycle (TCA cycle)	20	11	11	0.0035	11	11	0.0053	11	10	0.0045
Cyanoamino acid metabolism	16	8	8	0.0071	8	7	0.0505	8	7	0.0137
Cysteine and methionine metabolism	56	39	33	0.0032	39	30	0.0481	39	30	0.0043
D-Arginine and D-ornithine metabolism	8	8	8	0.0071	8	8	0.0114	8	6	0.0561

D-Glutamine and D-glutamate metabolism	11	7	6	0.0472	7	7	0.0161	7	6	0.0226
Drug metabolism - cytochrome P450	86	2	1	1.0000	2	2	0.2264	2	1	1.0000
Drug metabolism - other enzymes	38	2	2	0.1850	2	2	0.2264	2	1	1.0000
Ether lipid metabolism	23	2	2	0.1850	2	2	0.2264	2	2	0.1312
Fatty acid biosynthesis	49	5	1	1.0000	5	1	1.0000	5	2	0.4851
Fatty acid metabolism	50	6	3	0.4527	6	3	0.5258	6	1	1.0000
Folate biosynthesis	42	16	10	0.2537	16	11	0.2204	16	8	0.3720
Fructose and mannose metabolism	48	36	31	0.0029	36	33	0.0025	36	33	0.0014
Galactose metabolism	41	31	28	0.0022	31	26	0.0104	31	28	0.0015
Glutathione metabolism	38	14	12	0.0130	14	12	0.0250	14	9	0.1124
Glycerolipid metabolism	32	12	12	0.0031	12	11	0.0132	12	10	0.0099
Glycerophosphol ipid metabolism	39	15	10	0.1739	15	12	0.0565	15	10	0.0816
Glycine, serine and threonine metabolism	48	36	30	0.0043	36	30	0.0096	36	26	0.0144
Glycolysis or Gluconeogenesis	31	19	16	0.0097	19	15	0.0532	19	16	0.0038
Glyoxylate and dicarboxylate metabolism	50	38	28	0.0409	38	28	0.1046	38	26	0.0361
Histidine metabolism	44	23	21	0.0027	23	21	0.0042	23	17	0.0165
Inositol phosphate metabolism	39	20	15	0.0490	20	16	0.0418	20	17	0.0031
Lysine biosynthesis	32	20	19	0.0024	20	20	0.0023	20	15	0.0161
Lysine degradation	47	30	26	0.0033	30	25	0.0123	30	22	0.0135
Metabolism of xenobiotics by cytochrome P450	65	2	1	1.0000	2	1	1.0000	2	1	1.0000
Methane metabolism	34	16	12	0.0594	16	12	0.1096	16	12	0.0218

Nicotinate and nicotinamide metabolism	44	29	22	0.0297	29	21	0.1357	29	24	0.0025
Nitrogen metabolism	39	20	18	0.0037	20	18	0.0064	20	18	0.0020
One carbon pool by folate	9	6	4	0.2329	6	2	0.7287	6	2	0.5739
Pantothenate and CoA biosynthesis	27	24	21	0.0039	24	20	0.0169	24	19	0.0056
Pentose and glucuronate interconversions	53	41	36	0.0022	41	39	0.0021	41	33	0.0023
Pentose phosphate pathway	32	28	25	0.0026	28	25	0.0042	28	24	0.0020
Phenylalanine metabolism	45	27	23	0.0047	27	25	0.0029	27	21	0.0061
Phenylalanine, tyrosine and tryptophan biosynthesis	27	24	22	0.0025	24	20	0.0169	24	22	0.0016
Porphyrin and chlorophyll metabolism	104	17	13	0.0445	17	12	0.1824	17	10	0.1939
Primary bile acid biosynthesis	47	5	2	0.5833	5	4	0.1702	5	4	0.0717
Propanoate metabolism	35	17	15	0.0062	17	17	0.0026	17	15	0.0028
Purine metabolism	92	59	42	0.0698	59	45	0.0481	59	47	0.0018
Pyrimidine metabolism	60	44	34	0.0136	44	36	0.0109	44	35	0.0024
Pyruvate metabolism	32	21	17	0.0151	21	19	0.0054	21	18	0.0027
Riboflavin metabolism	21	15	11	0.0793	15	13	0.0190	15	12	0.0107
Selenoamino acid metabolism	22	2	2	0.1850	2	2	0.2264	2	2	0.1312
Sphingolipid metabolism	25	5	4	0.1233	5	3	0.4016	5	4	0.0717
Starch and sucrose metabolism	50	30	26	0.0033	30	25	0.0123	30	18	0.1835
Steroid hormone biosynthesis	99	21	7	0.8596	21	9	0.8038	21	6	0.8260
Sulfur metabolism	18	12	11	0.0075	12	12	0.0044	12	12	0.0019
Synthesis and degradation of	6	3	3	0.0865	3	3	0.1172	3	3	0.0525

ketone bodies										
Taurine and hypotaurine metabolism	20	12	11	0.0075	12	10	0.0455	12	10	0.0099
Terpenoid backbone biosynthesis	33	12	8	0.1819	12	8	0.2647	12	7	0.2039
Thiamine metabolism	24	13	10	0.0550	13	8	0.3669	13	10	0.0218
Tryptophan metabolism	79	38	25	0.2057	38	35	0.0023	38	27	0.0184
Tyrosine metabolism	76	40	29	0.0537	40	37	0.0022	40	28	0.0232
Ubiquinone and other terpenoid-quinone biosynthesis	36	11	10	0.0100	11	11	0.0053	11	9	0.0145
Valine, leucine and isoleucine biosynthesis	27	17	12	0.1069	17	12	0.1824	17	10	0.1939
Valine, leucine and isoleucine degradation	40	17	12	0.1069	17	13	0.0863	17	5	0.7708
Vitamin B6 metabolism	32	20	20	0.0019	20	16	0.0418	20	16	0.0065

HILIC positive mode

	Pathway total	MB-EP			MB-PA			EP-PA		
		Hits.total	Hits.sig	Adjusted P-value	Hits.total	Hits.sig	Adjusted P-value	Hits.total	Hits.sig	Adjusted P-value
Alanine, aspartate and glutamate metabolism	24	19	15	0.006534	19	17	0.004512	19	19	0.002214
alpha-Linolenic acid metabolism	29	1	1	1	1	1	1	1	1	1
Amino sugar and nucleotide sugar metabolism	88	56	35	0.058567	56	43	0.014146	56	42	0.005622
Aminoacyl-tRNA biosynthesis	75	22	19	0.002846	22	21	0.00215	22	20	0.002574
Arachidonic acid metabolism	62	10	1	1	10	6	0.30409	10	4	0.55011
Arginine and proline metabolism	77	55	41	0.003436	55	45	0.003746	55	49	0.002167
Ascorbate and aldarate metabolism	45	33	15	0.52941	33	25	0.03034	33	20	0.1895
beta-Alanine metabolism	28	19	15	0.006534	19	13	0.14527	19	13	0.063758
Biotin metabolism	11	7	5	0.074535	7	6	0.049325	7	6	0.028291
Butanoate metabolism	40	23	15	0.048466	23	19	0.010339	23	17	0.020354
Caffeine metabolism	21	2	2	0.12814	2	2	0.18675	2	2	0.15243
Citrate cycle (TCA cycle)	20	10	6	0.14867	10	9	0.014695	10	6	0.20786
Cyanoamino acid metabolism	16	7	6	0.019023	7	6	0.049325	7	6	0.028291

Cysteine and methionine metabolism	56	34	22	0.04159	34	28	0.006115	34	26	0.0075
D-Arginine and D-ornithine metabolism	8	8	8	0.004191	8	8	0.007404	8	8	0.005187
D-Glutamine and D-glutamate metabolism	11	7	6	0.019023	7	7	0.010486	7	7	0.006985
Drug metabolism - other enzymes	38	2	1	1	2	2	0.18675	2	1	1
Ether lipid metabolism	23	2	2	0.12814	2	2	0.18675	2	2	0.15243
Fatty acid biosynthesis	49	5	3	0.21976	5	2	0.58438	5	2	0.52678
Fatty acid metabolism	50	9	2	0.75651	9	4	0.55538	9	4	0.46665
Folate biosynthesis	42	16	6	0.58581	16	11	0.14449	16	8	0.40515
Fructose and mannose metabolism	48	36	17	0.49223	36	21	0.46443	36	21	0.26214
Galactose metabolism	41	31	20	0.045701	31	21	0.15774	31	27	0.002497
Glutathione metabolism	38	18	13	0.019095	18	12	0.17893	18	11	0.171
Glycerolipid metabolism	32	9	6	0.087305	9	7	0.078208	9	8	0.011768
Glycerophospholipid metabolism	39	14	11	0.011199	14	14	0.002511	14	13	0.003536
Glycine, serine and threonine metabolism	48	33	21	0.053092	33	25	0.03034	33	25	0.008958
Glycolysis or Gluconeogenesis	31	16	10	0.090944	16	11	0.14449	16	11	0.068519
Glyoxylate and dicarboxylate metabolism	50	30	21	0.014974	30	23	0.026612	30	18	0.20182
Histidine metabolism	44	24	20	0.003169	24	21	0.004143	24	19	0.007506
Inositol	39	20	12	0.1159	20	14	0.1168	20	10	0.4314

phosphate metabolism				6			5			9
Limonene and pinene degradation	59	7	3	0.42166	7	1	1	7	2	0.6893
Lipoic acid metabolism	6	1	1	1	1	1	1	1	1	1
Lysine biosynthesis	32	20	17	0.003351	20	18	0.003882	20	18	0.002901
Lysine degradation	47	32	20	0.067675	32	28	0.002873	32	29	0.002244
Metabolism of xenobiotics by cytochrome P450	65	2	2	0.12814	2	2	0.18675	2	2	0.15243
Methane metabolism	34	13	10	0.01579	13	10	0.058611	13	10	0.026995
Nicotinate and nicotinamide metabolism	44	29	22	0.005566	29	22	0.033032	29	20	0.043621
Nitrogen metabolism	39	18	14	0.008281	18	17	0.002806	18	14	0.014498
One carbon pool by folate	9	7	4	0.21393	7	6	0.049325	7	4	0.27095
Pantothenate and CoA biosynthesis	27	22	13	0.12868	22	15	0.14735	22	17	0.01172
Pentose and glucuronate interconversions	53	40	20	0.41829	40	26	0.25041	40	21	0.47898
Pentose phosphate pathway	32	26	17	0.043113	26	20	0.02893	26	18	0.044603
Phenylalanine metabolism	45	25	21	0.00294	25	21	0.006953	25	24	0.002202
Phenylalanine, tyrosine and tryptophan biosynthesis	27	24	20	0.003169	24	22	0.002571	24	18	0.015706
Porphyrin and chlorophyll metabolism	104	19	12	0.075934	19	13	0.14527	19	12	0.13369
Primary bile acid	47	9	4	0.39669	9	4	0.55538	9	5	0.28147

biosynthesis										
Propanoate metabolism	35	18	9	0.318	18	10	0.42791	18	14	0.014498
Purine metabolism	92	55	33	0.10974	55	40	0.051766	55	37	0.047833
Pyrimidine metabolism	60	42	34	0.002548	42	34	0.006264	42	29	0.033694
Pyruvate metabolism	32	15	10	0.054537	15	14	0.004143	15	13	0.005687
Retinol metabolism	22	2	1	1	2	1	1	2	2	0.15243
Riboflavin metabolism	21	13	12	0.003348	13	10	0.058611	13	8	0.17228
Selenoamino acid metabolism	22	3	2	0.25067	3	2	0.34064	3	2	0.28963
Sphingolipid metabolism	25	9	3	0.58595	9	4	0.55538	9	3	0.64469
Starch and sucrose metabolism	50	29	7	0.9184	29	19	0.21306	29	17	0.23735
Steroid hormone biosynthesis	99	28	6	0.93656	28	6	0.97858	28	6	0.95976
Sulfur metabolism	18	11	7	0.10016	11	9	0.037316	11	8	0.05806
Synthesis and degradation of ketone bodies	6	3	1	1	3	2	0.34064	3	3	0.063626
Taurine and hypotaurine metabolism	20	11	8	0.035328	11	7	0.24144	11	8	0.05806
Terpenoid backbone biosynthesis	33	13	6	0.38028	13	7	0.42871	13	5	0.61112
Thiamine metabolism	24	12	8	0.066808	12	10	0.0263	12	10	0.012876
Tryptophan metabolism	79	37	28	0.004311	37	32	0.002784	37	28	0.007888
Tyrosine metabolism	76	39	31	0.002851	39	30	0.019309	39	31	0.00388
Ubiquinone and other terpenoid-quinone	36	14	9	0.078743	14	10	0.11139	14	8	0.24786

biosynthesis										
Valine, leucine and isoleucine biosynthesis	27	16	13	0.006426	16	13	0.023195	16	14	0.004687
Valine, leucine and isoleucine degradation	40	19	9	0.38582	19	11	0.3787	19	12	0.13369
Vitamin B6 metabolism	32	20	15	0.010578	20	17	0.008337	20	15	0.019948

Appendix 3 – Published first author paper

www.nature.com/scientificreports

SCIENTIFIC REPORTS

OPEN

Tissue metabolite profiles for the characterisation of paediatric cerebellar tumours

Received: 14 February 2018
Accepted: 10 July 2018

Christopher D. Bennett[1,2], Sarah E. Kohe[1,2], Simrandip K. Gill[1,2], Nigel P. Davies[2,3], Martin Wilson[4], Lisa C. D. Storer[5], Timothy Ritzmann[5], Simon M. L. Paine[6], Ian S. Scott[6], Ina Nicklaus-Wollenteit[2], Daniel A. Tennant[7], Richard G. Grundy[5] & Andrew C. Peet[1,2]

Paediatric brain tumors are becoming well characterized due to large genomic and epigenomic studies. Metabolomics is a powerful analytical approach aiding in the characterization of tumors. This study shows that common cerebellar tumors have metabolite profiles sufficiently different to build accurate, robust diagnostic classifiers, and that the metabolite profiles can be used to assess differences in metabolism between the tumors. Tissue metabolite profiles were obtained from cerebellar ependymoma ($n = 18$), medulloblastoma ($n = 36$), pilocytic astrocytoma ($n = 24$) and atypical teratoid/rhabdoid tumors ($n = 5$) samples using HR-MAS. Quantified metabolites accurately discriminated the tumors; classification accuracies were 94% for ependymoma and medulloblastoma and 92% for pilocytic astrocytoma. Using current intraoperative examination the diagnostic accuracy was 72% for ependymoma, 90% for medulloblastoma and 89% for pilocytic astrocytoma. Elevated *myo*-inositol was characteristic of ependymoma whilst high taurine, phosphocholine and glycine distinguished medulloblastoma. Glutamine, hypotaurine and N-acetylaspartate (NAA) were increased in pilocytic astrocytoma. High lipids, phosphocholine and glutathione were important for separating ATRTs from medulloblastomas. This study demonstrates the ability of metabolic profiling by HR-MAS on small biopsy tissue samples to characterize these tumors. Analysis of tissue metabolite profiles has advantages in terms of minimal tissue pre-processing, short data acquisition time giving the potential to be used as part of a rapid diagnostic work-up.

Paediatric tumors of the central nervous system (CNS) are the most common solid cancers diagnosed in children[1]. They are now the highest cause of cancer related deaths in this population, causing death in around a third of cases after 10 years[1]. In broad terms the treatment for these tumors is maximal safe resection followed by chemotherapy and/or radiotherapy as appropriate according to treatment protocols. Whilst there has been an improvement in survival over the past 40 years there have been fewer gains recently[2] and there is a pressing need to elucidate the molecular pathology as well as identify biomarkers of diagnosis and prognosis of these tumors.

In children, approximately 50% of CNS tumors occur in the posterior fossa, with the cerebellum being the most common site. The three most common tumors arising in the cerebellum are pilocytic astrocytoma, medulloblastoma and ependymoma[1]. Other tumors can occur in the cerebellum, most notably atypical teratoid/rhabdoid tumors (ATRT)[3]. Paediatric brain tumors are becoming well characterized in terms of their genetic and epigenetic alterations and clinically relevant subgroups have been identified[4–7]. Metabolomics is a powerful characterizing feature of tumors that may have clinical value. *In vivo* magnetic resonance spectroscopy (MRS) has previously been used to characterize the metabolite profiles of paediatric cerebellar tumors, and reported differences in several metabolites[8]. However, *in vivo* MRS produces low resolution spectra where high concentration metabolites dominate those of a lower concentration and makes quantification of overlapping resonances difficult.

[1]Institute of Cancer and Genomic Sciences, University of Birmingham, Birmingham, UK. [2]Birmingham Children's Hospital, Birmingham, UK. [3]University Hospitals Birmingham, Birmingham, UK. [4]Bimingham University Imaging Centre (BUIC), School of Psychology, University of Birmingham, Birmingham, UK. [5]Childrens Brain Tumour Research Centre, University of Nottingham, Nottingham, UK. [6]Department of Neuropathology, Nottingham University Hospitals NHS Trust, Nottingham, UK. [7]Institute of Metabolism and Systems Research, University of Birmingham, Birmingham, UK. Correspondence and requests for materials should be addressed to A.C.P. (email: a.peet@bham.ac.uk)

Highly detailed spectroscopic studies can be performed on surgically resected tissue using high-resolution magic-angle spinning magnetic resonance spectroscopy (HR-MAS). The combination of a stronger magnetic field, the ability to rapidly spin the sample at 54.7° with regard to the magnetic field and the proximity of the radiofrequency coils to the sample leads to greatly improved spectral resolution[9] and accurate quantitation of low abundance metabolites not visible using MRS. HR-MAS has been used with great success to examine the metabolite profiles of a wide range of cancers including prostate[10], breast[11] and lung[12] cancers, as well as brain tumors from children[13] and adults[14]. Many metabolite concentrations measured by *in vivo* MRS have been shown to correlate with *ex vivo* HR-MAS[15]. Better characterization of paediatric brain tumor tissue metabolite profiles has the potential to be translated to *in vivo* MRS. Increased metabolite quantitative accuracy would provide clinicians with valuable diagnostic and prognostic information. Given that HR-MAS is able to rapidly characterize the metabolite profile of small surgically resected tissue samples without any complex preparation, it shows potential to aid the surgical management of patients undergoing surgery for cerebellar tumors in real time. The treatment protocol for each of the four tumors in this study are different, and so obtaining a real time diagnosis is crucial to a child's treatment both in terms of maximizing surgical outcome and minimizing the delay between surgery and chemo- or radiotherapy, particularly for fast growing, aggressive tumors such as ATRTs. Therefore, the primary aim of this study is to examine the diagnostic ability of HR-MAS using biopsy tissue in a retrospective manner.

Metabolism is the result of expression of metabolic enzymes, which are altered by the tumorigenic drivers of the tumors[16,17]. The concentrations of the metabolites can provide an insight into how the metabolic pathways are altered, and identify potential targets to interfere with tumor metabolism. The secondary aim of this study is to identify metabolic pathways that are differentially activated between the three tumor types.

Methods and Materials

Acquisition of tissue. Frozen diagnostic cerebellar tumor tissue for 24 pilocytic astrocytomas, 36 medulloblastomas, 18 ependymomas and 5 atypical teratoid/rhabdoid tumors (ATRTs) were acquired from Birmingham Children's Hospital (BCH) and the Children's Cancer and Leukaemia Group (CCLG) tissue banks. This study has Research Ethical Committee approval (NRES East Midlands-Derby, 04/MRE04/41) and CCLG Biological Studies Committee approval. Informed consent was obtained from the patient or parent/legal guardian. All methods were carried out in accordance with relevant guidelines and regulations. All experimental protocols were approved by the University of Birmingham. Tissue was snap frozen in liquid nitrogen shortly after surgical resection, prior to tumor treatment and stored at −80 °C. The final diagnosis was made following full histopathological examination of the tissue including immunohistochemistry where required and reviewed and agreed upon by multi-disciplinary teams.

HRMAS preparation. HR-MAS was performed at the Henry Wellcome Building Biomolecular NMR Facility at the University of Birmingham. Tissue was cut with a scalpel over dry ice to fit into a 12 μl or 50 μl zirconium rotor before being weighed. The internal standard 3-(Trimethylsilyl)propionic-2,2,3,3-d4 acid sodium salt (TMSP) (Cambridge Biosciences, Cambridge, UK) was added to the sample in a rotor dependent manner. 3 μl of standard was added to 12 μl rotors whilst 5 μl of standard was added to 50 μl rotors. D2O (Sigma Aldrich, Dorset, UK) was added to completely fill the rotor before it was fully assembled. The sample and rotor were kept cold over dry ice during preparation to prevent tissue degradation.

Spectra acquisition. Spectra were acquired using a Bruker Avance spectrometer (Bruker, Coventry, UK) with a magnetic field strength of 500 MHz fitted with a 4 mm three channel HCD HRMAS z-PFG band probe. The rotor was spun at a temperature of 4 °C to prevent metabolic activity and a frequency of 4800 Hz to remove spinning sidebands from the spectra. A NOESY pulse and acquire sequence was used with 2 s presaturation to suppress the water signal and a repetition time of 4 s. 256 or 512 averages were acquired for 50 μl and 12 μl rotors respectively. Using this protocol, an experiment with 256 averages was completed in 17 minutes.

Analysis. Free Induction Decays were Fourier transformed in Topsin 2.0 (Bruker, Coventry, UK) and the resulting spectra were imported into MestReNova 9.0.1 software suite (Mestrelab Research, Spain). To ensure quality control, the spectra were visually examined for a high signal to noise ratio, a well-defined TMSP peak and clear discrimination of the choline, phosphocholine and glycerophosphocholine peaks at 3.2–3.3 ppm. Based on *in vivo* ^{1}H and ^{31}P spectroscopy, normal tissue is expected to have a large NAA peak, small peaks corresponding to the choline containing compounds with a PCh/GPC ratio of 0.4, an intermediate creatine peak and very small lipid peaks[8,18]. Overall the metabolite profiles of these brain tumors differ greatly from normal brain tissue. The spectra were phased, baseline corrected and the chemical shift referenced with respect to TMSP at 0 ppm. Peaks were picked using the Global Spectral Deconvolution algorithm which improves the resolution of areas of the spectrum with overlapping resonances. Features were quantified by comparing the area of the peaks corresponding to the respective metabolite to the area of the internal standard peak, taking into account the number of protons contributing to both the metabolite and standard signal. Thirty one features were assigned (26 metabolites and 5 lipid groups; Supplementary Table 2) to the spectra and raw metabolite concentrations were obtained using the qNMR function in MestReNova. Experimentally acquired chemical shift information from Govindaraju *et al.*[19] and the Human Metabolome Database (HMDB)[20] were used to confirm signal assignment. Due to the low proportion of the tumors in which n-acetylaspartylglutamate and acetone could be confidently identified, and due to lactate accumulation in the tissue over a variable amount of time during surgical excision, these three metabolites were excluded from further analysis. Prior to statistical analyses, lipid concentrations were summed and the data were normalized to the sum of total non-lipid metabolite concentrations.

Normalized values were imported into the R statistical environment[21] for analyses. The differences in normalized metabolite concentrations were tested for significance using a Kruskal-Wallis test, followed by post hoc

Nemenyi tests. Bonferroni correction was applied to account for multiple comparisons. Each metabolite and total lipid was scaled to a mean of 0 and a standard deviation of 1 in order to perform principal component analysis and cluster analysis and visualize the structure of the data. Initially, a classification model was created for medulloblastoma, ependymoma and pilocytic astrocytoma cases. Principal components accounting for 90% of the total variation were then subjected to LDA. The robustness of the resulting model was assessed using a 10-fold cross validation. This technique builds the classifier on 90% of the cases selected randomly and tests it on the remaining 10% which therefore form an independent test set. The process is repeated 10 times so that all cases are included in a test set. A second model was created to incorporate the ATRT and to investigate the influence of adding rarer tumors to the analysis. Due to the low number of ATRT samples, a decision tree was used to classify samples as either embryonal or glial tumors, before attempting to classify the diagnosis. This model was validated using a leave-one-out cross validation, leading to each case being independently tested using a model created using the rest of the cohort.

Metabolic pathway analysis was conducted using the MetPA tool of Metaboanalyst 3.0[22], an online server allowing network analysis of the tumors to be performed. MetPA conducts pathway enrichment analysis and pathway topology analysis to identify metabolic pathways that are differentially activated in the samples of interest.

The datasets generated and analysed during the current study are available from the corresponding author on reasonable request.

Histopathological reports. BCH histopathological reports were available via the hospitals reporting system. The histopathological information for samples from other centres was requested through the CCLG tissue bank. For assessing the accuracy of current rapid intraoperative diagnosis, the rapid diagnosis was considered concordant if the diagnosis obtained via haematoxylin and eosin (H&E) stained smear preparations, frequently complemented by frozen sections, agreed with the final confirmed diagnosis for the case. Partial concordance was assigned when a distinct histopathological entity was diagnosed within a broader category, for example, an ependymoma described as a glial tumor.

Results

Cohort. In total, 83 samples were accrued, including 24 pilocytic astrocytomas, 18 ependymomas, 36 medulloblastomas and 5 ATRTs. The cohort features a male bias, in line with the fact that CNS tumors are known to be more prevalent in males[1] (Supplementary Table 1). There is no statistical difference between the observed and expected numbers of males and females (χ^2 $p = 0.12$).

Metabolic profiles of paediatric cerebellar tumors differ by tumor type. The HR-MAS protocol allowed the acquisition of high resolution metabolic profiles (Fig. 1). Of the 25 quantified metabolites in the analysis, 14 were significantly different between the three tumor types (Table 1). Medulloblastoma displayed significantly higher concentrations of ascorbate, aspartate, phosphocholine, taurine and lipids at 1.3 ppm and significantly lower glucose and *scyllo*-inositol. Ependymomas showed significantly higher concentrations of *myo*-inositol and glutathione and significantly lower leucine. Pilocytic astrocytoma tumors had significantly higher concentrations of glutamine and hypotaurine. When medulloblastomas and ATRTs were compared, creatine was significantly lower in ATRTs (Supplementary Table 3).

Unsupervised hierarchical clustering shows four distinct clusters (Fig. 2). The highest split in the dendrogram separates embryonal tumors from glial tumors. Each sub cluster largely corresponds with a particular tumor type. In particular, it is interesting to note that ATRT cases cluster together within one of the four sub clusters.

Paediatric cerebellar tumors can be discriminated using linear discriminant analysis (LDA). The LDA model shows clear separation of the three main tumor types (Fig. 3). The first linear discriminant function separates the medulloblastoma and pilocytic astrocytoma cases. Metabolites important for identifying medulloblastoma include phosphocholine, glycine, taurine and isoleucine. Glutamine, NAA, *scyllo*-inositol, hypotaurine and acetate are important for pilocytic astrocytoma classification. Ependymoma are separated from the other two tumor types by the second discriminant function. Metabolites important for ependymoma classification include *myo*-inositol, glycerophosphocholine, glucose and alanine.

The robustness of the model was tested using a 10-fold cross validation. Ependymoma and medulloblastoma had the joint highest classification accuracy with 94.4% of cases correctly classified. Pilocytic astrocytoma had the lowest accuracy with 91.7% of cases being classified correctly (Table 2). The high accuracy shows the model does not over fit the data and retains generalizability.

Although this study has focused on the three most common childhood tumors presenting in the cerebellum, five ATRT tumors were added to see how tumor classification was affected and how accurately this minority tumor class could be classified. Using a binary classification model validated by a leave-one-out cross validation, classification accuracies of 60% for ATRT, 83.3% for medulloblastoma, 94.4% for ependymoma and 91.7% for pilocytic astrocytoma were obtained (Supplementary Fig. 1).

Histopathological discrimination of paediatric cerebellar tumors. Ependymoma had the lowest diagnostic accuracy with 10 of the 14 cases (71%) reporting a concordant diagnosis where intra-operative preparations were assessed (Table 2). The remaining 4 cases were partially concordant; these samples were described as gliomas or low grade gliomas.

Metabolite	Mean normalized concentration			Kruskall-Wallis P value	Bonferroni corrected P value	Nemenyi post hoc P values		
	Medulloblastoma	Ependymoma	Pilocytic astrocytoma			Med vs Epen	Med vs PA	Epen vs PA
Ascorbate	0.039	0.018	0.022	3.2×10^{-5}	8.0×10^{-4}	4.0×10^{-4}	2.0×10^{-3}	N.S
Aspartate	0.0076	0.0014	0.0009	2.8×10^{-5}	7.0×10^{-4}	8.6×10^{-3}	1.0×10^{-4}	N.S
Glucose	0.002	0.014	0.019	2.5×10^{-4}	6.2×10^{-3}	1.3×10^{-2}	1.1×10^{-3}	N.S
Glutamine	0.093	0.14	0.26	1.4×10^{-9}	3.5×10^{-8}	N.S	1.4×10^{-9}	4.2×10^{-3}
GPC	0.014	0.031	0.036	2.2×10^{-5}	5.5×10^{-4}	N.S	2.6×10^{-5}	N.S
Glutathione	0.026	0.041	0.023	1.0×10^{-4}	2.5×10^{-3}	N.S	3.6×10^{-2}	1.1×10^{-4}
Hypotaurine	0.022	0.017	0.045	1.3×10^{-4}	3.2×10^{-3}	N.S	2.2×10^{-2}	1.7×10^{-4}
Leucine	0.0082	0.0014	0.0096	1.7×10^{-4}	4.2×10^{-3}	1.7×10^{-4}	N.S	3.7×10^{-2}
Myo inositol	0.12	0.28	0.13	2.0×10^{-7}	5.0×10^{-6}	6.5×10^{-7}	N.S	4.1×10^{-5}
NAA	0.013	0.0036	0.025	3.5×10^{-7}	8.8×10^{-6}	4.2×10^{-3}	1.9×10^{-2}	3.5×10^{-7}
PCh	0.12	0.03	0.03	1.3×10^{-10}	3.3×10^{-9}	2.5×10^{-6}	1.6×10^{-8}	N.S
Scyllo inositol	0.0019	0.0072	0.008	1.2×10^{-5}	3.0×10^{-4}	2.3×10^{-4}	8.0×10^{-4}	N.S
Succinate	0.0024	0.0049	0.0099	7.7×10^{-5}	1.9×10^{-3}	N.S	7.9×10^{-5}	N.S
Taurine	0.17	0.088	0.037	6.6×10^{-11}	1.7×10^{-9}	8.9×10^{-3}	8.1×10^{-11}	1.4×10^{-2}

Table 1. Kruskal Wallis tests identify 14 metabolites with concentrations that vary according to diagnosis. Post hoc tests identify which tumors have significantly different metabolite concentrations. Abbreviations – GPC, glycerophosphocholine; NAA, N-acetylaspartate; PCh, phosphocholine.

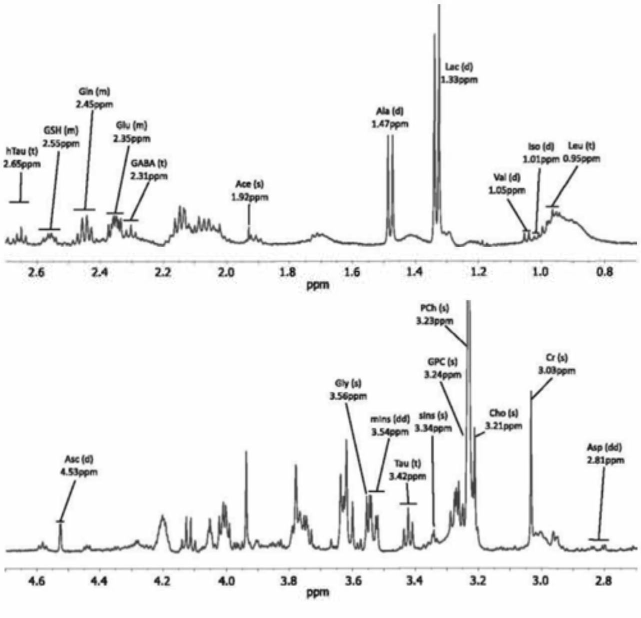

Figure 1. Example spectrum of a medulloblastoma acquired using HR-MAS. Metabolite assignments are shown along with their peak pattern. The resolution of the spectrum allows the accurate assignment and quantitation of a range of metabolites. Abbreviations: s - singlet, d – doublet, dd – doublet of doublets, t – triplet, m – multiplet, Ace – acetate, Ala – alanine, Asc – ascorbate, Asp – aspartate, Cho – Choline, Cr – Creatine, GABA - gamma-aminobutyric acid, Gln – glutamine, Glu – Glutamate, Gly – Glycine, GSH – glutathione, Htau – hypotaurine, Iso – Isoleucine, Leu – leucine, mIns - *myo*-inositol, sIns - *scyllo*-inositol, Tau – taurine, Val - valine.

The pilocytic astrocytoma group were intermediate in the analysis, with 16 of 18 cases (89%) reporting a concordant diagnosis where an intra-operative diagnosis was given. The remaining two cases were discordant and were diagnosed as medulloblastoma and ependymoma.

Classification accuracy of linear discriminant analysis				
	Ependymoma	Medulloblastoma	Pilocytic astrocytoma	% correct
Ependymoma	17	0	1	94.4
Medulloblastoma	1	34	1	94.4
Pilocytic astrocytoma	1	1	22	91.7
Rapid intraoperative histopathological diagnostic accuracy				
	Number of concordant diagnoses	**Number of partially concordant diagnoses**	**Number of discordant diagnoses**	**% concordant**
Ependymoma	10	4	0	71.4
Medulloblastoma	28	1	2	90.3
Pilocytic astrocytoma	16	0	2	88.9

Table 2. The cross-validated diagnostic accuracy of the LDA for the three cerebellar tumor types. The linear discriminant classifier achieved accuracies greater than 90% for all three tumor types. Furthermore, for all tumor types, the classification accuracy was greater than the rapid intraoperative diagnostic examination; however, this appears to be due to partial concordance as opposed to an incorrect diagnosis.

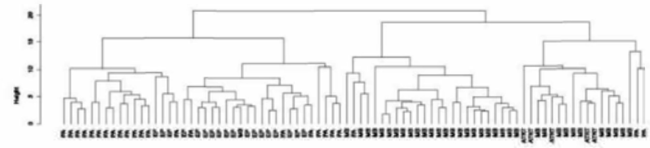

Figure 2. Hierarchical clustering of paediatric cerebellar tumors based on metabolite concentrations. The highest split in the figure separates glial tumors from embryonal tumors. The subsequent split broadly separates the tumor types. Abbreviations: MB, medulloblastoma; EP, ependymoma; PA, pilocytic astrocytoma; ATRT, Atypical Teratoid/Rhabdoid Tumor.

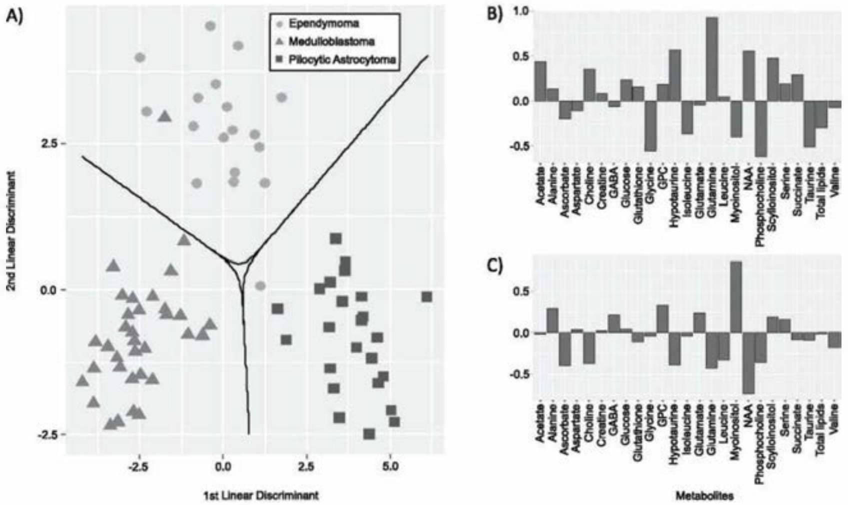

Figure 3. The output of the linear discriminant analysis. (**A**) The LDA scatterplot displays clear separation of the ependymoma (n = 18), medulloblastoma (n = 36) and pilocytic astrocytoma (n = 24). The decision boundaries, shown by the solid line, define the regions of the plot for each tumor type. (**B**) The loadings for the first discriminant function. The metabolites with more negative loadings are important for medulloblastoma classification, whilst metabolites with more positive loadings are important for pilocytic astrocytoma classification. (**C**) The loadings for the second discriminant function. Metabolites with more positive loadings are important for separating ependymoma from the other two tumor types. Abbreviations – GABA, gamma-aminobutyric acid; GPC, glycerophosphocholine; NAA, N-acetylaspartate; PCh, phosphocholine.

Metabolic pathway	Total number of compounds	Hits	P value	Impact	Pairwise P values		
					Med vs Epen	Med vs PA	Epen vs PA
Glycerophospholipid metabolism	39	4	5.5×10^{-20}	0.20	1.0×10^{-8}	8.6×10^{-11}	N.S.
Taurine and hypotaurine metabolism	20	4	3.6×10^{-15}	0.44	1.9×10^{-3}	9.1×10^{-9}	4.9×10^{-5}
Alanine, aspartate and glutamate metabolism	24	7	5.2×10^{-15}	0.81	6.0×10^{-3}	3.2×10^{-11}	2.0×10^{-4}
Arginine and proline metabolism	77	5	1.3×10^{-14}	0.087	5.9×10^{-3}	4.8×10^{-11}	2.5×10^{-4}

Table 3. The top 4 most significantly different pathways between the three most common cerebellar tumors. Glycerophospholipid metabolism is enriched in medulloblastoma compared to the other two tumor types. The alanine, aspartate and glutamate metabolism pathway has the highest topological metric, and it is likely that this pathway is strongly associated with tumor type.

Medulloblastoma had the highest rate of concordant diagnoses using rapid intraoperative preparations, with 28 of the 31 cases (90%). Two cases were discordant; one case was thought to represent an astrocytoma whilst the other a low grade glioma. The remaining case was partially concordant as it was diagnosed as a malignant intrinsic tumor. Of the 5 ATRT cases, 2 (40%) reported a concordant diagnosis. The remaining 3 were partially concordant; two were given with a medulloblastoma differential diagnosis and one was described as a high grade tumor.

The individual metabolite profile classification results of the partially concordant and discordant cases were reviewed. All partially concordant and discordant pilocytic astrocytoma, ependymoma and medulloblastoma were correctly classified by the LDA. Of the 3 partially concordant ATRT cases, 1 was correctly classified by the decision tree, whilst 1 was classified as an ependymoma and the other as a medulloblastoma.

Metabolic pathways are altered between the three main tumor types. The normalized metabolite concentrations were submitted to the MetPA online tool[22] for pathway analysis to identify altered pathways between the tumor groups. The four most statistically differentially activated pathways were: glycerophospholipid metabolism; taurine and hypotaurine metabolism; alanine, aspartate and glutamate metabolism; and arginine and proline metabolism (Table 3). The alanine, aspartate and glutamate had the highest impact factor, indicating that the key metabolites in this pathway were present in the analysis and that the tumors use these metabolites differently relative to each other. Conversely, arginine and proline metabolism had the lowest impact factor of the four pathways, indicating a lack of key metabolite quantification. Post hoc tests revealed that glycerophospholipid metabolism is enriched in medulloblastoma relative to the other two tumor types.

Discussion

This work has demonstrated that the metabolite profiles of *ex vivo* tumor tissue are different for the three major paediatric tumors of the cerebellum through unsupervised analysis, and are sufficiently different that robust diagnostic classifiers can be built with high rates of diagnostic accuracy. Also, we have shown that metabolic pathway analysis using quantified metabolites can identify pathways with altered activity between tumor types giving the potential for future targeted treatments. Given the ease of sample handling, the short data acquisition time and potential for automated analysis, the technique could find a role in aiding clinical diagnosis. Although not investigated for the samples in this work, HR-MAS is a non-destructive method and prior studies suggest that post analysis tissue is of suitable quality for subsequent histological and molecular analysis[23,24]. HR-MAS and *in vivo* MRS share the same technical principles, therefore tissue studies such as ours can be used to inform and refine non-invasive spectroscopic examination.

Alternative tissue based techniques have been proposed in the literature to aid the real time surgical management of patients. The alternative metabolomic technique, mass spectrometry, has been shown to have potential with regards to diagnosing pediatric brain tumors[25]. Unlike HR-MAS, the metabolites must be extracted from the tissue rendering it unavailable for further study. Raman spectroscopy and optical coherence tomography are two non-metabolomic techniques that have been shown to have intra-operative diagnostic potential for brain tumors[26,27]. Both are limited by the tissue penetrance they can achieve. Due to their intrinsic technical properties, none of the above three techniques can be translated to a non-invasive methodology.

The *ex vivo* spectroscopy provides further evidence for characteristic metabolite profiles of these tumor types. In particular, high phosphocholine and taurine in medulloblastoma, high glutamine in pilocytic astrocytoma and high *myo*-inositol in ependymoma tumors were important for tumor identification. Previous work[28] has compared the metabolite profiles of paediatric cerebellar tumors and our studies agree on most of the key characteristic metabolite markers. Our study showed that *myo*-inositol is higher in concentration in ependymoma than medulloblastoma, agreeing with *in vivo* MRS but contrary to the findings reported in Cuellar-Baena *et al.*[28] This is likely to be a consequence of the larger sample size in our study particularly for ependymoma. Furthermore, our study constructs an accurate and robust classifier with clinical utility and identifies metabolic pathways with different activity.

It has been shown that the most concentrated metabolites in brain tumors are quantifiable *in vivo* and correlate with the *ex vivo* spectroscopy[15]. Further technical development of *in vivo* MRS has shown that it is possible to accurately measure the concentration of metabolites with overlapping resonances[29–31]. Therefore, the metabolites described in this work have the potential be to be used as diagnostic markers.

The decision boundaries clearly separate the tumor types, with only two cases lying outside the decision boundary for their respective tumor type. It is interesting to note the loadings of the discriminant analysis reflect the findings of the average concentrations of the metabolites discussed previously, confirming that typical spectroscopic features can be used to separate the three tumor types. The classification algorithm is robust against overfitting, as demonstrated by the high classification accuracy after 10-fold cross validation.

Whilst our preliminary results for ATRT classification are encouraging, incorporation of rare tumor types may require statistical oversampling methods to compensate for the large differences in tumor frequency[32]. ATRT are rare but important tumors in childhood; they represent the majority of the tumors in the cerebellum which are not medulloblastomas, pilocytic astrocytomas or ependymomas and commonly represent a diagnostic dilemma particularly with medulloblastoma[33]. They are particularly aggressive tumors with a very poor prognosis and for which it is essential that maximal resection is obtained and that adjuvant treatment is started as soon as possible. There is currently no rapid diagnostic test for this tumor group since diagnosis relies on immunohistochemical staining for INI1. On an interesting note, the classification accuracy for pilocytic astrocytoma and ependymoma remain the same when ATRTs are incorporated. Therefore, metabolite profiles are able to confidently identify and separate glial and embryonal tumors, which is important if the tumor in question is a rare entity.

HR-MAS has shown promise for examining tissue from several cancer types[10,11], and may be used to complement the histological data. Indeed, some work has been published on the use of rapid metabolite profiling and its clinical application in the surgical management of tumors[34] which reported histopathology matching tumor identification in 17 mins. With metabolism under the control of the oncogenic drivers, HR-MAS has the potential to identify tumor subgroups in a short time frame, as shown in adults with SDH mutated paraganglioma or pheochromocytoma[35] or IDH mutated gliomas[36]. HR-MAS also has the ability to identify novel metabolic subgroups which correlate with histopathological features. This was demonstrated in retinoblastoma where 3 clinicopathological subgroups were identified in which taurine, lipids and phosphosholine correlated with differentiation, necrosis and invasion respectively[37]. Other work performed using neuroblastoma tissue found taurine correlated with a worse prognosis whilst glutamine, *myo*-inositol and glycine was associated with stage I-II neuroblastoma[38]. Whilst our study has not attempted to classify tumors into recognized molecular subgroups, there is evidence that MRS is able to identify medulloblastoma molecular subgroup[39] and this warrants further investigation. Brain tumors in adults are different in terms of the types of tumors and their anatomical location[40]. HR-MAS has been used to predict grade of astrocytic tumors[41], and assess the extent of microheterogeneity in glioblastoma[23].

To put the accuracy of the HR-MAS classification into context, a comparison was made with accuracy of current rapid intraoperative assessment using clinical reports for the tissue used in this analysis. Rapid intraoperative testing consists of smear cytological preparations often complemented by frozen sections stained with H&E to assess the cytological aspect as well as architectural features[42]. This method is cheap, rapid without the need for expensive equipment and gives reasonably accurate results to guide surgical management decisions.

The results of our analysis broadly agree with published retrospective analyses of rapid intraoperative assessment[43,44]; complete agreement of the rapid intraoperative assessment and final histological diagnosis is achieved in the majority of astrocytoma and medulloblastoma cases. Ependymoma, however, have a higher rate of partial concordance. Currently, the greatest prognostic marker for ependymoma is extent of surgical resection[45], therefore it is imperative to identify ependymomas and optimize surgical treatment. Although there were no discordant ependymoma diagnoses by intraoperative assessment in our study, the partially concordant diagnoses could include tumors for which a complete resection is far less important. HR-MAS may aid in the identification of such tumors in real time and improve surgical management when intraoperative H&E assessment is ambiguous. In support of this, the metabolite profiles of the partially concordant and discordant pilocytic astrocytoma, ependymoma and medulloblastoma were not different from those of their respective tumor types. Metabolite profiles aided in the identification of one of the partially concordant ATRT cases, but not in the other two.

The pathway analysis identified metabolic pathways that were differentially activated between the three tumor types. Of these pathways, the alanine, glutamate and aspartate metabolic pathway had the highest impact factor. Therefore, it is likely that the biochemistry within this pathway is different between tumor groups. This pathway is closely linked to supplementing the tricarboxylic acid cycle through the conversion of amino acids to TCA cycle intermediaries[46] and provides nitrogen for the de novo nucleotide synthesis[47]. Upregulation of glutamine catabolising pathways has been linked to more aggressive, higher grade tumors which rely on glutaminolysis to support their increased proliferation[48]. Consequently, lower glutamine is observed in medulloblastoma and ependymoma compared to pilocytic astrocytoma.

Hypotaurine and taurine metabolism and glycerophospholipid metabolism also differed between the tumor types. The high concentration of taurine in embryonal tumors is likely related to their developmental stage when compared to the glial ependymoma and pilocytic astrocytoma, as high taurine concentration has been described in other paediatric embryonal CNS tumors[37,49]. Taurine has been shown to be important for neuronal stem cell proliferation and neurogenesis[50,51] and the migration of neuronal cells from the external to the internal granular layer in the cerebellum[52]. Hypotaurine is a poorly understood metabolite whose function is not clear and warrants further study to elucidate its role in normal and neoplastic tissue.

Glycerophospholipid metabolism is primarily responsible for synthesizing components for cellular and organelle membranes. Alterations in choline metabolism is a hallmark of malignancies[53]. In brain tumors, increased concentration of choline containing compounds as detected by *in vivo* ^{1}H MRS have been associated with higher grade[54]. In addition, ^{31}P MRS has identified alterations in the ratios of phosphorylated choline metabolites between normal tissue and brain tumors[18]. This is supported by *ex vivo* work, where it was shown that phosphocholine concentration correlated with grade, phospholipase C and choline kinase β expression[55]. These factors influencing synthesis may explain the observed increase in phosphocholine concentration in medulloblastoma tissue. As well as meeting the cells biosynthetic needs, this pathway is involved in intracellular signalling. The action of phospholipase C enzymes generates diacylglycerol and a free head group such as phosphocholine or phosphoinositol which act as secondary messengers. Our results suggest this pathway is enriched in medulloblastoma, and is an ideal candidate pathway for further examination to identify targeted therapies.

The arginine and proline metabolism pathway was detected to be significantly different between the three tumor types. HR-MAS is not able to identify the very low abundance key metabolites in this pathway, leading to a low impact score and an inability to draw firm conclusions regarding this pathway. Further examination of the metabolic pathways using other more sensitive metabolomic approaches will improve the metabolome coverage and lead to a more comprehensive metabolic pathway analysis. This approach will be vital to gaining a complete understanding of how metabolism varies between these tumor types and identify potential treatment targets.

In conclusion, this study has shown that HR-MAS can detect characteristic metabolic profiles from small pieces of fresh frozen biopsy tissue which can be used to build an accurate and clinically relevant classifier, with potential for future development as an intraoperative technique for improved surgical management. It has also shown that biological information can be extracted and differentially activated metabolic pathways can start to be identified. This may lead to improved insights into the metabolism of these tumors and the development of targeted therapies.

References

1. Ostrom, Q. T. *et al.* Alex's Lemonade Stand Foundation Infant and Childhood Primary Brain and Central Nervous System Tumors Diagnosed in the United States in 2007–2011. *Neuro-oncology* **16**, x1–x36, https://doi.org/10.1093/neuonc/nou327 (2015).
2. Smith, M. A. *et al.* Outcomes for children and adolescents with cancer: challenges for the twenty-first century. *Journal of clinical oncology: official journal of the American Society of Clinical Oncology* **28**, 2625–2634, https://doi.org/10.1200/jco.2009.27.0421 (2010).
3. Parwani, A. V., Stelow, E. B., Pambuccian, S. E., Burger, P. C. & Ali, S. Z. Atypical teratoid/rhabdoid tumor of the brain. *Cancer Cytopathology* **105**, 65–70, https://doi.org/10.1002/cncr.20872 (2005).
4. Taylor, M. D. *et al.* Molecular subgroups of medulloblastoma: the current consensus. *Acta Neuropathologica* **123**, 465–472, https://doi.org/10.1007/s00401-011-0922-z (2012).
5. Pajtler, K. W. *et al.* Molecular Classification of Ependymal Tumors across All CNS Compartments, Histopathological Grades, and Age Groups. *Cancer cell* **27**, 728–743, https://doi.org/10.1016/j.ccell.2015.04.002 (2015).
6. Forshew, T. *et al.* Activation of the ERK/MAPK pathway: a signature genetic defect in posterior fossa pilocytic astrocytomas. *The Journal of pathology* **218**, 172–181, https://doi.org/10.1002/path.2558 (2009).
7. Jones, D. T. *et al.* Tandem duplication producing a novel oncogenic BRAF fusion gene defines the majority of pilocytic astrocytomas. *Cancer research* **68**, 8673–8677, https://doi.org/10.1158/0008-5472.can-08-2097 (2008).
8. Davies, N. P. *et al.* Identification and characterisation of childhood cerebellar tumours by *in vivo* proton MRS. *NMR in biomedicine* **21**, 908–918, https://doi.org/10.1002/nbm.1283 (2008).
9. Andrew, E. R. & Newing, R. A. The Narrowing of Nuclear Magnetic Resonance Spectra by Molecular Rotation in Solids. *Proceedings of the Physical Society* **72**, 959, https://doi.org/10.1088/0370-1328/72/6/304 (1958).
10. Decelle, E. A. & Cheng, L. L. High-resolution magic angle spinning 1H MRS in prostate cancer. *NMR in biomedicine* **27**, 90–99, https://doi.org/10.1002/nbm.2944 (2014).
11. Sitter, B. *et al.* Comparison of HR MAS MR spectroscopic profiles of breast cancer tissue with clinical parameters. *NMR in biomedicine* **19**, 30–40, https://doi.org/10.1002/nbm.992 (2006).
12. Rocha, C. M. *et al.* Metabolic profiling of human lung cancer tissue by 1H high resolution magic angle spinning (HRMAS) NMR spectroscopy. *Journal of proteome research* **9**, 319–332, https://doi.org/10.1021/pr9006574 (2010).
13. Wilson, M. *et al.* High resolution magic angle spinning 1H NMR of childhood brain and nervous system tumours. *Molecular Cancer* **8**, 6–6, https://doi.org/10.1186/1476-4598-8-6 (2009).
14. Wright, A. *et al.* *Ex-vivo* HRMAS of adult brain tumours: metabolite quantification and assignment of tumour biomarkers. *Molecular Cancer* **9**, 66, https://doi.org/10.1186/1476-4598-9-66 (2010).
15. Wilson, M., Davies, N. P., Grundy, R. G. & Peet, A. C. A quantitative comparison of metabolite signals as detected by *in vivo* MRS with *ex vivo* 1H HR-MAS for childhood brain tumours. *NMR in biomedicine* **22**, 213–219, https://doi.org/10.1002/nbm.1306 (2009).
16. Morrish, F., Isern, N., Sadilek, M., Jeffrey, M. & Hockenbery, D. M. c-Myc activates multiple metabolic networks to generate substrates for cell-cycle entry. *Oncogene* **28**, 2485–2491, https://doi.org/10.1038/onc.2009.112 (2009).
17. Berkers, C. R., Maddocks, O. D., Cheung, E. C., Mor, I. & Vousden, K. H. Metabolic regulation by p53 family members. *Cell Metab* **18**, 617–633, https://doi.org/10.1016/j.cmet.2013.06.019 (2013).
18. Novak, J. *et al.* Clinical protocols for (3)(1)P MRS of the brain and their use in evaluating optic pathway gliomas in children. *European journal of radiology* **83**, e106–112, https://doi.org/10.1016/j.ejrad.2013.11.009 (2014).
19. Govindaraju, V., Young, K. & Maudsley, A. A. Proton NMR chemical shifts and coupling constants for brain metabolites. *NMR in biomedicine* **13**, 129–153, https://doi.org/10.1002/1009-1492(200005)13:3<129::AID-NBM619>3.0.CO;2-V (2000).
20. Wishart, D. S. *et al.* HMDB 3.0–The Human Metabolome Database in 2013. *Nucleic acids research* **41**, D801–807, https://doi.org/10.1093/nar/gks1065 (2013).
21. R: A Language and Environment for Statistical Computing. R Foundation for Statistical Computing, Vienna, Austria. https://www.R-project.org/ (2015).
22. Xia, J., Sinelnikov, I. V., Han, B. & Wishart, D. S. MetaboAnalyst 3.0–making metabolomics more meaningful. *Nucleic acids research*, https://doi.org/10.1093/nar/gkv380 (2015).
23. Cheng, L. L. *et al.* Quantification of microheterogeneity in glioblastoma multiforme with *ex vivo* high-resolution magic-angle spinning (HRMAS) proton magnetic resonance spectroscopy. *Neuro-oncology* **2**, 87–95, https://doi.org/10.1093/neuonc/2.2.87 (2000).
24. Tzika, A. A. *et al.* Combination of high-resolution magic angle spinning proton magnetic resonance spectroscopy and microscale genomics to type brain tumor biopsies. *International journal of molecular medicine* **20**, 199–208, https://doi.org/10.3892/ijmm.20.2.199 (2007).
25. Woolman, M. *et al.* Rapid determination of medulloblastoma subgroup affiliation with mass spectrometry using a handheld picosecond infrared laser desorption probe. *Chemical Science* **8**, 6508–6519, https://doi.org/10.1039/c7sc01974b (2017).
26. Leslie, D. G. *et al.* Identification of pediatric brain neoplasms using Raman spectroscopy. *Pediatric neurosurgery* **48**, 109–117, https://doi.org/10.1159/000343285 (2012).
27. Kut, C. *et al.* Detection of Human Brain Cancer Infiltration *ex vivo* and *in vivo* Using Quantitative Optical Coherence Tomography. *Sci Transl Med* **7**, 292ra100, https://doi.org/10.1126/scitranslmed.3010611 (2015).
28. Cuellar-Baena, S. *et al.* Comparative metabolic profiling of paediatric ependymoma, medulloblastoma and pilocytic astrocytoma. *International journal of molecular medicine* **26**, 941–948, https://doi.org/10.3892/ijmm_00000546 (2010).
29. Choi, C. *et al.* Measurement of brain glutamate and glutamine by spectrally-selective refocusing at 3 Tesla. *Magnetic resonance in medicine* **55**, 997–1005, https://doi.org/10.1002/mrm.20875 (2006).
30. Hurd, R. *et al.* Measurement of brain glutamate using TE-averaged PRESS at 3T. *Magnetic resonance in medicine* **51**, 435–440, https://doi.org/10.1002/mrm.20007 (2004).

31. Jang, D. P. *et al.* Interindividual reproducibility of glutamate quantification using 1.5-T proton magnetic resonance spectroscopy. *Magnetic resonance in medicine* **53**, 708–712, https://doi.org/10.1002/mrm.20387 (2005).
32. Zarinabad, N. *et al.* Multiclass imbalance learning: Improving classification of pediatric brain tumors from magnetic resonance spectroscopy. *Magnetic resonance in medicine* **77**, 2114–2124, https://doi.org/10.1002/mrm.26318 (2017).
33. Reddy, A. T. Atypical teratoid/rhabdoid tumors of the central nervous system. *Journal of neuro-oncology* **75**, 309–313, https://doi.org/10.1007/s11060-005-6762-8 (2005).
34. Piotto, M. *et al.* Towards real-time metabolic profiling of a biopsy specimen during a surgical operation by 1H high resolution magic angle spinning nuclear magnetic resonance: a case report. *Journal of Medical Case Reports* **6**, 22, https://doi.org/10.1186/1752-1947-6-22 (2012).
35. Imperiale, A. *et al.* Metabolome Profiling by HRMAS NMR Spectroscopy of Pheochromocytomas and Paragangliomas Detects SDH Deficiency: Clinical and Pathophysiological Implications()(). *Neoplasia (New York, N.Y.)* **17**, 55–65, https://doi.org/10.1016/j.neo.2014.10.010 (2015).
36. Elkhaled, A. *et al.* Magnetic Resonance of 2-Hydroxyglutarate in IDH1-Mutated Low-Grade Gliomas. *Science translational medicine* **4**, 116ra115–116ra115, https://doi.org/10.1126/scitranslmed.3002796 (2012).
37. Kohe, S. *et al.* Metabolite profiling in retinoblastoma identifies novel clinicopathological subgroups. *British journal of cancer* **113**, 1216–1224, https://doi.org/10.1038/bjc.2015.318 (2015).
38. Imperiale, A. *et al.* Metabolomic pattern of childhood neuroblastoma obtained by (1)H-high-resolution magic angle spinning (HRMAS) NMR spectroscopy. *Pediatric blood & cancer* **56**, 24–34, https://doi.org/10.1002/pbc.22668 (2011).
39. Bluml, S. *et al.* Molecular subgroups of medulloblastoma identification using noninvasive magnetic resonance spectroscopy. *Neuro-oncology* **18**, 126–131, https://doi.org/10.1093/neuonc/nov097 (2016).
40. Ostrom, Q. T. *et al.* CBTRUS Statistical Report: Primary brain and other central nervous system tumors diagnosed in the United States in 2010–2014. *Neuro-oncology* **19**, v1–v88, https://doi.org/10.1093/neuonc/nox158 (2017).
41. Elkhaled, A. *et al.* Characterization of metabolites in infiltrating gliomas using *ex vivo* (1)H high-resolution magic angle spinning spectroscopy. *NMR in biomedicine* **27**, 578–593, https://doi.org/10.1002/nbm.3097 (2014).
42. Mitra, S., Kumar, M., Sharma, V. & Mukhopadhyay, D. Squash preparation: A reliable diagnostic tool in the intraoperative diagnosis of central nervous system tumors. *Journal of cytology/Indian Academy of Cytologists* **27**, 81–85, https://doi.org/10.4103/0970-9371.71870 (2010).
43. Krishnani, N., Kumari, N., Behari, S., Rana, C. & Gupta, P. Intraoperative squash cytology: accuracy and impact on immediate surgical management of central nervous system tumours. https://doi.org/10.1111/j.1365-2303.2011.00905.x (2012).
44. Roessler, K., Dietrich, W. & Kitz, K. High diagnostic accuracy of cytologic smears of central nervous system tumors. A 15-year experience based on 4,172 patients. https://doi.org/10.1159/000326973 (2002).
45. Lin, F. Y. & Chintagumpala, M. Advances in Management of Pediatric Ependymomas. *Current Oncology Reports* **17**, 1–7, https://doi.org/10.1007/s11912-015-0470-0 (2015).
46. DeBerardinis, R. J. *et al.* Beyond aerobic glycolysis: Transformed cells can engage in glutamine metabolism that exceeds the requirement for protein and nucleotide synthesis. *Proceedings of the National Academy of Sciences* **104**, 19345–19350, https://doi.org/10.1073/pnas.0709747104 (2007).
47. Patel, D. *et al.* Aspartate Rescues S-phase Arrest Caused by Suppression of Glutamine Utilization in KRas-driven Cancer Cells. *The Journal of Biological Chemistry* **291**, 9322–9329, https://doi.org/10.1074/jbc.M115.710145 (2016).
48. Panosyan, E. H. *et al.* Clinical aggressiveness of malignant gliomas is linked to augmented metabolism of amino acids. *Journal of neuro-oncology* **128**, 57–66, https://doi.org/10.1007/s11060-016-2073-5 (2016).
49. Kohe, S. E. *et al.* Metabolic profiling of the three neural derived embryonal pediatric tumors retinoblastoma, neuroblastoma and medulloblastoma, identifies distinct metabolic profiles. *Oncotarget* **9**, 11336–11351, https://doi.org/10.18632/oncotarget.24168 (2018).
50. Hernandez-Benitez, R., Pasantes-Morales, H., Saldana, I. T. & Ramos-Mandujano, G. Taurine stimulates proliferation of mice embryonic cultured neural progenitor cells. *Journal of neuroscience research* **88**, 1673–1681, https://doi.org/10.1002/jnr.22328 (2010).
51. Hernandez-Benitez, R., Ramos-Mandujano, G. & Pasantes-Morales, H. Taurine stimulates proliferation and promotes neurogenesis of mouse adult cultured neural stem/progenitor cells. *Stem cell research* **9**, 24–34, https://doi.org/10.1016/j.scr.2012.02.004 (2012).
52. Sturman, J. A., Moretz, R. C., French, J. H. & Wisniewski, H. M. Taurine deficiency in the developing cat: persistence of the cerebellar external granule cell layer. *Journal of neuroscience research* **13**, 405–416, https://doi.org/10.1002/jnr.490130307 (1985).
53. Glunde, K., Bhujwalla, Z. M. & Ronen, S. M. Choline metabolism in malignant transformation. *Nature reviews. Cancer* **11**, 835–848, https://doi.org/10.1038/nrc3162 (2011).
54. Hourani, R. *et al.* Proton magnetic resonance spectroscopic imaging to differentiate between nonneoplastic lesions and brain tumors in children. *Journal of magnetic resonance imaging: JMRI* **23**, 99–107, https://doi.org/10.1002/jmri.20480 (2006).
55. Righi, V. *et al.* 1H HR-MAS and genomic analysis of human tumor biopsies discriminate between high and low grade astrocytomas. *NMR in biomedicine* **22**, 629–637, https://doi.org/10.1002/nbm.1377 (2009).

Acknowledgements

We would like to thank all members of staff at the Henry Wellcome Building NMR facility at the University of Birmingham for their technical support and all clinical and histopathological staff involved in tissue collection and storage. This work was funded by grants from the NIHR (NIHR-RP-02-12-019), Action Medical Research and the Brain Tumour Charity (GN2181), Birmingham Children's Hospital Research Foundation (BCHRF353) and Children with Cancer (15–188). The CCLG tissue bank is funded by the CCLG and Cancer Research UK. We would also like to thank the Andrew McCartney Trust Fund and Poppy Fields Appeal for their support.

Author Contributions

Conception and design: C.D.B., A.C.P. Collection and organization of samples and clinical information: C.D.B., S.E.K., S.K.G., L.C.D.S., T.R., S.M.L.P., I.S.S., I.N.W., R.G.G. Raw data collection and design of 1H-MRS protocols: C.D.B., S.E.K., S.K.G., M.W. Data processing and analysis of metabolite concentrations: C.D.B., S.E.K., S.K.G. Statistical and pathway analysis: C.D.B. Writing of draft manuscript: C.D.B. Revision and preparation of final manuscript: C.D.B, S.E.K., D.A.T., A.C.P. Financial support: N.P.D, A.C.P. Overall supervision of the work: A.C.P. All authors read and approved the content of the final manuscript.

Additional Information

Supplementary information accompanies this paper at https://doi.org/10.1038/s41598-018-30342-8.

Competing Interests: The authors declare no competing interests.

Appendix 4 – First author conference abstracts

17th International Symposium on Pediatric Neuro-Oncology, Liverpool, 2016

Tissue metabolite profiles in the characterisation and diagnosis of childhood posterior fossa tumours

[1,2]Christopher D. Bennett, [1,2]Simrandip K. Gill, [1,2]Sarah Kohe, [1,2]Niloufar Zarinabad, [2,3]Nigel P. Davies, [4]Martin Wilson, [5]Lisa Storer, [5]Timothy Ritzmann, [6]Simon Paine, [6]Ian Scott, [2]Ina Nicklaus, [5]Richard G. Grundy and [1,2]Andrew C. Peet

[1]Institute of Cancer and Genomic Sciences, University of Birmingham, Birmingham, UK, [2]Birmingham Children's Hospital, Birmingham, UK, [3]University Hospitals Birmingham, Birmingham, UK, [4]Bimingham University Imaging Centre (BUIC), School of Psychology, University of Birmingham, Birmingham, UK, [5]Childrens Brain Tumour Research Centre, Queen's Medical Centre, University of Nottingham, Nottingham, UK, [6]Department of Neuropathology, Queen's Medical Centre, University of Nottingham, Nottingham, UK

In vivo metabolite profiles are a powerful characteristic of children's posterior fossa tumours and can be used to aid their non-invasive diagnosis. However, information is limited to a small number of detectable metabolites and it is challenging to accrue representative numbers of rare tumours. Tissue metabolite profiles can be obtained on small samples (10 to 50mg) using high resolution magic angle spinning magnetic resonance spectroscopy (HRMAS). This technique can rapidly acquire metabolite profiles providing more extensive metabolite information than available in vivo. The use of tissue banks can help to provide more samples on the rarer tumour types such as ependymoma aiding their characterisation. Metabolite profiles were obtained from freshly frozen ependymomas (n=18), medulloblastomas (n=37) and pilocytic astrocytomas (n=24) using HRMAS and concentrations were quantified using the Mestrenova software package. Automated pattern recognition techniques were used to classify the samples according to tumour type. Elevated myo-inositol was characteristic of ependymoma whilst high taurine, phosphocholine and glycine distinguished medulloblastoma. Glutamine, hypotaurine and NAA were increased in pilocytic astrocytoma. Metabolite profiles gave a cross-validated diagnostic accuracy of 94%, 92% and 88% for ependymoma, medulloblastoma and pilocytic astrocytoma respectively. Metabolite profiles of tissue can classify posterior fossa tumours with enhanced metabolite information. The strength of HRMAS lies in its ability to rapidly obtain metabolite profiles from small pieces of tissue in a non-destructive manner. The tissue retains its protein markers and structure, and so is available for future immunohistochemical staining and other investigative techniques on the same piece of tissue.

18th International Symposium on Pediatric Neuro-Oncology, Denver, 2018, Abstract 1

Mass spectrometry of common cerebellar tumours identifies differences in metabolism

Christopher D. Bennett[1,2], Sarah E. Kohe[1,2], Simrandip K. Gill[1,2], Nigel P. Davies[2,3], Lisa C.D. Storer[4], Timothy Ritzmann[4], Warwick B. Dunn[5,6], Daniel A. Tennant[6], Richard G. Grundy[4], Andrew C. Peet[1,2]

[1]Institute of Cancer and Genomic Sciences, University of Birmingham, Birmingham, UK

[2]Birmingham Children's Hospital, Birmingham, UK

[3]University Hospitals Birmingham NHS Foundation Trust, Birmingham, UK

Childrens Brain Tumour Research Centre, University of Nottingham, Nottingham, UK

[5]Phenome Centre Birmingham, School of Biosciences, University of Birmingham, Birmingham, UK

[6]Institute of Metabolism and Systems Research, University of Birmingham, Birmingham, UK

Metabolic profiling by Magnetic Resonance Spectroscopy has shown the three most common paediatric cerebellar tumours are metabolically distinct; however, these techniques are limited by their sensitivity. Mass spectrometry is more sensitive and able to detect many more metabolites. In this study, metabolic phenotyping was performed to investigate the water-soluble metabolome and the lipidome of the three most common paediatric cerebellar tumours with the aim of informing a detailed metabolic pathway analysis.

A discovery based experiment was performed on 60 surgically resected snap frozen pilocytic astrocytomas, ependymomas and medulloblastomas using UPLC-MS assays to detect water soluble and lipid metabolites.

Principal component analysis demonstrates separation of the tumours based on the relative concentration of thousands of detected metabolites. The relative concentrations of glucose and glycolytic intermediates varied between the tumour types, as did metabolites involved in purine and pyrimidine metabolism. Key metabolites within the taurine metabolism pathway were found to be higher in medulloblastoma. Alterations were observed in lipid metabolism, with a wide range of relative concentration differences in di- and triacylglycerides, sphingolipids, ceramides, cardiolipins and glycerophospholipids.

This study has shown that these tumours are metabolically distinct and offer the opportunities for stratified diagnosis and treatment. Some of the observed changes in relative concentration between the tumours reflect findings from spectroscopic studies, particularly with regards to taurine which is known to be higher in medulloblastoma. The ability of mass spectrometry to identify and measure lipid species and low concentration metabolites from tissue could allow targetable metabolic differences to be characterised and exploited.

18th International Symposium on Pediatric Neuro-Oncology, Denver, 2018, Abstract 2

Ex vivo tissue metabolite profiles predict progression free survival in paediatric cerebellar pilocytic astrocytomas

Christopher D Bennett[1,2], Sarah Kohe[1,2], Simrandip K Gill[1,2], Neelakshi Ghosh[1,2], Karen Manias[1,2], Adam Oates[2], Martin English[2], Jenny Adamski[2], Daniel A Tennant[3], Andrew C Peet[1,2]

[1]Institute of Cancer and Genomic Sciences, University of Birmingham, UK

[2]Birmingham Children's Hospital, Birmingham, UK

[3]Institute of Metabolism and Systems Research, University of Birmingham, UK

Pilocytic astrocytomas are the most common brain tumours arising in children, accounting for ~18% of primary brain tumours. 42% are cerebellar in origin and, whilst they have an excellent 10 year overall survival rate of >90%, progression free survival for these tumours is variable. Identifying tumours more likely to progress will help define those requiring more aggressive treatment.

Metabolite profiles were obtained from 23 cerebellar pilocytic astrocytomas using High Resolution Magic Angle Spinning NMR (HR-MAS). Cox regression tested the ability of individual metabolites to predict progression free survival. Progression was defined as the time point at which the local MDT decided to further treat the tumour.

Low normalised tissue glutamine concentration was found to be associated with a poorer progression free survival ($P<0.05$, $HR=4.58$). Glutamine was found to significantly negatively correlate with glutamate ($P<0.05$, $R^2=-0.48$), suggesting a metabolic link between the

metabolites and a mechanism for low glutamine in high risk tumours. Greater post-surgical residual was associated with poorer progression free survival (log-rank $P<0.05$) in this cohort; however, there was no significant correlation between the size of residual tumour and glutamine.

This study has shown that metabolite concentrations obtained from tissue samples are associated with progression free survival of cerebellar pilocytic astrocytoma patients. Low glutamine has previously been associated with worse overall survival in children's brain tumours. Knowledge of a higher risk of progression may have altered the clinical management of one patient in our cohort with disease progression. HR-MAS acquires data in minutes, and could detect high risk tumours intraoperatively.